Interface magnetism in Co/CoO core-shell nanoparticles and their transformation to pure metallic nanoparticles

Vom Fachbereich Physik
der Universität Duisburg-Essen
(Campus Duisburg)
zur Erlangung des akademischen Grades eines
Doktors der Naturwissenschaften
genehmigte Dissertation

von

Ulf Wiedwald

aus

Bremen

Referent	:	Prof. Dr. Michael Farle
Korreferent	:	Prof. Dr. Wolfgang Kleemann
Tag der mündlichen Prüfung	:	10. Dezember 2004

Dedicated to my parents

Zusammenfassung

Monodisperse magnetische Nanopartikel haben in den letzten Jahren großes wissenschaftliches Interesse geweckt. Die Kontrolle über die Monodispersität der Partikel und ihre Oberflächenbeschaffenheit führt zu einer Reihe nanotechnologischer Anwendungen. Ihr Einsatz als nicht-flüchtige Datenspeichermedien und als Sensoren steht im Focus industrieller Forschung. Magnetische Nanopartikel stehen ebenfalls kurz vor dem routinemäßigen Einsatz in der Behandlung von Tumoren, beim Bio-Labelling und als Kontrastmittel in der Kernspintomographie. Nanopartikel werden mit wachsendem Interesse auch in der Grundlagenforschung benutzt, um die Lücke zwischen Atom- und Festkörperphysik zu schließen. Intrinsische magnetische Größen wie die magnetokristalline Anisotropie, das magnetisches Moment pro Atom und die Curie Temperatur hängen insbesondere von der Größe der Partikel ab.

Die vorliegende Arbeit beschäftigt sich mit magnetischen Co/CoO Kern-Hülle Nanopartikeln im Größenbereich von 9-14 nm. Die Nanopartikel sind mit Hilfe chemischer Methoden hergestellt worden und zeichnen sich durch einen hohen Grad der Monodispersität ($\sigma < 10\%$) aus. Die untersuchten kolloidalen Partikel bestehen aus einem fcc-artigen ferromagnetischen Co Kern, der von einer natürlich gewachsenen CoO Hülle umgeben ist. Das Hauptziel dieser Arbeit besteht in der direkten Korrelation von Struktur und Magnetismus der Partikel. Zum besseren Verständnis des Einflusses der antiferromagnetischen Hülle und der Co/CoO Grenzschicht auf die magnetischen Eigenschaften wurden ebenfalls metallische Co Partikel untersucht. Diese sind durch die Reduktion der oxidischen Hülle mit Hilfe eines reaktiven Plasmas hergestellt worden. Ein ferromagnetisch/antiferromagnetisch austauschgekoppeltes System zeigt einen zusätzlichen unidirektionalen Beitrag zur magnetischen Gesamtanisotropie, der über den so genannten "Exchange Bias" gemessen werden kann. Eine allgemeine Beschreibung der Austauschanisotropie an Grenzflächen zwischen Ferromagnet und Antiferromagnet ist bisher nicht gelungen, da der Exchange Bias sehr stark von der Beschaffenheit der Grenzschicht abhängt. Um den Grenzschichtmagnetismus zu untersuchen, werden Techniken benötigt, die den direkten Zugang zur Grenzschicht ermöglichen. Zum Vergleich mit metallischen Partikeln ist es wünschenswert, die Oxidhülle zu reduzieren, ohne dabei Co Atome zu entfernen.

Das System Co/CoO mit typischen CoO Schichtdicken von 2-3 nm ist ein Prototypsystem zur Untersuchung des Exchange Bias. Wie in dieser Arbeit dargestellt, zeigen die Partikel verglichen mit Filmen einen sehr großen Exchange Bias von bis zu $\mu_0 H_{EB}$ = 0,4 T bei einer Temperatur von 10 K. Die mikroskopischen Größen, die den Exchange Bias bestimmen, sind (i) die magnetischen Momente der Atome im Kern und der Hülle, (ii) die Anzahl der beitragenden Grenzschichtmomente und (iii) die magnetische Anisotropien von Co and CoO. Zum quantitativen Verständnis der Austauschanisotropie im untersuchten System wird die genaue Kenntnis des magnetischen Moments und seines Orbitalbeitrags als Maß für die magnetische Anisotropie benötigt.

Zwei Messtechniken, die diese Informationen liefern sind die Ferromagnetische Resonanz (FMR) und der Röntgenzirkulardichrismus (XMCD). Beide Verfahren erlauben die Bestimmung des Verhältnisses von Bahn- zu Spinmoment. FMR ist sensitiv auf den ferromagnetischen Kern während XMCD im eingesetzten Messmodus oberflächensensitiv ist. XMCD erlaubt dabei - wie in dieser Arbeit deutlich gezeigt - das Separieren des magnetischen Signals der Grenzschicht. Aus der besonderen Kombination beider Techniken bestimmt sich das magnetische Moment eines ferromagnetischen Kerns ($\geq$ 5 nm) als fcc volumenartig während an der Grenzschicht unkompensierte Co^{2+} Momente mit großem Orbitalbeitrag vorliegen. Diese sind dabei *parallel* an den ferromagnetischen Kern gekoppelt. Die effektive magnetische Anisotropieenergiedichte von Co/CoO Partikeln ist mit Hilfe der FMR zu $K^{eff} = 9\mu$eV/Atom bei 15 K bestimmt worden. Dieser Wert ist viel kleiner als der hcp-artige Volumenwert von Co von 65 μeV/Atom [1] und liegt sehr nahe am fcc-artigen Volumenwert von 8,5 μeV/Atom [2]. Das magnetische Altern der Nanopartikel unter Laborbedingungen ist mit frequenzabhängiger FMR in einem Zeitraum von 18 Monaten nach der Probenpräparation untersucht worden. Nach der Deposition stellt sich innerhalb von Stunden eine Hüllenstärke von 2,0-2,5 nm ein, die nach drei Wochen auf circa 3 nm anwächst. Ab diesem Zeitpunkt wirkt die Hülle als selbstpassivierende Schutzschicht auf den ferromagnetischen Kern und die fortschreitende Oxidation verlangsamt sich auf einige Atome pro Tag. Dieses Experiment zeigt, dass FMR Untersuchungen ebenfalls zur Bestimmung kleiner struktureller Veränderungen genutzt werden können.

Zur Messung der magnetischen Eigenschaften von rein metallischen Nanopartikeln sind die Co/CoO Partikel mit Hilfe des reaktiven Plasmaätzens *in-situ* (i) durch Sauerstoffplasma von ihrer Ligandenhülle befreit und (ii) durch Wasserstoffplasma vollständig reduziert worden. Diese Methode erlaubt die Oberflächenmodifikation einzelner Partikel ohne Agglomeration oder Bewegung der Partikel auf dem Substrat bis zu Bedeckungen nahe einer Monolage. Leicht größere Bedeckungen führen zum Versintern der Partikeln in der oberen Lage während die Partikel in der unteren Lage durch den Kontakt zum Substrat fixiert sind. Durch das ent-

fernen der organischen Hülle bildet sich ein Zweilagensystem, das senkrecht zum Substrat eine "gerichtete" Austauschkopplung der Partikel zeigt. An diesem Partikelsystem wurden elementspezifische Hysteresen aufgenommen und die Probenmorphologie genauestens untersucht. Die Resultate sind als Parameter in Simulationen eingeflossen, die den Landau-Lifshitz-Gilbert Ansatz zur Beschreibung der Bewegung der Magnetisierung folgen. Die Berechnungen zeigen, dass (i) die metallischen Partikel ein sehr kleines K^{eff} von 1,5 μeV/Atom aufweisen und (ii) die Stärke der Austauschkopplung es nahe legt, dass im Mittel nur vier atomare Paare an der Grenzschicht zwischen Partikeln aus unterer und oberer Lage austauschgekoppelt sind. Das magnetische Moment der rein metallischen Partikel wird mit XMCD auf 1.56 μ_B/Atom an Einzellagen bestimmt. Die Reduktion im Vergleich zum Volumenwert von 1.72 μ_B/Atom resultiert aus dem Beladen der Partikel mit Protonen durch das Wasserstoffplasma. Durch das Anlassen bei 950 K konnte der Wasserstoff ausgetrieben werden. Hiernach wird ein magnetisches Moment von 1.83 μ_B/Atom beobachtet. Diese Erhöhung zum Volumenwert kann auf den Anteil der Oberflächenatome von circa 10% zurückgeführt werden. Die reduzierte Symmetrie der Oberflächenatome manifestiert sich in der Erhöhung ihres Bahnmoments. In zukünftigen Untersuchungen kann die Oberflächenanisotropie von rein metallischen Partikeln bestimmt werden. Im Vergleich zu ultradünnen Filmen haben Nanopartikel den Vorteil, dass die Kontaktfläche zum Substrat sehr klein ist und somit der Einfluss der Grenzschicht Substrat/Ferromagnet vernachlässigt werden kann.

Um magnetische und strukturelle Eigenschaften der Nanopartikel zu korrelieren, sind detaillierte strukturelle Untersuchungen mit Hilfe der Transmissionselektronenmikroskopie (TEM) durchgeführt worden. Hochauflösende TEM zeigte, dass die Co/CoO Partikel im Kern aus vielfach verzwillingten fcc-artigen Co Kristalliten bestehen, während die fcc-artige CoO Hülle polykristallin ist. Die Schichtdicke der CoO Hülle ist mit Hilfe energiegefilterter TEM zu 2-2,5 nm bestimmt worden. Die passivierende Hülle umschließt dabei in Abhängigkeit des Gesamtdurchmessers einen 5-9 nm starken Co Kern. Aus diesen Resultaten lässt sich folgern, dass die geringe effektive magnetische Anisotropieenergiedichte K^{eff} = 1,5 μeV/Atom der metallischen Partikel auf die vielfach verzwillingte Struktur zurückzuführen ist. Einzelne Kristallite mit zufällig verteilten Anisotropieachsen reduzieren K^{eff} erheblich und bilden pro Nanopartikel eine effektive uniaxiale Anisotropie. Für Co/CoO Partikel bewirkt die CoO Hülle eine Erhöhung von K^{eff}, wodurch die Partikel magnetisch gehärtet werden.

Summary

Monodisperse magnetic nanoparticles have generated huge interest in applied research within the last years. The control of their monodispersity and surface properties leads to a variety of nanotechnological applications. The use as non-volatile data storage media and sensor applications are in the focus of industry. Moreover, magnetic nanoparticles are close to be employed in tumor therapy, bio-labelling or contrast agents in magnetic imaging. To an increasing extend these are studied in fundamental research as well, since nanoparticles with diameters of a few nm bridge the gap between atomic and solid state physics. In particular, the intrinsic magnetic properties of fine particles such as the magnetocrystalline anisotropy, the saturation magnetization and the Curie temperature are affected by the reduction of their size.

The subject of this thesis is the investigation of magnetic Co/CoO core-shell nanoparticles and metallic Co nanoparticles with diameters in the range of 9-14 nm. The nanoparticles have been prepared by means of organometallic synthesis, and they exhibit a high degree of monodispersity ($\sigma < 10\%$). The colloidal Co/CoO nanoparticles consist of a fcc ferromagnetic Co core covered with a naturally formed antiferromagnetic CoO shell. The main purpose of this study is the direct correlation of structure and magnetism in the particles. For better understanding of the influence of the antiferromagnetic shell and the Co/CoO interface on the magnetism of the particles pure metallic Co nanoparticles were studied. These have been prepared from Co/CoO particles by reduction of the oxidic shell with a reactive plasma treatment. A ferromagnetic/antiferromagnetic exchange coupled system shows an additional unidirectional contribution to the total magnetic anisotropy energy which can be measured by the so-called exchange bias. A general description of exchange anisotropy at ferromagnetic/antiferromagnetic interfaces is still lacking, since exchange bias strongly depends on the interface conditions. To address the interface magnetism explicitly, techniques have to be applied which give direct access to the interface. For direct comparison to metallic nanoparticles it is desirable to have control on the oxide shell without any loss of Co atoms.

The system Co/CoO with typical layer thicknesses of 2-3 nm of the antiferromagnet CoO is a prototype for exchange bias. As shown in this thesis, the nanoparticles present a very strong exchange bias of $\mu_0 H_{EB}$ = 0.4 T at 10 K compared to Co/CoO thin films. The microscopic quantities which govern the exchange bias are (i) the magnetic moments of the core and the shell Co atoms, (ii) the number of contributing interface moments, and (iii) the magnetic anisotropies of Co and CoO. The magnetic moment and its orbital contribution are quantitatively measured to understand the microscopic mechanisms which determine the exchange bias and the magnetic anisotropy energy.

Two techniques which provide the necessary information with submonolayer sensitivity are Ferromagnetic Resonance (FMR) and X-ray Magnetic Circular Dichroism (XMCD). Explicitly, the ratio of orbital-to-spin magnetic moment can be measured. FMR probes the ferromagnetic core, only, while XMCD in the total electron yield mode is surface sensitive and - as demonstrated in this thesis - can be employed to extract the contribution of buried interfaces. The unique combination of both techniques yields a fcc bulk-like Co magnetic moment of a ferromagnetically ordered Co core ($\geq$ 5 nm) and uncompensated Co^{2+} moments at the Co/CoO interface carrying a large orbital moment. XMCD studies at two different oxide shell thicknesses show that the interface moments are coupled *parallel* to the core. The effective magnetic anisotropy energy of Co/CoO particles has been determined by FMR to K^{eff} = 9 μeV/atom at T = 15 K which is much smaller than the hcp bulk value of 65 μeV/atom at T = 0 K [1] and surprisingly matches the fcc bulk Co value of 8.5 μeV/atom [2]. By frequency-dependent FMR in ambient conditions in a 18 months period of time after sample preparation, it has been measured that directly after the deposition of the particles on a substrate a 2-2.5 nm thick CoO shell forms within hours. After three weeks the shell grows to about 3 nm. From this point of time on the CoO shell acts as a self-passivating layer for each individual particle. The oxidation slows down to a few atoms per day. This experiment demonstrates that small structural modifications can be addressed by FMR investigations.

In order to verify and to compare the results of Co/CoO particles to pure metallic particles, an *in-situ* reactive plasma etching process has been employed. By successive oxygen and hydrogen plasma exposure it was possible (i) to remove the organic ligands and (ii) to reduce the entire CoO to metallic Co. This method allowed the controlled modification of the surface without any agglomeration or movement of the particles on the substrate for coverages up to one monolayer. Slightly larger coverages admitted to partial sintering of particles in a top layer while particles in the bottom layer remained fixed to the substrate. The removal of the organic ligands led to the formation of a double layer system which shows exchange coupling between particles perpendicular to the substrate. Using detailed structural and morphological studies as

input parameters for theory, Landau-Lifshitz-Gilbert type of simulations have been performed to simulate element-specific hysteresis loops. The calculations have shown that (i) the metallic particles exhibit a low effective magnetic anisotropy energy density K^{eff} = 1.5 μeV/atom at T = 15 K which is less than 20% of the fcc bulk Co anisotropy constant. (ii) The exchange coupling strength suggests that in medium only four atomic pairs of Co atoms are exchange coupled at the interface between top and bottom layer particles. The magnetic moment of the metallic particles has been determined to be 1.56 μ_B/atom by means of XMCD investigations on monolayer samples. The reduction compared to the bulk magnetic moment of 1.72 μ_B/atom has been assigned to the hydrogen-load of particles during the hydrogen plasma exposure. Annealing at T = 950 K successfully dissociates cobalt hydride and forms pure Co nanoparticles and a total magnetic moment of 1.83 μ_B/atom has been found. The enhancement compared to the bulk magnetic moment can be explained by the contribution of about 10% surface atoms in reduced symmetry which is manifested in an enhanced orbital moment. In future studies the surface anisotropy can be measured in pure metallic nanoparticles. Compared to ultrathin films the nanoparticle approach has the big advantage that the contact area to the substrate is very small and thus the influence of the substrate/ferromagnet interface is negligible.

To correlate the magnetic properties to the structure of the nanoparticles detailed transmission electron microscopy (TEM) investigations have been performed. High-resolution TEM has shown that the Co/CoO particles consist of multiply twinned fcc Co core and a multigrain fcc CoO shell. The thickness of the CoO shell has been determined to be 2-2.5 nm by energy-filtered TEM. The passivating CoO shell encases a metallic Co core of 5-9 nm depending on the total particle diameter. With these results the low effective magnetic anisotropy energy density K^{eff} = 1.5 μeV/atom found for metallic Co nanoparticles can be explained by the multiply twinned structure of the ferromagnet. Individual grains with randomly oriented anisotropy axes reduce K^{eff} remarkably and produce an effective uniaxial anisotropy. In the case of Co/CoO nanoparticles the oxide shell increases K^{eff} which results in a magnetic hardening.

Contents

Preface

The magnetism of small particles has been investigated over many decades. The sizes which can be prepared and are of technological interest range from clusters consisting of a few atoms to nanoparticles and colloids of a few micrometer diameter. Magnetic nanoparticles are of interest not only for applied research but to an increasing extend also for fundamental studies. The reason for this trend is that besides being promising candidates to further increase the density of magnetic storage devices towards the TBit/inch^2 range or for medical applications, nanoparticles with diameters of a few nm bridge the gap between atomic and solid state physics. All efforts on a detailed understanding of the magnetism of individual particles are hindered by the fact that particles prepared by cluster beam techniques or organometallic synthesis are never perfectly alike. Hence, the magnetic characterization average over the properties of particles with different sizes, surface conditions and shapes. For sufficiently small size distributions, however, the measurements yield general conclusions which are based on the increasing importance of finite-size effects in smaller particles.

As for smaller particles the ratio of surface-to-volume atoms increases, they allow to study surface effects on a variety of fundamental physical properties. In the case of magnetic nanoparticles surface magnetism can be studied. Often large surface magnetic anisotropies being accompanied by an enhanced orbital contribution to the magnetic moment at the surface, i. e. orbital magnetism can be investigated. In this thesis Co nanoparticles with diameters 9-14 nm and sharp size distributions are studied. The particles have been prepared by means of colloidal chemistry. Due to the preparation technique natural surface oxidation cannot be avoided and consequently core/shell particles have been formed. Each particle consists of a ferromagnetic core and an antiferromagnetic shell. Due to the core/shell structure of the particles one expects the presence of an exchange anisotropy. The exchange anisotropy governs the exchange bias. Also the orbital moment will be different at the interface as compared to the inner region of the particle. As the anisotropy of the orbital moment is connected to the magnetic anisotropy energy, a measurement of this fundamental quantity provides also information on the environment that is seen by the atomic magnetic moments within the particle core. The methods of

choice to address the above mentioned points are ferromagnetic resonance (FMR) and x-ray magnetic circular dichroism (XMCD). The correlation of magnetism and structure of the particles is achieved by detailed transmission electron microscopy (TEM) and scanning electron microscopy (SEM) studies. Reactive plasma etching allows to (i) remove the organic ligands surrounding each nanoparticle and (ii) reduce the CoO surface layer. Consequently, pure metallic particles can be investigated.

In chapter 1 of this thesis the fundamental physical quantities magnetic moment and magnetic anisotropy and their evolution with particle size are discussed as a general introduction. The exchange anisotropy in Co/CoO systems is introduced in section 1.4. Chapter 2 describes the experimental techniques FMR and XMCD. The organometallic synthesis of Co/CoO core-shell nanoparticles is presented in chapter 3. Detailed structural and morphological investigations are presented in chapter 4. Different sample preparation techniques and the self-assembly of particles have been evaluated by means of TEM, SEM, and atomic force microscopy (AFM). The effect of surface cleaning by Ar^+ ion etching and the reactive plasma etching has been tracked by x-ray absorption spectroscopy (section 4.3). The main part of this thesis is the discussion of the magnetic properties of Co/CoO core-shell nanoparticle investigated by FMR, XMCD and SQUID magnetometry (chapter 5). Firstly, the individual properties like magnetic blocking, the orbital contribution to the total magnetic moment, the exchange bias, the magnetic anisotropy, the magnetization dynamics and the nanoparticle aging are addressed. Secondly, the magnetic response of ordered 3d rod structures are examined. By reactive plasma exposure the oxide shell can be reduced. In chapter 6 the magnetic moment of metallic particles are determined from XMCD measurements by means of magneto-optical sum rules. Moreover, the plasma treatment can be employed to form exchange coupled double layer structures. The hysteresis loops of such a double layer sample has been recorded under UHV conditions and simulated by micromagnetic calculations based on the structural and morphological findings.

Abbreviations

AFM	Atomic Force Microscopy
EDX	Energy Dispersive X-ray Analysis
EELS	Electron Energy Loss Spectroscopy
EF-TEM	Energy-filtered Transmission Electron Microscopy
EPR	Electron Paramagnetic Resonance
FC	Field Cooling
FMR	Ferromagnetic Resonance
FWHM	Full Width at Half Maximum
HR-TEM	High-resolution Transmission Electron Microscopy
MAE	Magnetic Anisotropy Energy
SAED	Selected Area Electron Diffraction
SEM	Secondary Electron Microscopy
SQUID	Superconducting Quantum Interference Device
TEM	Transmission Electron Microscopy
TEY	Total Electron Yield
UEA	Unidirectional Exchange Anisotropy
XAS	X-ray Absorption Spectroscopy
XMCD	X-ray Magnetic Circular Dichroism
ZFC	Zero Field Cooling

1. General Introduction

1.1. From the Atom to the Solid State: Magnetic Moment of 3d Transition Metals Fe, Co, and Ni

The magnetism of single atoms has three different origins: The intrinsic spin of the electrons, their motion around the nucleus (orbital momentum) and the appearance of a non-zero orbital momentum in an external magnetic field [3]. The latter is a general property of matter and the magnetic moment is induced antiparallel to the applied magnetic field. This phenomenon is called diamagnetism. Atoms with completely filled shells which carry no net magnetic moment exhibit this diamagnetic behavior only. Materials which have at least one incompletely filled shell possess intrinsic magnetic moments which align parallel to an external field (paramagnetism). In the following the discussion is concentrated on paramagnetic atoms only. Iron, Cobalt, and Nickel are paramagnetic atoms with an incompletely filled 3d shell. These classical materials show ferromagnetism in the solid state at room temperature. In this section the evolution of the magnetic moment from the single isolated atom to the solid state is discussed.

Single Atoms and Ions

For not too heavy elements the electronic configuration of multi electron atoms can be described by the Pauli exclusion principle and the three Hund's rules. The spin momentum $\vec{s_i}$ and the orbital momentum $\vec{l_i}$ of all individual electrons in an incompletely filled shell of the atom couple within the Russel-Saunders coupling scheme by their vector sums [4]:

$$\vec{S} = \sum_i \vec{s_i} \quad \text{and} \quad \vec{L} = \sum_i \vec{l_i} \tag{1.1}$$

and the total spin momentum and the total orbital momentum are coupled by spin-orbit interaction. Similar to the one electron formalism the resultant atomic momenta S and L couple

to give a resultant total angular momentum J:

$$J = L + S \tag{1.2}$$

The Russel-Saunders coupling scheme is illustrated in Figure 1.1 for a two electron system. This scheme is based on the fact that the electrons are dominated by electrostatic interaction between them. It is valid for light elements including the 3d transition metal series. This finding motivates the order of summing up the individual orbital momenta and the individual orbital momenta to the resultant total angular momentum J. All experiments only measure the z-component of the total angular momentum J_z along the axis of the negative external field $-H$.

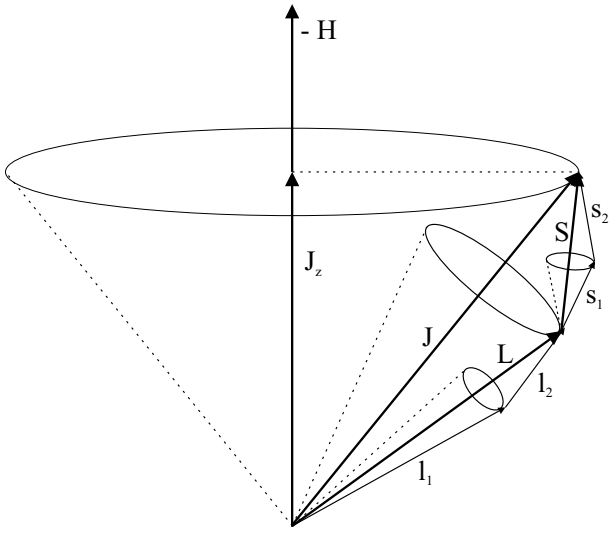

Figure 1.1.: Russel-Saunders coupling of two spins and the two orbits forming a total angular momentum J of unpaired electrons in an atom.

For the heavy elements with larger spin-orbit interaction the individual spin-orbit interactions are treated first, before the sum of the total angular momenta of all the electrons $\sum \vec{j}_i$ is calculated. This type of interaction is called j-j coupling. However, all the phenomena discussed in this thesis are based on the light elements where the L-S coupling represents the valid description.

The total magnetic moment μ_{tot} of a free atom [5] can be calculated using the simple equation:

$$|\mu_{tot}| = g \cdot \sqrt{J(J+1)}\mu_B \tag{1.3}$$

where g is the Landé factor:

$$g = 1 + \frac{J(J+1) + S(S+1) - L(L+1)}{2 \cdot J(J+1)} \tag{1.4}$$

Table 1.1.: Electronic configurations of free transition metal atoms and the resulting quantum numbers L, S, and J according to Hund's rules and their corresponding ground term. The Landé g-factor and the resulting total magnetic moment μ_{tot} are also given.

Element	Configuration	S	L	J	Ground Term	g	μ_{tot}
Iron	$3d^6 4s^2$	2	2	4	$^5D_4$	3/2	6.71 μ_B
Cobalt	$3d^7 4s^2$	3/2	3	9/2	$^4F_{9/2}$	8/6	6.63 μ_B
Nickel	$3d^8 4s^2$	1	3	4	$^3F_4$	5/4	5.59 μ_B

The g-factor would be 1 for pure orbital magnetism and 2 for pure spin magnetism which is the free electron value of g. These equations only hold as long as L and S are good quantum numbers and the coupling follows the third Hund's rule ($J = L - S$ for less than half full shells and $J = L + S$ for all other cases), which means that the atom is in its ground state. In table 1.1 the electronic configurations, the quantum numbers and the ground term for Fe, Co, and Ni are presented. From the quantum numbers the total magnetic moment μ_{tot} and the Landé g-factor can be calculated from equations 1.3 and 1.4. The values of μ_{tot} and g are also given in table 1.1. The orbital μ_L and the spin μ_S magnetic moment can be calculated from $\mu_L = -g_L\langle L_z\rangle$ and $\mu_S = -g_S\langle S_z\rangle$, respectively. One may note that in literature sometimes the ratio of expectation values $\langle L_z\rangle/\langle S_z\rangle$ is used to discuss the orbital contribution to the magnetic moment as in [6], for example. In this thesis the ratio of orbital-to-spin magnetic moment μ_L/μ_S is employed.

The calculations of the g-factor and the total magnetic moment μ_{tot} can be adapted to free ions. For example, a free Co^{2+}-ion gives identical results compared to a free Co atom, since the two 4s electrons do not give any contribution to the magnetic moment if the (small) hybridization of 3d/4s states is neglected. A free Fe^{3+}-ion has a $^6\mathrm{S}_{5/2}$ ground term and a g-factor of 2. These ground state calculations are correct for free atoms and ions where a spherical potential can be used. When paramagnetic impurities are studied in a host crystal the potential must be adapted to the crystal structure of the host. For example, the total magnetic moment of Co^{2+} impurities is found to be $\mu_{tot} \approx 4.8\mu_B$ depending on the studied system (see e. g. [7]). It is found to be significantly reduced compared to the free ion magnetic moment. Due to the high degree of symmetry of the surrounding atoms the orbital moment is partly quenched [8].

Clusters of Atoms

The study of the size-dependence of the magnetic moment in free metallic clusters is a very intuitive way of understanding the coupling mechanism between atoms. Neglecting the orbital

magnetic moment one finds within the Heisenberg model that the exchange interaction H_{ex} between two spins $S_{i,j}$ of two different atoms can be described by:

$$H_{ex} = -2JS_i \cdot S_j \tag{1.5}$$

where J is the exchange integral. One should note that the magnitude of J is typically 10^3 times larger than the dipole interaction [5]. Parallel alignment of the spins is favoured if $J > 0$, while antiparallel alignment is found for $J < 0$. The exchange interaction is short-range. Within certain size limits - the monodomain limit (discussed in section 1.3) - all spin moments of an agglomerate of Fe, Co or Ni atoms are aligned parallel. On the other hand the total magnetic moment is the sum of the spin moment and the orbital moment. The atoms in a cluster form bonds to their nearest neighbors. The surrounding crystal field partly quenches the orbital magnetism depending on the number of neighboring atoms and their crystal structure. The interplay of Coulomb and exchange interaction determines the shape of the cluster. For example, a cluster of 5 Ni atoms is thought to be a trigonal bipyramid with $\mu_{tot} = 1.8\mu_B$ per Ni atom. If just one atom is added Ni forms a more tightly bound Ni_6 octahedron with $\mu_{tot} = 1.5\mu_B$ per atom [9]. More open surfaces generally yield larger magnetic moments. A Ni_{13} cluster is a icosahedron with one interior atom and 12 atoms at the surface showing a small total magnetic moment of approximately $1\mu_B$ per atom. [9]. Closed-shell structures have also been found for Ni_{55} and Ni_{147} where the next shells are closed. Generally, the ratio of surface-to-volume atoms decreases and the magnetic moment reduces slowly to the bulk magnetic moment. In table 1.2 some results of the dependence of the magnetic moment of the cluster size are summarized. Clusters of 25 Fe atoms have shown a total magnetic moment of $\mu_{tot} = 3\mu_B$ per atom while the bulk value

Table 1.2.: Magnetic moment per atom of free metal clusters of Fe, Co, and Ni. All cluster experiments used a Stern-Gerlach-type magnetic deflection setup.

Element	Number of Atoms	magn. Moment	Reference
Fe	25	$3\mu_B$	[10]
	500	$2.2\mu_B$	[10]
	bulk	$2.22\mu_B$	[3]
Co	115	$2.1\mu_B$	[11]
	56-215	$2.2\mu_B$	[12]
	bulk	$1.72\mu_B$	[3]
Ni	5	$1.8\mu_B$	[9]
	740	$0.68\mu_B$	[9]
	bulk	$0.61\mu_B$	[3]

of $2.2\mu_B$ per atom has already been reached at a cluster size of about 500 atoms [10]. Co_{115} clusters carry a magnetic moment of $115 \times 2.1\mu_B$ [11]. Furthermore, it has been found that Co clusters with 56 to 215 atoms show a constant magnetic moment per atom of $\mu_{tot} = 2.2\mu_B$ [12]. The decrease of the magnetic moment with growing cluster sizes for Co has been determined to be less dramatic than for Fe. In the case of Ni clusters the magnetic moment gradually declines from $0.8\mu_B$ to $0.7\mu_B$ per atom for Ni_{210} and Ni_{740} clusters, respectively. Additionally a decrease of the Curie temperature T_C from 627 K in bulk Ni to 353 K in the Ni_{740} clusters has been reported [9].

Another approach to study the magnetism of finite structures is the deposition of single atoms and small clusters on clean surfaces [13,14]. Depending on the surface morphology it is possible to form linear chains, e. g. Co atomic wires on the vicinal Pt(997) surface [15], or two-dimensional oblate clusters like two monolayer thick islands on Au(111) [16,17]. In this case the magnetic moment strongly depends on the substrate. Co atoms or very small clusters on Na films show a reduction of the ratio of orbital-to-spin moment $\mu_L/\mu_S \approx 0.6$ compared to the free atom ratio of $\mu_L/\mu_S = 1$. The reduction is thought to be due to increased hybridization effects with the substrate [18]. A more dramatic result has been found for Ni atoms on *Na*. The impurities show no magnetic response in the x-ray magnetic circular dichroism up to a coverage of 1.2% of a monolayer implying a non-paramagnetic ground state [18]. This finding is explained by the charge transfer from Na to Ni which results in a completely filled 3d shell in Ni.

Nanoparticles

The next larger magnetic object is the magnetic nanoparticle. There is no well defined interval in which the term 'nanoparticle' should be used. The terms 'large cluster' or 'ultrafine nanoparticle' often define species of similar size. Mostly the definition of similar objects depends on the scientists' physical background. In the following, the term nanoparticle is used for the size interval 1.5 nm - 20 nm. A short summary on the evolution of the magnetic moment of metallic nanoparticles is given in table 1.3.

Within the last decade novel nanoparticle preparation techniques and improvements of known synthesis techniques in colloidal chemistry have been developed [21–23]. With these advances it is possible to prepare magnetic nanoparticles with diameters in the range of 1.5 nm to 15 nm with a very narrow size distribution ($\sigma < 5\%$). Monodisperse Co particles have been prepared by decomposition of an organometallic precursor in hydrogen saturated solution in the presence of a stabilizing polymer [19]. It has been reported that these nanoparticles with

Table 1.3.: Reported results of the evolution of the magnetic moment per atom for Co nanoparticles between 150 and 80000 atoms.

Species	No. of Atoms	Diameter d	Shape	μ_{tot} per atom	Ref.
Co in polymer matrix	150	1.5 nm	spherical	$1.94\mu_B(5\mathrm{T})$	[19]
				$2.1\mu_B(30\mathrm{T})$	
	310	2.0 nm	spherical	$1.83\mu_B(5\mathrm{T})$	[19]
				$1.9\mu_B(30\mathrm{T})$	
Co islands	400	$4.0\mathrm{nm} \times 2\mathrm{ML}$	prolate	$2.4\mu_B$	[16]
on $Au(111)$	1300	$7.2\mathrm{nm} \times 2\mathrm{ML}$		$2.2\mu_B$	[16]
	1600	$8.2\mathrm{nm} \times 2\mathrm{ML}$		$2.0\mu_B$	[16]
free Co nano-	80000	12 nm	spherical	$1.7\mu_B$	[20]
particles on SiO_2					

150 atoms and 310 atoms per particle do not show oxidation in the stabilizing polymer. The magnetic moments per Co atom in the particle are $1.94\mu_B$ per atom and $1.83\mu_B$ per atom in an applied magnetic field of 5 T, respectively. It has been proven that in this case the influence of the polymers is rather small. There is supposedly no influence on the magnetic moment of surface atoms. In even higher fields up to B = 30 T one finds a linear enhancement of the magnetic moment per atom to $2.1\mu_B$ per atom and $1.9\mu_B$ per atom for the Co nanoparticles with 150 and 310 atoms, respectively [19]. This enhancement is explained by an alignment of non-collinear surface spins due to a strong uniaxial surface anisotropy. Comparable magnetic objects with a similar number of atoms per particle are Co islands on $Au(111)$ surfaces. Prolate particles with a thickness of two monolayers and about 400, 1300, and 1650 atoms per island carry a magnetic moment per atom of $2.4\mu_B$, $2.2\mu_B$, and $2.0\mu_B$, respectively [16]. Here, practically all atoms within the Co islands are arranged in reduced coordination which results in a higher magnetic moment per atom than even for smaller spherical nanoparticles [19]. Much larger Co nanoparticles on SiO_2 with a medium diameter of 12 nm that corresponds to approximately 80000 atoms already show a bulk-like magnetic moment ($\mu_{tot} = 1.7\mu_B$ per atom) [20].

In summary, finite structures, e. g. spherical nanoparticles with diameters smaller than 5 nm, show an enhanced total magnetic moment per atom. The microscopic origin is the reduced dimensionality. As long as the ratio of surface-to-volume atoms remains large ($\geq 10\%$) an enhancement of the total magnetic moment per atom - due to the atoms in reduced symmetry - is detected. Larger magnetic structures are dominated by the huge number of volume atoms showing a bulk-like total magnetic moment.

Solid State

The magnetic properties of the room-temperature ferromagnets Fe, Co, and Ni are well understood. In a first approximation, the magnetic moment per atom is temperature-independent. This statement holds as long as no structural changes or melting of the specimen takes place. However, the macroscopic magnetization (A/m), which usually is the measured quantity, is temperature-dependent. The ground state magnetic moment can be determined from the magnetization M at T = 0 K, where all moments of the ferromagnet are aligned. At higher temperatures the magnetic moments start to fluctuate, spin waves are excited thermally, and only the average magnetization is detected. Therefore the magnetization decreases with increasing temperature. At the Curie temperature T_C the thermal energy overcomes the exchange coupling and the individual magnetic moments can rotate independently. Above the Curie temperature the magnetization of the sample vanishes, which does not mean that the magnetic moments of the paramagnet vanish, too. For the itinerant 3d transition metals the ferromagnetic properties are listed in table 1.4.

Table 1.4.: Solid state properties of the room-temperature ferromagnets Fe, Co, and Ni [3]. The magnetization M at T = 0 K, the corresponding magnetic moment μ_{tot} per atom and the Curie temperature T_C are listed.

Element	$M(T = 0$ K)	μ_{tot} per atom	T_C
Fe	1740 kA/m	$2.22\mu_B$	1043 K
Co	1446 kA/m	$1.72\mu_B$	1388 K
Ni	510 kA/m	$0.61\mu_B$	627 K

1.2. Cobalt Oxides

Two different Co oxides exist: CoO and Co_3O_4. Cobaltmonoxide (CoO) is an insulator and crystallizes in the rocksalt structure showing a lattice constant a = 0.42614 nm at 305 K [6]. An ionic bond between Co^{2+} and O^{2-} is formed. In the antiferromagnetic state below the Néel temperature $T_N \approx 293$ K CoO shows a monoclinic structure that can be described as a large tetragonal distortion along the cube's edges with c/a < 1 with an additional small deformation along the $\langle 111 \rangle$ direction [24]. At 10 K the cell parameters of the deformed face-centered lattice are determined to a = 0.42666 nm and c = 0.42151 nm which corresponds to a ratio c/a = 0.988 [6].

Table 1.5.: Theoretical and experimental results of the spin μ_S and the orbital μ_L contribution to the total magnetic moment μ_{tot} per Co atom in CoO. The magnetic moments of free Co^{2+} and Co^{3+} ions are also listed using Hund's rules. Note that the spin and orbital magnetic moment are generally not parallel. Thus, the total magnetic moment is calculated by equation 1.3 taking into account the Landé g factor.

Method	$\mu_S(\mu_B)$	$\mu_L(\mu_B)$	$\mu_{tot}(\mu_B)$	$\mu_L/\mu_S(\mu_B)$	Ref.
LSD	2.38	0.25	2.63	0.11	[25]
LSD+OP	2.52	1.01	3.53	0.4	[25]
XMCD in nanoparticles				0.6-1.1	[26]
γ-ray diffraction	2.40	1.58	3.98	0.66	[6,24]
Co^{2+} using Hund's rules	3	3	6.63	1	[3]
Co^{3+} using Hund's rules	4	2	6.71	0.5	[3]

In the antiferromagnetic state the Co moments are coupled ferromagnetically in $\{111\}$ planes with the moments in adjacent $\{111\}$ planes aligned antiparallel. The ionic quasi-octahedral environment deforms the 3d orbitals compared to the free Co^{2+} ion. An insulating gap of 0.4 eV width has been calculated by the local spin density (LSD) approach [25]. The quenching of the orbital magnetic moment in CoO is incomplete. Thus, Co^{2+} ions carry a large magnetic moment with a large orbital moment. LSD calculations including an orbital polarization correction OP [25] show a smaller orbital contribution to the total magnetic moment than the experiment. In table 1.5 some theoretical and experimental results on the magnetic moments of CoO are listed.

Co_3O_4 has a spinel structure. Unlike the rocksalt monoxide CoO, which has only a single type of cobalt ions (Co^{2+}) located at octahedral lattice sites, the Co_3O_4 has both octahedral Co^{3+} and tetrahedral Co^{2+} sublattices. The lattice constant is a = 0.809 nm [27]. The spinel Co_3O_4 is antiferromagnetic, too. The Néel-Temperature $T_N = 40K$ is remarkably reduced compared to CoO.

1.3. Magnetic Anisotropy of Nanoparticles: Individual Properties and Collective Phenomena

The ground state of a magnetic system is generally not invariant to the rotation of the magnetization. This effect is named magnetic anisotropy. The energy density difference between the total magnetic ground state (easy axis of magnetization) and the energy density in any other

specific direction is the so-called total magnetic anisotropy energy density. Usually this difference is given by two distinct directions in a crystal. The two microscopic origins of magnetic anisotropy are the dipole-dipole interaction between the magnetic moments and the spin-orbit interaction which couples the spins to the lattice. The exchange interaction introduced in equation 1.5 does not contribute to the magnetic anisotropy because the scalar product of the spin vectors is independent of the angles with respect to the crystal axes of the lattice. Dipole-dipole interaction leads to the so-called shape anisotropy and the strength of spin-orbit interaction determines the magnetocrystalline anisotropy energy density (MAE). For Fe, Co, and Ni the magnitude of MAE is on the order of μeV/atom and tiny compared to the total energy of a bulk crystal ($\sim$ 1000 eV / atom). For any magnetic application, however, the MAE is the quantity which determines the easy direction of magnetization, coercive fields, and the thermal stability, for example [19,28].

Magnetic interactions of densely packed particles like Co particle multilayers in a diamagnetic host may lead to interesting phenomena like superspin glass ordering and collective memory effects at low temperatures [29,30]. Therefore, in quasi two-dimensional well-separated arrays of nanoparticles as the ones investigated in this thesis it is useful to split up the different contributions of the total magnetic anisotropy energy density in two categories: (i) the individual magnetic anisotropy of a single nanoparticle and (ii) the magnetic anisotropy due to dipolar interactions and/or percolation of the nanoparticles. Firstly, a short review on the magnetic anisotropy of an individual nanoparticle is given and afterwards the interactions between nanoparticles and their consequences are discussed.

Individual Properties

The source of the so-called shape anisotropy is the long-range dipolar interaction. A magnetic dipole $\vec{\mu_i}$ (Am^2) produces a magnetic field $\vec{H}_i$ (A/m) at distance $\vec{r_i}$:

$$\vec{H}_i(\vec{r}_i) = \frac{3(\vec{r}_i \cdot \vec{\mu}_i) \cdot \vec{r}_i}{r_i^5} - \frac{\vec{\mu}_i}{r_i^3} \tag{1.6}$$

The resulting dipole interaction energy E_{dd} between two dipoles $\vec{\mu}_{i,j}$ at distance $\vec{r}_{ij}$ is:

$$E_{dd} = -\frac{\mu_0}{4\pi}\left(\vec{\mu}_j \cdot \vec{H}_i\right) = \frac{\mu_0}{4\pi}\left(\frac{(\vec{\mu}_i \cdot \vec{\mu}_j)}{r_{ij}^3} - \frac{3(\vec{r}_{ij} \cdot \vec{\mu}_i) \cdot (\vec{r}_{ij} \cdot \vec{\mu}_j)}{r_{ij}^5}\right) \tag{1.7}$$

The magnetic dipoles are located at distinct places within the lattice. Hence, the distance vector $\vec{r}_{ij}$ is correlated to the crystal lattice axes which means that the dipolar interaction energy E_{dd} depends on the relative orientation of the magnetic moment with respect to the crystal axes. The anisotropic part of the shape anisotropy can easily be described in terms of a free energy

density function F approach [31], since the total free energy of a system with constant number of atoms equals the sum of all contributions to the MAE and the shape anisotropy at a constant temperature [32]. For a homogenously magnetized sample the shape anisotropy energy density F_{dd} [33] is given by:

$$F_{dd} = \frac{1}{2}\mu_0(N_x M_x^2 + N_y M_y^2 + N_z M_z^2) \tag{1.8}$$

with the components of the magnetization M_i and the components of the demagnetization tensor N_i which fulfill $N_x + N_y + N_z = 1$. Here, the magnetization M has to be used in units of A/m. The diagonal elements of the demagnetization tensor can be calculated in terms of the general ellipsoid [34]. The demagnetization tensor of a spherical particle and an infinite thin disk are the limiting cases of this general approach. For the infinite thin disk one calculates

$$F_{dd} = \frac{1}{2}\mu_0 M^2 \cos^2\theta \tag{1.9}$$

with $N_x = N_y = 0$ and $N_z = 1$ and the z-component of the magnetization transformed to $M_z = M\cos\theta$. The shape anisotropy always favors an easy direction of magnetization in the film plane.

For a spherical particle where all three principal axes of the ellipsoid have identical lengths it follows from equation 1.8 that $N_x = N_y = N_z = 1/3$. Hence, a spherical particle does not show shape anisotropy. Since the whole thesis deals with imperfectly shaped nanoparticles, one may have to take into account shape effects of individual particles. As an example, an unusual non-spherical nanoparticle investigated in this thesis (chapter 4) has dimensions of $7\ \mathrm{nm} \times 6\ \mathrm{nm} \times 5\ \mathrm{nm}$ of the principal half-axes of an ellipsoid. The ratios of the half-axes a, b, c are

$$\frac{c}{a} \approx 0.71 \quad \text{and} \quad \frac{b}{a} \approx 0.86 \tag{1.10}$$

Tabulated data [34] of the half-axes ratios and the demagnetization factors yield

$$N_x \approx 0.28 \qquad N_y \approx 0.33 \qquad N_z \approx 0.38 \tag{1.11}$$

which give a maximum difference $N_z - N_x = 0.1$. Hence, the shape anisotropy of an extremely non-spherical nanoparticle is 10% of the shape anisotropy of a thin film and cannot be neglected anymore, if the magnetic response of a single nanoparticle is detected. In general, the investigated nanoparticles are closer to spheres. Since all measurements performed in this thesis are averaging over an array of many particles with randomly distributed axes of the ellipsoids the shape anisotropy of a single particle is neglected.

The second source of magnetic anisotropy besides the dipolar interaction is the spin-orbit interaction. The orbital motion of the unpaired electrons is influenced by the electrical field produced by the surrounding atoms in the lattice. The perturbed orbital motion couples the

spins to the lattice. Perturbation theory can be employed to explain this effect. The spin-orbit coupling (LS-coupling) can be approximated by the one electron term $\hat{H} = -\xi \hat{L} \cdot \hat{S}$ where ξ is the spin-orbit coupling constant. The constant ξ is on the order of 0.05 eV that is much smaller than the bandwidth of 3d metals (few eV) [35] justifying this perturbation ansatz. This approach reveals an energy correction of the magnetic ground state in 2^{nd} order for uniaxial symmetries and in 4^{th} order for cubic systems. It has been found that the magnetocrystalline anisotropy energy density (MAE) is proportional to the difference of the orbital magnetic moment in the easy and hard axis of the magnetization

$$MAE = \alpha \cdot \frac{\xi}{4\mu_B} \cdot (\mu_L^{easy} - \mu_L^{hard}) \tag{1.12}$$

The parameter α reflects the electronic structure. The easy direction of magnetization is found where the orbital magnetic moment and therefore the total magnetic moment is the largest. Perturbation theory gives reasonable qualitative agreement to the experiment. More precise results are obtained by *ab initio* methods which incorporate the LS coupling by a full relativistic approach. Very high accuracy in these calculations is needed since the magnetic anisotropy energy is tiny compared to the total energy per atom ($\sim$ 1000 eV/atom). Faster computers, however, have lead to remarkable, quantitative agreement between calculations and experiments [36–39] and have shown that the parameter α is not truly a constant [40].

The spin-orbit coupling is the origin of several contributions to the MAE. In cubic environments (fcc Ni and bcc Fe) the orbital magnetic moment is nearly completely quenched. A small anisotropic contribution of μ_L is obtained using fourth-order perturbation theory $\mathrm{K}_4 \propto \xi^4/\Delta\mathrm{W}^3$. ΔW is the bandwidth of the 3d band. In an uniaxial lattice (hcp Co) second order perturbation finds the second order anisotropy $\mathrm{K}_2 \propto \xi^2/\Delta\mathrm{W}$ [41]. Experimental values at T = 300 K of the second and fourth order terms of the MAE are given in table 1.6. One must take care when comparing computed and measured anisotropy coefficients, since the calculations usually consider no thermal fluctuations (T = 0 K). It is well known that the MAE is temperature-dependent [1]. Hence, the experimental data must be either measured at 4 K or at least extrapolated from the temperature dependence at higher temperatures [28]. Addi-

Table 1.6.: Volume anisotropy coefficient of second and fourth order at room temperature [3].

Element	Structure	K_2 $\mu\mathrm{eV/atom}$	K_4 $\mu\mathrm{eV/atom}$
Fe	bcc	0	3.5
Co	hcp	31.1	9.9
Ni	fcc	0	-0.4

tional enhancing contributions to the MAE are always found in low dimensional systems, e. g. ultrathin magnetic films [32] or one-dimensional chains [15]. Typical origins are stress at the sample/substrate interface, steps that reduce the symmetry, grain boundaries, or rough interfaces.

The magnetic anisotropy of single metallic nanoparticles is usually described in terms of an effective anisotropy K^{eff}. Contributions to K^{eff} are the volume anisotropy K^V which is usually considered to be bulk-like and the surface anisotropy K^S. The effective anisotropy K^{eff} depends on the ratio of surface-to-volume atoms which can be controlled by the nanoparticle diameter. The surface anisotropy K^S itself combines the anisotropy of a flat surface (facet) and the step anisotropy caused by the bent surface. In Figure 1.2 the atomic structure of an ideal spherical 12 nm particle is shown. Facets form on the surface which are usually the closest packed ones for a given crystal structure, for example the (111) plane for the fcc structure. The facets are connected by a large number of steps. The smaller the particle the more surface atoms compared to the total number of atoms in the particle are located at the boundaries of different facets which enhances the step anisotropy remarkably. Hence, it is surprising that the phenomenological approach assuming perfect spheres

$$K^{eff} = K^V + \frac{S}{V}K^S = K^V + \frac{6}{d}K^S \tag{1.13}$$

seems to work reasonable well for nanoparticles [42]. Here, for perfect spheres the surface of the nanoparticle is given by $S = \pi d^2$ and the volume by $V = (\pi d^3)/6$. d is the particle

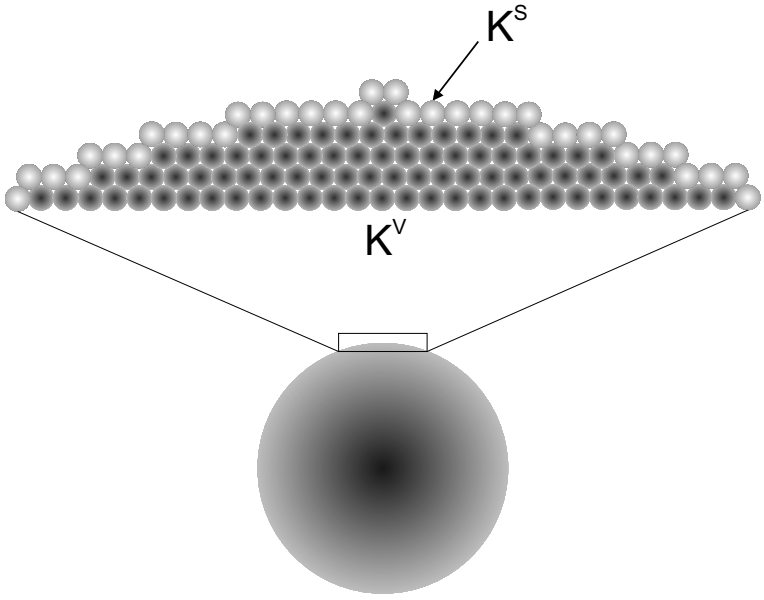

Figure 1.2.: Illustration of the surface and volume contributions to the effective anisotropy constant K^{eff}. The bending of the surface of the nanoparticle corresponds to an ideal sphere of 12 nm diameter using the bulk lattice constant of fcc Co (a = 0.35447 nm).

diameter. This phenomenological ansatz is similar to surface- and volume-separated anisotropy in ultrathin magnetic films. In case of ultrasmall Co nanoparticles ($d < 2$ nm) this simple model has been successfully applied to explain a larger K^{eff} for smaller particles, although particles of less than 2 nm diameter are far from being perfect spheres [19].

The effective magnetic anisotropy is the all-dominant quantity of many phenomena in magnetism. For nanoparticles the two most important consequences driven by the magnetic anisotropy are the single domain limit and the superparamagnetic limit. These two limits are briefly discussed here. Magnetic nanoparticles are in the single domain state, if the creation of a domain wall costs more energy than it is saved by the reduction of the stray field of the nanoparticle. The domain wall energy $E_{dw} = \sigma_{dw}\pi d^2 = \pi d^2\sqrt{AK^{eff}}$ is needed to form a domain wall in a spherical nanoparticle of diameter d. σ_{dw} is the domain wall energy density, $A \approx 10^{-11}$ J/m is the exchange stiffness constant. The magnetostatic energy difference between a single domain and a double domain state is $\Delta E_{ms} \approx (\mu_0 M_S^2 V)/3$ with the saturation magnetization M_S in units of A/m and the particle volume V [43]. For materials with a strong anisotropy the critical diameter of the particle d_c is reached when $E_{dw} = \Delta E_{ms}$:

$$d_c \approx 18\frac{\sqrt{AK^{eff}}}{\mu_0 M_S^2} \tag{1.14}$$

Assuming bulk values of hcp Co of $\mu_0 M_S^2 = 24 \cdot 10^5$ J/m^3 and $K^{eff} = 4.1 \cdot 10^5$ J/m^3 at room temperature the critical diameter is calculated to $d_c \approx 15$ nm. For fcc Co the cubic anisotropy constant $K^{eff} = 0.6 \cdot 10^5$ J/m^3 [2] is smaller and d_c reduces to about 7 nm. One should note that for small particles the effective magnetic anisotropy differs much from the bulk value due to the large surface contribution. Single domain particles show a broad range of coercive fields from $\mu_0 H_c = 0$ to $\mu_0 H_c = 2K^{eff}/M_S$. The first applies for small anisotropy and small diameter while the upper limit is reached for particle sizes close to the critical diameter d_c [42].

The second important consequence of the magnetic anisotropy is the superparamagnetic limit reached by the reduction of particle size. Below the critical volume the magnetization direction of a nanoparticle at a given temperature is not stable anymore. Considering an uniaxial single-domain particle the magnetization can flip between the two directions of the easy axis. This random fluctuation is thermally activated. The time-averaged magnetization of such a particle is zero. One should note that the time-averaging is identical to the time window of the technique of investigation. The magnetization process of a single-domain nanoparticle involves the rotation of the magnetization in the direction of the external field. The first theoretical approach of magnetization reversal has been suggested by Stoner and Wohlfarth [44]. The energy E at a certain angle θ with respect to the easy axis of magnetization of particle with uniaxial

anisotropy is described by:

$$E(\theta) = K^{eff} V \sin^2(\theta) \tag{1.15}$$

V is the particle volume. The energy barrier $K^{eff}V$ separates the two energetically equivalent easy directions of magnetization. When the thermal energy k_BT exceeds this energy barrier the magnetization fluctuates between the two minima. Néel and Brown [45,46] suggested a law describing the relaxation time τ as a function of the involved energies:

$$\tau = \tau_0 \cdot \exp \frac{K^{eff} V}{k_B T} \tag{1.16}$$

with the so-called attempt time $\tau_0 \sim 10^{-12}$ s - 10^{-9} s. The probability for a stable magnetization can be expressed by $P(t) = \exp -t/\tau$. The remanent magnetization M_R is obtained after a time t according to $M_R/M_0 = \exp -t/\tau$ where M_0 the remanent magnetization at $t = 0$. When τ is much larger than the characteristic detection time of the experiment, no change of the magnetization is detected in the time window t, and the particle shows stable ferromagnetism. In standard magnetometry the time window is around 100 s and an unstable direction of magnetization is detected when the condition $30k_BT > K^{eff}V$ is fulfilled. The blocking temperature T_B can be defined by this simple equation. In the case of FMR experiments the time window is on the order of 10^{-10} s. Accordingly, the equation for stable magnetization reads $2(\pm1)k_BT < K^{eff}V$. Vice versa, when the blocking temperature and the particle diameter are measured the effective anisotropy energy $K^{eff}V$ can be estimated. One should note that this estimation often yields too large values for $K^{eff}V$, since the blocking effect scales by the third power with the diameter of the particle, and a small size distribution is always present. Furthermore, the model of Stoner-Wohlfarth particles is often not fulfilled for real particle systems.

Above the blocking temperature T_B and below the Curie temperature T_C, however, the particles keep their spontaneous magnetization which however fluctuates in time. In an external field the magnetization of an array of non-interacting identical particles follows the Langevin law:

$$M(B) = M_S \cdot L\Big(\frac{\mu B}{k_B T}\Big) = M_S \cdot \Big(\coth \xi - \frac{1}{\xi}\Big) \qquad \text{with} \quad \xi = \frac{\mu \mathrm{B}}{\mathrm{k_B T}} \tag{1.17}$$

where M_S is the saturation magnetization of the array of particles, L is the Langevin function, and μ the magnetic moment of a particle. M_S is connected to the particle magnetic moment μ by $M_S = N \cdot \mu$. N is the number of particles. Consequently, the each individual particle behaves like a paramagnet with a giant magnetic moment. The susceptibility χ of such a superparamagnet is proportional to $\chi \propto \frac{\mu^2}{T}$.

These results are strictly valid only for individual particles or arrays of non-interacting particles with identical diameter. However, real magnetic particles always show some size distribution $f(V)$. The integral over all Langevin functions with distributed values of the magnetic

moments $\mu = M_S V$ has to be calculated. The magnetization process of non-interacting superparamagnetic particles is described by a weighted sum of Langevin functions [47]:

$$M(B) = M_S \cdot \int_0^\infty L\Big(\frac{\mu(V)B}{k_B T}\Big) f(V) dV \tag{1.18}$$

Moreover, the distribution of particle volumes results via $K^{eff}V$ in a distribution of blocking temperatures. For a single particle the blocking temperature is defined from equation 1.16 to

$$T_B = \frac{K^{eff}V}{k_B \ln(\tau/\tau_0)} \tag{1.19}$$

with τ the characteristic detection time of the experiment, i. e. $\tau = 100$ s for SQUID magnetometry and $\tau = 10^{-10}$ s for FMR. For a single particle T_B coincides with the maximum magnetization of a zero-field cooled (ZFC) measurement. In a particle ensemble with some size distribution, however, the blocking temperature T_B of the system is no longer well-defined. T_B has to be assigned to a distinct particle volume. In this thesis, the blocking temperature of a particle ensemble is defined as the mean blocking temperature $T_{B,mean}$, according to the mean particle volume. One should note that in case of log-normal volume distributions the mean particle volume lies at a slightly larger volume than the peak of the volume distribution which corresponds to the most probable particle volume. Assuming spherical particles, $T_C \gg T_B$, and a constant effective anisotropy energy density constant K^{eff} one finds that the mean blocking temperature $T_{B,mean}$ is remarkably smaller than the ZFC maximum would suggest. ZFC magnetization simulations using the Néel-Brown model (equation 1.16) have shown that $T_{B,mean}$ is reduced by a factor 1.5-2 compared to the ZFC maximum position for volume distributions $\sigma_V = 0.25 - 0.45$ which are typical for chemically prepared particles [48]. Note that the reduction only depends on the volume distribution of the particles and not on the mean volume. Thus, it is a statistical effect.

Collective Phenomena

Most experiments measure the collective magnetic response of a nanoparticle array. To prepare a square lattice with one layer of nanoparticles on a 1 cm^2-substrate at a center-to-center distance of d_{cc} = 15 nm $4.4 \cdot 10^{11}$ nanoparticles are needed. The maximum dipolar interaction energy $E_{dd,max}$ (parallel alignment of magnetic moments) of two point dipoles can be calculated by equation 1.7. For 2 nm particles (310 atoms, 1.9 μ_B) one finds $E_{dd,max} = 140$ μeV at a distance of 15 nm. Two 12 nm particles (80000 atoms, 1.7 μ_B) show a maximum dipolar energy of $E_{dd,max} = 7.3$ eV at the same distance. The coupling of an array of nanoparticles depends on

the magnitude of the moment, the relative directions of the moments, and the center-to-center distance of the particles. In practice, the particles can be treated as non-interacting magnetic objects when the center-to-center distance exceeds five times the particle diameter. However, most of the studies presented in this thesis show a center-to-center distance of less than two times the particle diameter. The particle interactions cannot be neglected, but, however, remain small in many cases as indicated in the discussion of the results.

The sum over all dipoles in infinite cubic lattices (sc, bcc, fcc) is zero [49] yielding an antiferromagnetic order of dipoles. In finite structures the dipole sum does not vanish producing the demagnetizing field. The magnetic ground state of a finite dipolar coupled system cannot be calculated easily. However, some general rules can be drawn. The magnetic ground state of fcc ordered particles arranged in an ellipsoid with an axis ratio $c/a > 6$ has been calculated to be ferromagnetic [50]. Thus, a ferromagnetic order of dipolar coupled perfectly ordered identical particles is expected for samples being not too thick (e. g. surface area 1 cm^2 and thickness < 1 mm). Also chain-like structures reveal a ferromagnetic order [51]. In samples with a random distribution of magnetic dipoles the ordered state will be the one of a spin glass [52]. In 2D arrays of dipolar coupled particles with randomly distributed anisotropy axes and some size distribution the magnetic ground state can only be calculated by numerical methods [53].

1.4. Exchange Anisotropy in Co/CoO Systems

When systems with a ferromagnetic-antiferromagnetic interface are cooled below the Néel temperature of the antiferromagnet and the Curie temperature T_C of the ferromagnet is larger than the Néel temperature T_N an unidirectional exchange anisotropy UEA is induced in the system [54,55]. Meiklejohn and Bean [56] discovered the exchange anisotropy in 1957. By cooling naturally oxidized Co particles with diameters of 10 nm - 100 nm in an applied field they found a shift of the hysteresis loop of the specimen in the opposite direction of the cooling field. When the sample was cooled in absence of a field a standard hysteresis loop - symmetrical to the origin - has been observed. It should be noted that the exchange anisotropy is always present. The field cooling results in the alignment of the antiferromagnetic moments at the interface parallel to the ferromagnetically coupled moments in the core of the particle. After field cooling, the switching behavior of the particles is changed by the aligned frozen spins of the antiferromagnet acting as an effective magnetic exchange field. This additional field directed parallel to the cooling field supports a magnetization direction parallel to the cooling field and hardens the antiparallel orientation. This effect is called exchange bias. In the case of Co/CoO exchange biased systems the magnetic anisotropy of the antiferromagnet is more than one order of magnitude larger than

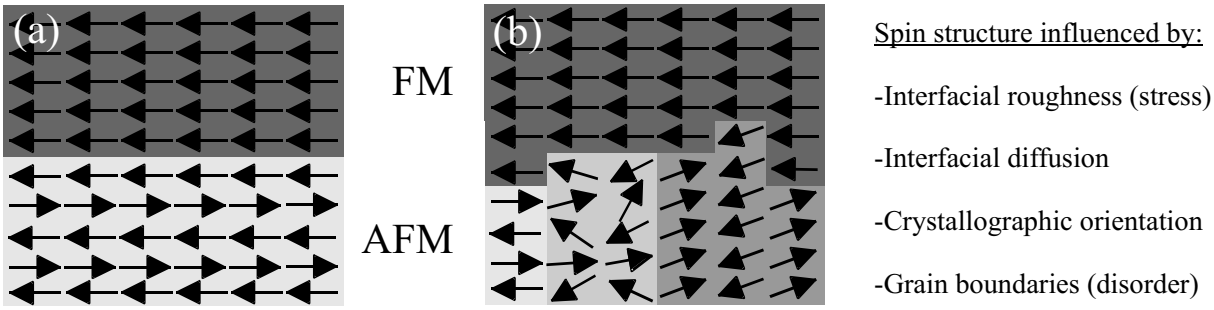

Figure 1.3.: Interface spin structure of (a) an ideal ferromagnetic/antiferromagnetic (FM/AFM) interface. Both, ferromagnetic and antiferromagnetic layers are single crystals with an atomically smooth interface. (b) Polycrystalline ferromagnetic/antiferromagnetic interface. The strength of the exchange anisotropy is strongly influenced by roughness and diffusion at the interface, grain boundaries and the crystallographic orientation (see text).

the one of the ferromagnet. Thus, the spin orientation of the antiferromagnet is not reversed in typical laboratory magnetic fields of up to ~ 5 T.

At the interface to the ferromagnet the antiferromagnet exhibits localized net magnetic moments. In Figure 1.3 (a) an atomically smooth interface is shown. The topmost layer of the antiferromagnet is coupled ferromagnetically to the ferromagnetic material and remains uncompensated. An uneven number of antiferromagnetic lattice planes would give rise to this effect. A more realistic picture is drawn in Figure 1.3 (b). Even in antiferromagnetic grains with compensated interfacial spin planes, the formation of unequal numbers of parallel and anti-parallel spins is likely due to roughness and intermixing at the interface, disorder generated by grain boundaries or tilted crystallographic orientations of the antiferromagnetic spins with respect to the ferromagnetic spins [54].

A general description of the exchange bias phenomenon is still lacking. Since exchange bias is an interface effect and in experiments the quality of the interface depends on the investigated system and the preparation technique, the experimental data are spread over a wide range. For an ideal interface as shown in Figure 1.3 (a) a model is suggested that predicts the exchange bias field (for a review see e. g. [54,55]). Here, both layers are single crystals exhibiting an atomically smooth ferromagnetic/antiferromagnetic interface. The antiferromagnetic monoxides are composed of atomic planes of ferromagnetically oriented spins with an antiparallel alignment of adjacent planes showing no net magnetization. The interfacial antiferromagnetic spins are fully uncompensated. The magnetization reversal in the ferromagnet is assumed to be a coherent rotation while the spins of the antiferromagnet remain fixed. The energy for this rotation is

equal to the UEA and can be described in terms of an exchange bias field [54]:

$$|H_{EB}| = \frac{\Delta\sigma}{\mu_0 M_{FM} t_{FM}} = \frac{J\mu_{FM}\mu_{AFM}}{a_{AFM}^2 \mu_0 M_{FM} t_{FM}} \tag{1.20}$$

with $\Delta\sigma$ the interfacial exchange energy density, J the interface exchange energy, μ_{FM} and μ_{AFM} the atomic magnetic moments of the ferromagnet and the antiferromagnet, a_{AFM} the (cubic) lattice parameter of the antiferromagnet, M_{FM} the magnetization of the ferromagnet, and t_{FM} the thickness of ferromagnetic. Experimentally, however, it is always observed that $|H_{EB}|$ is two to three orders of magnitude smaller than predicted by this model. Obviously this simple model assuming ideal interfaces is not a realistic representation of the interfacial environment. Intermixing and roughness have to be invoked to account for the large reduction of the interfacial coupling strength. Ohldag et al. [57] suggest that only a small pinned fraction ρ of the uncompensated interfacial moments contribute to the exchange bias. When replacing $\Delta\sigma$ and J by their effective values $J_{eff} = \rho \cdot J$ and $\Delta\sigma_{eff} = \rho \cdot \Delta\sigma$ it has been found that only 3% - 5% of a monolayer constitute the exchange bias. This finding is a unique feature of several different layered systems as shown in [57].

In this thesis naturally oxidized Co particles with sizes of 9 nm to 14 nm and narrow size distribution are investigated. The particles have been prepared by organo-metallic synthesis. Since the particles have a core/shell structure of Co and CoO I will use the nomenclature Co/CoO in the following. A typical set of hysteresis loops is shown in Figure 1.4. Hysteresis loops of an array of Co/CoO nanoparticles were measured both, after zero-field cooling (ZFC) and field cooling (FC) in 5 T from 370 K to 10 K. The loops were taken at 10 K. The ZFC loop is symmetrical to the origin. The FC loop is shifted along the negative field direction applied during the cooling process. The hysteresis loop of the ferromagnet is biased by the antiferromagnet. The strength of the UEA is measured by the exchange bias field $H_{EB} = |(H_1^{FC} + H_2^{FC})/2|$. The FC coercivity $H_C^{FC} = |(H_1^{FC} - H_2^{FC})/2|$ is always found enhanced compared to the ZFC hysteresis loop. [56,58,59]. Both effects disappear at the Néel temperature of the antiferromagnet or the blocking temperature of the antiferromagnet. This finding confirms that it is the presence of the antiferromagnetic material that causes this anisotropy. In some cases [58,61] a vanishing exchange bias is found below T_N that is explained by the finite grain size or layer thickness of the antiferromagnet. Here, it is assumed that T_N is reduced remarkably for a 2-3 nm thick CoO layer around a ferromagnetic core. Below a critical size or thickness on the order of 1-3 nm small antiferromagnetic grains become superparamagnetic above a critical 'blocking' temperature T_B^{AFM} of the antiferromagnetic material. The FC hysteresis loops of an array of 13 nm Co/CoO particles (Figure 1.4) shows an exchange bias field of $\mu_0 H_{EB} = 0.4$ T. This finding indicates the strong unidirectional exchange anisotropy (UEA) in the sample. An interface

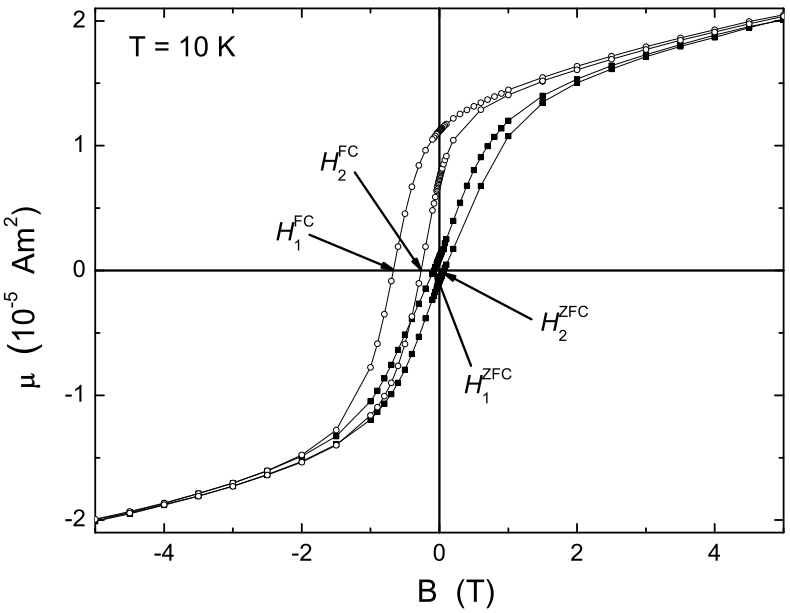

Figure 1.4.: Zero-field cooled (■) and field-cooled hysteresis (○) loops of 13 nm Co/CoO nanoparticles measured at 10 K. A magnetic field of $\mu_0 H$ = 5 T has been applied during the FC process from 350 K to 10 K. Coercive fields for FC and ZFC are indicated by the arrows. The figure has been adapted from [60].

exchange energy ΔE per unit area [55] for spherical nanoparticles can be calculated from

$$\Delta E = \mu_0 H_{EB} M_{FM} d_{FM}/6. \tag{1.21}$$

M_{FM} is the saturation magnetization of the ferromagnetic core in units of A/m with a diameter of d_{FM}. The factor 6 arises from the ratio of the volume to the surface area of a sphere.

The temperature dependence of the exchange bias field has been studied in the framework of the random-field model of anisotropy [62] for cubic AFM crystals. The authors predicted a linear decrease of $H_{EB}(T)$ as a function of temperature. In many thin-film systems [54,55] the predicted linear temperature dependence has been observed. In the case of nanoparticles or polycrystalline antiferromagnets with a small grain size, the temperature degradation of the exchange energy can be described better by the model of thermal instabilities of superparamagnetism of small antiferromagnetic grains [63]. This approach can also explain that the exchange bias field vanishes at temperatures below T_N taking into account the blocking temperature T_B^{AFM} of antiferromagnetic grains. The temperature dependence of the exchange bias field H_{EB} can be described by $H_{EB}(T) = H_{EB}(0\,\mathrm{K})\left(1 - T/T_B^{AFM}\right)^{\mathrm{n}}$ [60]. In the case of Co/CoO particles where the exchange bias vanishes at T = 100-150 K the degradation law suggests

n = 3.2 [60]. This model includes the linear decrease of the exchange bias with temperature with n = 1 and the substitution of T_B^{AFM} by T_N of the antiferromagnet.

Using data for Co with a layer thickness of $t = 8$ nm (neglecting the spherical shape of the particles), a bulk magnetization of $M_{FM} = 1400$ kA/m, an exchange energy of 20 meV per Co/CoO bond and a square lattice parameter of $a^2 = 0.182$ nm^2 of CoO one calculates the exchange bias from equation 1.20 to be $\mu_0 H_{EB} = 10.7$ T that is indeed one to two orders of magnitude larger than the experimental observations. Using the effective $J_{eff} = 0.04 \cdot J$ for Co/NiO thin films [57] one finds a resultant $\mu_0 H_{EB} = 0.43$ T. This estimate reflects the different experiments summarized in table 1.7 fairly well taking into account the crude assumptions. One may note, that the experimental results listed in table 1.7 and the estimate from equation 1.20 suggest a decreasing biasing field with growing thickness of the ferromagnet. The series of experiments with varying thickness t_{FM} show this tendency for films [64] and particles [58].

Table 1.7.: Experimental data of Co/CoO exchange biased systems. The preparation technique and the arrangement (powder, matrix *etc.*) are given in the first column. Particle diameter and thickness of the CoO shell (or film) are shown for comparison. The field cooling procedure is always from above T_N of CoO ($T \geq 300K$) to the measuring temperature T in a applied field B_{FC}. The observed coercitive fields and exchange bias fields are listed besides the temperature where the exchange bias vanishes.

Preparation technique of Co/CoO	Particle diameter (nm)	t_{CoO} (nm)	Procedure B_{FC} , T	$\mu_0 H_C$ (T)	$\mu_0 H_{EB}$ (T)	$T(\mu_0 H_{EB} = 0)$ (K)	Ref.
Cluster gun sputtering, in Al_2O_3 matrix	4.7	1	5 T, 5 K	0	0	-	[65]
compacted	4.7	1	5 T, 5 K	0.6	0.95	not given	[65]
in CoO matrix	4.7	1	5 T, 5 K	0.76	0.74	T_N	[65]
PMMA sphere templates, in carbon	3-4	unknown	1 T, 10 K	0.62	0.34	180	[66]
Cluster beam deposition, in polyimide	6	1	2 T, 5 K	0.50	1.02	200	[58]
	13	1	2 T, 5 K	0.24	0.36	200	[58]
Vapor deposition, in paraffin	11.5	2	2 T, 10 K	0.60	0.57	150	[59]
	35	2	2 T, 10 K	0.3	0.1	150	[59]
Electrodeposition, Powder	10-100	unknown	1 T, 77 K	0.11	0.16	T_N	[56]
rf-sputtering, continuous film	2.7 (film)	2.5	0.2 T, 10 K	0.36	0.23	186	[64]
	11.9 (film)	2.5	0.2 T, 10 K	0.09	0.06	186	[64]
	39.8 (film)	2.5	0.2 T, 10 K	0.03	0.02	186	[64]
Colloidal chemistry, covered by ligands	9.5	2-3	5 T, 35 K	0.27	0.20	100	this thesis
	11.4	2-3	5 T, 10 K	0.39	0.41	-	this thesis
	13.6	2-3	5 T, 10 K	0.39	0.39	150	this thesis

2. Experimental Techniques

In this thesis, two complementary techniques have been used to probe the magnetic properties of Co/CoO nanoparticles: Ferromagnetic Resonance (FMR) and X-ray Magnetic Circular Dichroism (XMCD). Both techniques allow to measure the orbital contribution to the total magnetic moment with different probing depths. This magnetic characterization is supported by Superconducting Quantum Interference Device (SQUID) magnetometry and element-specific hysteresis loops using the XMCD effect. In addition, X-ray Absorption Spectroscopy (XAS) supplies information of the chemical environment of the investigated specimen. The results are compared and correlated to structural and morphological investigations in terms of high-resolution Transmission Electron Microscopy (HR-TEM), energy-filtered TEM, Electron Energy Loss Spectroscopy (EELS), Selected Area Electron Diffraction (SAED), Scanning Electron Microscopy (SEM) and Atomic Force Microscopy (AFM). In this chapter the physical background, the efforts and drawbacks and the experimental setups of FMR and XMCD are discussed. The description of all other methods is restricted to the particular experimental devices used to achieve the presented results.

2.1. Ferromagnetic Resonance

Spin resonance in ferromagnetic materials is similar to electron spin resonance [67]. The total magnetization of a sample, e. g. a single nanoparticle, precesses around the direction of the local static magnetic field $B_{eff} = \mu_0 H_{eff}$ at the Larmor frequency. The basic principles can be discussed in terms of electron paramagnetic resonance (EPR) [68].

Non-interacting paramagnetic impurities in a diamagnetic host show the Zeeman effect [68] in an external magnetic field. In the most simple case of a two-level system ($S = \pm 1/2$) the energy difference ΔE between the two states is $\Delta E = g\mu_B B_0$. Here g is the Landé g-factor, μ_B Bohr's magneton and B_0 the externally applied magnetic field. In Figure 2.1 (upper panel) the splitting is shown. A transverse alternating electromagnetic field of energy $\hbar\omega$ can induce

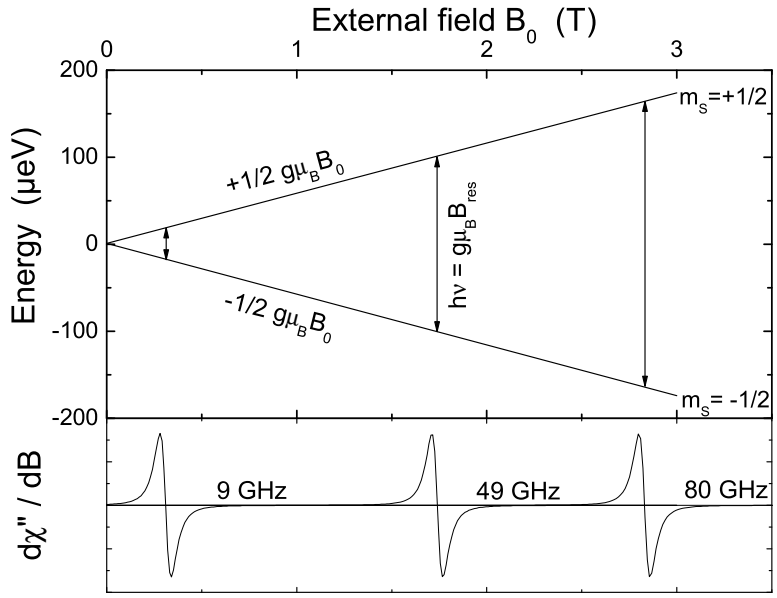

Figure 2.1.: Principle of an EPR (FMR) experiment of a two-level system (upper panel). A degenerate energy state splits by the external field B_0. Magnetic dipole transitions can be induced by a transverse microwave field at frequencies μ = 9, 49, and 80 GHz, for example. The lower panel shows a typical frequency-dependent measurement for paramagnetic species with g = 2. The derivative of the absorptive part of the susceptibility χ'' is detected due to the use of a lock-in amplifier.

magnetic dipole transition if both energies coincide ($\hbar\omega = g\mu_B B_0$). Thus, the Landé g-factor can be easily measured by a single experiment fulfilling the resonance condition

$$\omega = \gamma B_0 \tag{2.1}$$

with the gyromagnetic ratio $\gamma = g\mu_B/\hbar$. For the free electron value $g = 2.0023$ one finds

$$\frac{\gamma}{2\pi} = \frac{g\mu_B}{h} = 28.02\frac{\text{GHz}}{\text{T}} \tag{2.2}$$

Obviously, microwaves have to be used to study this effect in magnetic fields of 0-3 T which can be reached by standard electromagnets. According to equation 2.1 one may vary both the microwave frequency or the external field. However, most experimental stations operate at fixed microwave frequency using the resonator technique [67] to increase sensitivity. The external field is swept and the field at which resonance is observed is defined as the resonance field B_{res}. Since a lock-in technique is used for the signal acquisition, the derivative of the absorption is detected. The minimum number of spins which is necessary for signal detection is on the order of $10^{10} - 10^{14}$ [69] strongly dependent on the linewidth of the detected signal. The sensitivity

of an EPR experiment increases at higher microwave frequency directly implying that high magnetic fields are needed. The experiments presented in this thesis use a frequency range of 9-80 GHz. Thus, magnetic fields of B_0 = 0.3 T - 2.9 T are required for paramagnetic resonance of materials with g $\approx$ 2.

When ferromagnetic materials are examined this type of investigation is called Ferromagnetic Resonance (FMR). In ferromagnets the exchange coupling results in a huge magnetization. Strong internal fields play an important role, which vary the local magnetic field in the FMR experiment. Additionally, the internal fields are varied by the anisotropy fields. The local magnetic field can be shifted up to Teslas from the value of the external field.

The physical description of the motion of the magnetization $\vec{M}$ around its equilibrium position is given by the Landau-Lifshitz equation [28,33]:

$$\frac{d\vec{M}}{dt} = -\frac{\gamma}{1+\alpha^2}\left(\vec{M} \times \vec{B}_{eff}\right) + \frac{\alpha}{M}\left(\vec{M} \times \frac{d\vec{M}}{dt}\right) \tag{2.3}$$

with $M = M(T, H)$ the temperature- and field-dependent magnetization in units of A/m or T, the effective magnetic field B_{eff} in units of T which includes (i) the external field, (ii) the rf-microwave magnetic field of frequency ν, and (iii) the anisotropy field. The second term on the right hand side denotes the relaxation of the magnetization towards the direction of the effective field B_{eff} with α being a dimensionless parameter that provides a phenomenological way of taking into account all various relaxation mechanisms. Thus, it becomes possible to model the linewidth of the resonance signal [28,33,70,71]. In general, the relaxation influences the resonance field, since α enters the first term on the right hand side of the equation 2.3. The value of alpha, however, is on the order of 10^{-2} or smaller, and consequently α^2 can be neglected within the first term. Moreover, for small values of α the second term can be transformed into the so-called Gilbert form [33]. In this case, equation 2.3 is usually termed Landau-Lifshitz-Gilbert equation of motion and reads:

$$\frac{d\vec{M}}{dt} = -\gamma\left(\vec{M} \times \vec{B}_{eff}\right) + \frac{G}{\gamma M^2}\left(\vec{M} \times \frac{d\vec{M}}{dt}\right) \tag{2.4}$$

Here $G = \alpha\gamma M$ is the Gilbert relaxation parameter. G has the unit Hz. M in units of T has to be used here. Figure 2.2 shows both, the precession of the magnetization and the damping towards the axis of the effective field. One may note that equation 2.3 and equation 2.4 only hold for a single magnetic object like an ultrathin film [28] or a single nanoparticle where a giant spin precesses around the direction of the field axis. In case of a nanoparticle ensemble the distribution of anisotropy axes has to be taken into account.

To find the resonance fields from equation 2.3 two different approaches can be employed. One is the solution of coupled differential equations for the time-dependent magnetization com-

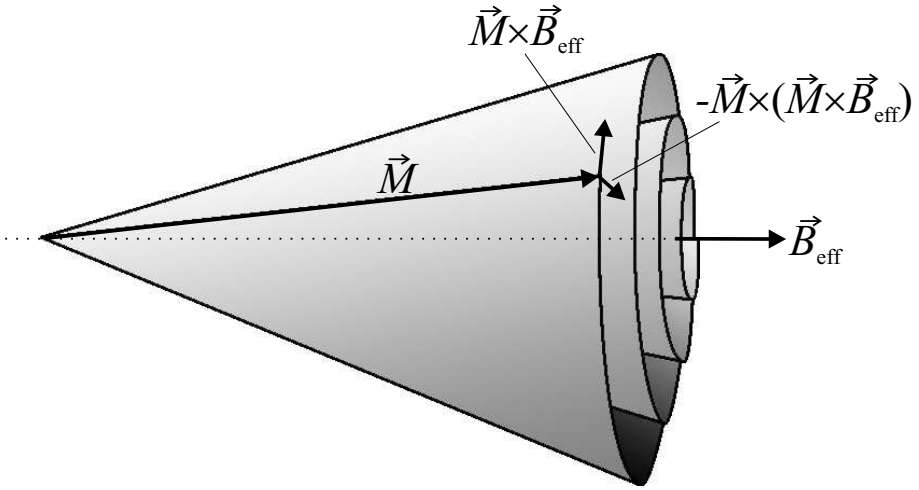

Figure 2.2.: Movement of the magnetization around the effective field axis. The Landau-Lifshitz-Gilbert equation describes both the precession around and the relaxation towards the effective field axis.

ponents which reveals resonance position, intensity ($\propto M$), signal shape, and the linewidth of the FMR experiment. Details are discussed elsewhere [28,70,72].

Neglecting the dynamics of FMR and focussing on the resonance position a much simpler approach has been derived [73]. Here, instead of the effective field B_{eff} the free energy density is used in the equation of motion of the magnetization. The anisotropic magnetic energies due to the sample shape and the atomic structure of the sample are described in terms of symmetry as shown below. Gilbert derived the identical result by using the Lagrange formalism to describe the precession of the magnetization [74] solving the following equations:

$$\frac{d\theta}{dt} = -\frac{\gamma}{M\sin\theta}\frac{\partial F}{\partial \phi} \qquad \text{and} \qquad \frac{d\phi}{dt} = \frac{\gamma}{M\sin\theta}\frac{\partial F}{\partial \theta} \tag{2.5}$$

$d\theta/dt$ and $d\phi/dt$ are the derivatives of time of the Euler angles and F denotes the free energy density of the system arising from the potential energy. Assuming that the precession is limited to small changes $\Delta\theta = \theta(t) - \theta_0$ and $\Delta\phi = \phi(t) - \phi_0$ around the equilibrium positions θ_0 and ϕ_0 one finds by series expansion truncated after the linear expression:

$$\frac{\partial F}{\partial \theta} = \frac{\partial^2 F}{\partial \theta^2}\Delta\theta + \frac{\partial^2 F}{\partial\theta\partial\phi}\Delta\phi \qquad \text{and} \qquad \frac{\partial F}{\partial \phi} = \frac{\partial^2 F}{\partial \phi^2}\Delta\phi + \frac{\partial^2 F}{\partial\theta\partial\phi}\Delta\theta \tag{2.6}$$

Now, the periodic solutions proportional to $e^{i\omega t}$ are found for $\Delta\theta$ and $\Delta\phi$ if the determinant of the coefficients vanishes. The solution is

$$\left(\frac{\partial^2 F}{\partial\phi\partial\theta}\right)^2 - \frac{\partial^2 F}{\partial\phi^2}\cdot\frac{\partial^2 F}{\partial\theta^2} + \frac{\omega_{res}^2}{\gamma^2}M^2\sin^2\theta_0 = 0 \tag{2.7}$$

and the resonance frequency can be expressed as

$$\omega_{res} = \frac{\gamma}{M\sin\theta_0}\sqrt{\frac{\partial^2 F}{\partial\phi^2}\cdot\frac{\partial^2 F}{\partial\theta^2} - \left(\frac{\partial^2 F}{\partial\theta\partial\phi}\right)^2} \tag{2.8}$$

Thus, the resonance frequency is given by the double derivatives of F with respect to the angles θ and ϕ. Equation 2.8 must be evaluated at equilibrium angles θ and ϕ of the magnetization $M = M(T, H)$ in an external field. Here, M is needed in units of A/m. The FMR experiment probes the spatial distribution of the free energy density from which (i) magnetic anisotropies can be deduced with high precision (μeV resolution) and (ii) the gyromagnetic ratio γ and hence the g-factor can be determined.

The free energy density F is expressed as the sum of all types of magnetic energies in a given system. Since the double derivatives are needed in equation 2.8, only anisotropic contributions have to be taken into account. The most important contributions are the energy densities of the demagnetizing field and the crystallographic magnetic anisotropy. In some cases magnetoelastic effects and magnetostriction play an important role [28] that is neglected in the following. Examples for tetragonal symmetries are given in [72] and [70] taking into account the magnetocrystalline anisotropy energy density constant of second and fourth order. Dealing with magnetic nanoparticles all contributions to the magnetic anisotropy energy density are usually summarized to an effective anisotropy constant K^{eff} as discussed in section 1.3.

In order to quantify the effective anisotropy of the particles the distribution of the easy axis has to be taken into account explicitly. For this purpose, the general Kittel relation [28] for arbitrary angles of the external field with respect to the easy axis of magnetization

$$\left(\frac{\omega}{\gamma}\right)^2 = \Big[B_{res}\cos(\theta-\psi) + B_A\cos^2\theta\Big] \cdot \Big[B_{res}\cos(\theta-\psi) + B_A\cos 2\theta\Big] \tag{2.9}$$

has to be used. Here θ and ψ denote the angles of the easy axis with respect to the particle magnetization and the external field applied in an FMR experiment, respectively. For simplicity, the anisotropy field B_A is assumed to be uniaxial and identical for all particles. Under these assumption Wiekhorst et al. [75] derived a numerical relation that contains the anisotropy of the particles after averaging the resonance fields $B_{res}(\theta_0, \omega, \psi)$ of the particles at their equilibrium positions given by $\theta = \theta_0(B, \psi)$ over ψ:

$$B_{res} = \left(\frac{\omega}{\gamma}\right)\left[1 - \left(\frac{\gamma B_A}{\omega}\right)^2\right]^{0.36} . \tag{2.10}$$

This relation has been used to estimate the effective anisotropy energy barrier $E_A = (\mu_P B_A)/2\mu_0$ of $FePt$ [75] and Co/CoO [76] nanoparticles where μ_P is the magnetic moment of a particle. From $E_A = K^{eff}V$ the effective magnetic anisotropy density constant K^{eff} can be determined.

When nanoparticle ensembles are examined well above their blocking temperature the isotropic superparamagnetic regime is reached [77]. In this case, the individual total anisotropy

energy of a single particle is much smaller than the thermal energy. Thus, the only contribution shifting the observed resonance fields from the paramagnetic resonance field is the shape anisotropy resulting from the sample shape and morphology. When the particles are deposited as a single layer or a few layers of particles on the substrate, consequently, the dipolar stray fields of the whole ensemble are minimized in an external field when the particle moments are oriented in the film plane. This leads to a preferential alignment of the magnetic moments within the film plane. By the solution of the Landau-Lifshitz-Gilbert equation (damping is neglected) in this special case one finds that the experiments can be described by the well-known Kittel resonance conditions for the situation that the external field is applied parallel ($\|$) or perpendicular ($\perp$) to the sample plane

$$\left(\frac{\omega}{\gamma}\right)^2 = B_{res\|}\left[B_{res\|} + fM_{eff}(B_{res\|})\right] \tag{2.11}$$

$$\left(\frac{\omega}{\gamma}\right) = B_{res\perp} - fM_{eff}(B_{res\perp}). \tag{2.12}$$

Here, fM_{eff} denotes the effective anisotropy field arising from the sample shape and any magnetocrystalline anisotropy. The volumetric filling factor f takes into account the discontinuous medium of an array of nanoparticles. $B_{res\|(\perp)}$ are the observed resonance fields. For non-interacting particles and hence a small volumetric filling factor f the second terms in equations 2.11 and 2.12 can be neglected in the superparamagnetic regime. Consequently, equations 2.11 and 2.12 read as paramagnetic resonance conditions (equation 2.1) with $B_{res\|} = B_{res\perp}$. In the case of a continuous film it follows that the volumetric filling factor f = 1.

The main effort of the measurement of nanoparticles above their blocking temperature is the determination of the g-factor and thus the ratio of orbital-to-spin magnetism. In ferromagnetic materials the determination of the g-factor based on FMR experiments is very complicated due to large intrinsic magnetic anisotropy fields being temperature dependent [78]. In ensembles of superparamagnetic nanoparticles above their blocking temperature, however, the intrinsic magnetic fields become negligibly small due to thermal fluctuations. A straightforward g-factor analysis in terms of the paramagnetic resonance conditions becomes possible.

Experimental Setup

The FMR experiments presented in this thesis were conducted in a wide range of microwave frequencies between 9 GHz and 80 GHz. At 9 GHz the so-called resonator technique [67] has been used for enhanced sensitivity. The measurements were mostly performed using a TE102 resonator producing a rectangular distribution of the magnetic field vector of the microwaves. Detailed descriptions can be found in [67,79]. The resonator has an 11 mm sample access

hole arranged rectangular to both the magnet poles producing the homogeneous static magnetic field and the incident microwaves. The access hole easily allows the user to perform angular-dependent FMR measurements of a typically 5×5 mm^2 sized sample at room temperature. Cooling of the sample is achieved by a He continuous flow cryostat allowing a minimum temperature of T = 20 K. For isolation a double wall ion- and water-free quartz tube (Suprasil) has been used that can be evacuated. The quartz tube which is almost transparent for microwaves is placed in the resonator. The small absorption of the quartz tube is nearly frequency-independent for the microwave X-band (8.8 GHz - 9.8 GHz). For experiments at low temperatures the sample is positioned within the quartz tube allowing a maximum sample width of 4 mm.

The slowly sweeping magnetic field is produced by an electromagnet reaching a maximum field of 1.6 T. This magnetic field is superimposed by a small ac magnetic field which is produced by two small additional coils reaching field amplitudes of up to 2 mT at a modulation frequency of 10 kHz. The field modulation frequency is used as the time base of a lock-in amplifier [67].

Microwaves are created by a klystron at constant power of 200 mW. The microwave power can be chosen by a attenuator down to 60 dB attenuation. The microwaves are directed by a waveguide system to the resonator and a reference arm. The system resonator/sample has a fixed resonance frequency. By an iris screw the microwave field within the resonator is tuned until no reflections from the cavity are detected. Small losses of microwave power in the cavity are permanently compensated by the incident microwaves. Thus the system resonator/sample is permanently exposed to a microwave field which does not depend on time as long as no resonant absorption of the sample occurs. In this state the cavity has a constant quality factor Q [67]. By sweeping the magnetic field at some point resonant absorption of the microwaves takes place and the absorption directly changes the quality factor Q of the cavity. Then, microwaves are partially reflected and guided back to the waveguide system. The reflected power is detected by a diode. The signal channel is modulated by the 10 kHz field modulation. Both, the sample signal channel and the reference signal are fed to a lock-in amplifier working at the time base of the field modulation frequency.

The lock-in signal (first derivative of the absorptive part of the high-frequency susceptibility) is read out by a standard PC computer system. The PC combines the lock-in signal with the actual field value measured by a teslameter. The accuracy of the magnetic field measurement is $\Delta B/B \approx 10^{-4}$. The microwave frequency can be determined by a frequency counter with a relative uncertainty of $\Delta\nu/\nu = 10^{-6} - 10^{-7}$. Thus, the field determination is the quantity that defines the error bar of the experiments. Typical uncertainties of the experimental setup are on the order of ± 2 mT that results in a g-factor error bar of $\Delta \mathrm{g} = \pm 0.015$ in paramagnetic reso-

nance. The expansion to measurements at several microwave frequencies enhances the accuracy of the g-factor determination enormously.

At higher frequencies (17 GHz - 80 GHz) all experiments were performed at room temperature. Several sets of waveguide systems were mounted allowing an external field orientation in the plane of the sample (parallel configuration) or perpendicular to the sample plane (normal configuration) at all frequencies. Low-resistivity manganin ($Cu_{86}Mn_{12}Ni_2$) has been used as a substrate. The metallic substrate with the nanoparticles on top formed a part of a shortened waveguide system. The reflected microwave power from the sample is decoupled from the incident one by a bidirectional coupler and detected by a semiconductor diode. The sweeping magnetic field has been modulated by a small ac-field ($\sim$ 0.1-0.3 mT) at 95 kHz enabling the sensitive lock-in detection of the reflected microwave power.

2.2. X-ray Magnetic Circular Dichroism

The x-ray magnetic circular dichroism (XMCD) technique is based on the changes in the absorption cross section of a magnetic material using circularly polarized photons. XMCD is a magneto-optical effect which relate the spectroscopic spectra - measured in transmission or absorption geometries - to the magnetic properties of a given material. In this section the basic approach of the interpretation of the XMCD spectra will be discussed. The interaction of x-rays and matter, i. e. the x-ray absorption cross section, is introduced. The so-called saturation effect which is due to the "self-absorption" of excited electrons in the sample is reviewed and some consequences for nanoparticle absorption spectra are discussed. The theoretical approach for the interpretation of the XMCD effect is presented. The development of the magneto-optical sum rules in core-level spectroscopy in the 1990's resulted in a huge progress in the interpretation of the measured spectra, especially in the determination of separated orbital and spin magnetic moments. Finally, the analysis procedures of the experimental data and the technical details of the synchrotron beamlines generated the presented data are described.

Based on the pioneering work of Faraday [80] in 1846 and Kerr [81] in 1877 for transmission and reflection geometries, respectively, magneto-optical characterization techniques are widely used nowadays, e. g. the magneto-optical Kerr effect (MOKE) using laser light. Photon energies of a few eV (within or close to the visible range) are used to excite intraband transitions from occupied to unoccupied valence states. Due to the dipole selection rules the absorption in the exchange-splitted valence states is different for the two circular components of the incident linear polarized light. The reflected beam (in Kerr geometry) is found elliptically polarized, and

the so-called Kerr rotation is a measure of the magnetization of the sample. However, the quantitative interpretation of intraband transitions is very difficult [82] and the discrimination of different magnetic elements is generally not possible. Hence, the probing of core-level excitations, e. g. the $L_{3,2}$ edges of the 3d transition metals is favorable, since each element of the investigated specimen features its characteristic excitation energy. The core states are highly localized with well-defined quantum numbers and thus the quantitative description of the transitions simplifies. However, a continuous spectrum of circularly polarized x-rays with high photon flux is necessary to perform such measurements. These requirements are only available at synchrotron radiation sources. The first experimental proof of XMCD has been measured at the K edge of Fe by Schütz et al. [83] in 1987.

X-ray Absorption Spectroscopy

X-ray absorption spectroscopy (XAS) is an experimental technique that probes the electronic structure and gives both magnetic and structural information of the investigated sample. The fundamental interactions of x-ray photons and matter are the photo effect, the scattering process, and the production of electron-positron pairs. Within the energy range used for x-ray absorption spectroscopy (10 eV - 100 keV) the creation of electron-positron pairs is not possible. The scattering involves elastic (Thomson scattering) and inelastic (Compton and Raman scattering) processes. In the energy range of 10 eV to 30 keV the photoelectric absorption process is larger than the scattering process by two to three orders of magnitude [84] and so the intensity $I(E, d)$ transmitted through matter of thickness d can be described by Lambert and Beer's law:

$$I(E, d) = I_0(E) \cdot e^{-\mu(E)d} \tag{2.13}$$

where $I_0(E)$ denotes the incident photon intensity as a function of energy and μ the absorption coefficient. Figure 2.3 (a) shows a typical geometry for transmission experiments. The x-ray intensity $I(E, d)$ passing the sample of thickness d is detected. The absorption coefficient $\mu(E)$ is measured by I/I_0 as a function of photon energy $h\nu$. For a measurable photon intensity after transmission the sample must be of finite thickness of about $2/\mu_{max}$ [85]. μ_{max} is the maximum absorption coefficient in the energy range of interest. In the case of Co $L_{3,2}$ transmission experiments one finds $\mu_{max}(E_{L_3}) \approx 5.9 \cdot 10^7$ 1/m [85]. In literature, mostly the reciprocal value of $\mu(E) = 1/\lambda_x(E)$ is reported that is the x-ray attenuation length. For Co one finds a maximum sample thickness of 34 nm. However, for substrate supported samples, e. g. magnetic films or nanoparticles on metallic or thicker dielectric substrates, the absorption coefficient cannot be directly measured in transmission geometry. Due to the thickness of the sample including the substrate and the high off-resonant absorption coefficient of the photons in the soft x-ray regime

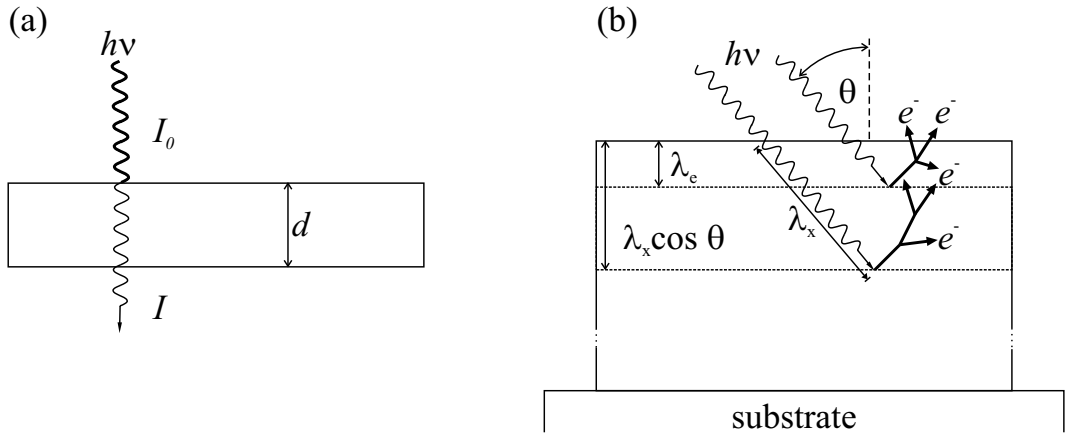

Figure 2.3.: X-ray absorption spectroscopy in two detection modes. (a) shows a typical transmission experiment that directly yields the absorption coefficient. In (b) the total electron yield of an infinite thick film is detected that is produced by the cascading inelastic scattering processes of the primary Auger electrons. The x-rays deeply penetrate the sample (λ_x). Free electrons escape from the sample only close to the surface indicated by the electron escape depth λ_e.

(100 eV - 1000 eV), the transmitted intensity is zero. Instead the total electron yield (TEY) is measured which is directly proportional to the absorption coefficient within certain limits [86]. The limitations are discussed below. In Figure 2.3 (b) the typical geometry for TEY detection is shown.

Each absorption process is most likely followed by the emission of one or several electrons. In a simple picture, the x-ray absorption can be described by two independent processes: excitation of a photoelectron testing the atomic potential, creation of a core hole followed by the rearrangement of the electrons into the ground state. The rearrangement produces primary (spin-polarized) Auger electrons. The further the excited atom is away from the sample surface the less likely the Auger electrons may escape from the sample. The TEY signal is dominated by the inelastically scattered electron cascade (not spin-polarized) originating from the primary Auger electrons [85]. Above approximately 50 eV spin-polarized (spin-up or spin-down) electrons produce an equal number of secondary electrons per primary electron. The total number of secondary electrons (TEY) is therefore proportional to the number of Auger electrons produced by core hole decay. Thus, the TEY is a good measure of the x-ray absorption coefficient.

The absorption coefficient $\mu(E)$ is mainly determined by the electronic structure within the specimen, and is proportional to the sum of the transition probabilities $P_{i,f}$ from the initial state $|i\rangle$ to the final states $\langle f|$:

$$P_{i,f} = \frac{2\pi}{\hbar}|\langle f|\hat{V}|i\rangle|^2 \rho_f(E) \tag{2.14}$$

where $\hat{V}$ and $\rho_f(E)$ are the time-dependent perturbation potential and the density of final states,

respectively. Finally, one has to sum over all initial states $|i\rangle$ with binding energy lower than the energy of the exciting photons.

The absorption spectrum of each element shows characteristic jumps indicating the successive excitation of the core shells, i. e. $K(1s), L_1(2s), L_2(2p_{1/2}), L_3(2p_{3/2})$ etc. The energy region in the vicinity of these transitions can be divided into the so-called near edge x-ray absorption fine structure (NEXAFS) reflecting excitations of the photoelectron into unoccupied valence states, and the extended x-ray absorption fine structure (EXAFS) region where the photoelectron is excited into a continuum state and scatters with the neighbors of the absorbing atom (for a review see e. g. [87,88]).

Basic Principle of XMCD

X-ray magnetic circular dichroism is based on x-ray absorption spectroscopy using circularly polarized light. The difference of the absorption spectra for left and right circularly polarized photons is called XMCD. The difference arises from the imbalance of majority and minority electrons in a ferromagnet or a paramagnet in an applied field that leads to different cross

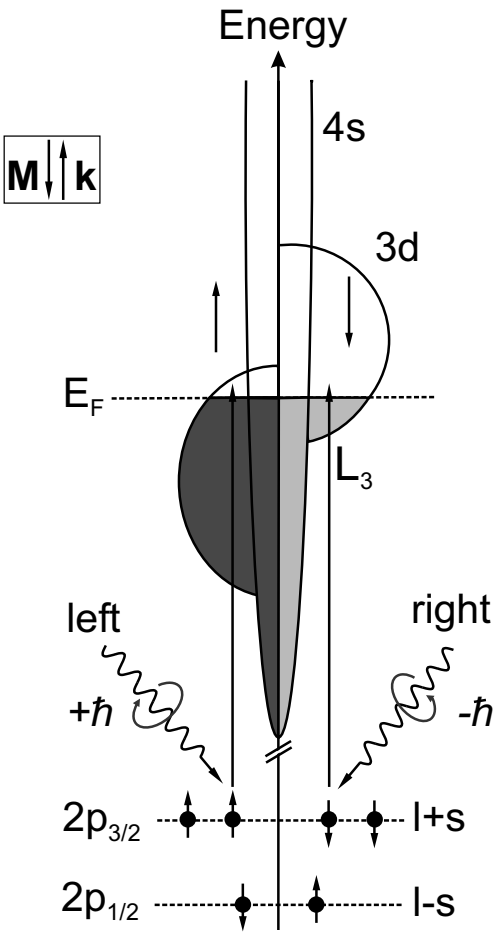

Figure 2.4: Basic model of XMCD in the 3d transition metals. Left (right) circularly polarized x-rays excite spin-up (spin-down) electrons of the spin-orbit split $2p_{3/2,1/2}$ levels. In a second step, the electron accepting unoccupied states of the exchange-split 3d band act as a spin detector. Spin conservation in optical transitions leads to a predominantly probing of the majority band unoccupied states by left-circularly polarized light with respect to the magnetization direction. Right polarized x-rays act vice versa testing the minority band. Both helicities of light therefore show a different cross-section due to the imbalance of unoccupied states. The effect has opposite signs for L_3 and L_2 transitions due to the spin-orbit coupling in the core levels: L_3 (l+s) and L_2 (l-s).

sections and finally to different absorptions coefficients for both helicities of light. Due to the electric dipole transition rules in optics for circularly polarized light

$$\Delta s = 0 \qquad \Delta l = \pm 1 \qquad \Delta j = 0 \text{ or } \pm 1 \tag{2.15}$$

the spin is conserved. Left or right circularly polarized photons transfer their angular momentum ($-\hbar$ or $+\hbar$) to the excited photoelectrons. Figure 2.4 illustrates the excitation of the core electrons from the spin-orbit split $2p_{3/2,1/2}$ levels to the valence band of the 3d transition metals. Left circularly polarized light transfers the opposite momentum to the electron with respect to right circularly polarized light. The spin polarization is opposite at the two 2p levels since the levels show opposite spin-orbit coupling (L_3: l+s and L_2: l-s).

The generated photoelectrons probe in a second step the exchange-split valence band. Majority and minority bands have a different number of electron-accepting unoccupied states acting as a spin detector. Thus, the cross sections differ for both helicities of light. The cross sections can be evaluated from the transition probabilities described as matrix elements of the electron excitation process [89]. As a result, the absorption coefficients (which are measured) also show a difference for left and right circularly polarized light.

The discussion above assumes that the magnetization direction of the sample is fixed and the XMCD difference is the difference of the two helicities of light. Most experiments, however, switch the magnetization direction and detect the XMCD signal at constant helicity. The equivalence of both approaches has been shown in [90], for example.

Depth Sensitivity and Saturation Effect

The different absorption coefficients and thus the XMCD signal can be measured by the detection of the amount of transmitted x-rays or the counting of secondary electrons escaping the sample. The two detection modes presented in Figure 2.3 show strongly different probing depths. Transmission experiments for Co are possible for thicknesses up to 30-40 nm in the soft x-ray regime yielding information of the complete transmitted cross section. The TEY detection method mainly probes the atoms at or close to the surface of the specimen since the electron escape depth λ_e lies on the order of 1.7 nm - 5.0 nm for the pure $3d$ metals Fe, Co, or Ni and their oxides [91]. The combination of both, transmission experiments and TEY detection would yield the most complete information about the investigated specimen, i. e. bulk and surface properties, respectively.

Since substrate supported samples were investigated, the TEY detection mode is used for XAS experiments throughout this thesis. In the following the proportionality of the TEY

$Y(E) \propto \mu(E)$ is critically surveyed since the proportionality is not always fulfilled. The energy dependent electron yield $Y(E)$ is defined by

$$Y(E) = \int_0^\infty I(x,E)\mu(E)e^{-x/\lambda_e}dx. \tag{2.16}$$

Here x is the location with respect to the surface where the absorption process takes place, λ_e the electron escape depth, and $\mu(E)$ the photon absorption coefficient. The photon intensity at depth x and energy E is expressed by

$$I(x,E) = I_0 \cdot e^{-x\mu(E)} \tag{2.17}$$

where $I_0(E)$ represents the incident intensity. At normal incidence ($\theta = 0°$ in Figure 2.3 (b)) the x-ray intensity decays with the x-ray attenuation length $\lambda_x = 1/\mu(E)$ producing the primary Auger yield. Secondary electrons, however, only leave the sample from a much shorter depth described by the electron escape depth λ_e. The energy dependent absorption coefficient causes a modification of $I_0(x,E)$ per absorption layer dx resulting in smaller intensities where μ is largest ($L_{3,2}$-edges) [85]. This effect is often neglected since $\lambda_x \gg \lambda_e$ and thus the variation of the signal originated from different depths is very small. When the angle of the incident x-rays with respect to the sample plane is off-normal ($\theta \neq 0°$), e. g. for probing an in-plane magnetization, the penetration depth $\lambda_x \cdot \cos\theta$ of the x-rays shrinks and at grazing angles $\lambda_x \cdot \cos\theta \approx \lambda_e$ is found. In this case all x-rays contribute to the sample drain current and the measured signal is proportional to the incident x-ray intensity. The relation $Y(E) \propto \mu(E)$ does not hold anymore. From thin films (see e. g. [85,89,92]) it is well known how corrections can be applied to the measured spectra. For samples of finite thickness d one finds:

$$Y(E) \propto \frac{\mu(E)}{1 + \frac{\lambda_e}{\lambda_x}\cos\theta} \cdot \left[1 - \exp\left(-\left(\frac{1}{\lambda_e} + \frac{1}{\lambda_x \cos\theta}\right) \cdot d\right)\right]. \tag{2.18}$$

Equation 2.18 shows that only in the limit of small values for either $\mu = 1/\lambda_x$ or d (or both) the often cited linear relation $Y(E) \propto \mu(E)d/\cos\theta$ is justified. This modelling is also extendable to multilayer samples [89,92]. Experimentally, the necessary corrections are obtained from thickness- and angular-dependent measurements [92,93].

In the case of nanoparticles the correction of saturation cannot be described within simple analytical calculations due to the more complex geometry (spheres) and the lateral confinement of the particles on the nanometer scale. The differences of supported nanoparticles in comparison to a continuous film of finite thickness arise as follows: (i) the nanoparticle volume is more uniformly sampled than a film of comparable thickness. Thus, secondary electrons generated at some distance from the nanoparticle surface escape more easily. (ii) the illumination

cross-section and consequently the amount of light absorbed within the single nanoparticle is independent of the angle of incidence ($\theta = 0° - 80°$) for well-separated spheres. Small interparticle spacings yield smaller effective probing depths due to partial shadowing of x-rays and the absorption of free electrons by the neighbors in the TEY detection mode. One should note that the magnitude of the measured signal increases at grazing incidence, since the number of illuminated nanoparticles increases. After correct signal normalization no angular dependence should be expected.

The experimental proof [94] of the above considerations was recently found by measuring XAS and XMCD of 10 nm micellar Co particles at different angles of incidence. Spectra at normal incidence and at $\theta = 60°$ coincide within 2% in the complete spectral range. However, the reported results in literature on XAS and XMCD usually neglect the saturation process [95,96]. Fauth et al. suggest a numerical ansatz to estimate the saturation effect in nanoparticles [94]. Within these calculations the generation of secondary electrons after absorption and Auger decay inside a spherical nanoparticle are simulated by a Monte Carlo algorithm. As a result, the linear relation between the number of absorbed photons and the absorption coefficient $\mu(E)$ is valid until the attenuation length $\lambda_x = \mu^{-1}$ reaches the order of the particle diameter. Co transmission experiments (free of saturation) find λ_x = 17 nm (35 nm) at the L_3 (L_2) edge [85] being just a factor of two to four times larger than the typical diameter of the particles investigated in this thesis. Further evaluation of the expected total electron yield signal by calculating the escape depth probability of the secondary electrons ($\lambda_e(Co) = 2.2$ nm [91]) shows that deviations from the linear relation $Y(E) \propto \mu(E)$ are found for x-ray attenuation lengths of less than 100 nm. Thus, the pre-edge region remains unaffected ($\lambda_x \gg 100$ nm). The calculated total electron yield of the L_3, L_2 peak, and post-edge region are found to be reduced by approximately 18%, 15%, and 4%, respectively. These findings directly imply that the $L_{3,2}$ peak areas are underestimated resulting in an erroneous determination of the magnetic moments when applying the magneto-optical sum rules to the experimental XAS and XMCD spectra. In chapter 6 these difficulties are addressed.

To evaluate the effective probing depth of TEY measurements of nanoparticle systems the above described modelling of secondary electrons has been performed on substrate supported 9.5 nm Co/CoO core-shell particles using the characteristic electron escape depthes of 2.2 nm (Co) and 3.0 nm (CoO) [91]. One should note that the CoO electron escape depth was estimated and not experimentally verified. The calculations were kindly provided by K. Fauth. Figure 2.5 shows the integrated total electron yield as a function of nanoparticle cross sections from the substrate to the upper point of the nanoparticle sphere. Simulations were performed for both, an isolated Co/CoO core-shell particle (4.5 nm Co core diameter, 2.5 nm CoO shell

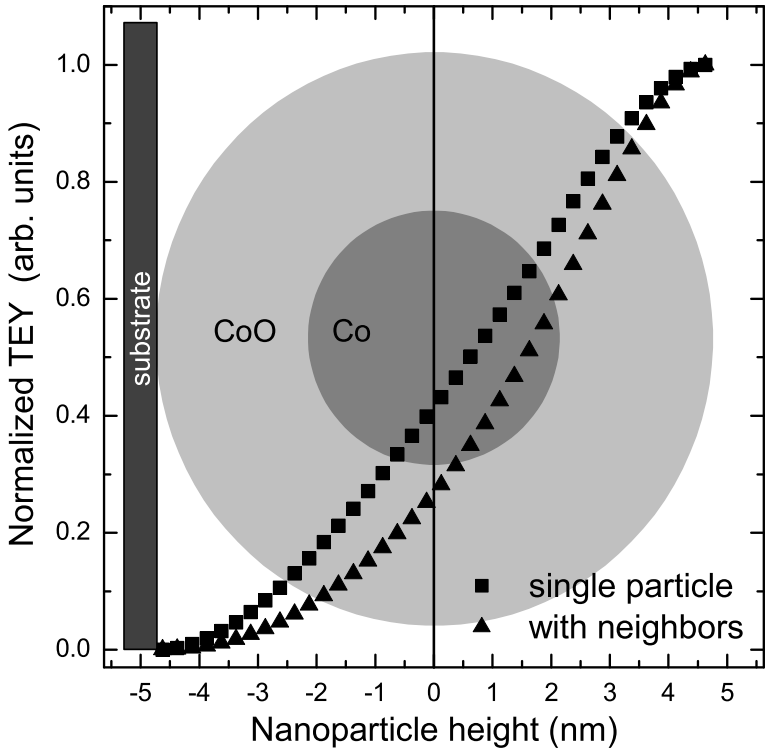

Figure 2.5.: Integrated total electron yield contribution as a function of cross sections with respect to the substrate plane of an isolated 9.5 nm Co/CoO core-shell particle and a particle surrounded by 12 neighbors at a center-to-center distance $d_{cc} = 13nm$. The particle center is set to zero height. For details see text.

thickness) and a particle that is surrounded by 12 nearest neighbors (two shells of a perfectly hexagonal ordered two-dimensional particle array) at a center-to-center distance d_{cc} = 13 nm. The escaping electrons have to pass the ligand shell before detection. The TEY signal in Figure 2.5 is calculated for low absorption coefficients μ (pre-edge region) to explicitly investigate the electron escape depths of the electrons in the spherical geometry. The nanoparticle center is set to zero. The integrated normalized total electron yield is found asymmetrical to the particle center due to the fact that the electron escape depth is smaller than the particle diameter. The isolated particle shows a electron escape depth (1/e-value) in the TEY of 5 nm which is remarkably enhanced compared to the electron escape depth values for thin films given above. The neighboring particles block most electrons ($\approx 80\%$) generated at the lower particle half sphere. Hence, the 1/e-value of the TEY is found at shorter distance (4 nm) from the top most point of the particle sphere with respect to the substrate. However, the value is still enhanced compared to the film. In summary, it can be concluded that the particle's spherical shape results

in a deeper sampling depth of a TEY experiment. The strongest contribution to the TEY (slope of the integrated total electron yield) is found around the upper Co/CoO interface at 2.3 nm - 2.7 nm from the particle's top most point. As a result, the interface magnetism of Co/CoO particles can be addressed with high sensitivity.

By variation of the number of Co atoms in metallic and oxidic environment it is now possible to scale the sampling depth profile to reference spectra of Co and CoO. The relative contributions from Co and CoO signatures to the measured XAS spectra can supply information about the Co metal core diameter and the CoO shell thickness. The method described here represents an independent experimental approach of the determination of the particle composition besides HR-TEM, for example.

Theoretical Approach to XMCD: The Magneto-Optical Sum Rules

The interpretation of the XMCD difference spectra is based on the so-called sum rules. The use of these rules provides the separate determination of the orbital moment and the spin moment. However, a number of approximations and limitations are discussed throughout the literature. A brief overview - limited to 3d metals where the $L_{3,2}$-edges in the soft x-ray regime are examined - is given below.

Magneto-optical sum rules in general are commonly found in atomic physics [97]. Using an atomistic picture which only takes into account intra-atomic hybridization of the wave functions, three sum rules for x-ray absorption were suggested in 1988, 1992 and 1993:

1. The integrated x-ray absorption is proportional to the ground state expectation value of the number of holes in the final state (unoccupied states sum rule) [98].

2. The integrated XMCD signal is proportional to the ground state expectation value of the operator L_Z acting on the shell which the photoelectron receives (orbital sum rule) [99].

3. The linear combination of the XMCD signal at the core split edges is proportional to the expectation values of the two operators S_Z and T_Z acting on the shell that receives the photoelectron (spin sum rule) [100].

The operators L_Z, S_Z, and T_Z are the orbital, the spin, and the magnetic dipole operator, respectively, acting on the quantization axis. The importance of these sum rules is that the experimentally measured XMCD integrated area is directly connected to the ground-state properties.

For a transition between a core level c towards a valence level l with n electrons in the ground state, the sum rules read as follows [101]:

$$\frac{\int(I^{-1}_{c+1/2} - I^{+1}_{c+1/2})d\omega + \int(I^{-1}_{c-1/2} - I^{+1}_{c-1/2})d\omega}{\int(I^{-1}_{c+1/2} + I^{+1}_{c+1/2} + I^{0}_{c+1/2})d\omega + \int(I^{-1}_{c-1/2} + I^{+1}_{c-1/2} + I^{0}_{c-1/2})d\omega} = A(c,l,n)\langle L_Z\rangle \tag{2.19}$$

and

$$A(c,l,n) = \frac{l(l+1) - c(c+1) + 2}{2l(l+1)[2(2l+1) - n]} \tag{2.20}$$

for the orbital sum rule. The spin sum rule is expressed by:

$$\begin{aligned}\frac{\int(I^{-1}_{c+1/2} - I^{+1}_{c+1/2})d\omega - \frac{c+1}{c}\int(I^{-1}_{c-1/2} - I^{+1}_{c-1/2})d\omega}{\int(I^{-1}_{c+1/2} + I^{+1}_{c+1/2} + I^{0}_{c+1/2})d\omega + \int(I^{-1}_{c-1/2} + I^{+1}_{c-1/2} + I^{0}_{c-1/2})d\omega} = \\ = B(c,l,n)\langle S_Z\rangle + C(c,l,n)\langle T_Z\rangle\end{aligned} \tag{2.21}$$

with

$$\begin{aligned}B(c,l,n) &= \frac{l(l+1) - c(c+1) - 2}{3c[2(2l+1) - n]} \\ C(c,l,n) &= \frac{l(l+1)[l(l+1) + 2c(c+1) + 4] - 3(c-1)^2(c+2)^2}{6cl(l+1)[2(2l+1) - n]}\end{aligned} \tag{2.22}$$

The $I^{q}_{c\pm1/2}$ are normalized absorption cross sections for polarization q = -1,1, or 0 corresponding to left, right circularly or linearly polarized light, respectively. The indices $c\pm1/2$ correspond to the two spin-orbit split core level edges. The $I^{q}_{c\pm1/2}$ integrals are proportional to the sum of the transition matrix elements squared. The integrals are calculated for photon angular frequency ω from $-\infty$ to $+\infty$, although only transitions to final states l^{n+1} should be included. From these sum rules the magnetic moments can be determined:

- the orbital magnetic moment: $\mu_L = -\frac{\mu_B}{\hbar}\langle L_Z\rangle$
- the spin magnetic moment: $\mu_S = -\frac{2\mu_B}{\hbar}\langle S_Z\rangle$
- the magnetic dipole moment: $\mu_T = +\frac{\mu_B}{\hbar}\langle T_Z\rangle$

The determination of the magnetic moments from XMCD difference spectra by using the sum rules are limited by several aspects [101]. At first, energy independent cross sections σ are assumed. If the range of integration is not too large this holds in a first approximation for the measured intensity $I \propto \sigma$ assuming that the proportionality constant is independent of energy.

According to the dipole selection rules, there are two possible transitions from the core state c. The conservation of the orbital angular momentum implies transitions to $l = c + 1$ and $l = c - 1$ states. The sum rules for these two channels are different. The x-ray absorption

spectra contain both contributions which cannot be separated easily and make the simultaneous application of the two different sum rules impossible. However, in the case of $L_{3,2}$ absorption edges of the 3d transition metals, the ratio of the radial dipole matrix elements $2p \rightarrow 4s(l = c-1)$ to $2p \rightarrow 3d(l = c+1)$ is small [102]:

$$\frac{|\langle 4s||r||2p\rangle|^2}{|\langle 3d||r||2p\rangle|^2} \approx \frac{1}{50} \tag{2.23}$$

The measured XMCD difference signal is strongly dominated by the $2p \rightarrow 3d$ transitions and the $2p \rightarrow 4s$ are neglected.

In the atomistic picture the initial and final states are treated as pure states without any intermixing which generally does not hold for the 3d metals. The radial integral is assumed to be independent of energy and spin direction, which brings additional complications into the spin sum rule. For example, it has been shown [103] for the $L_{3,2}$ edges of Ni that the radial matrix elements are not constant but vary linearly with the photoelectron energy by 30% from the bottom to the top of the 3d band. The orbital sum rule is not affected by this additional complication. The total discrepancies between the well-known values of Fe, Co, and Ni and the separated magnetic moments determined by the sum rules are found to be about 4% to 10% for the orbital sum rule and up to 30% for the spin rule checked by experiment [104] and theory [105].

However, the sum rules yield an easy approach to the interpretation of XMCD difference spectra. Experimentally the validation of them in the case of Fe, Co, Ni films has been checked by many experiments (for reviews see e. g. [106,107]). The sum rules do not take into account intermixing of the core holes $c-1/2$ and $c+1/2$. Hence, the application for the light 3d elements fails. In this case *ab initio* calculations explain the measured spectra taking into account the intermixing [38]. In compounds and alloys the validity of the sum rules has to be proven in all cases. For systems in reduced dimensions especially the magnitude of $\langle T_Z \rangle$ has to be taken into account to calculate correct moments. Throughout the literature one finds many examples, where $\langle T_Z \rangle$ is neglected. The critical reader should be aware of this fact.

Experimental Determination of Magnetic Moments

For the heavy 3d metals the determination of the orbital and spin magnetic moments according to the sum rules from experimental spectra is straightforward. However, it should be again emphasized that the spectra have to be free of saturation effects as discussed above. In Figure 2.6 the necessary steps are illustrated. From majority and minority XAS spectra both the

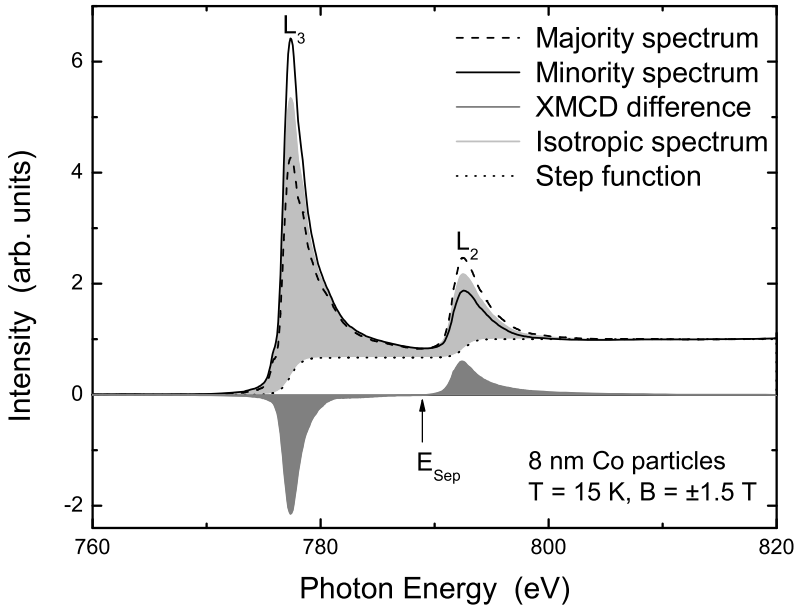

Figure 2.6.: Experimental majority and minority x-ray absorption spectra of 8 nm metallic Co particles recorded at applied fields of ± 1.5 T, normal incidence, and 15 K. In dark grey the XMCD area $XAS^+ - XAS^-$ is shown. The separation energy $\mathrm{E_{Sep}}$ divides the $\mathrm{L_3}$ and $\mathrm{L_2}$ peak areas. The light grey area represents the isotropic peak area $A_{iso} = A_{(XAS^+ + XAS^-)/2}$ after step function substraction to account for excitations into continuum states. From the three areas $\Delta A_{L_3}, \Delta A_{L_2}$ of the XMCD and the isotropic peak area A_{iso} the orbital and spin magnetic moments can be evaluated separately.

XMCD difference $XAS^+ - XAS^-$ and the isotropic spectrum $(XAS^+ + XAS^-)/2$ are calculated. The integrated area of the XMCD difference is divided into the contributions from $\mathrm{L_3}$ and $\mathrm{L_2}$ at the separating energy $\mathrm{E_{Sep}}$ and the areas ΔA_{L_3} and ΔA_{L_2} are achieved. The isotropic spectrum must be freed from transitions to continuum states. It is common to use a 2:1 step function [104] for removal of the $\mathrm{L_3}$ and $\mathrm{L_2}$ edge jumps according to the quantum degeneracy (2j+1). The thresholds are set to the peak positions of the isotropic spectrum. This area is defined as A_{iso} in the following. Experimentally, the determination of A_{iso} that normalizes the XMCD spectrum on a per-unoccupied-3d-state basis gives the largest uncertainties in the magnetic moment evaluation [92].

Finally, the three areas ΔA_{L_3}, ΔA_{L_2}, and A_{iso} define the spin and orbital magnetic moment (for a review see e. g. [108]):

$$\mu_S^{eff} = -2\frac{n_h}{P_C \cos\theta} \cdot \frac{\Delta A_{L_3} - 2\Delta A_{L_2}}{2A_{iso}} \tag{2.24}$$

$$\mu_L = -\frac{4}{3}\frac{n_h}{P_C \cos\theta} \cdot \frac{\Delta A_{L_3} + \Delta A_{L_2}}{2A_{iso}} \tag{2.25}$$

Here n_h defines the number of unoccupied 3d states often denoted as the number of 3d holes. In the following n_h is set to 2.49 calculated for fcc bulk Co [104]. Since synchrotron beamlines do not offer perfectly polarized light one has to divide by the degree of circular polarization P_C. Finally, the $\cos\theta$ accounts for the angle of incident light with respect to the sample magnetization direction. As already mentioned, the spin sum rule supplies a linear combination of μ_S and μ_T. Thus, one measures an effective spin moment $\mu_S^{eff} = \mu_S - 7\mu_T$. In cubic symmetries μ_T can be neglected [89] while its contribution increases for lower symmetries of finite structures like monatomic wires [15].

From equations 2.24 and 2.25 one may easily calculate the ratio of orbital-to-spin magnetic moment m_L/m_S^{eff}:

$$\frac{\mu_L}{\mu_S - 7\mu_T} = \frac{\mu_L}{\mu_S^{eff}} = \frac{2R+1}{3R-2} \quad \text{with} \quad R = \frac{\Delta A_{L_3}}{\Delta A_{L_2}}. \tag{2.26}$$

Throughout the literature it is very popular to give this relative value, since one finds it directly from the XMCD difference spectrum. The ratio μ_L/μ_S^{eff} is independent of the number of unoccupied 3d states, the degree of polarization, and the angle of incidence of light and reduces the discussed uncertainties. Moreover, this value (after μ_T correction) can be directly compared to the g-factor analysis by FMR by the relation $\mu_L/\mu_S = (g-2)/2$ and consequently allows the independent measure of the identical microscopic quantity by two experimental techniques.

Experiments at Synchrotron Facilities

The synchrotron experiments presented in this thesis were performed at two synchrotron facilities: MAX-Laboratory in Lund, Sweden and Bessy II in Berlin, Germany. Since the magnetic properties of Co-based nanoparticles are in the focus of this thesis, the measurements were conducted at beamlines providing circularly polarized light at the Co $L_{3,2}$ edges. Suitable for such investigations are the bending magnet beamlines D1011 at MAX-Laboratory and PM-3 at Bessy II. Both beamlines are equipped with a modified SX-700 monochromator working in the soft x-ray regime under UHV conditions. Detailed descriptions of the beamlines can be found in [109,110] for D1011 and [111] for PM-3 beamline, respectively.

Beamline D1011 operates in an energy range of 30 eV - 1500 eV. At a typical ring current of 100 mA it provides $2 \cdot 10^{10} - 2 \cdot 10^{11}$ photons per second at a photon energy of 800 eV for exit slits of width 6 μm and 92 μm, respectively. The energy resolution (ΔE/E) varies with the width of the exit slit from ΔE/E = 800 (92 μm slit) to ΔE/E = 3600 (6 μm slit). The degree

of circular polarization P_C is tunable by a local modulation (bump) of the electron bunch in the accelerator [109]. Besides linear polarized light the operation modes allow a P_C of 63% or 85% depending on the magnitude of the bump (0.25 mrad or 0.50 mrad). The UHV end station is equipped with a pair of solenoids into which soft iron poles are fitted giving static fields up to $\pm$50 mT. The solenoids are mounted on a platform, which is fully rotatable about the manipulator axis [110]. This provides the possibility to apply magnetic fields at different angles to the photon beam direction. Sample cooling is achieved by a continuous flow He-cryostat reaching 25 K at the sample. The beam spot size on the sample is less than 1×3 mm^2. The photon absorption is detected by the electron yield escaping the sample using both the sample drain current and a channel plate detector. The small currents (pA - nA) are amplified and then transformed by a frequency converter whose signal is recorded by a standard PC system. To scale the signal to the incoming flux a gold grid is installed as a I_0 monitor section. In order to measure the XMCD a pair of XAS is recorded in remanence. The sample magnetization is flipped by two methods: (i) by a 50 mT field pulse or (ii) by heating the sample above the its blocking temperature followed by a field cooling procedure in 50 mT to the measuring temperature. All spectra presented in this thesis are the result of at least three measurements for each magnetization direction. The typical recording time of one spectrum is about 15 minutes, thus the measuring time for one set of parameters is 2-3 h depending on the magnetization reversal procedure.

The operating energy of beamline PM-3 at Bessy II synchrotron facility lies in the range of 30 - 1900 eV. Circularly polarized light is collected above the synchrotron plane by a premirror collimating the light to the monochromator. All spectra are measured at a degree of polarization $P_C = 0.92$. The energy resolution used here is ΔE/E > 4000. The UHV end station is equipped with a fast-switching superconducting magnet ($\pm$3 T) applying the magnetic field parallel or antiparallel with respect to the propagation direction of the incoming light. The sample is cooled by a lHe system achieving a lowest temperature of 15 K at the sample position. The x-ray absorption is detected in the total electron yield mode applying a negative potential of 100 V to the sample in order to push the excited electrons away. Typical currents are on the order of 2-50 pA measured by an ultrahigh precision ampere meter. Measurements in an applied field show typically a reduction of the drain current by a factor of 2 to 10 compared to the zero field signal, since free electrons may return to the sample because of the Lorentz force. Thus, extreme care is taken in the isolation of the sample with respect to the chamber in order to measure the drain current with highest accuracy. The isolation of the sample is realized by a kapton foil on which the samples are glued by epoxi resin showing a resistance of more than 200 GΩ (range of the Ohmmeter). The computer system allows fully automatic control of the photon energy, the applied field and the current detection. The XMCD is recorded by switching the magnetic

field at each energy point which increases the accuracy of magnetic moment evaluation since the beam characteristic does not change dramatically between two points. A field sweep from +1 T to -1 T takes about 15 s. All spectra are normalized by a gold grid I_0 monitor section. Additionally, the electron beam current in the accelerator is detected at each point.

The possibility of measurements in an applied field allows the user to take element-specific hysteresis loops. The loops were always measured at the maximum of the L_3 dichroic signal and at a reference point in the pre-edge region to account for changing drain currents as a function of the applied magnetic field. The validity of this procedure has been experimentally proven by the comparison of hysteresis loops of the identical sample by SQUID magnetometry and hysteresis loops using the XMCD effect [112].

2.3. Other Structural and Magnetic Characterization Techniques

Additionally to FMR and XAS/XMCD investigations various other, mostly structural and morphological characterization methods were employed to obtain information on both, structure and magnetism of the Co/CoO particles. Here, only a short description of the experimental setups is given that are used to achieve the presented results. For more detailed information especially on the operation principles the reader is referred to the literature.

Besides the already mentioned FMR and XMCD, SQUID magnetometry is a powerful tool to measure the field- and temperature-dependent magnetic response of a magnetic sample. Changes of the magnetic stray field of the dipole are detected by linear motion of the sample through so-called pick-up coils. A well-shielded SQUID sensor "counts" the change of flux. Finally, the magnetization of the sample is achieved by a fit routine considering the stray field of the moving point dipole with respect to the detecting coils. The experiments were performed in a commercially available Quantum Design MPMS-XL SQUID magnetometer system working at fields up to 5 T and in a temperature range of 2-400 K. Both, the so-called rapid-scan (RSO) and the standard linear motion modes were used.

The structure of individual nanoparticles and their assembly into superlattices were mostly characterized by TEM. For conventional TEM and SAED a Philips CM12 and a JEOL 3010 microscope were utilized which both are working at an acceleration voltage of 200 kV. Images were always taken by a multipixel CCD camera. Diffraction patterns were calibrated by a gold standard as a reference. HR-TEM studies were performed with the Berkeley atomic resolution microscope working at 800 kV and a Tecnai F20 microscope with an operating voltage of 200

kV and a point resolution of 0.24 nm. A Philips CM200 field emission microscope supplied the microchemical analysis with a probe size of 0.8 nm using an imaging energy filter and an energy-dispersive x-ray analyzer both with an energy resolution of 2 eV. For all TEM investigations Cu grids with an amorphous carbon or silica film were used as substrates.

The sample morphology of arrays of Co/CoO particles was additionally investigated by SEM employing a LEO 1530 standard electron microscope using the in-lens detector at 10 kV acceleration voltage. Topographic images of plasma treated samples were recorded with a Digital Instruments AFM on Si(001) substrates. Standard Si tips scanned the sample in the tapping mode. Before the plasma treatment AFM has been found unprofitable since the tip is able to move the particles on the substrate and the excess of organic ligands after solvent evaporation covers the whole sample surface. After O plasma treatment, however, the organic ligands have been burned away, allowing the nanoparticles to stick to the substrate being unmoveable by the tip and exhibiting a "free" surface that can be scanned by AFM.

3. Organometallic Synthesis of Co/CoO nanoparticles

Nanosized Co/CoO particles can be prepared by both physical and chemical preparation methods. The investigation of size-dependent magnetic properties demands the fabrication of large amounts of particles with a small size distribution. Physical preparation typically uses sputtering methods [59] often combined with gas flow driven cluster formation and deposition [65,113]. Metallic Co particles can be oxidized within the preparation chamber by controlled admixture of O_2 forming a CoO shell. The shell thickness is adjustable [59] allowing the investigation of oxide overlayer thickness-dependent magnetism in the nanoparticles. A variety of preparation methods is listed in table 3.1. All techniques prepare spherical particles with size distributions of 10%-25%. The bigger the particle the smaller is the size distribution.

Another cost-efficient way of preparation of Co/CoO nanoparticles is the chemical synthesis by organometallic precursors [114,115] or the salt loading of inverse micelles [116]. Large amounts on the order of grams can be routinely prepared with size distributions smaller than 10%. Within the last decade large progress in terms of chemical stability and monodispersity has been achieved. Besides single element magnetic nanoparticles chemists succeeded in the synthesis of bimetallic magnetic particles such as $FePt$ [117], $CoRh$ [118], or $AgCo$ [119], too. Here, however, the discussion is focussed to preparation procedures of Co/CoO particles. An arbitrary selection of preparation methods is listed in table 3.1. For example, the organometallic precursor $Co(\eta^3-C_8H_{13})(\eta^4-C_8H_{12})$ reacts with hydrogen in tetrahydrofurane in the presence of polydimethyl phenyloxide to 7.5 - 11.5 nm Co particles which slightly oxidize after preparation. Generally, metallic Co particles are synthesized under oxygen-free conditions. After the preparation, however, some oxygen provided by air, organic compounds in the solution for particle stabilization, or some contaminants in the solvent donate oxygen to the particle surface. An oxidic shell is forming that stabilizes the metallic Co core at a CoO layer thickness of 2-3.5 nm (table 3.1) preventing further oxidation. One may note that some authors do not analyze surface oxidation and thus claim that chemically prepared Co particles do not oxidize at the surface. Structural characterization by TEM or x-ray diffraction (XRD) are not sufficient methods to

Table 3.1.: Arbitrary selection of Co/CoO nanoparticles prepared by both, physical and chemical preparation methods. The total diameter, its distribution (full width at half maximum), the CoO shell thickness, and the structure of the metallic core and the oxidic shell are listed.

Preparation method	Total diameter	Size distribution	CoO shell thickness	Structure Co/CoO	Ref.
Vapor deposition	8-35 nm	1.5-5 nm	2 nm	fcc/fcc	[59]
Cluster gun sputtering	4.7 nm	1.1 nm	1 nm	fcc/fcc	[65]
Cluster beam deposition	6,13 nm	< 10%	2-3 nm	fcc/fcc	[113]
Organometallic synthesis	7.5-11.5 nm	large	2.5-3.5 nm	hcp/fcc	[27]
Organometallic synthesis	9,11,13 nm	1.2-1.5 nm	2-3 nm	fcc/fcc	this thesis

exclude surface oxidation. XAS in the TEY mode reveals more detailed surface information. This technique is able to prove surface oxidation of less than one monolayer (section 4.3.2).

Another widely used organometallic precursor is dicobaltoctacarbonyl ($Co_2(CO)_8$) [115, 120,121]. By the thermal decomposition in organic solvents spherical particles of 6-14 nm in diameter can be routinely prepared. All batches of Co/CoO nanoparticles investigated in this thesis have been synthesized by M. Hilgendorff [115] using this method. His approach was the use of commercially available chemicals for the synthesis of monodisperse colloidal nanoparticles, which yields the cost-efficient preparation of huge amounts of nanoparticle solution.

The synthesis of Co/CoO nanoparticles is based on the thermal decomposition of dicobaltoctacarbonyl ($Co_2(CO)_8$) in non-polar solvents such as decane in the presence of a combination of stabilizers, i. e. oleic acid ($CH_3(CH_2)_7CH = CH(CH_2)_7COOH$) and oleyl amine ($CH_3(CH2)_7CH = CH(CH_2)_8NH_2$). The providers of the chemicals have been published elsewhere [115]. Oleic acid has been found to be the best stabilizer to slow down the oxidation of the particles efficiently. Oleic acid as the only stabilizer is not sufficient for size-controlling. Thus, oleylamine has been added to control particle growth. In a typical experiment, 50 ml Ar-saturated toluene containing 0.6 mmol oleic acid and 0.6 mmol oleylamine was heated to reflux for 30 min. After cooling to 330 K 1 mmol $Co_2(CO)_8$ has been added, and again the solution was heated to reflux for 60 min. The preparation is scalable up to 1.5 molar concentration (200 ml) with standard laboratory equipment. Highly concentrated solutions were found very useful for long-term stability. Quasi-monodisperse particles have been obtained using an external magnetic field to separate particles of similar size and magnetic moment. For simplicity, a magnetic stirrer has been used during the particle growth. Very large particles and some agglomerates were present after preparation. These can be easily removed, together with the magnetic stirring bar, after cooling to room temperature. A further stepwise size selection by a strong $NdFeB$

permanent magnet (B $\sim$ 1 T) has been repeated until a small size distribution was obtained (typically three steps). However, the separation of sizes led to the loss of an unknown amount of material. Furthermore, size-selection can be increased by size-selective precipitation [122]. If a small amount of ethanol is added to the solvent the barrier to aggregation is reduced and the nanoparticle dispersion is destabilized. Since larger particles experience the greatest attractive forces, these particles aggregate first and can be separated from the dispersion by filtering, centrifugation or exposure to a magnetic field gradient.

In summary, colloidal chemistry allows the fabrication of monodisperse ligand-stabilized Co/CoO particles in organic solvents. Long-term chemical stability ($\sim$ 1 year) is achieved by the oxygen free storage of the particle containing solvents [95]. The particles oxidize at the surface most probably by the donation of oxygen by oleic acid. After nanoparticle deposition on a substrate and their exposure to air the oxidation continues faster. This phenomenon is discussed in terms of magnetic aging in section 5.1.6. Particles with diameters below 6 nm are found fully oxidized within days after the deposition on the substrate in ambient conditions. Larger particles maintain a small metallic Co core surrounded by 2-3 nm thick CoO overlayer protecting the further oxidation. Once the 2-3 nm thick CoO shell is formed, the oxidation slows down to a few atoms per day although the particles are stored under ambient conditions.

Compared to physical fabrications the chemical route allows the self-assembly of the nanoparticles on different substrates. Inverse micelles and Langmuir-Blodgett deposition techniques, for example, yield well-ordered lattices of "Co" particles on Si substrates. Here, the nanoparticle distance is given by the doubled chain length of the micelle being in minimum five times larger than the nanoparticle diameter. This results in a total coverage of approximately 1%

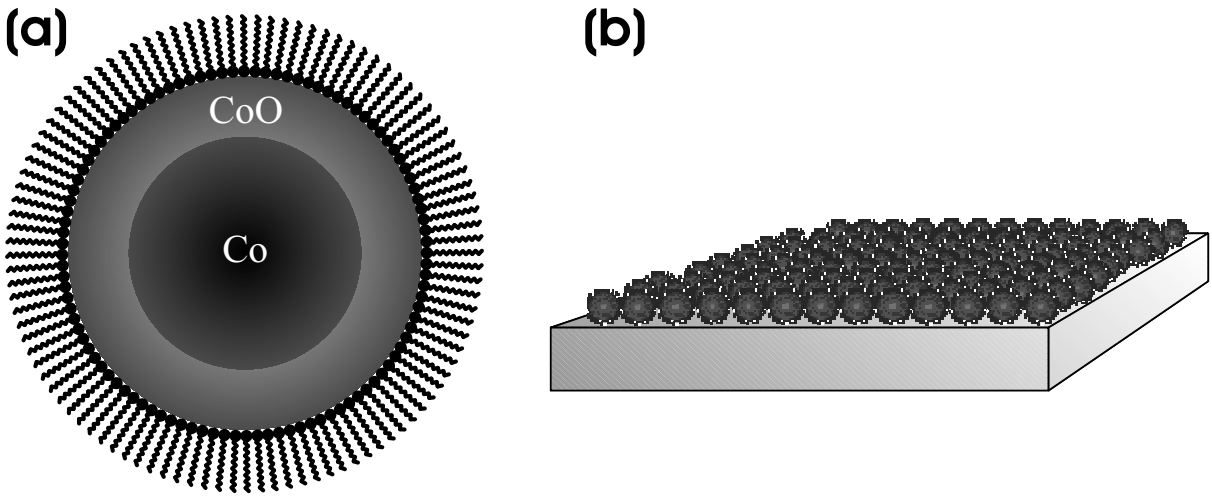

Figure 3.1.: Idealized 11 nm Co/CoO nanoparticle with a 2 nm CoO shell (a). The ligand length is also approximately 2 nm. In (b) a close packed superlattice of particles is shown.

of the total substrate area [116]. A simple approach to enhance the coverage without losing the self-assembly opportunities is the usage of nanoparticles stabilized by short length ($\approx$ 2 nm) organic ligands and the dispersion in non-polar solvents. An idealized Co/CoO particle is shown in Figure 3.1 (a). Superlattices of particles can be prepared by droplet evaporation, spin coating or magnetophoretic deposition (section 4.2). An ideal superlattice of particles is shown in Figure 3.1 (b).

The two most important requirements for the self assembly of colloidal particles into well-ordered superlattices are a narrow size distribution and the absence of any agglomeration of the particles. Both requirements are satisfied for quasi-monodisperse nanoparticles [115,122,123]. Additionally to the self-assembly properties it is now possible to scale the magnetic properties to the nanoparticle sizes and confinement that was previously only possible with clusters (diameter d < 2 nm) or lithographically produced structures (d > 20 nm). Colloidal magnetic nanoparticles close this gap.

4. Structural and Morphological Characterization

Detailed structural investigations on both, the atomic structure and composition of a single nanoparticle and their superstructure morphology, e. g. the ordering into ordered arrays of the particles, are absolutely necessary for the interpretation of magnetic characterization. Firstly, the shape, the size distribution, the composition, and the atomic structure of single nanoparticles are discussed in this chapter. Secondly, the organization into 2D and 3D superlattices is presented using droplet evaporation, spin coating, or magnetophoretic deposition. Finally, post deposition sample manipulation by means of reactive plasma etching is discussed that allows investigation of metallic Co nanoparticles free of organic ligands and surface oxides.

4.1. Structure of Single Nanoparticles

The Co/CoO nanoparticles have been characterized by means of Transmission Electron Microscopy (TEM). The size distribution and the shape of the nanoparticles were investigated for all batches. More detailed information on the local atomic structure and the distribution of elements in a single nanoparticle or a small array of particles ($\sim$10-20 particles) have been achieved by sophisticated techniques found in a well-equipped TEM such as high resolution TEM (HR-TEM), energy filtered TEM (EF-TEM), selected area electron diffraction (SAED), and element dispersive x-ray (EDX) analysis.

The size distributions of the nominally 9, 11, and 13 nm Co/CoO particles are shown in Figure 4.1. For the evaluation of the size histograms several low magnification TEM images have been used for each batch. The diameter of a single nanoparticle was averaged by two measurements perpendicular to each other. Total numbers of particles of 573, 75, and 205 for the 9 nm, 11 nm, and 13 nm particles were taken into account, respectively. The resulting histograms were fitted by the log-normal size distribution

$$f(d) = \frac{1}{\sqrt{2\pi}\sigma d} \exp\left(-\frac{1}{2\sigma^2} \ln^2\left(\frac{d}{d_{mp}}\right)\right) \tag{4.1}$$

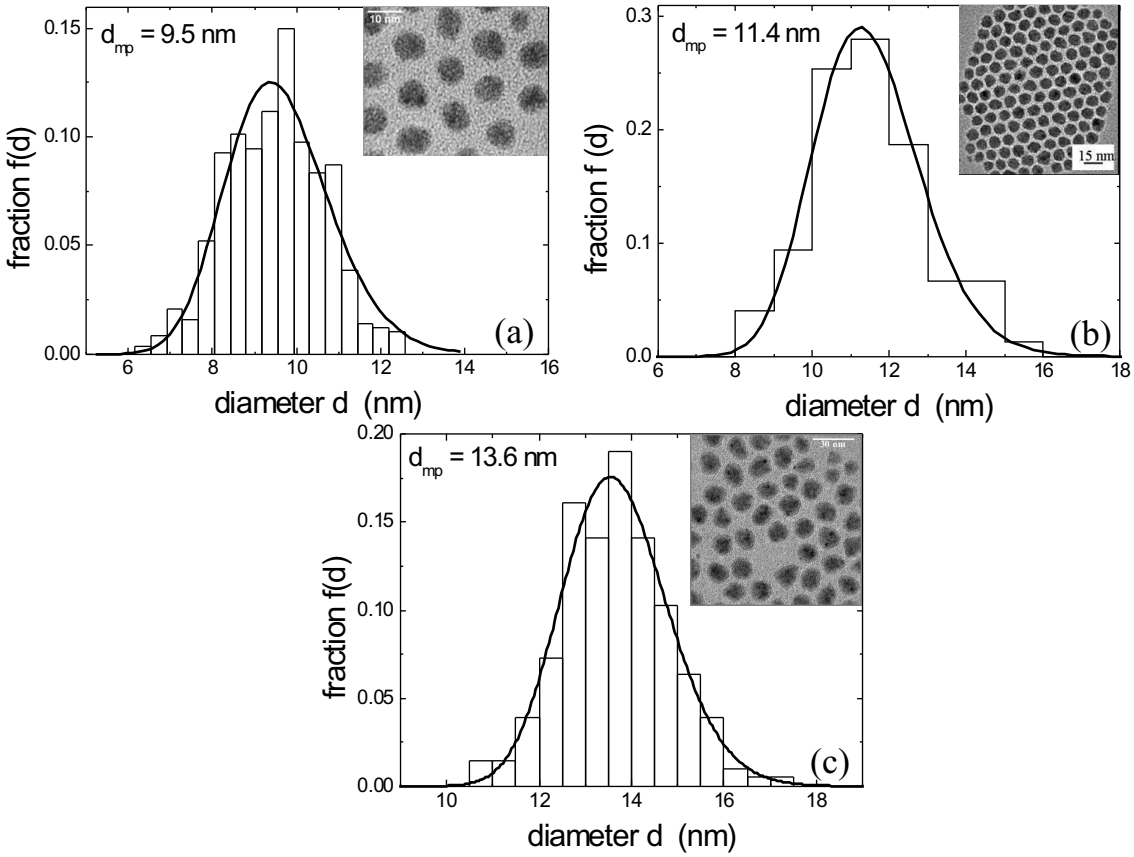

Figure 4.1.: Size histograms of the nominally 9 nm (a), 11 nm (b), and 13 nm (c) Co/CoO particles and their corresponding log-normal fit functions. The most probable diameter d_{mp} (size distribution full width at half maximum) are 9.5 nm (2.7 nm), 11.4 nm (3.0 nm), and 13.6 nm (2.6 nm), respectively. The insets represent typical low-magnification TEM images used for the size characterization.

where $f(d)$ is the fraction of the total amount of particles in a specific diameter range, σ is the size distribution and d_{mp} is the most probable diameter indicated by the maximum of the log-normal size distribution function. The log-normal fit functions (also shown in Figure 4.1) give a most probable diameter of 9.5 nm, 11.4 nm, and 13.6 nm for the three batches of Co/CoO particles. The size distributions show a full width at half maximum (FWHM) of 2.7 nm, 3.0 nm, and 2.6 nm, respectively. Although the size distribution is commonly calculated by a log-normal function, the evaluation of the size distribution by a Gaussian function gives identical results in the case of the 9 nm Co/CoO particles. The typical broadening at larger diameters is not observed in this batch.

A typical high resolution TEM image of a 11 nm Co/CoO particle is presented in Figure 4.2 (a). It shows that the particle is polycrystalline with a core-shell structure. Atomic resolution

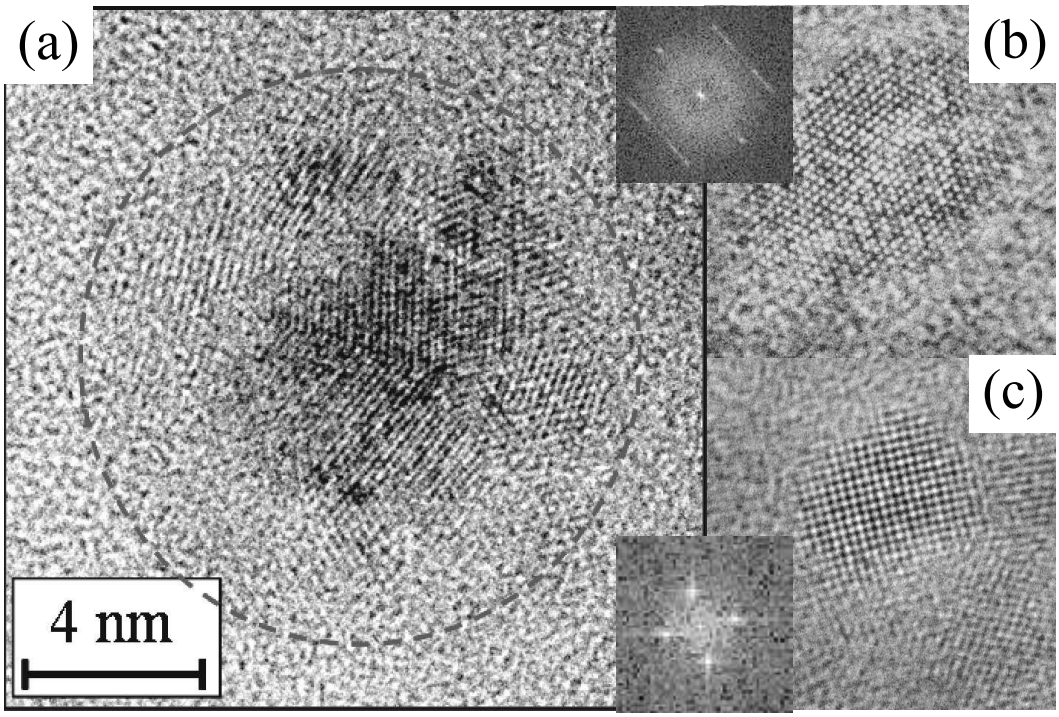

Figure 4.2.: High-resolution TEM image of a 11 nm Co/CoO particle on an amorphous carbon-coated copper grid (a). Atomic resolution images of the particle core (b) and the particle shell (c). A twin boundary parallel to the common (111) plane is clearly visible in the core (b). The insets show the Fourier transforms of the images (b) and (c), respectively. The figure has been adapted from [61].

studies of single grains located close to the particle center and at the particle surface are printed in Figure 4.2 (b) and (c), respectively. Detailed analysis of the atomic resolution images by Fourier transforms (Fig 4.2 insets), angle determination and center-to-spot distance calibrated by a gold reference sample yields a fcc CoO structure in the shell and a multiply twinned Co fcc structure in the core of a particle. The twinning boundary is also visible in Figure 4.2 (b). The stripe structure of four points in the Co core Fourier transform spots is due to the twinning boundary. Fourier transforms on both single crystalline parts of the image yield a clear 6-spot structure. The Co core is multiply twinned with the twin boundaries parallel to the common (111) plane. The typical grain diameter is 2-3 nm. Detailed structure determination has been performed on more than 10 particles. SAED studies (shown in appendix B) are in full agreement with the HR-TEM results. SAED patterns of the Co/CoO particles present full sets of diffraction rings of the fcc Co and fcc CoO phases (Appendix B). The lattice parameters are close to bulk fcc Co and bulk fcc CoO structures.

The core-shell structure of the Co/CoO particles becomes more apparent in Figure 4.3. Nominally 13 nm Co/CoO particles exhibit a CoO shell thickness of 2-3 nm. Individual grains are clearly visible in Figure 4.3. Lattice plane spacings of CoO $d_{220} = 0.150$ nm and $d_{200} =$

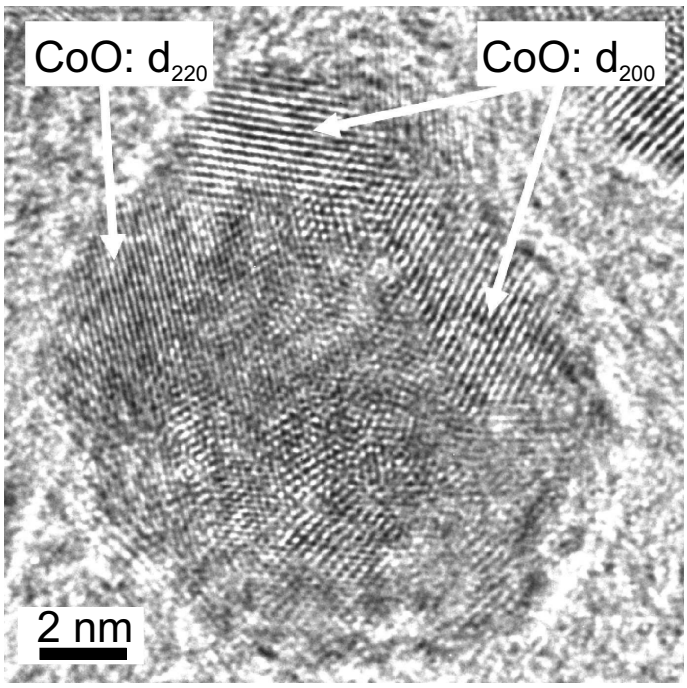

Figure 4.3.: High-resolution TEM image of a 13 nm Co/CoO particle on an amorphous carbon-coated copper grid. The core-shell structure of the particle is clearly visible. The arrows mark single CoO grains with lattice plane spacings of $d_{220} = 0.150$ nm and $d_{200} = 0.213$ nm.

0.213 nm have been identified. The metallic core has a diameter of approximately 7.5 nm.

Spatially resolved compositional analysis of the particles has been performed by spectral imaging of the sample using the electron energy-loss signal. Figure 4.4 (a) and (b) show EF-TEM images of a single isolated nanoparticle filtered at the Co L_3-edge at 778 eV and the O-K edge at 525 eV, respectively. The oxygen-filtered image directly reveals a non-uniform distribution of oxygen along a single nanoparticle. The corresponding intensity line scans (Figure 4.4 (c) and (d)) along the line shown in Figure 4.4 (a) reveal a rather uniform distribution of Co in the particle. The Gaussian shape of the intensity signal is characteristic for spherical particles. The O-mapping exhibits a double peak distribution. Using a Gaussian double peak fitting routine for the simulation of the intensity histogram in Figure 4.4 (d) the thickness of the CoO shell has been determined to 2-2.5 nm, and the diameter of the Co core is approximately 7 nm. The results of the element-specific imaging are in full agreement with the HR-TEM analysis described above.

Energy filtering has also been performed on lower magnification images. An example is shown in Figure 4.5. A standard TEM image of an array of Co/CoO particles is shown in Figure 4.5 (a) while the energy-filtered images at the Co L_3 edge (778 eV) and the O K edge (525 eV) are presented in (b) and (c), respectively. The whole arrangement of more than 50

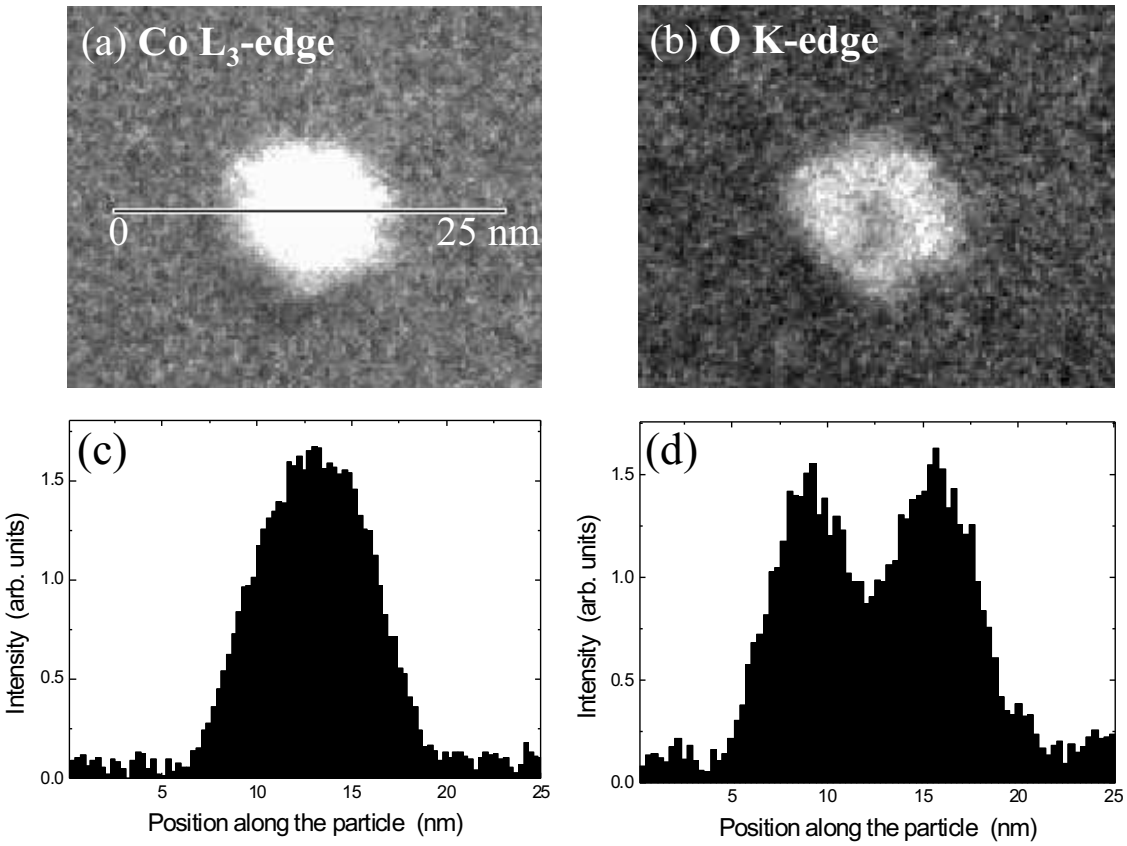

Figure 4.4.: EF-TEM images of a single nominally 11 nm Co/CoO nanoparticle filtered out (a) the cobalt L_3 edge and on (b) the oxygen K edge. In (c) and (d) the corresponding linescans are shown. The figure has been adapted from [95].

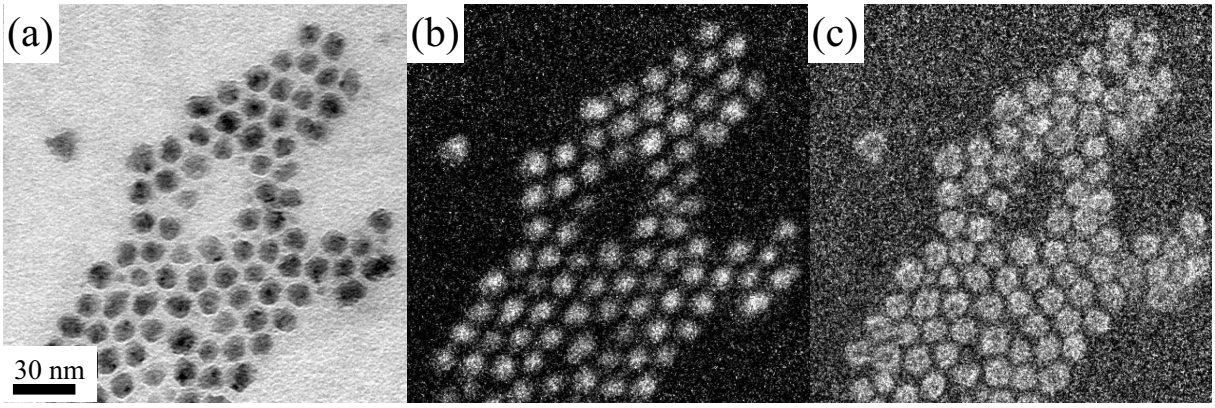

Figure 4.5.: TEM images of an array of the 11 nm Co/CoO nanoparticles. In (a) the standard TEM images is presented, (b) and (c) are filtered on the Co L_3 edge and on the O K edge, respectively. The figure has been adapted from [61].

Co/CoO particles show the same tendency. Co atoms are rather uniformly distributed along a nanoparticle while O atoms are preferentially located at the surface.

Finally, it is important to note that the 2-2.5 nm CoO shell acts as a protective layer to the encased Co core when the particles are deposited on a substrate and are exposed to air. The development of this protective oxide shell takes place in two steps: (i) directly after the chemical preparation a thin CoO shell forms within minutes until the small amount of molecular oxygen in the solvent is consumed. Further oxidation within the solution can only take place by cracking the $COOH$ group of oleic acid. Oleic acid binds to the Co particle via oxygen. Then, the degree of oxidation remains nearly constant, since the solubility of oxygen in an organic solvent is low and the solution is kept in a tightly closed container. (ii) When the particles are deposited on a substrate the ligand surrounded particles are exposed to air after the evaporation of the solvent. Then, within hours, the CoO shell grows to a shell thickness of about 1-2 nm forming an early stage of a protective oxide layer. Only from this degree of oxidation on, structural information by means of TEM is available. The further growth of the CoO shell slows down. After half a year 9 nm Co/CoO particles have not shown a noticeable thicker CoO shell by TEM. One should note that the measurements have been performed within one hour after the deposition of the particles on a TEM grid. Thus, the particles were exposed to air for identical periods of time. This finding proves the first process of oxidation. The growth of the CoO shell by the exposure to air is not easy to detect by imaging techniques since high-resolution imaging is always needed. More profitable investigations of the oxidation as a function of air exposure are XAS/XMCD and FMR. XAS and XMCD in the total electron yield mode are surface sensitive and FMR detects the ferromagnetic core only. The results of these measurements are presented in chapter 5. To complete the discussion the main findings are given here.

Only two days after the nanoparticle synthesis and directly after the sample preparation (less than one hour air exposure) 9 nm Co/CoO particles have been transferred into a UHV chamber for XAS/XMCD characterization. At this stage, a CoO shell thickness of 1.0$\pm$0.3 nm has been found. Half a year later, however, the shell thickness has increased to 2.5 nm [124]. Meanwhile the sample has been kept in ambient conditions. FMR experiments over a period of 18 months suggest an upper limit of the CoO shell thickness of about 2 nm four hours after the nanoparticle deposition from the solution and a relatively fast further growth to about 2.8 nm three weeks after the deposition. From this point of time on the oxidation process slows down to only a few atoms per day reaching an upper limit of 3.2 nm after 18 months. These findings confirm the second mechanism of oxidation mentioned above.

In summary, all three batches of Co/CoO nanoparticles have shown a typical fcc CoO shell thickness of 2-3 nm after the chemical preparation and deposition onto a substrate. The metallic core consists of multiply twinned Co grains with a typical diameter of 2-3 nm. For both, the core and the shell the observed lattice constants are close to the bulk lattice constants of fcc Co

Table 4.1.: Results of the structural characterization for the nominally 9 nm, 11 nm and 13 nm Co/CoO particles. The total number of Co atoms is calculated from the core and shell volumes. The given numbers are averaged over the uncertainty of the CoO shell thickness.

Batch	9 nm Co/CoO	11 nm Co/CoO	13 nm Co/CoO
Diameter	9.5 nm	11.4 nm	13.6 nm
Size distribution (FWHM)	2.7 nm	3.0 nm	2.6 nm
Size distribution	14%	13 %	14 %
Thickness of CoO shell	2-2.5 nm	2-2.5 nm	2-2.5 nm
Core diameter	4.5-5.5 nm	6.5-7.5 nm	8.5-9.5 nm
Total number of Co atoms	25800	47100	82800
Number of Co core atoms	6100	16400	34600
Number of Co^{2+} ions in shell	19700	30700	48200

and fcc CoO, respectively. The results of the size distributions and the compositional analysis are summarized in Table 4.1 for the three batches of particles of slightly different diameter. From the constant thickness of the CoO shell the metallic core diameter has been calculated to 4.5-5.5 nm, 7-8 nm and 8.5-9.5 nm for the 9 nm, 11 nm and 13 nm particles, respectively. Using bulk lattice constants (Co: 0.35447 nm, CoO: 0.42614 nm) and the bulk densities of Co and CoO (Co: 8900 kg/m^3, CoO: 6400 kg/m^3) the number of Co atoms in the core and in the shell can be calculated for the most probable diameter and spherical particles. Although the shell thickness of a spherical particle has been found to be constant, the number of Co atoms in the core and the shell changes dramatically with the most probable diameter, since length scales enter by third power to the volume.

4.2. Self-assembly

Marbles on the cm length scale with nearly identical diameter show the tendency to self-assemble into ordered superlattices when they are shaken on a flat surface. Spheres on the nanometer scale behave similarly [123] although the shaking of particles is not driven by the movement of the substrate only (e. g. spin coating) but also strongly influenced by Brownian motion and electro- and magnetostatic interactions between particles and to the substrate. In this section the ordering of Co/CoO nanoparticles into ordered and non-ordered arrays in two and three dimensions is presented. The detailed knowledge of the self-assembly mechanism is essential, since the morphology of the sample directly influences the magnetic properties in

terms of magnetostatic interaction between the particles. Three different sample preparation techniques will be described. At first, the most intuitive way of nanoparticle deposition - the controlled drying of a droplet of solution containing the particles - is presented. To achieve lower but very uniform coverage spin coating has been found to be the method of choice. Finally, the drying in an applied magnetic field is discussed, where 3d rod structures are formed consisting of several thousands of particles. Within the rods the particles are coupled by magnetostatic forces. The advantages and the drawbacks of the three techniques are discussed in this section while the detailed parameters of the investigated samples are always given when the magnetic response of the individual samples are presented.

Droplet Evaporation Technique

The simplest way to arrange nanoparticles on a substrate is the controlled drying of a droplet of particle-carrying solution. This technique yields the formation of well-ordered close-packed arrays of particles on the scale of a few μm^2 under appropriate conditions [123]. The most important tuning parameters are the wetting properties of the substrate with respect to the solvent medium and the drying time. The concentration of particles in the solvent determines the total coverage of the substrate tunable from very low concentrations (<10%) with large interparticle spacings to several tens of multilayers of particles [95]. In Figure 4.6 the effect of the wetting properties of the substrate is clearly visible. The SEM image in Figure 4.6 (a) shows the 9 nm Co/CoO particles prepared from 1:20 diluted toluene-based nanoparticle solution deposited on a B doped Si (Si:B) substrate with a native 3 nm layer of SiO_2. Each light spot represents a single particle. Very locally a closed-packed arrangement of 20-30 particles is found. Enhanced closed-packed ordering shows the TEM image in Figure 4.6 (b). The 11 nm Co/CoO particles arrange into a hexagonal closed-packed superlattice. Defect-free arrangements of several hundreds of particles have been observed for this specimen. The drying of the toluene-based solution onto carbon-supported TEM Cu grids obviously enhances the self-assembly of the particles. The center-to-center distance d_{cc} of approximately 100 particles of each batch has been measured. The 9 nm particles show a d_{cc} of 13 ± 1 nm in a hexagonal arrangement and the 11 nm particle exhibit a d_{cc} of 14.9 ± 1 nm. Using the most probable sizes of the different batches one finds an interparticle spacing of 3-3.5 nm for both Co/CoO particle batches. The chain length of the stabilizing ligands is around 2 nm. Hence, it cannot be expected that the separation of particles is less than 2 nm and more than twice the chain length of 4 nm for a closed-packed superlattice. The interparticle spacings are found in this range. The spacing of 3 nm reveals a partial interlocking of the particle surrounding ligands shells. In the case of 9 nm Co/CoO particles the toothing between neighboring particles is less pronounced. Distances be-

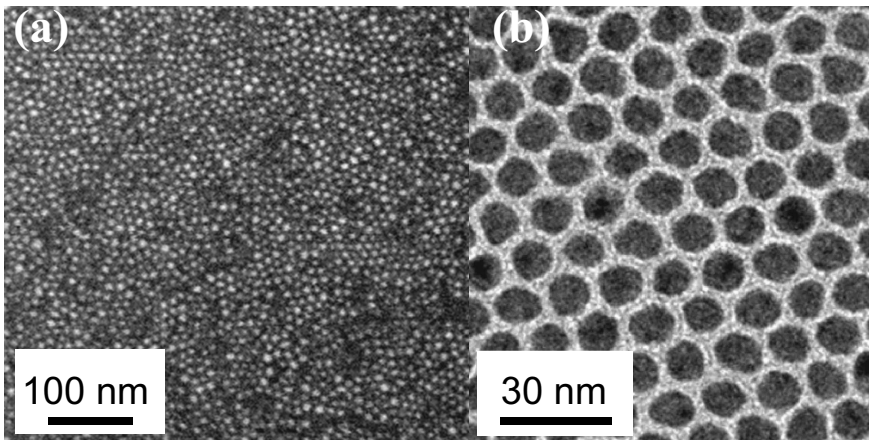

Figure 4.6.: SEM image of a typical result for 9 nm Co particles a on Si:B substrate using the droplet evaporation technique (a). Closed-packed arrangements of 20-30 particle are found. (b) shows a TEM image of a closed-packed superlattice of the 11 nm Co/CoO particles.

tween particles are larger in average, since only short range arrangements of 20-30 particles are observed. Distances between ordered domains are larger than the interparticle distance within the ordered regions. This result shows that the spacing of nanoparticles with an identical ligand shell may vary with the wetting properties, the drying time, and also the particle diameter (not shown). Thus, the detailed knowledge of the particle spacing is essential and has to be measured for all individual samples. Moreover, it has been published [125] that an excess surfactants can lead to enhanced long-range ordering. Generally, a small excess surfactants is used in colloidal chemistry to achieve long-term stability of the particles.

Spin Coating Technique

Nanoparticle deposition by spin coating is a commonly used technique to achieve large scale two-dimensional arrangements [23]. The advantage of this technique is the large scale uniformity of the sample, the drawback is the loss of nanoparticle ordering due to the fast drying. The preparation of coverages between 1% and 90% of a close-packed superlattice is possible. In Figure 4.7 two examples are shown with different particle densities of 54% (a) and 89% (b) of the corresponding close-packed nanoparticle arrangement. It is important to note that the projection of a 2D hexagonal superlattice perpendicular to the sample plane is only 56% of the total sample area for 9 nm Co/CoO particles (interparticle spacing 3.5 nm). The two examples have been prepared from hexane-based Co/CoO particle solution with an initial concentration of 1:10 and 1:30 of the concentrated toluene-based solution on native $Si(001)$ substrates ($4 \cdot 4$ mm^2) at 6000 rotations per minute (rpm) in ambient conditions. An area of $3 \cdot 3$ mm^2 in the

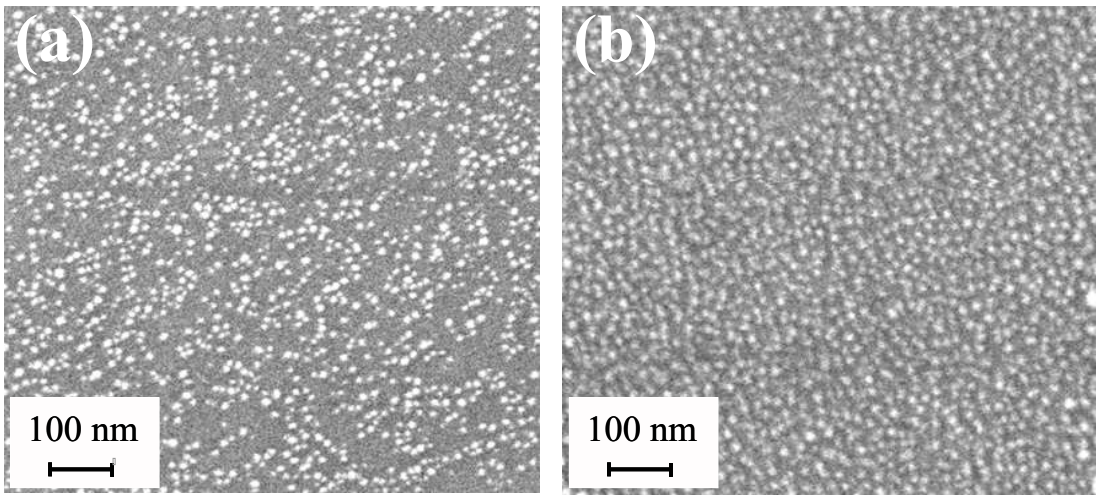

Figure 4.7.: SEM images of spin coated nanoparticle assemblies on native $Si(001)$ substrates at 6000 rotations per minute. Different filling factors of 54% (a) and 89% (b) of a corresponding 2D hexagonal arrangement are observed. For the spin coating different initial concentrations have been used. Details are described in the text.

sample center exhibits a uniform coverage for all samples. At the edges of the samples multilayer formation takes place. The fast rotation speed spins away the particle carrying solution. Only a thin film of hexane resists the centrifugal force and the hexane film instantaneously breaks up into drops on the micrometer scale since the hexane starts evaporating. Whenever a particle gets into contact to the substrate the particle sticks at its position due to electrostatic attraction. The whole process takes place within a few seconds depending on the rotation speed and the temperature. The velocity of the preparation process is responsible for the lack of close-packed hexagonal arrangements on the sample. Detailed parameter tuning might give rise to a hexagonal ordering as observed for $FePt$ nanoparticles [23].

Here, however, the aim is the preparation of uniform coverages over large areas. For the synchrotron measurements partly spin coated samples were used, where a uniformly covered area of $4 \cdot 8$ mm^2 on a $5 \cdot 10$ mm^2 $Si(001)$ substrate has been achieved. To scale the magnetic response of this type of samples in absolute units one only can employ magnetic characterization techniques with limited probing spots such as magneto-optical methods. Stray-field methods like SQUID magnetometry provide information of the total magnetic response of the sample, thus measuring the sum of the uniformly covered area and the multilayers at the sample edges. Only the removal of multilayer regions with several layers of particles, e. g. by breaking the edges of the substrate, would give rise to a scalable magnetic response by counting the particles per unit area. One should note that especially for low coverages at the sample center up to 90% of the total number of particles are found at the edges of the sample. Thus, a SQUID signal dominantly measures the region where several layers of particles are found.

Magnetophoretic Deposition Technique

The formation of regular arrays of Co/CoO particles can be achieved by drying of the nanoparticle solution in an applied magnetic field [126,127]. Detailed investigations of the superlattices formation as a function of the applied field in the sample plane [115] have shown that (i) at low external magnetic fields (B < 0.7 T) the close-packed superlattices formation is enhanced with increasing external fields, (ii) the formation of an ordered double layer is observed at B = 1.5 T and (iii) an external magnetic field of B = 6 T yields the formation of a third layer in ABA configuration with respect to the nanoparticle layers underneath. These experiments were performed at low nanoparticle concentration. However, to achieve a sufficiently strong magnetic response from the investigated sample we used a higher concentration for our experiments. A typical example is shown in Figure 4.8. An external magnetic field of B = 0.35 T parallel to the grid plane was sufficient to produce a stripe structure onto a carbon-coated Cu grid by drying 5 μl toluene-based solution in ambient conditions. Stripes consisting of a regular close-packed arrangement of the Co/CoO particles with a width of 200-250 nm and a length of 1.5-3 μm were formed along the external field axis. Mostly, the stripes consist of 3-4 layers of particles forming a nearly perfect 3D fcc lattice with the (111) planes parallel to the substrate. The nearest neighbor distance is about 16 nm in this case. These stripe structures provide the possibility to investigate the dipolar interaction of the particles within a stripe and between stripes by angular-dependent ferromagnetic resonance close to the blocking temperature (T = 300 K) as shown in section 5.2.

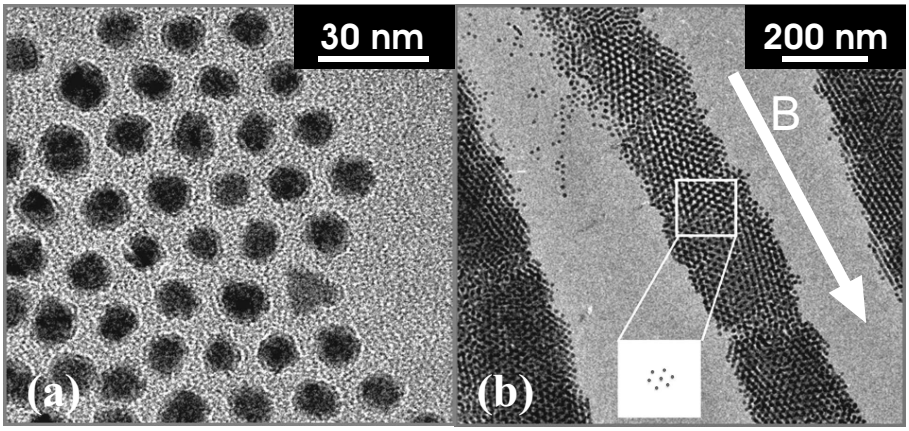

Figure 4.8.: TEM micrographs of the 11 nm Co/CoO particles deposited onto a carbon-coated Cu grid in a magnetic field of 0.35 T parallel to the grid plane at high resolution (a) and lower magnification (b). The high degree of crystallinity is shown by the Fourier transform in the inset on the right image. The figure has been adapted from [126].

4.3. Post Deposition Manipulation

The deposition techniques provide 2D and 3D nanoparticle arrays as described above. All particles are surrounded by organic ligands. Characterization by x-ray methods (XAS and XMCD) using the total electron yield mode provides high surface sensitivity. Thus, the electrons excited in the particle by XAS, e. g. at the Co-$L_{3,2}$ edges, have to pass the organic ligands around the particles. Additionally some excess of surfactant is generally used in colloidal chemistry to achieve long-term stability of the particles which results in some overlayers of free organic molecules on top of the particle array. The organic material damps the total electron yield signal remarkably. When a scientist looks for small magnetic signals, i. e. the XMCD signal of Co particles in remanence, the organic molecules make it basically impossible to quantify the measured signal in terms of magnetic moment determination. Two methods are used to remove the chemical residue: (i) Ar^+ ion etching and (ii) reactive hydrogen and oxygen plasma exposure. Details on the processes are discussed in this section.

Besides the technical point of damped signals a removal of the ligand shell and the reduction of the CoO allows to study well-separated free metallic Co particles. A route to achieve metallic Co particles without any agglomeration using single layer arrays is the reactive plasma exposure as described below.

4.3.1. Surface Cleaning by Ar^+ Ion Etching

Ion etching using noble gas ions is a commonly used technique to clean metal surfaces [79], [89]. In the case of Co/CoO nanoparticles surrounded by organic ligands the Ar^+ ion etching process results in a preferential sputtering of the lighter elements, i. e. carbon and oxygen, while pin holes in the particles are induced simultaneously. However, the ion etching at typically 2-3 keV acceleration voltage and a drain current of a few μA increases the total electron yield signal intensity from Co by a factor of 5. Thus the organic ligands are – at least – partially removed.

The effect of the Ar^+ ion etching as a function of exposure time is shown in Figure 4.9. A 3D array of ordered Co/CoO nanoparticles (20-30 layers) was deposited on polished Mo foil as a substrate. At a pressure of $1 \cdot 10^{-3}$ Pa Ar^+ ions were accelerated at an energy of 3 keV towards the sample resulting in a typical drain current of 4 μA. For comparison, the spectra were normalized on a per atom basis. The XAS spectrum of the as deposited Co/CoO nanoparticle array reveals the typical line shape of CoO. Here, the fine structure of the multiplet states is not visible since the beam line exit slit was opened to achieve higher x-ray flux resulting in a reduced

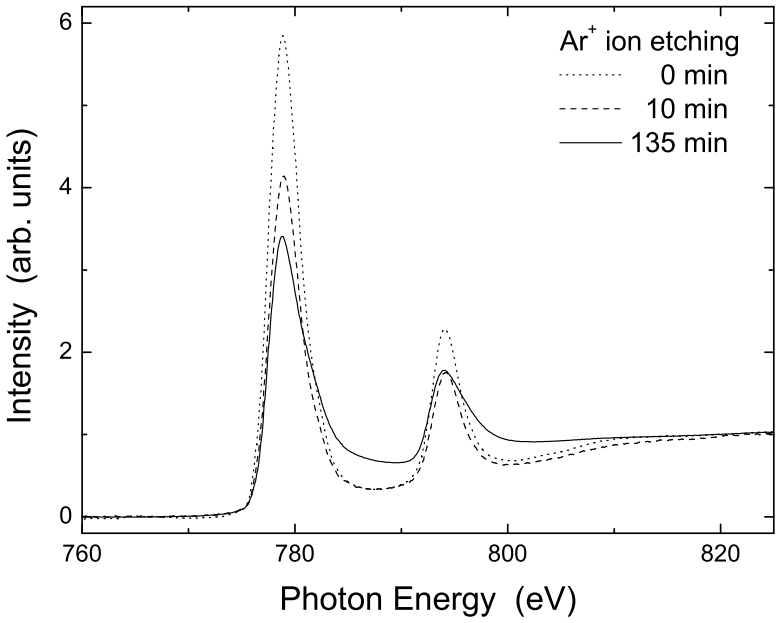

Figure 4.9.: XAS spectra of 11 nm Co/CoO particles as a function of the Ar^+ ion etching time at an energy of 3 keV and 4 μA drain current. The spectra were taken with linearly polarized x-rays at normal incidence and are normalized on a per atom basis for comparison.

energy resolution. A 10 min Ar^+ ion etching process strongly decreases the peak intensities while the edge jump remained nearly constant. Longer ion etching times, however, revealed a continuous decrease of the peak intensity while the edge jump increased. After 135 min of Ar^+ ion etching no further change in the absorption spectra has been observed. One should note that non of the spectra shows a pure metallic character as observed in Co thin films, for example. Accordingly, the further analysis of the magnetic response (XMCD) has to take into account contributions from both, Co atoms in a metallic and a oxidic environment.

4.3.2. Reactive Plasma Etching

Compared to the Ar^+ ion etching process at energies on the order of kV that creates pin holes and intermixing of atoms reactive plasma etching is favorable, since the sample structure and morphology is not or only slightly modified [116]. Process gases (hydrogen and oxygen) are much lighter than argon and thus the ballistic removal of target atoms at energies far below 1 kV is unlikely. In fact, these "slow" excited atoms are able to chemically react with the target surface atoms [128]. Here, a soft method is presented that allows the controlled (i) removal of

organic ligands and (ii) the reduction and oxidation of the Co/CoO nanoparticles.

For the processing a radio-frequency (rf) plasma source (13 MHz) has been employed for reactive etching. The samples were positioned far off the plasma cloud. Thus, the samples were mostly exposed to slow excited free radicals. The maximum kinetic energy of the free radicals is given by the so called dc-bias voltage applied between the two electrodes. Low dc-bias voltages (100 - 500 V) and the chamber geometry yield a soft reactive etching of the specimen, since the sample is placed either far off and rectangular to the electrode geometry or close to one electrode shadowing the plasma. Free radicals, i. e. hydrogen or oxygen atoms, chemically react with the exposed specimen. Due to the tiny kinetic energy a sputtering of sample atoms is not possible.

The efficiency of such a reactive plasma etching process has been demonstrated by the creation of metallic nanoparticles from Au [129] or Co [116] salt loaded micelles. Oxygen radicals react with carbon and hydrogen atoms of the micelles forming organic gases and water. In the case of Co salt loaded micelles, however, this process oxidizes the metal salt core completely. Co_3O_4 nanoparticles were formed. By hydrogen plasma exposure in a second step the Co_3O_4 particles can be reduced to metallic Co particles. Thus, the reactive plasma etching exposure yield the preparation of well-isolated metallic Co nanoparticles free of any contaminants.

The reactive plasma etching process can easily be adapted to metal nanoparticles prepared by means of colloidal chemistry. For example, $FePt$ [23] and Co/CoO (this thesis) particles have been exposed to hydrogen or oxygen plasmas, successively. For the evaluation of the oxidation and reduction process surface sensitive chemical fingerprints are needed which can be provided by XAS, x-ray photoelectron spectroscopy (XPS) or Auger spectroscopy. Thus, a fully UHV-compatible plasma reaction chamber has been employed to perform sample manipulation processes allowing an immediate *in situ* characterization. Here, 2D arrays of 9 nm Co/CoO particles with a sample thickness of 10% of a monolayer to about 2-3 layers were exposed to the free radicals guaranteeing that the reactive etching can take place on all nanoparticles. The particles were deposited directly from the toluene-based solution on naturally oxidized Si(001) substrates.

Transformation to Metallic Particles

The effect of the reactive plasma exposure to a submonolayer coverage is presented in Figure 4.10. At several steps of the processing Co-$L_{3,2}$, O-K, and C-K edges have been tracked by means of XAS in the total electron yield mode. In the as-deposited state (0 min H plasma) the XAS at the Co edges of the ligand surrounded Co/CoO particles show a mixture of metallic

and oxidic Co contributions. Details on the XAS of untreated particles are discussed in section 5.1.2. The oxygen spectrum in the untreated state reveals two sharp peaks around 525 eV and 527 eV. Several higher energy peaks of lower intensity overlap to a broad absorption peak and cannot be assigned to a special chemical environment. The total O-K edge spectrum can be assigned as the sum of three different contributions originating from (i) the CoO shell of each individual particle, (ii) the organic ligands (oleic acid and oleyl amine) and their bonds to the nanoparticle surface and (iii) the native SiO_2 layer of the Si substrate. The C-K XAS spectrum is dominated by the double peak at 288 eV while a small additional contribution is found at 285 eV. Carbon is only located in the ligands forming single and double bonds in oleic acid and oleyl amine.

In a first step starting from the untreated nanoparticle array we exposed the specimen to mild H plasma (100 W, 5-10 Pa) until we measured a pure metallic Co XAS response of the nanoparticles. After 46 min the Co XAS spectrum revealed a pure metallic character indicated by the lack of fine structure and the increase of the edge jump in the metallic XAS spectrum. Examining the O-K XAS spectrum after 6 min and 46 min H plasma exposure one finds that the peak at 527 eV vanishes instantaneously while the sharp peak at 525 eV decreases continuously as a function of time of exposure. The overlap of peaks at higher energies smears out. The shape of the C-K XAS response does not change much by the H plasma, but the total signal intensity decreases by a factor of three. Thus, the H plasma exposure yields a reduction of Co/CoO core-shell particles to pure metallic particles through the ligand shell removing some carbon from the ligands. However, since the C-K spectroscopic response does not change significantly, it is likely that only the CoO shell is reduced and the chemisorbed ligand $COOH$-group docking to the particle surface (mediated by an oxygen atom) is cracked producing water while the carbonyl-group of the ligands remains partially stable.

After the reduction of CoO through the ligand shell the sample has been exposed to an oxygen plasma (100 W, 7-10 Pa, 20 min) resulting in a complete removal of the ligand shell by chemical reaction of the long-chain ligands to organic gases, e. g. CO, CO_2, and water. These gases can be easily pumped away yielding ligand-free nanoparticles. The O plasma exposure, however, also results in fully oxidized Co_3O_4 particles [116]. Hence, another H plasma treatment (100 W, 5-10 Pa, 30 min) of the specimen was necessary to prepare ligand-free, metallic Co nanoparticles. The final XAS spectra for Co, O, and C are also shown in Fig 4.10 indicated by $H/O/H$ plasma. The Co spectrum is clearly dominated by the metallic response, showing only a slight shoulder in the onset of the L_3 edge. Employing reference spectra for Co and CoO [91] it can be concluded that an equivalent of less than one monolayer CoO remains. A longer H plasma exposure time would reduce the remaining CoO. The oxygen spectrum re-

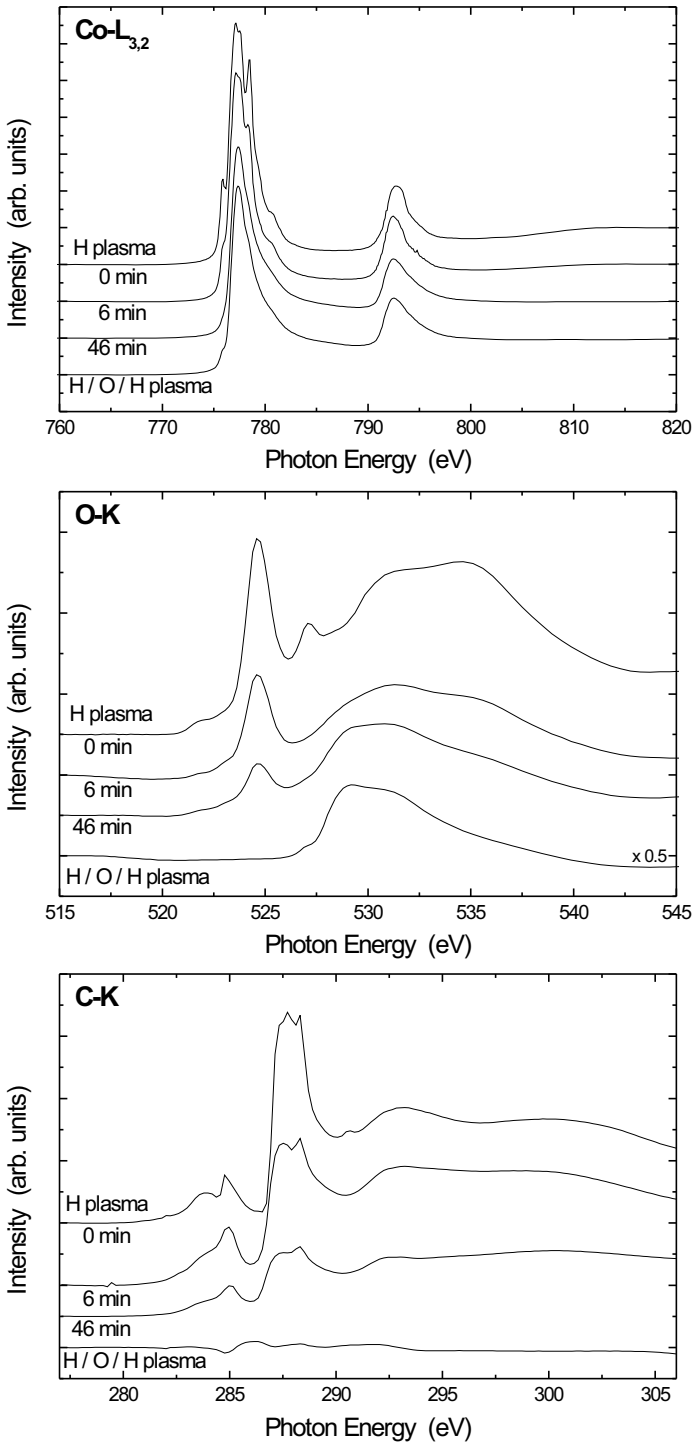

Figure 4.10.: XAS spectra showing the evolution of the successive hydrogen and oxygen plasma exposure for Co-$L_{3,2}$, O-K, and C-K edges, respectively. The details are described in the text.

veals a sharpened peak at 530 eV which is assigned to the slightly transformed SiO_2 substrate surface. The lack of any C-K XAS signal proves that the ligands could be removed completely. The small inverse structure at the C-K edge is due to a slight contamination of carbon of the x-ray mirrors in the monochromator and the gold grid measuring the incoming intensity (I_0). Thus the intensity can not be perfectly scaled by the I_0-monitor.

The spectroscopic measurements have shown that the $H/O/H$ plasma exposure results in ligand-free metallic Co particles. However, from XAS alone, no information can be achieved about changes of the shape of the particles and the sample morphology. Aggregation or sintering of particles may take place when the protective ligands are removed. To quantify the possible changes in the particle morphology lithographically marked substrates have been used to find the identical particles before and after the successive plasma treatment. In Figure 4.11 the effect of the different plasma treatments is presented. The as-deposited Co/CoO particles surrounded by ligands are shown in Figure 4.11 (a) using a low concentration of particles on the substrate. Figure 4.11 (b) shows the morphology after the plasma treatment without the ligands. One should note that the sample had to be transferred in ambient conditions before the post-plasma SEM image was taken. Thus, the particles are oxidized at the surface. Each dark spot represents a single nanoparticle. Comparing the particle array before and after the plasma exposure one can conclude that all nanoparticles remain isolated, even if the distance is small between the particles. It is obvious from Figure 4.11 that the particles do not move during the plasma exposure which yields the possibility of the removal of the ligands without particle agglomeration. Using high-resolution SEM the sizes of single particles can be evaluated before

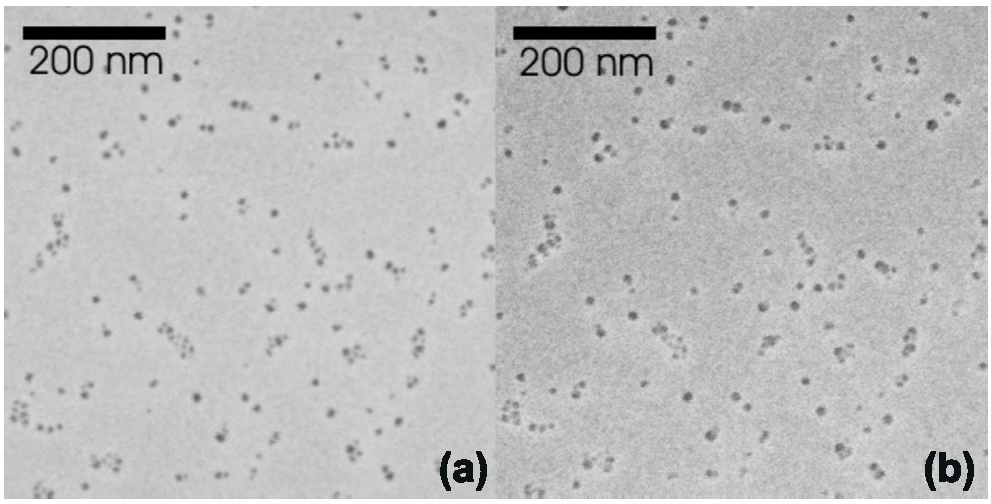

Figure 4.11.: SEM images of the 9 nm particles of the initial state (a) and after successive oxygen and hydrogen plasma exposure (b). Lithographically marked Si:B substrates were used to find the identical sample area before and after the plasma exposure.

and after the plasma treatment. Within the error bar ($\pm$ 1 nm) the diameter of the Co/CoO particles does not change for identical particles. Thus, most probably also ligand-free particles form a core protective CoO shell with a typical thickness of a few nanometers.

Well-separated contaminant-free Co particles can be prepared by the plasma exposure up to a coverage close to one completely filled monolayer. Figure 4.12 (a) represents such a arrangement of particles. 9 nm Co/CoO particles were let to self-assemble by the droplet evaporation method from toluene based solution onto a native Si(001) substrate. The coverage is homogeneous over areas of several mm^2. About 85% of the total sample area is covered from which XAS/XMCD spectra were taken. At a first glance, it is obvious that around 7% of the total number of particles are bigger than the majority of all particles. These bigger particles have not been observed before the plasma exposure. To quantify changes in diameter a size distribution is evaluated by means of SEM imaging. The log-normal fit to the size histogram in Figure 4.12 (b) reveals a most probable diameter of 9.4 nm and a full width at half maximum of 3.9 nm. The contribution from larger particles to the histogram is not as large as the visual inspection suggests. Compared to the pre-plasma size distribution of the 9 nm Co/CoO particles shown in Figure 4.1 the most probable diameter remains constant within the error bar. One should note that SEM imaging has a uncertainty in the size evaluation of ± 1 nm. The size distribution, however, clearly increases from a FWHM of 2.7 nm (14%) to 3.9 nm (19%) after the $H/O/H$ reactive plasma etching and additional oxidation after the XAS experiments. The particle center-to-center distance d_{cc} = 12.6 nm (not shown) that is slightly smaller than

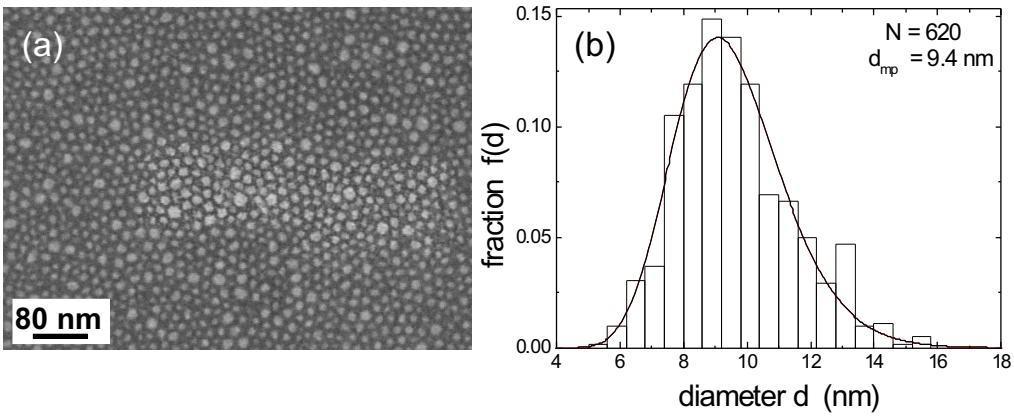

Figure 4.12.: (a) SEM image of the sample inspected by XAS/XMCD (Figure 4.10) after the successive $H/O/H$ plasma exposure. About 7% of the particles appear larger than the majority of particles. (b) quantifies the size distribution of plasma treated particles. A most probable diameter of 9.4 nm is found by log-normal fitting.

d_{cc} = 13.0 nm suggested by TEM imaging shown in Figure 4.7. The difference, however, lies within the error bar of the SEM apparatus. From the results above it can be concluded that in case of coverages up to one monolayer the particles in contact to the substrate do not move or agglomerate by the exposure to the free radicals. It seems probable that larger particles grow by a small amount of particles in a second layer during the oxygen plasma exposure, since the ligand shell were removed from initially agglomeration protected Co/CoO particles. Once the shell is removed touching particles are free to sinter forming particles of larger diameter.

When more particles are deposited onto the substrate they cannot remain isolated perpendicular to the substrate if the ligand shell is removed. Thus, one expects the formation of particles in contact to each other - exhibiting exchange interaction - normal to the sample plane. To see the effects of exchange interaction more easily the concentration has been chosen so that an array of Co particles with a coverage of 1.7 particle layers is formed over macroscopic areas (mm^2). Then, the ligand shell has been removed and the CoO shell has been transformed to metallic Co by the oxygen/hydrogen plasma exposure yielding an array of metallic particles partially in contact to each other. The position of the particles was imaged after the plasma treatment by means of SEM and Atomic Force Microscopy (AFM) at many different positions on the sample. In Figure 4.13 (a) a characteristic SEM image of the quasi two-dimensional array of 9 nm Co particles is shown. Approximately 30% of the total sample area ($8 \cdot 4$ mm^2) is covered by a single layer while 70% is covered by two layers of nanoparticles. Nowhere a third layer or three-dimensional agglomerates are detected by AFM or SEM. Each small bright spot represents a single nanoparticle. Areas of typically 100 μm^2 are covered by one monolayer. Double layer regions cover about 70% of the whole substrate area, surrounding the one

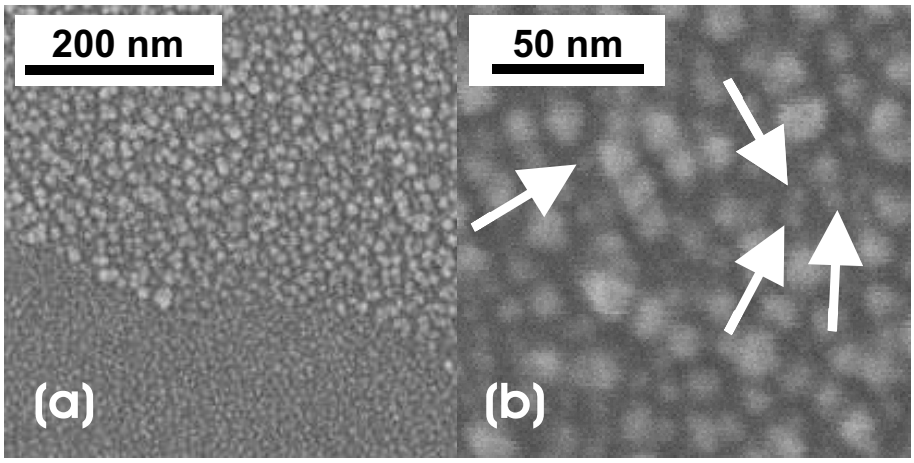

Figure 4.13.: SEM images of the 9 nm Co/CoO particles after the plasma exposure. The initial coverage of the substrate is not uniform. Single layer regions are encased by areas of two layers of particles (a). Image (b) shows a higher magnification of the double layer region. For details see text.

monolayer regions. The filling factor of the particles in the first is layer is 35%. The particles in the top layer have a larger average diameter of about 14 nm which corresponds to a five times larger volume and is the result of the plasma treatment as discussed below.

The existence of the bottom layer of small particles underlying the top layer is proven by the high-resolution SEM image in Figure 4.13 (b). The arrows indicate some bottom layer particles in the double layer region. The size distribution of the monolayer regions reveals no significant change of the diameter of the particles. In the double layer region no proper size histogram can be given, since most particles are partially covered by the top layer. However, by comparison of the a few bottom layer particles in the double layer regions with the ones in the single layer regions it is evident that the sizes and shapes of the particles in the first layer are similar.

The AFM imaging confirms these results. Figure 4.14 represents a typical AFM image with two single and one double layer regions. Below the AFM image the calibrated height variation along the line scan indicated by the white line in the image is shown. The error bar of the height determination is 1 nm. In the single layer regions the AFM detects a roughness of less than 1.5

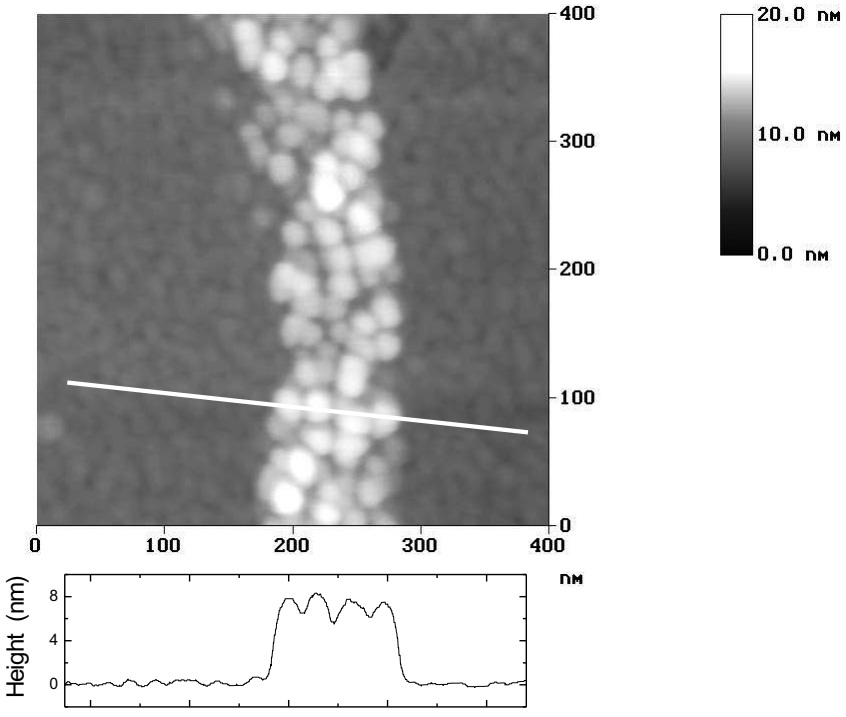

Figure 4.14.: AFM image of the initially 9 nm Co/CoO particles after the plasma exposure. The lower panel shows a line scan according the line in the AFM image. The bottom layer appears nearly flat while in the top layer particles of larger diameter are visible. The line scan shows the height variation between bottom and top layer. Details are described in the text.

nm. Note that a standard Si tips with a tip radius of 30 nm have been used. Thus, the tip cannot properly detect the height variation between the particles. In the line scan diagram nearly flat regions (single layer) are set to zero, so that the height difference between the bottom and the top layer is visualized. The bigger particles in the top layer appear 8 nm higher than the bottom layer particles. Taking into account the filling factor of 30% of the particles in the first layer one can conclude that particles in the top layer partly fill the space between the bottom layer particles. Thus, we assume in section 6.2 spherical particles of 14 nm diameter forming the top layer for micromagnetic simulations. From SEM and AFM imaging no direct information on the size of the contact area of bottom and top layer particles could be achieved.

Finally, one has to discuss changes of the particle diameter by the plasma exposure. Due to the strongly different lattice constants of fcc Co (a = 0.354 nm) and paramagnetic CoO (a = 0.426 nm) one expects a shrinking particle diameter in the pure metallic state. Using the CoO shell thickness of $t_{CoO} = 2.5$ nm that is determined by TEM, a simple geometrical consideration using $d_{Co/CoO} = d_{core} + 2 \cdot t_{CoO}$ = 9.5 nm reveals a most probable particle diameter d_{Co} after plasma reduction of

$$d_{Co} = \left[d_{core}^3 + \left(d_{Co/CoO}^3 - d_{core}^3 \right) \left(\frac{a_{Co}}{a_{CoO}} \right) \right]^{1/3} = 8.1 \ \text{nm}. \tag{4.2}$$

Here, $d_{Co/CoO}$ is the initial particle diameter and d_{core} is the Co core diameter. One may note that this simple consideration has not been directly proven by microscopy techniques since the plasma reduction chamber could not be attached to the SEM or TEM apparatus. The post-plasma SEM characterization presented in Figure 4.12 yields a most probable diameter that is identical compared to the initial diameter determined by TEM. The reader may remember that the free metallic particles were exposed to air before the SEM imaging. This experimental finding suggests that (i) the oxidation process of free metallic particles is similar to ligand-stabilized particles and (ii) no loss of Co atoms takes place during the reactive plasma etching. These simple considerations become important within the interpretation of the magnetic response - especially in terms of micromagnetic simulations (section 6.2).

In summary, the successive oxygen and hydrogen plasma exposure is found very efficient to prepare metallic Co particles free of ligands on Si(001) substrates. The morphological investigations before (TEM) and after (SEM, AFM) suggest that no loss of Co atoms takes place during the plasma exposure. Below a coverage of one monolayer the particles remain isolated and keep their position on the substrate. By the deposition of more than one monolayer SEM and AFM images show that a double layer structure is formed after plasma treatment. Interestingly, the particles in the top layer have a five times larger volume indicating that a sintering or agglomeration take place during the plasma exposure. Particles in the single layer regions,

which are in contact to the substrate, do not agglomerate or sinter. One can conclude from these results that the mobility of particles in the second layer is higher than those of the particles touching the substrate.

5. Magnetic Properties of Co/CoO Core-Shell Nanoparticle Systems

The magnetism of Co/CoO nanoparticles shows a variety of interesting phenomena. Ferromagnetic blocking which stabilizes a distinct magnetization direction in a given time window below a certain temperature T_B is caused by the magnitude of the magnetic anisotropy energy (MAE) compared to the thermal energy. Since the anisotropy of the orbital magnetic moment is directly connected to the MAE detailed information of the orbital magnetism in the nanoparticles is highly desired. Moreover, the situation in Co/CoO particles becomes even more interesting since in this system ferromagnetic/antiferromagnetic exchange coupling is present. The coupling is the origin of a unidirectional exchange anisotropy UEA (exchange bias) and governs the usually observed uniaxial anisotropy of nanoparticles, too. In this chapter these mechanisms are addressed. At first, the discussion focusses on the magnetism of individual particles. Afterwards, the magnetostatic coupling of these particles is discussed in terms of a field induced anisotropy employing magnetophoretic deposition.

5.1. Individual Magnetic Properties

Starting from the blocking temperature T_B as a general parameter for stable magnetization direction of nanoparticles in a given time window this section concentrates on the basic quantities like MAE and the ratio of orbital-to-spin magnetic moment μ_L/μ_S. The g-factor is an intrinsic magnetic quantity which is a direct measure of μ_L/μ_S. Using frequency-dependent FMR measurements the g-factor can be determined with high accuracy. Besides the FMR experiments the ratio of orbital-to-spin magnetic moment is independently measured by XMCD. Moreover, the frequency-dependent FMR yields information on the Gilbert damping parameter G. The temperature dependence of the magnetic anisotropy energy density of 9 nm Co/CoO particles is determined with a simplified model already introduced in section 2.1. Magnetic aging, which here means the slow growth of the CoO shell of the individual particles with time in ambient conditions is investigated by both by frequency-dependent FMR and by element-specific

hysteresis loops using the XMCD signal. Finally, the UEA in a Co/CoO nanoparticles is investigated.

5.1.1. Magnetic Blocking of Particles

The blocking temperature T_B indicates the temperature at which the thermal energy becomes sufficient to reverse the magnetization direction over the energy barrier E_B of a system with uniaxial symmetry in a certain time window (usually given by the type of experiment). In this case, the energy barrier E_B is given by the MAE for non-interacting ideal spheres. Besides the MAE of a single particle magnetostatic interactions between neighboring particles may have to be taken into account. The dipole-dipole interacting energy E_{dd} enters equation 1.16 [130]:

$$\ln \frac{\tau}{\tau_0} = \frac{E_B}{k_B T} = \frac{K^{eff} V + E_{dd}}{k_B T} \tag{5.1}$$

Accordingly, when interparticle interactions cannot be neglected the energy barrier increases. The maximum dipolar interaction energy (parallel alignment of magnetic moments) of two particles can be calculated by $E_{dd}/k_B = (\mu_0 \mu_P)^2 / 4\pi\mu_0 d_{cc}^3 k_B$ [76]. μ_P defines the total moment of a particle. For 9 nm (11 nm) Co/CoO particles E_{dd}/k_B is found about 30 K (120 K). Thus, magnetostatic interactions cannot be neglected. In this estimate only the volume of the ferromagnetic core of 5 nm (7 nm) was used assuming the bulk magnetic moment of $1.7\mu_B$/atom and parallel alignment of all atomar magnetic moments forming a giant spin located at the particle center. The center-to-center distance d_{cc} is 13 nm (16 nm) for 9 nm (11 nm) particles. When the blocking temperature is measured the effective anisotropy energy density constant K^{eff} could be calculated free of interactions. One should point out that this simple model neglects any influence of the CoO shell which is antiferromagnetic below $T_N = 293$ K. Since the exchange coupling at the ferromagnetic/antiferromagnetic interface enhances the coercivity and thus also the MAE [42,59] of a Co/CoO particle this simple model is misleading. Moreover, the CoO shell is stabilizing the magnetization of a particle at higher temperatures than it can be expected from the MAE of a ferromagnetic core alone.

An estimate of blocking temperatures of fcc multiply twinned, pure metallic particles can be given using the anisotropy constant $K^{eff} = 1.5 \cdot 10^4$ J/m^3 found by micromagnetic simulations of hysteresis loops after plasma transformation. Details on the simulations can be found in section 6.2. From equation 5.1 the expected blocking temperature can be calculated by setting $\ln(\tau/\tau_0) = 30$ that accounts for the time window of a SQUID magnetometry experiment. Further the calculated dipolar energy given above enters equation 5.1. Using these assumptions the expected blocking temperatures of magnetostatically coupled Co particle cores of 5 nm (7 nm) is found to be $T_B = 6$ K (17 K).

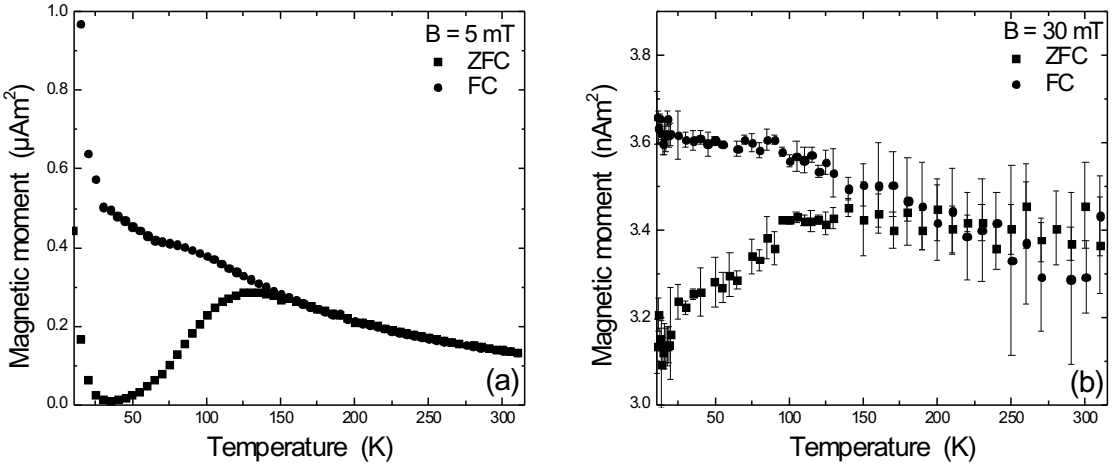

Figure 5.1.: ZFC/FC magnetization process as a function of temperature for the nominally 9 nm Co/CoO particles. (a) shows the temperature dependence of approximately 100 layers of particles on a native Si(001) substrate. A field of 5 mT has been applied. In (b) the identical experiment has been performed for one monolayer of particles. The measuring field had to be increased for sufficient signal strength to 30 mT. Both measurements show identical positions of the ZFC maximum at $T \approx 150$ K. According to the volume size distribution σ_V = 0.38 one finds a mean blocking temperature $T_{B,mean} \approx$ 85 K.

In Figure 5.1 the zero-field cooled (ZFC/FC) magnetization process of the 9 nm Co/CoO particles is presented as a function of temperature. For both, a sample consisting of about 100 layers of particles and a single layer of particles, the ZFC maximum is found at $T \approx 150$ K. Using the volume size distribution σ_V = 0.38 of the particles one finds the mean blocking temperature being $T_{B,mean} \approx$ 85 K. Both experiments have been performed with the magnetic field applied in the film plane. One may note that the magnitude of the magnetic response of a single layer is only slightly larger than the detection limit of the magnetometer indicated by the large error bars. However, the blocking effect is clearly visible. The origin of the paramagnetic contribution at temperatures $T \leq 20$ K in Figure 5.1 (a) is assigned to paramagnetic Co salts present after the synthesis. By careful washing of the particle solution these contaminants were eliminated for further investigations. Figure 5.2 shows the ZFC/FC magnetization process of 11 nm and 13 nm Co/CoO particles as a function of temperature in a magnetic field of $B = 5$ mT. The maxima of the ZFC measurements are found at $T \approx 290$ K and 270 K for the 11 nm and 13 nm Co/CoO particles. The mean blocking temperature $T_{B,mean} = 167$ K (184 K) has been estimated from the volume size distributions $\sigma_V = 0.36$ (0.24) for the 11 nm (13 nm) Co/CoO particles. Interesting in these experiments is the fact that the irreversibility point of the ZFC/FC measurements are found slightly lower but very close to Néel temperature T_N of

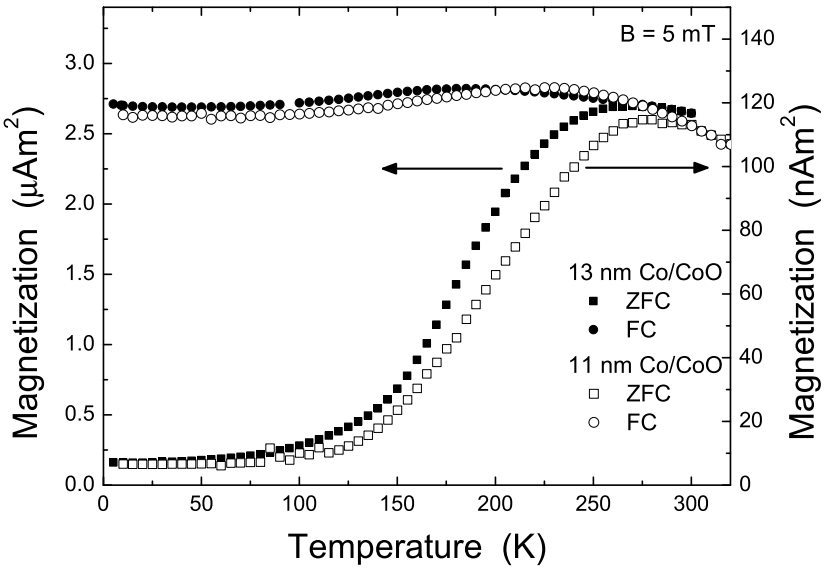

Figure 5.2.: ZFC/FC magnetization process for nominally 11 nm and 13 nm Co/CoO particles assemblies as a function of temperature. Interestingly, the ZFC maximum at $T \approx 290$ K of the 11 nm particles is found at higher temperatures than the one of the 13 nm particles ($T \approx 270$ K). The mean blocking temperature has been estimated from the volume distribution $\sigma_V = 0.36$ (0.24) to $T_{B,mean} = 167$ K (184 K) for the 11 nm (13 nm) particles.

the antiferromagnet CoO. Thus, it seems likely that the CoO shell determines the blocking temperature of the largest particles. Above T_N there does not exist any additional stabilizing mechanism of the magnetization of a single particle and the MAE of the core alone cannot form a stable direction of magnetization as discussed above.

The irreversibility point of ZFC/FC measurements at about 150 K of the 9 nm particles is found strongly reduced compared to the larger particles. At this temperature FC hysteresis loops show a vanishing exchange bias field as shown below. This finding is attributed to the superparamagnetism of the CoO shell above 150 K. Moreover, the magnetic moment (Am^2) of the ferromagnet enters the estimation of the exchange bias field in equation 1.20. The magnetic moment of a 5 nm Co core in a 9.5 nm Co/CoO particle is more than two times smaller than in the case of a 7 nm Co core in 11 nm particles due to the difference in the number of core atoms. The limited range of sizes, however, does not allow to quantify the arguments given above. From equation 1.13 one is tempted to separate the volume K^V and surface contribution K^S of the effective anisotropy energy density constant $K^{eff} = K^V + \frac{6}{d}K^S$. One may note that dipolar interactions have to be included by equation 5.1. $K^{eff}V$ is determined to 217 meV/particle, 421 meV/particle, and 449 meV/particle for the 9 nm, 11 nm, and 13 nm Co/CoO particles,

respectively. Equation 1.13 does not take into account exchange interaction between the core and the shell of the particles. On the other hand, the discussion above has shown that the CoO determines the blocking temperature T_B. Consequently, the estimate of K^S and the verification of the 6/d-law fails. Only in the case of pure metallic particles equation 1.13 can be applied.

In summary, the ZFC/FC magnetization experiments of different sized particles suggest that the antiferromagnetic CoO shell mainly defines the blocking temperature of Co/CoO particles. The superparamagnetism in the CoO shell may reduce the blocking temperature while magnetostatic interactions between the particles increase the energy barrier.

5.1.2. Orbital Contribution to the Total Magnetic Moment

The FMR and XMCD experiments for the g-factor and the ratio of orbital-to-spin magnetic moment determination are presented in the following. Frequency-dependent FMR experiments allow the accurate determination of the g-factor that is a direct measure of the ratio of orbital-to-spin magnetic moment via $\mu_L/\mu_S = (g-2)/2$. FMR only detects the metallic core of the Co/CoO particles. Core-level spectroscopies in the total electron yield mode like XAS and XMCD have a much smaller probing depth allowing the measurement of the magnetic response of both, the Co core and the CoO shell. The ratio of orbital-to-spin magnetic moment is investigated in remanence and in external magnetic fields at various temperatures. Especially the coupling mechanism between the core and the shell of the particles is addressed in this section.

Frequency-dependent FMR: g-factor Determination

Ensembles of magnetic nanoparticles which add up $10^{16} - 10^{17}$ magnetic moments can be measured by FMR, even when the linewidth of the absorption spectrum is on the order of several hundred mT. As an example, Figure 5.3 (a) shows experimental FMR absorption spectra for parallel (pc) and normal configuration (nc) with respect to the sample plane at three different frequencies at room temperature. At 9.8 GHz $Si(001)$ substrates with a native SiO_2 surface layer and at higher frequencies (35.7 GHz and 69.7 GHz) low-resistivity manganin ($Cu_{86}Mn_{12}Ni_2$) substrates have been used because of technical reasons. The different substrates had no influence on the resonance field and thus on the g-factor determination. A 5 μl drop of toluene-based highly-concentrated 11 nm Co/CoO particle solution has been dried on the substrates in ambient conditions. As a result, 40-50 layers of nanoparticles have been deposited on the substrate. The asymmetry at 35.7 GHz and 69.7 GHz is due to the positioning of the sample which is very

critical ($\ll$ mm) in the used setup. Different intensities occur, since the waveguide systems at 35.7 GHz and 69.7 GHz are different for pc and nc configurations. These technical differences do not have any influence on the determination of the resonance field. At 9.8 GHz the sample is not saturated and thus the sample magnetization changes during the field scan. The line shape can be explained by a superparamagnetic magnetization $(M(H))$, as discussed below.

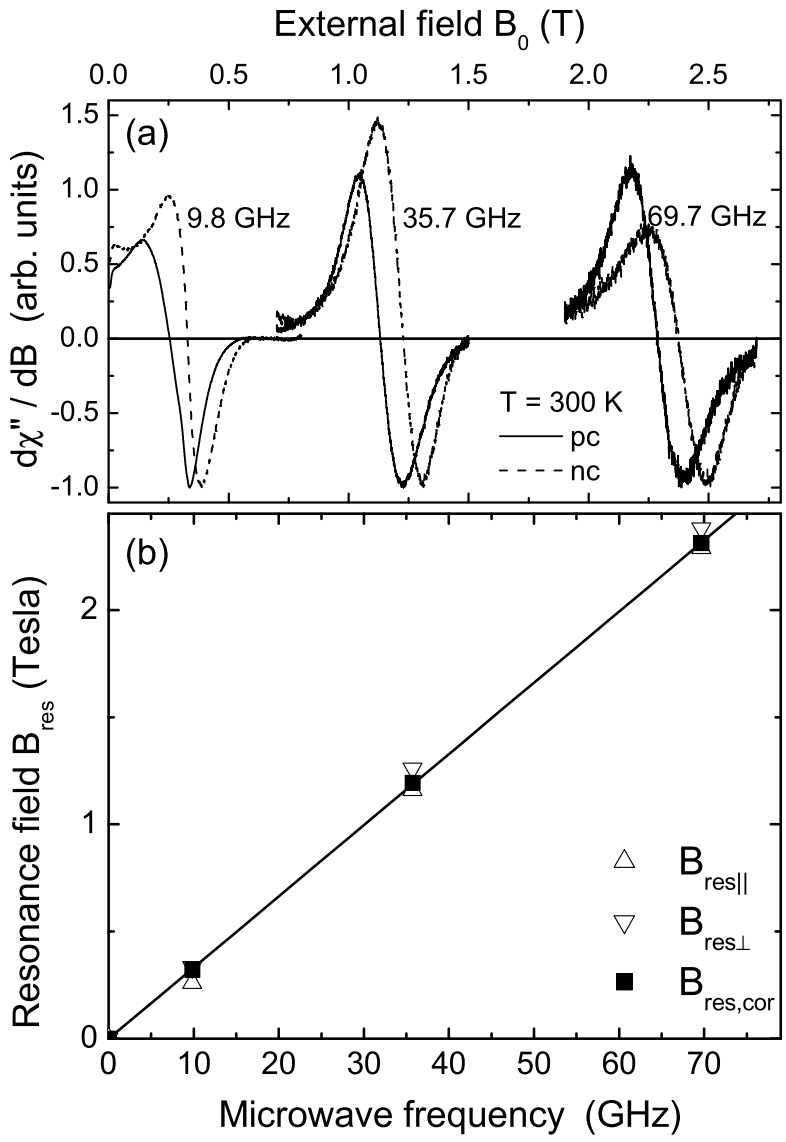

Figure 5.3.: (a) FMR/EPR absorption spectra for three different microwave frequencies for pc (solid) and nc (dashed) configurations at room temperature. (b) Experimental resonance fields $B_{res||}$ and $B_{res\perp}$ as a function of the microwave frequency at T = 300 K. The resonance fields $B_{res,cor}$ corrected for the effective magnetization are also shown (see text for details). The error bars are smaller than the symbol size. The figure has been adapted from [95].

The resonance spectra were fitted by a Lorentzian line profile for all measurements and the pc and nc resonance fields can be determined within an error bar of 3 mT. The lower resonance field is always found in the pc configuration as shown in Figure 5.3 (b). It is smaller than the paramagnetic resonance field (ω/γ), which shows that there exists an additional intrinsic magnetic field due to an effective magnetization M_{eff}. The easy axes of M_{eff} is parallel to the film plane. Using equations 2.11 and 2.12 M_{eff} can be calculated by an iterative procedure allowing a slight variation of the g-factor ($g = \frac{\gamma\hbar}{\mu_B}$) starting from the fcc bulk Co value $g = 2.16$. This calculation has been performed for 35.7 GHz and 69.7 GHz only, showing an $fM_{eff} = 67 \pm 11$ mT. f is the volumetric filling factor that accounts for the discontinuous medium of nanoparticles. At 9.8 GHz additional information about the magnetization at the resonance position is needed. SQUID magnetometry of the identical sample showed the magnetization $M(B_{res}) = 0.94M_{eff}$ at resonance. Using the corrected value of fM_{eff} at 9.8 GHz and 67 ± 11 mT for higher frequencies one can calculate the corrected resonance field $B_{res,cor}$ that does not depend on M_{eff} anymore. In this case, the g-factor has been determined by the paramagnetic resonance condition $\hbar\omega = g\mu_B B_{res,cor}$. In Figure 5.3 (b) the experimental resonance fields for pc and nc configurations ($B_{res||}$ and $B_{res\perp}$) and $B_{res,cor}$ are plotted as a function of the microwave frequency $\nu = \omega/2\pi$. A linear fit of the three frequencies and the origin yields a g-factor of 2.150 ± 0.015, which lies very close to the bulk value of fcc Co ($g = 2.16$). Within the given error bar the same g-factor is obtained in parallel geometry when using the ferromagnetic resonance condition which requires a quadratic fit according equation 2.11. However, if the sample is not saturated at the resonance position, the method used here is favorable since each frequency can be corrected separately. The quadratic fit averages directly over fM_{eff} which only holds for saturated samples at all frequencies used in the experiments.

The g-factor determination according equation 2.11 for parallel configuration and equation 2.12 for perpendicular configuration has also been performed on the 11 nm Co/CoO nanoparticles on a second, independently prepared sample on manganin substrates. While in the experiments shown in Figure 5.3 the particles were deposited on the substrate two weeks after the chemical synthesis the sample investigated in Figure 5.4 has been prepared five months later from the concentrated solution. The solution has been kept tightly closed in ambient conditions. The FMR experiments were performed at seven frequencies between 9.82 GHz and 79.34 GHz. The experimental spectra displayed in the upper panels of Figure 5.4 were taken three to seven weeks after the sample preparation where a nearly stable effective magnetization fM_{eff} has been observed as discussed below in terms of nanoparticle aging.

Figure 5.4 (a) shows a choice of spectra for parallel and (b) for perpendicular configurations. The lower panels represent the squared microwave frequency (a) and the microwave frequency

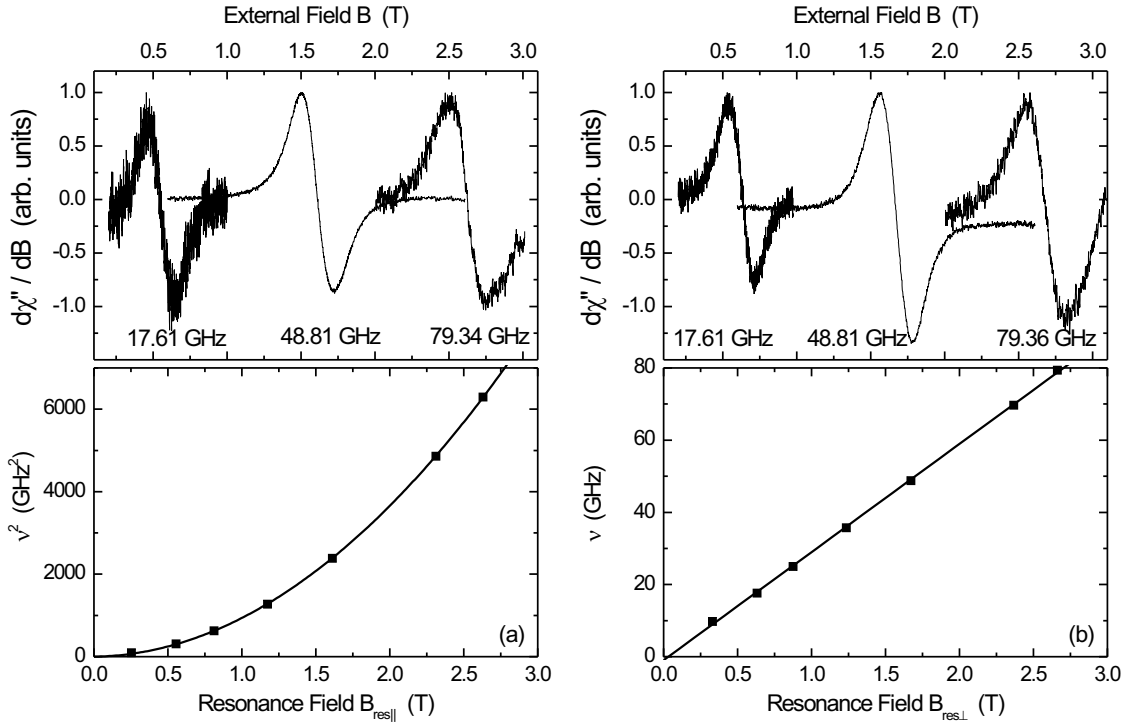

Figure 5.4.: FMR spectra of the 11 nm Co/CoO particles as a function of microwave frequency for parallel (left) and normal configuration (right) at room temperature (upper panels). For clarity, only the FMR spectra of three frequencies are shown. The lower panels show the microwave frequency dependence as a function of the resonance fields for parallel (a) and perpendicular (b) geometry. The lines in the lower panels are fits according to equations 2.11 and 2.12.The figure has been adapted from [60].

(b) as functions of the resonance fields $B_{res||}$ and $B_{res\perp}$, respectively. The solid lines are fits according the equation 2.11 (a) and equation 2.12 (b). In the parallel configuration a deviation from linear behavior is revealed which directly proofs the presence of internal anisotropy fields. From the quadratic fit using equation 2.11 the g-factor for the 11 nm Co/CoO particles has been determined to be 2.13 ± 0.01 and an effective magnetization of $fM_{eff} = 55 \pm 14$ mT was found. The effective magnetization fM_{eff} is due to the measurement in a applied field in FMR. The particle ensemble is superparamagnetic at T = 300 K. The analysis of the resonance fields in perpendicular geometry yields $g = 2.13 \pm 0.02$, showing the isotropic behavior.

Both, the g-factor determination two weeks and five months after the chemical synthesis coincide within the error bar. The averaged g-factor is found to be 2.14 ± 0.02. The effective magnetization fM_{eff} is found to be remarkably reduced by 18% from 67 ± 11 mT to 55 ± 14 mT. Thus, a further oxidation of the particles in the solution is evident. It should be pointed out that the direct fits to equations 2.11 and 2.12 demand saturated samples. Apart from a paramagnetic slope saturation of the 11 nm Co/CoO is achieved around 0.8 T as measured

by SQUID magnetometry. Since our FMR setup detects only the ferromagnetic part of each particle (which might be influenced by the CoO shell), and CoO cannot be detected in terms of antiferromagnetic resonance the most reliable results are found at high microwave frequencies where the resonance fields are large. In this special case, FMR experiments above 25 GHz ($B_{res} \sim 0.8$ T) fulfill the demand of a saturated sample. The use of the frequency range of 25-80 GHz applying single frequency analysis of equations 2.11 and 2.12 reveals a g-factor of 2.14 ± 0.01 and $fM_{eff} = 40 \pm 9$ mT. As a result, the error bar of the g-factor determination reduces to the uncertainties of the resonance field determination ($\Delta B/B \approx 10^{-4}$) and the statistical error of the frequency-dependent measurements decreases. Thus, it is obvious that when highest accuracy is needed the low-frequency FMR measurements must be corrected for saturation values, e. g. measured by SQUID magnetometry. Alternatively, only FMR experiments can be employed for a g-factor analysis which show resonance fields larger than the saturation field of the sample.

Finally, one has to consider the possible influence of CoO on the FMR experiments. As pointed out in the description of the FMR technique (section 2.1) the sampling depth of an FMR experiment is much larger than the diameter of the Co/CoO particles. Therefore the whole particle will be probed. The signal of the oxide layer is expected to be rather small, since CoO in the bulk orders antiferromagnetically which – in case of a perfect antiparallel alignment of the adjacent magnetic moments – does not produce a resonance absorption in the used frequency range. Antiferromagnetic resonance is typically observed at frequencies $\nu \gg 100$ GHz. The only possible signal could arise from uncompensated moments within the oxide layer which occur due to the spherical shape of the particles and the multi-grain structure in the shell. As bulk CoO has a Néel temperature of $T_N = 293$ K, a further reduction of the expected signal results from the fact that the oxidic layer is paramagnetic at ambient temperature. Only the spins in contact to the metallic core could possibly be ordered. Therefore, the strongest contribution of the oxide layer to the magnetization may be expected to arise from moments located directly at the interface of the metallic core to the oxide layer. Following Hund's rules free Co^{2+}-ions have a $3d^7$-configuration and thus a spin quantum number of $S = 3/2$ and an orbital quantum number of $L = 3$ which yields a very large $\mu_L/\mu_S = 1$. In a quasi-cubic environment (section 1.2), however, the orbital moment is partly quenched. Experimentally, a large $\mu_L/\mu_S \approx 0.6$ has been observed [131]. Thus, if the contribution to the FMR signal originating from the interface spins would be large, an enhanced orbital moment would be expected. Since this enhancement is not observed, we conclude that the response within FMR mainly results from the metallic core.

In summary, frequency-dependent FMR measurements reveal a g-factor of 2.145 ± 0.015 which directly corresponds to a ratio of orbital-to-spin magnetic moment of $\mu_L/\mu_S =$

0.07 ± 0.01 for the 11 nm Co/CoO particles. Comparing the measured value to the known values for hcp Co bulk of $\mu_L/\mu_S = 0.09$ one comes to the conclusion that the Co particles most likely have an fcc structure (bulk: $\mu_L/\mu_S = 0.08$) resulting in a reduction of orbital magnetism due to the cubic environment. The effective magnetization $f \cdot M_{eff}$ has been found to decrease by 18% within 5 months between nanoparticles synthesis and sample preparation which suggests a slow growth of the CoO shell in the solution while kept in ambient conditions.

Temperature- and Field-dependent XMCD: μ_L/μ_S Determination

To get further insight into the orbital magnetism and the coupling mechanisms at the interface, the FMR results are complemented by XMCD investigations at the Co $L_{3,2}$ edges. Employing the XMCD sum rules, the orbital and the spin magnetic moment can be extracted separately, if the sample is saturated and the XAS spectra can be split into metallic and oxidic contributions. When the dichroism in XAS is tiny, e. g. in case of the remanent magnetization of Co/CoO particles, the datasets do not allow a reasonable analysis of separated magnetic moments. The reliable outcome of such an experiment is the ratio of orbital-to-spin magnetic moment μ_L/μ_S^{eff}. One should note that $\mu_S^{eff} = \mu_S - 7\mu_T$ accounts for the possible contribution of the magnetic dipole moment due to the asphericity of the electron clouds involved. Moreover, XAS in the TEY detection mode has a limited sampling depth of only a few nanometers due to the exponential decay of secondary electrons originated deeper in the sample. Thus, the XAS signal of the overlying CoO is expected to be large, while the XAS signal of the metallic core is small. As discussed earlier, any magnetic contrast that arises from CoO can only be due to uncompensated moments and the exchange coupling to the ferromagnetic core. In the following a number of experiments are described which give an insight into the complex coupling mechanisms at the Co/CoO interface. Two sets of experiments have been accomplished: Firstly, the determination of μ_L/μ_S^{eff} is presented for 13 nm Co/CoO particles treated by Ar^+ ions to remove chemical residue. These experiments were performed in the remanent state only. After that, experiments in external fields up to 2 T are presented for 9 nm particles without any further treatment. The external field results in a much stronger dichroic signal, since Co/CoO particles are magnetized close to their saturation magnetization allowing the examination of particles in their native state. The external field allows a more precise analysis and the qualitative elaboration of the XMCD signal from CoO. Moreover, from experiments on particles having different CoO shell thicknesses one finds quantitative agreement between experiments and a simple model taking into account weighted contributions to the measured XMCD signal.

Experiments in the Remanent State of Magnetization

In the first set of experiments the XMCD difference has been recorded as a function of angle with respect to the substrate plane and temperature after Ar^+ ion etching. The particles have been deposited by droplet evaporation on a clean Mo foil. In regard to Figure 4.9 it should be

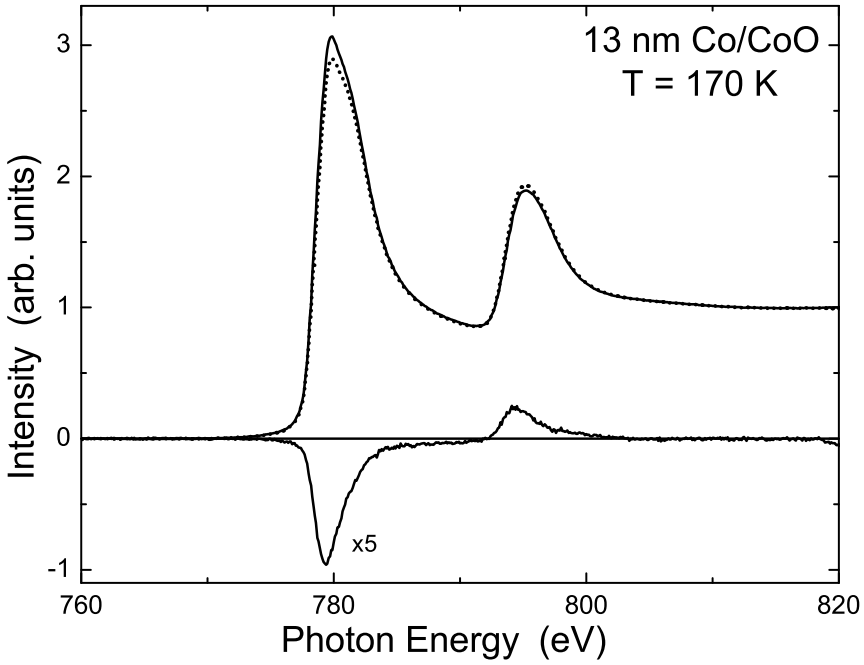

Figure 5.5.: Majority (dotted) and minority (solid) XAS spectra of an array of 13 nm Co/CoO particles on a Mo substrate after Ar^+-ion etching (3 kV, 4μA, 135 min) at 170 K and an angle of incidence of 20° with respect to the substrate plane. For clarity, the XMCD difference spectrum is magnified by a factor of 5.

pointed out that the non-etched sample reveals the typical line shape of CoO. By successive Ar^+ ion etching the white line intensity has been found continuously decreasing while the edge jump increases up to an etching time of 135 min after which no further changes in XAS have been observed. The particles become more metallic indicating a partial removal of oxygen. None of the spectra reveals a pure metallic character although the branching ratio $A_{L_3}/(A_{L_3} + A_{L_2})$ = 0.72 of the isotropic spectrum matches the reported value for a bulk-like Co film [89]. Angular-dependent XMCD difference spectra (20°-90°) with respect to the substrate plane were recorded confirming the in-plane easy axis of magnetization. No perpendicular component was found. The magnetization of the array of particles has been reversed by a 50 mT pulse. For temperatures between 100 K and 200 K a well-resolved XMCD difference spectrum has been

observed. Above and below these temperatures no signal is resolved since either the remanent magnetization vanishes or the coercive field is larger than the available external field (50 mT) for magnetization reversal. Figure 5.5 shows the polarized XAS spectra for 13 nm Co/CoO particles taken at 20° grazing incidence and T = 170 K after ion etching. At this temperature the largest dichroic signal has been observed. The ratio of orbital-to-spin magnetic moment is found to be $\mu_L/\mu_S^{eff} = 0.24 \pm 0.06$, that is a 300% enhancement compared to fcc bulk Co (μ_L/μ_S^{eff} = 0.08). The rather large error bar is caused by the low remanent magnetization of the particles and the difficulty in averaging the metallic and oxidic contributions. Within the error bar no temperature dependence of μ_L/μ_S^{eff} is evident.

In a second series of experiments an ensemble of approximately 50 layers of the 13 nm Co/CoO particles has been deposited from toluene-based solution onto a clean Mo substrate about half a year after the nanoparticle synthesis. Similar to the first experiments the sample has been Ar^+ ion etched at an energy of 3 kV for 135 min. The Ar pressure within the ion gun was adjusted to $0.5 - 1.0 \cdot 10^{-3}$ Pa. After ion etching two different reversal mechanisms for the magnetization were employed: (i) Similar to the first experiments the sample has been cooled to 135 K, 150 K, and 180 K in absence of a magnetic field, after which the sample has been magnetized by a 50 mT field pulse directly before the majority and minority spectra were taken. (ii) The sample has been thermally demagnetized to $T = 330$ K > T_B and field cooled in 50 mT to 26 K, 135 K, 150 K, and 180 K. The field cooling results in a larger remanent magnetization of the sample due to exchange bias shifting of the hysteresis loop (Figure 1.4). Two examples will be discussed in the following which present the largest XMCD difference signals: (i) the measurement at T = 150 K for pulse reversal and (ii) the XMCD spectrum for FC procedures at 26 K. Figure 5.6 shows the resulting XMCD spectra for the two methods of magnetization reversal. Pulse reversal provokes a dichroism of 15% at the L_3 peak position while the FC procedure reveals an enhanced XMCD difference of 24% with respect to the isotropic XAS spectrum. The dichroic signals have been corrected for the degree of circular polarization and the angle of incidence. For comparison of the orbital contribution to the total magnetic moment the XMCD difference spectra were normalized onto each other. The spectroscopic line shapes of the isotropic spectra (not shown) are identical in the whole spectral range for both experiments. The dichroism at the L_3 peak position is a measure of the magnetization of the sample [112] and thus the ratio of the relative dichroic signals $M_{rem,FC}/M_{rem,pulse} = 1.60$ can be compared to SQUID magnetometry.

Hysteresis loops of the as-deposited particles show that method (i) reaches a remanent magnetization of 32% by a field pulse of 50 mT compared to the magnetization value at 4 T (Figure 1.4) which is the normalization point in the following. One may note that the external field

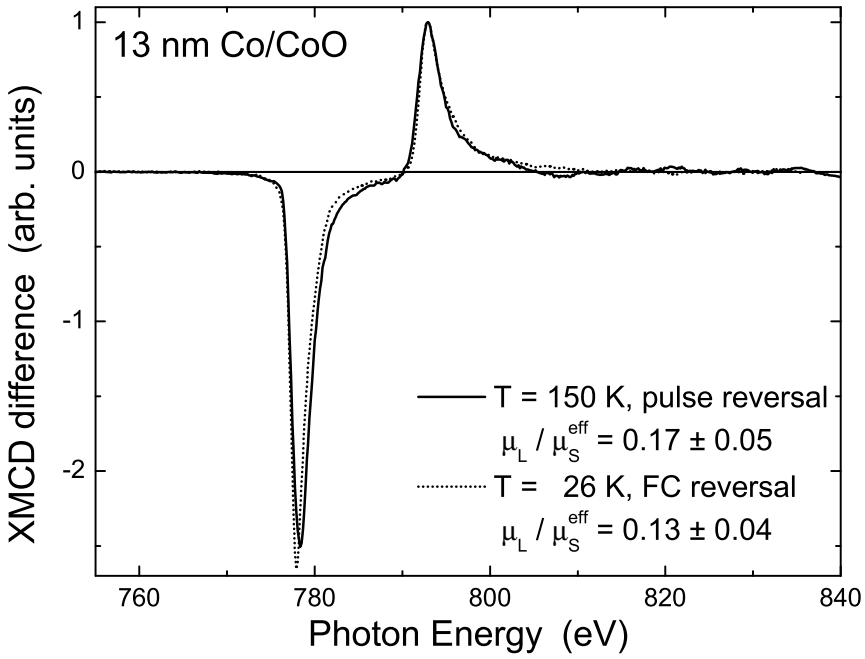

Figure 5.6.: XMCD difference spectra of Ar^+ ion etched 13 nm Co/CoO particles. Two reversal mechanisms of the magnetization were employed: pulse reversal (50 mT) after ZFC of the sample to 150 K and FC at 50 mT to 26 K from a thermally demagnetized state at an angle of incidence of 30° with respect to the substrate plane. For comparison the XMCD difference spectra were normalized onto each other at the L_2 peak position. The ratios of the orbital-to-spin magnetic moment are given in the figure.

of 4 T is far above the irreversibility point of the hysteresis but the saturation magnetization is not reached. Method (ii) shows a remanent magnetization of 50% of M(4T). The ratio of remanent magnetizations $M_{rem,FC}/M_{rem,pulse} = 1.56$ is in good agreement to the ratio determined by XMCD. Two consequences arise from this finding: (i) Ar^+ ion etching does not dramatically change the remanent magnetization of an array of Co/CoO nanoparticles and (ii) the field cooling process manifests itself in an 60% enhanced remanent magnetization compared to the pulse reversal that enhances the XMCD difference signal. Thus, the analysis of the ratio of orbital-to-spin magnetic moment from XMCD difference spectra becomes more reliable. Minor looping of the magnetization using a field lower than the irreversibility point ($\approx$ 400 mT at 150 K for ZFC) includes the possibility that the remanent magnetization after pulse reversal and the at least three spectra taken per magnetization direction are not identical. Although extreme care has been taken for identical conditions the statistical error of the ratio of orbital-to-spin magnetic moment increases for the pulse reversal of the magnetization. When the sample has been cooled in a defined field of 50 mT from a thermally demagnetized state the final state

of remanent magnetization is more reproducible.

The ratio of orbital-to-spin magnetic moment evaluated for both approaches is discussed in the following. Figure 5.6 presents the strongest XMCD response for both, (i) pulse reversal at 150 K and (ii) FC reversal at the lowest temperature T = 26 K that could be reached. Method (i) allows the XMCD signal detection in the temperature interval 135 K - 180 K flipping the magnetization by a 50 mT pulse. The ratio of orbital-to-spin magnetic moment is determined to $\mu_L/\mu_S^{eff} = 0.17 \pm 0.05$. No temperature dependence has been found. Method (ii) yields a $\mu_L/\mu_S^{eff} = 0.13 \pm 0.04$ in the temperature range 26 K - 150 K. At 180 K, however, an increase of the ratio to $\mu_L/\mu_S^{eff} = 0.18 \pm 0.05$ has been observed. The spectroscopic line shape of the FC dichroism shows a slightly smaller peak intensity at the L_3 resonance (A_{L_3}) while the L_2 intensities are set to coincide. The energy shift of the L_3 peak position of 0.2 eV with respect to the pulse reversal signal is not fully understood, yet. Beam shifts can be excluded since the L_2 edges fit onto each other. The point density of the XMCD difference spectra shown in Figure 5.6 is 0.15 eV. The shift consist basically of only one experimental point. Hence, it cannot be decided if the shift has a physical origin or is due to technical reasons.

In summary, the two independent sets of experiments employing pulsed magnetization reversal show a strongly enhanced ratio of orbital-to-spin magnetic moment of $\mu_L/\mu_S^{eff} = 0.24 \pm 0.06$ and 0.17 ± 0.05 compared to the bulk fcc Co value of 0.08. Within the large error bars the two experiments coincide. μ_L/μ_S^{eff} is found temperature-independent in the temperature range 100 K - 200 K. The reversal of the magnetization from a thermally demagnetized state results in an enhanced remanent magnetization due to the exchange biased hysteresis. This phenomenon directly reveals a stronger magnetic dichroism and consequently a smaller statistical error in the μ_L/μ_S^{eff} evaluation. Moreover, when the sample is cooled from a demagnetized state in a defined magnetic field to low temperatures, the resulting magnetization state will be more reproducible than field pulsing reversal at small external fields (B = 50 mT)acting on minor loops only. The FC magnetization reversal shows an temperature-independent $\mu_L/\mu_S^{eff} = 0.13 \pm 0.04$ between 26 K and 150 K. Above 150 K the exchange bias vanishes (compare to section 5.1.3) and both magnetization reversal procedures are identical. At 180 K both methods show a $\mu_L/\mu_S^{eff} = 0.17 - 0.18 \pm 0.05$. It is noticeable that the FC procedure shows a decrease of μ_L/μ_S^{eff} for temperatures where a loop shift by exchange bias is present. The large statistical errors, however, do not provide an unambiguous proof of the experimental findings. From the experimental result of a changing ratio of orbital-to-spin magnetic moment at the temperature where exchange biasing of hysteresis loops vanishes one may argue that the exchange interaction at the interface Co/CoO produces this effect.

FC results in a partial alignment of the magnetic moments along the field direction depend-

ing on the local magnetocrystalline anisotropy of the single grains of both, the core and the shell and their interaction at the interface. Below 150 K the exchange bias adds an additional aligning field to the spin- and the orbital moments. Since the anisotropy of the orbital moment is coupled to the magnetocrystalline anisotropy it seems convincing that the spin moment can be more easily aligned by the FC procedure. Enhanced spin moments along the FC direction would directly reveal a reduction of μ_L/μ_S^{eff} as observed in the experiments. For FC above 150 K and ZFC there is not any additional field component present since either the antiferromagnetic core grains are superparamagnetic (FC) or the exchange interaction at the interface favors isotropically distributed additional field components which average out in the experiments. In this case the particles find their magnetic "ground state". In a simple picture, one may conclude that the FC procedure is comparable to the measurement in a locally applied field while in ZFC there is no preferential direction of this field. It is well known [42,59] from exchange bias investigations that biased Co/CoO particles reveal a larger squareness in hysteresis loops indicating the difference of FC and ZFC measurements (Figure 1.4).

Experiments in External Magnetic Fields

In general, a big advantage for XMCD investigations is the possibility to apply a magnetic field during the spectra acquisition. A low remanent magnetization often makes it difficult to extract quantitative information from XMCD difference spectra. External fields increase the observed dichroism resulting in smaller statistical errors. From element-specific hysteresis loops one can adjust the external fields to exclude minor loop effects. Such experiments are discussed in the following. All experiments presented were measured on a single layer of particles similar to the one shown in Figure 4.12. The measurements were performed before any plasma exposure. Only two days after the chemical synthesis the 9 nm Co/CoO particles were deposited on native $Si(001)$ by droplet evaporation. After about one hour preparation time the sample was transferred into the UHV chamber and examined in the as-deposited state.

The upper panel of Figure 5.7 shows the spin-polarized XAS and the resulting XMCD spectrum taken at normal incidence, in external fields of B = $\pm$1 T, and T = 15 K. The XAS spectra exhibit a mixture of Co and CoO responses. The multiplet structure of CoO is clearly visible. The contributions from Co atoms in metallic and oxidic environments can be deduced by Monte-Carlo simulations [94,124]. The discussion of the results of the simulations is presented below in more detail. Here, the description of the experimental findings is continued. The maximum dichroic difference is 22% of the isotropic spectrum and thus about 3.5 times larger than the XMCD difference taken in remanence (Figure 5.6). The ratio of orbital-to-spin magnetic moment is $\mu_L/\mu_S^{eff} = 0.14 \pm 0.03$ supporting the value obtained for FC remanence detection.

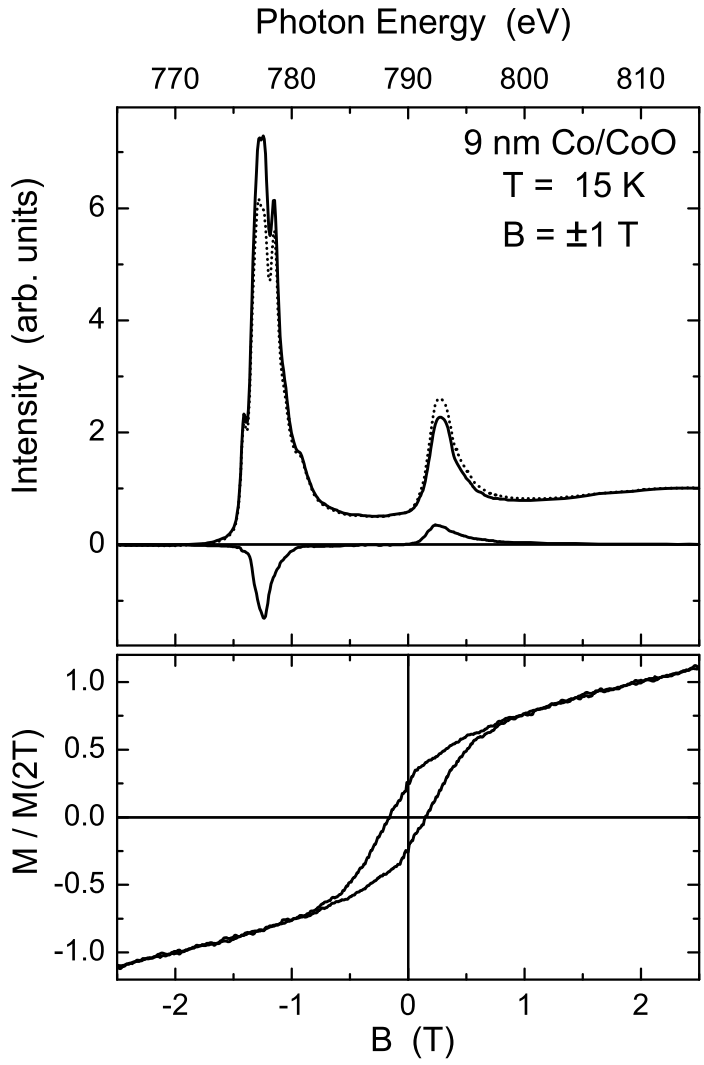

Figure 5.7.: The upper panel shows the XAS and XMCD spectra of 9 nm Co/CoO particles deposited as a single layer on native $Si(001)$. The spectra were measured at normal incidence in external fields of B = $\pm$1 T parallel and antiparallel to the x-ray propagation direction. Multiplet peaks from CoO are clearly visible. A well-resolved XMCD difference is observed. The lower panel shows the field dependence of the maximum L_3 dichroism that is proportional to the magnetization. The loop has been normalized to M(2T). The element-specific hysteresis loop reveals a coercitive field of $\mu_0 H_C = 0.15$ T and a closing of the hysteresis at about 0.7 T. The high field susceptibility is discussed in the text.

From the hysteresis loop in the lower panel of Figure 5.7 it is obvious that the XMCD was not taken on a minor loop. The major hysteresis loop closes at about 0.7 T. The coercive field is found to be $\mu_0 H_C = 0.15$ T. At high fields a linear slope of 22% / T is observed which coincides within 2% to the more precise but time consuming measurement of the XMCD at external fields of 1 T (Figure 5.7), 1.5 T, and 2 T (not shown). Additional experiments at T = 250 K reveal

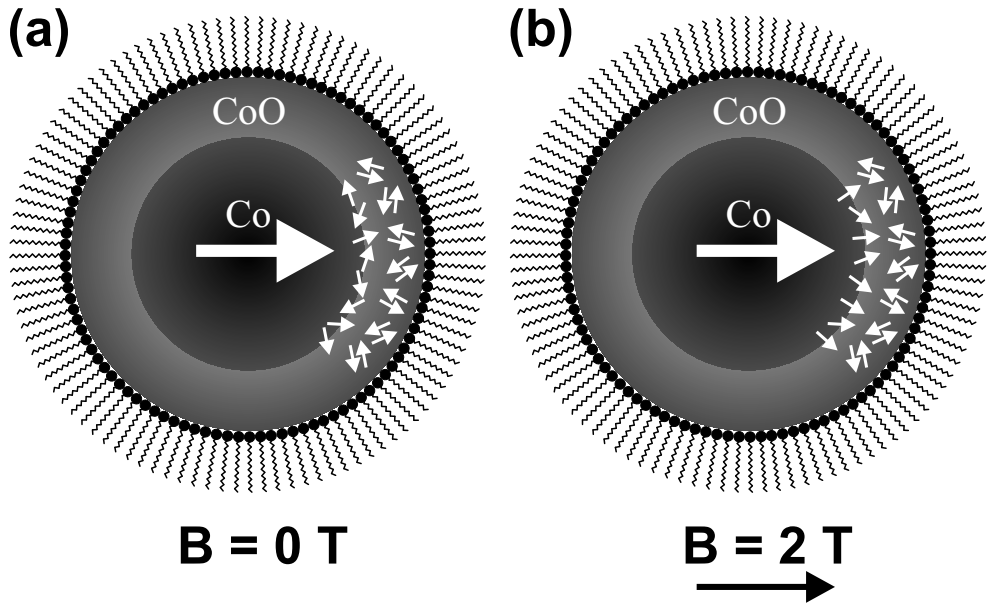

Figure 5.8.: Schematics of the magnetic moments of the ferromagnetic core, the interface, and the antiferromagnetic shell at $B = 0$ T (a) and $B = 2$ T (b). The core is represented by a single-domain, giant spin. In (a) the direction of the magnetic moments at the interface are determined by local internal fields produced by the core and the shell. Antiferromagnetic grains in the shell are randomly oriented due to the zero-field cooling (Figure 5.7). In an external field (b) the interface moments partially rotate in the direction of the external field.

a superparamagnetic XMCD magnetization as expected from ZFC/FC measurements which showed a blocking temperature $T_{B,mean} \approx 85$ K and an irreversibility point of $T_{irr} \approx 150$ K. The normalized magnetization as a function of the external field (normalization point 2 T) shows a high field slope of 15% / T that reflects an reduction by 7% / T compared to the hysteresis loop at T = 15 K. The XMCD analysis yields $\mu_L/\mu_S^{eff} = 0.17 \pm 0.03$ at normal incidence using a reversal field of B = $\pm$ 1 T. This finding reflects once more a possible change of μ_L/μ_S^{eff} above the temperature where the exchange bias vanishes (compare to the XMCD investigations in remanence detection mode presented above). The linear slope at large external fields is due to the field-dependent partial alignment of uncompensated Co^{2+} magnetic moments. Figure 5.8 reflects the situation. At B = 0 T the uncompensated moment at the interface orient in directions given by the interaction with local fields produced by the Co core and the CoO shell grains. At B = 2 T the external field partially rotates the uncompensated interface moments in the direction of the external field. Thus, the XMCD difference signal increases. The proof that interface moments mainly produce the slope of the hysteresis loop will be given below. Firstly, the focus is set to the spectroscopic shape of the XMCD difference.

The upper panel of Figure 5.9 shows two XMCD difference spectra. The solid line represents the dichroism of the as-deposited 9 nm Co/CoO particle from Figure 5.7. The dotted

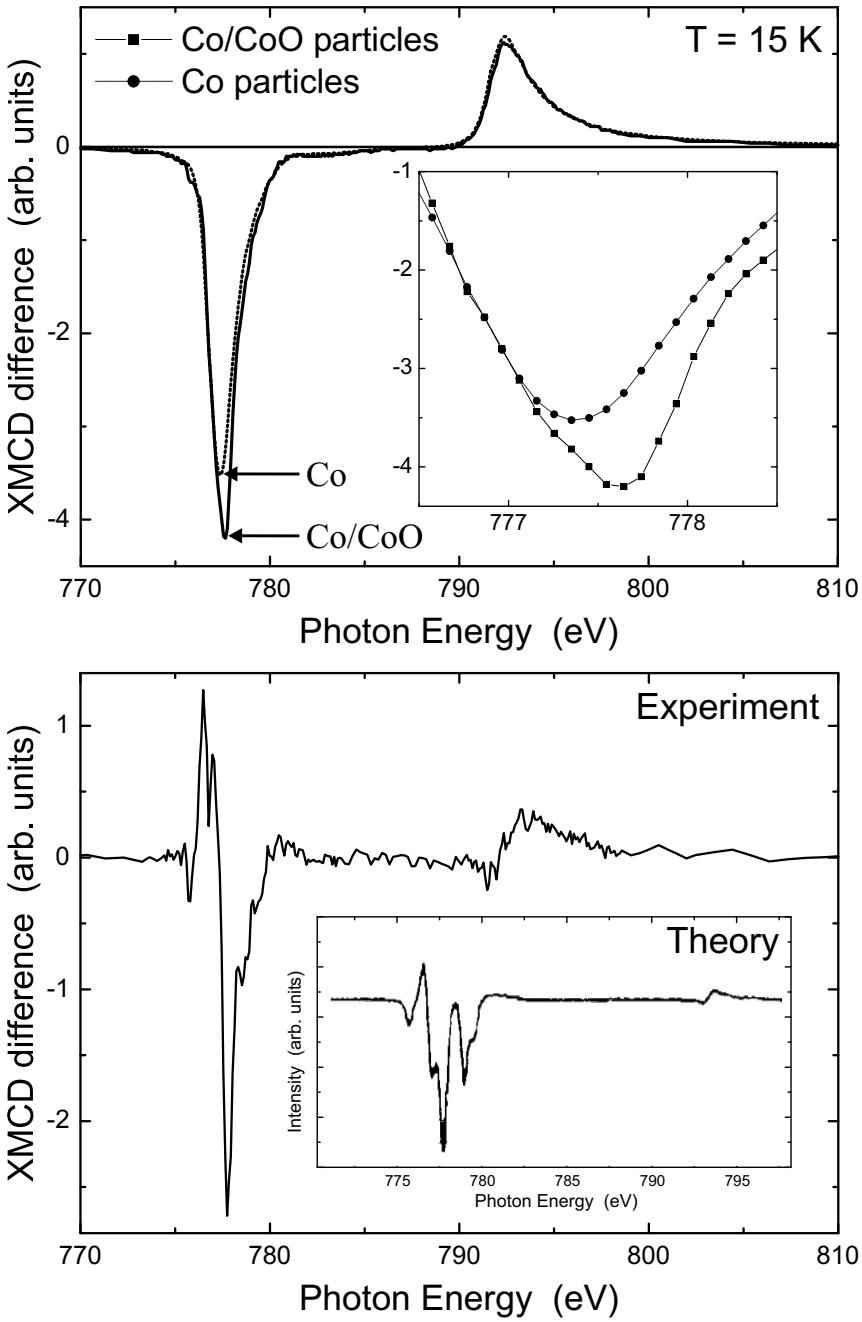

Figure 5.9.: The upper panel shows the XMCD difference spectrum of the 9 nm Co/CoO particles from Figure 5.7 and the XMCD difference from metallic particles after plasma-assisted removal of the ligands and the reduction of Co oxides. The two XMCD difference spectra were scaled onto each other by a single factor. The inset shows a magnification of the L_3 dichroic signal. The lower panel presents the difference of the two XMCD spectra from the upper panel. A complicated magnetic signature is found. The inset shows a calculated XMCD spectrum of magnetically ordered Co^{2+} ions in an octahedral potential ($10D_q$ = 1 eV) using *ab initio* methods. The calculated spectrum is taken from [132] and sign-reversed to account for the different definition of the XMCD difference in the reference.

line shows the XMCD difference spectrum of purely metallic particles after plasma transformation. The XAS spectra were taken at identical geometry at B = $\pm$ 1.25 T. At this field the particles exhibit their saturation magnetization. Both spectra were scaled by a single factor to fit the interpeak regions onto each other. This procedure accounts for the difference in the absolute dichroisms due to CoO overlayers which damp the XMCD signal from the metallic core underneath. The inset presents a magnification of the L_3 dichroic signal. The XMCD signal of the Co/CoO nanoparticles shows a shift of the maximum dichroic response by 0.3 eV towards higher energies. At the maximum L_3 XMCD of the metallic spectrum the Co/CoO nanoparticle spectrum shows a slight shoulder. From this finding and the fact that the XMCDs in the interpeak region (782 eV -788 eV) are equal to each other, one can conclude that the XMCD response of Co/CoO particles is a composition of both, a pure metallic spectrum and some additional component from Co in a non-metallic environment.

To clarify the nature of this non-metallic XMCD it is helpful to extract this information from the total XMCD difference spectrum. The lower panel of Figure 5.9 shows the simple difference of the two spectra in the upper panel. A complicated XMCD difference including zero crossings in the L_3 and L_2 edges becomes visible. The inset presents a calculated XMCD spectrum for magnetically ordered Co^{2+} ions in an octahedral potential using *ab initio* methods. The spectrum has been adapted from van der Laan and Thole [132] and sign-reversed to account for different definitions of XMCD. The extracted experimental XMCD difference resemblances the calculated spectrum. All extrema in the experimental spectrum are also predicted from theory for Co^{2+} ions in an octahedral environment. Calculations neglecting the exchange splitting or the cross-over to a spherical potential results in completely different XMCD lineshapes [132]. Co^{2+} ions in an octahedral environment are present in the shell of the Co/CoO particles. Thus, this results suggest that the origin of the oxidic XMCD is the CoO shell. Moreover, the XMCD of CoO has its largest contribution to the XMCD parallel to the metallic dichroism. Thus, the magnetic moments of the metallic and the uncompensated oxidic interface contributions are parallel.

In conclusion, it has been found that the XMCD spectrum of Co/CoO particles consist of both metallic and oxidic contributions. The enhancement in the ratio of orbital-to-spin magnetic moment originate from the parallel alignment of the metallic core magnetic moments and a small additional contribution by Co^{2+} ions in an octahedral environment from CoO aligned parallel to the core magnetic moment. Co^{2+} ions carry a large magnetic moment of about 4 μ_B and show a large $\mu_L/\mu_S^{eff} = 0.6$ [6,24]. Thus, an enhanced ratio μ_L/μ_S^{eff} is expected in the experiments (Table 1.5).

Local Coupling of CoO to Co

The experimental findings above clearly reveal the existence of a CoO XMCD signal in Co/CoO nanoparticles. Generally, antiferromagnetic CoO does not show any XMCD difference signal since adjacent planes of Co^{2+} ions cancel out the dichroism of each single plane. For thin layers (shells) of CoO, however, several origins of the existence of an antiferromagnetic XMCD response have to take into account: (i) an odd number of Co^{2+} planes in the antiferromagnet, (ii) uncompensated moments at the ferromagnetic/antiferromagnetic interface, and (iii) non-collinear moments due to the grain structure of the CoO shell.

Simulations [124] of the experimental XAS spectra using weighted contributions from Co and CoO thin film reference data [91] taking into account the depth information profile described in chapter 2 show that the CoO shell thickness is about 1.0$\pm$0.2 nm in the experiments shown in Figure 5.7. The shell is found to be thinner than the one observed in TEM investigations (chapter 3), since the particles were examined only two days after chemical synthesis. Moreover, only about one hour after deposition on $Si(001)$ substrates the sample has been transferred into the UHV chamber. In all other investigations the time window after preparation and deposition is usually larger allowing a further oxidation. A long term investigation of the development of the CoO with time is presented in chapter 5.1.6. In a second set of experiments, investigations of the nominally 9 nm particles were repeated about six month after the particle synthesis. Additionally, the particles were kept for three days in ambient conditions. In this case, the CoO shell thickness has been found to be 2.5$\pm$0.4 nm. In the following these two sets of measurements will be compared to give an insight into the coupling mechanisms of the Co core and the CoO shell.

Figure 5.10 (a) and (b) present the experimental XAS white lines and the XMCD difference signal of the 9 nm Co/CoO particles with different shell thicknesses. Both experiments have been conducted at T = 15 K, normal incidence and of B = $\pm$1 T. The XAS of both experiments clearly reveals the CoO multiplet structure. The points show the linear combinations of Co and CoO reference spectra [91] with a metallic contribution of 55% (a) and 10% (b) as suggested by the simulations of the core/shell response of the particles (Figure 2.5). The linear combinations neglect the attenuation of the metallic contribution by the oxidic overlayer. The electrons generated in the core have to pass the CoO shell in which they are partially absorbed. Thus, the expected metal spectrum is slightly convoluted by the inverse XAS of CoO. However, this effect is neglected in the following. The simple linear combination fits the interpeak and the post-edge regions perfectly. Moreover, the relative peak intensities of the CoO multiplet peaks are reproduced. The absolute peak heights do not fit perfectly due to the modulation of detected electrons as mentioned above. Also, the XAS of a nanoparticle is not necessarily identical to

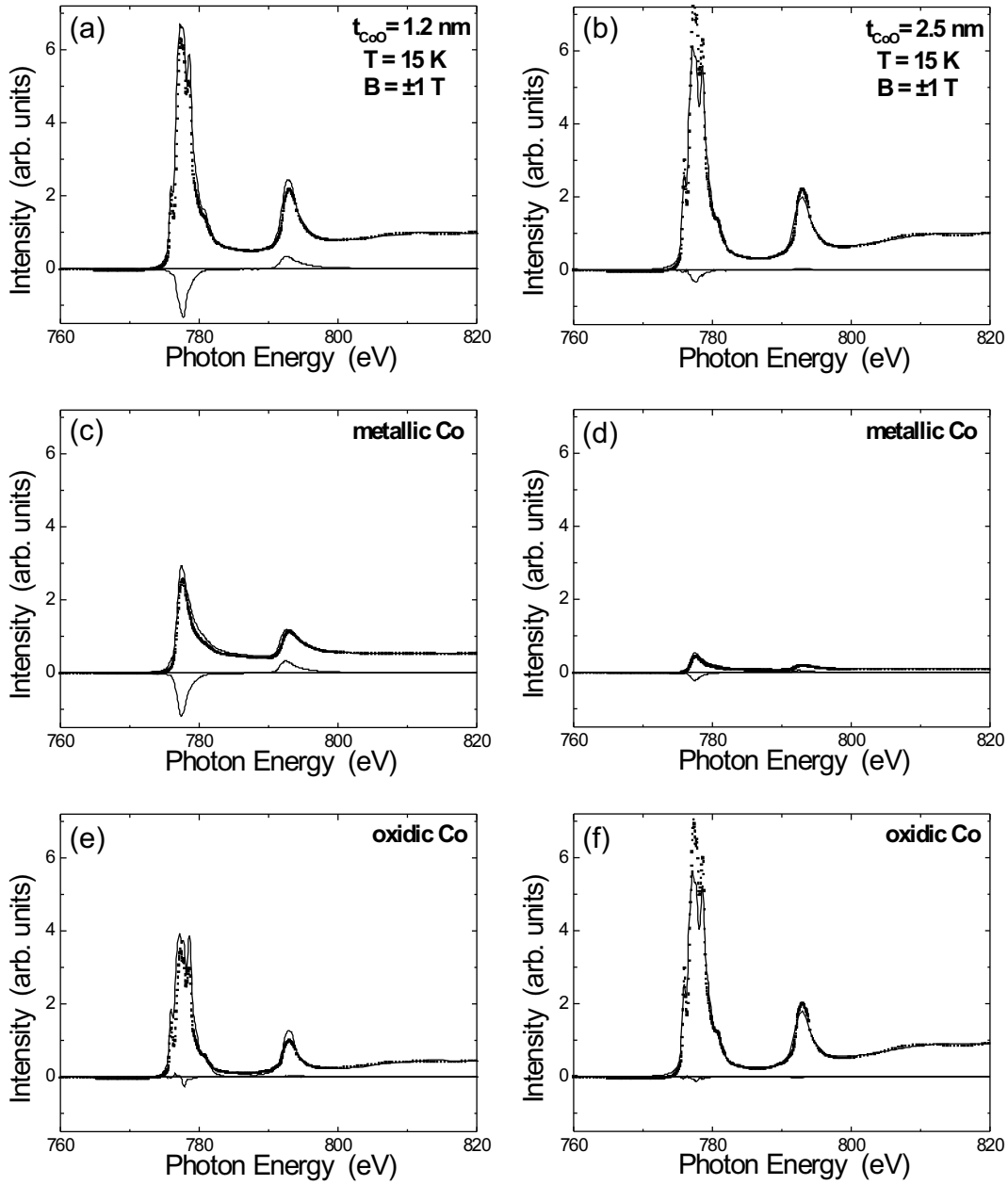

Figure 5.10.: Experimental XAS white lines and XMCD difference signals (solid lines) for the 9 nm Co/CoO particles for shell thicknesses of $t_{CoO} = 1.0 \pm 0.2$ nm (a) and $t_{CoO} = 2.5 \pm 0.4$ nm (b) at T = 15 K and flipping fields of ± 1 T. The points represent the linear combination of Co and CoO XAS thin films reference spectra [91] neglecting the variation of the metallic Co XAS signal by the overlying CoO shell. Best agreement is found for metallic contributions of 55% (a) and 10% (b). (c) and (d) show the metallic contributions in the XAS and XMCD of (a) and (b), respectively. The XAS and XMCD spectra of metallic Co particles after plasma treatment are used as a metallic reference. The XAS and XMCD signals of the Co^{2+} ions in the shell are shown in (e) and (f).

the superposition of reference spectra. The XMCD signal decreases for a thicker CoO shell from 20% (t_{CoO} = 1 nm) to about 6% for the 2.5 nm CoO shell. This can be understood in terms of damping of the metallic XAS signals by the growth of the CoO shell. Additionally, the oxidation strongly reduces the number of metallic Co atoms from 15600 to 5300 for an ideal spherical particle. As discussed above in more detail, the XMCD signal of Co/CoO consist of a metallic XMCD and a small oxidic XMCD produced by Co^{2+} ions. The metallic and oxidic contributions to the experimental XAS and XMCD are also shown in Figure 5.10 (c)-(f).

The experimental XAS and XMCD spectra of the plasma treated oxide-free Co particles are used as representants of the metallic contribution to the experimental XAS and XMCD spectra. The oxidic Co spectra shown in Figure 5.10 (e) and (f) for 45% (t_{CoO} = 1 nm) and 90% (t_{CoO} = 2.5nm) relative contributions, respectively, are calculated from the differences of experimental Co/CoO and metallic spectra. Although the examination of particles with a 2.5 nm CoO shell has twice as much Co^{2+} ions per particle compared to the particle with the 1 nm CoO shell (see Table 5.1) the XMCD signal shrinks by a factor of two. This result shows that the Co^{2+} XMCD cannot be due to uncompensated Co^{2+} surface moments, since the number of surface ions slightly increases for growing shell thickness from 4300 to 4900 Co^{2+} surface ions per particle. The increase of surface ions is due to the growth of the particles by oxidation. Moreover, the density of grain boundaries in the CoO shell should not change considerably by further oxidation from 1 nm to 2.5 nm shell thickness. Thus, the only possible origin of the Co^{2+} ion XMCD signal is the ferromagnetic/antiferromagnetic core-shell interface. Due to the shrinking core diameter with oxidation the number of interface Co^{2+} ions decreases for thicker shells confirming the experimental findings.

To quantify the number of interface moments and the consequences for XAS and XMCD signals a simple model is employed which is described in the following. Table 5.1 summarizes the results of the modelling. TEM investigations show a most probable particle diameter of 9.5 nm with a 2.5 nm CoO shell of the nominally 9 nm particles. The second set of XMCD experiments confirms those findings. In the first set of experiments the shell thickness is only about 1 nm. Due to different densities of Co and CoO the particle diameter is smaller than for a 2.5 nm shell while the number of Co atoms is constant. Accordingly, the particle diameter of a Co/CoO particle with a 1 nm shell is 8.9 nm. The shell consists of small grains randomly oriented in space. Thus, at both, the interface to the core and the surface, a mixture of Co^{2+} ions with bulk-like atomic distances between 0.301 nm along (111) and 0.426 nm along (001) is expected. Here, the interface and surface is defined as a single layer with averaged distances of neighboring Co^{2+} of 0.363 nm. The number of surface ions is 4300 and 4900 for the particles with a 1 nm and 2.5 nm shell, respectively. The number of Co^{2+} planes with respect to the

particle center is about 2-3 layers for 1 nm CoO and 5-8 layers for 2.5 nm CoO. As a rough estimate it is assumed in the following that 50% of the Co^{2+} ions are uncompensated either at the surface or the interface. In XAS the sampling depth has to be taken into account. Surface ions contribute their full information to the XAS. The simulation [124] of the secondary electron escape depth for this system suggests that at the interface the depth information is 85% (65%) for the 1 nm (2.5 nm) CoO shell. The mean core information in XAS is reduced to 78% (50%) for the 1 nm (2.5 nm) shell. Using these correction factors the attenuation-free equivalent of Co atoms at different sites in the nanoparticle can be calculated. One may note that these corrections hold for the TEY mode only. The equivalent number of Co^{2+} ions at the interface is 2.6 times larger for the 1 nm shell than for the thicker shell. It has already been proven that the signal originates at the interface. The Co^{2+} XMCD of the 1 nm shell particles is about two times larger than for the particles with the thicker shell. The model quantitatively predicts a 2.6 times larger Co^{2+} ion XMCD for the particles with the thinner shell which is in good agreement to the experimental result despite the simplified model assumptions.

The corrected number of atoms contributing to XAS and XMCD from CoO and Co can also be used for the calculation of the expected ratio of the orbital-to-spin magnetic moment μ_L/μ_S^{eff}. The weighted sum is:

$$\frac{\mu_L}{\mu_S^{eff}}(Co/CoO) = \frac{N_{I,S}}{N_{I,S}+N_C}\cdot\frac{\mu_L}{\mu_S^{eff}}(CoO) + \frac{N_C}{N_{I,S}+N_C}\cdot\frac{\mu_L}{\mu_S^{eff}}(Co) \tag{5.2}$$

Here, N_I, N_S, and N_C are the attenuation-free numbers of atoms contributing to XMCD at the interface, the surface, and the metallic core. The ratio of orbital-to-spin magnetic moment of Co^{2+} in CoO μ_L/μ_S^{eff} = 0.6 [6,24] and μ_L/μ_S^{eff} = 0.08 of bulk fcc Co [3] were taken from literature. The expected ratio of orbital-to-spin magnetic moment in the nanoparticles is calculated to μ_L/μ_S^{eff} = 0.16 (t_{CoO}= 1 nm) and μ_L/μ_S^{eff} = 0.33 (t_{CoO}= 2.5 nm) for surface Co^{2+} ion XMCD. If the Co^{2+} ion XMCD is located at the interface the model predicts μ_L/μ_S^{eff} = 0.13 (t_{CoO}= 1 nm) and μ_L/μ_S^{eff} = 0.16 (t_{CoO}= 2.5 nm). All parameters and results are summarized in Table 5.1.

Additionally, the results adapted to the 13 nm Co/CoO particles are listed in Table 5.1. Similar to the arguments above the calculated ratios of orbital-to-spin magnetic moment describe the experimental findings best for uncompensated moments located at the core/shell interface. The ratios μ_L/μ_S^{eff} for uncompensated surface moments are generally predicted larger than for uncompensated interface moments. As a consequence of these investigations, it can be concluded that *parallel alignment* of uncompensated moments in the antiferromagnet with respect to the metal core results in an effectively measured enhanced ratio of orbital-to-spin magnetic moment. Antiparallel alignment would yield reduced values of μ_L/μ_S^{eff}. The results were obtained using magnetic bulk properties that may underestimate the μ_L/μ_S^{eff} of the metallic core,

Table 5.1.: Results of the modelling of the experimental XAS and XMCD signals of the nominally 9 nm and 13 nm Co/CoO particles. Based on the CoO shell thickness the number of Co core and shell atoms is calculated. Additionally, the numbers of surface and interface Co^{2+} ions are given. These numbers of atoms can be corrected for compensation of Co^{2+} moments and the sampling depth of the total electron yield detection mode. The corrections allow to calculate an expected ratio of orbital-to-spin magnetic moment by the weighted contributions of Co in metallic and oxidic environment. The modelling is described in the text.

Nominal nanoparticle diameter CoO shell thickness	9 nm t_{CoO} = 1.0 nm	9 nm t_{CoO} = 2.5 nm	13 nm t_{CoO} = 2.5 nm
Total no. of atoms	25800	25800	82800
No. of Co core atoms	15600	5300	34600
No. of Co^{2+} shell ions	10200	20500	48200
Particle diameter	8.9 nm	9.5 nm	13.6 nm
No. of Co^{2+} ions at surface	4300	4900	10400
No. of Co^{2+} ions at interface	3100	1400	5200
Sampling depth corrected No. of Co core atoms	12200	2650	17300
Compensation corrected No. of Co^{2+} ions at surface	2150	2550	5200
Sampling depth and compensation corrected No. of Co^{2+} ions at interface	1300	500	1700
μ_L/μ_S^{eff} of Co^{2+} XMCD at surface	0.16	0.33	0.20
μ_L/μ_S^{eff} of Co^{2+} XMCD at interface	0.13	0.16	0.13

especially for small core diameters. Larger metal μ_L/μ_S^{eff} would directly lead to the expectation of higher values of μ_L/μ_S^{eff} in the Co/CoO core-shell nanoparticles or a reduced contribution of uncompensated Co^{2+} interface ions.

XMCD versus FMR

The XMCD experiments generally reveal an enhanced ratio of orbital-to-spin magnetic moment for nanoparticles of different sizes and shell thicknesses. In the temperature range 15 K - 250 K the values of μ_L/μ_S^{eff} slightly vary but always remain enhanced compared to fcc bulk Co. XMCD is very surface sensitive and measures the inner-atomic excitations into unoccupied 3d states by spin-polarized investigations. Thus, it is not surprising that the small effect of Co^{2+} ions could be detected. FMR experiments at room temperature on the other hand suggest a fcc

bulk-like ratio of orbital-to-spin magnetic moment. FMR has a sampling depth of more than 20 nm at the resonance position in the case of ferromagnetic materials [95]. In the paramagnetic state the penetration depth of the microwaves increases to several microns for metals [67]. Therefore, the whole particle is examined by FMR. The signal of the oxide layer is expected to be rather small, since CoO in the bulk shows an antiferromagnetic ordering which – in case of a perfect antiparallel alignment of the spins – does not produce a resonant absorption as the resonance frequency is at much higher energies. The only possible signal could arise from frustrated spins within the oxide layer that occur due to the spherical shape of the particles. As bulk CoO has a Néel temperature of $T_{\mathrm{N}} = 293$ K a further reduction of the FMR signal results from the fact that the oxidic layer is in the antiferromagnetic/paramagnetic transition region which causes an extremely large linewidth. Only the spins in contact to the metallic core possibly present some ordering. Therefore, the strongest contribution of the oxide layer to the magnetization is expected to arise from spins located directly at the interface of the metallic core to the oxide layer. If the contribution to the FMR signal originating from the interface spins would be large, an enhanced orbital moment would be expected. Since this enhancement has not been observed, one can conclude that the response within FMR mainly results from the metallic core. To the author's best knowledge a paramagnetic signal of CoO has never been observed in terms of paramagnetic resonance. Antiferromagnetic resonance at temperatures lower than the Néel temperature cannot be detected with our experimental set-up. At low temperatures future frequency-dependent experiments may show the influence of the oxide shell to the nanoparticle core.

5.1.3. Exchange bias

In the previous sections the influence of the CoO shell on (i) the blocking temperature and (ii) the orbital contribution of the magnetic moment has been discussed in detail. The results show that the CoO shell strongly influences the blocking temperature and Co^{2+} uncompensated moments exist at the ferromagnet/antiferromagnet interface. The magnetic moments at the interface are aligned parallel to the ferromagnetic core. In this section the focus is set to the exchange coupling between Co core and CoO shell which governs exchange anisotropy. A measure of the exchange anisotropy is (i) the exchange bias field and (ii) the difference of FC/ZFC coercive fields.

For exchange bias measurements $10^{13} - 10^{14}$ Co/CoO particles of all three batches were deposited onto $Si(001)$ substrates by droplet evaporation. The samples were transferred into the cryostat system immediately after the particle deposition. Figure 1.4 shows a typical experiment

for the nominally 13 nm particles. Hysteresis loops of an array of the Co/CoO particles were measured at 10 K both after ZFC and FC in an applied field of 5 T from 350 K to 10 K. The magnetic field to measure the hysteresis loop was parallel to that of the cooling field. The ZFC loop is symmetrical about the origin while the FC loop is shifted opposite to the cooling field direction. The value of the exchange bias field $\mu_0 H_{eb} = 0.4$ T at T = 10 K indicates a strong unidirectional exchange anisotropy (UEA) in the sample. The interface exchange energy ΔE per unit area [55] for spherical nanoparticles can be calculated from equation 1.21. $\Delta E = 0.68$ mJ/m^2 is found at 10 K that is smaller than for oxidized Co films ($\Delta E = 3.5$ mJ/m^2 at 10 K) [55] in spite of very rough ferromagnetic/antiferromagnetic interfaces. The smaller exchange anisotropy for our nanoparticles can be due to the thin AFM layer. The FC coercivity is two times increased ($\mu_0 H_C^{FC} = \mu_0|(H_1^{FC} - H_2^{FC})/2|$ = 0.39 T) in comparison to the ZFC case ($\mu_0 H_C^{ZFC} = |(H_1^{ZFC} - H_2^{ZFC})/2|$ = 0.21 T) where the UEA is randomly distributed. H_1 and H_2 are marked in Figure 1.4.

The exchange bias field measured as a function of temperature during heating of the FC sample is shown in Figure 5.11 for all three batches of particles. $\mu_0 H_{EB}$ decreases very strongly with increasing temperature and completely vanishes at 150 K in the case of 13 nm particles. For 9 nm particles the exchange bias vanishes already at T $\approx$ 100 K which indicates that a smaller ferromagnetic core (or smaller interface area) at constant shell thickness produces a smaller exchange bias field. Moreover, equation 1.21 predicts a decreasing exchange interaction with decreasing core diameter. Similar results have been observed for gas-phase prepared oxidized Co nanoparticles [58,59,133]. Fitting the experimental results to $H_{EB} = H_{EB}(0\mathrm{K})\left(1 - T/T_B^{AFM}\right)^{\mathrm{n}}$ of the 13 nm particles in a temperature range from 10 K to 100 K results in $\mu_0 H_{EB}(0\mathrm{K}) = 0.49$ T, T_B = 150 K and n $\approx$ 3.2. A linear decrease of the exchange bias field has been predicted in the framework of the random-field model of anisotropy [62] for cubic AFM crystals. The linear behavior (n = 1) of $H_{EB}(T)$ has been observed experimentally in many thin-film systems [54,55]. In the case of nanoparticles or polycrystalline antiferromagnets with a small grain size, the temperature degradation of the exchange energy can be described better by the model of thermal instabilities of superparamagnetism of small antiferromagnetic grains [63]. The strength of the exchange bias is therefore determined by the magnetic blocking. This model explains a decreased temperature at which the exchange bias vanishes ($T_B^{AFM} =$ 100-150 K) for our systems in comparison with a Néel temperature of bulk CoO ($T_N = 293$ K). Future investigations of the exchange bias field as functions of temperature and cooling field are necessary to correlate the power law coefficient with the interface area, the superparamagnetism of antiferromagnetic grains in the shell, and the volume of the ferromagnetic core.

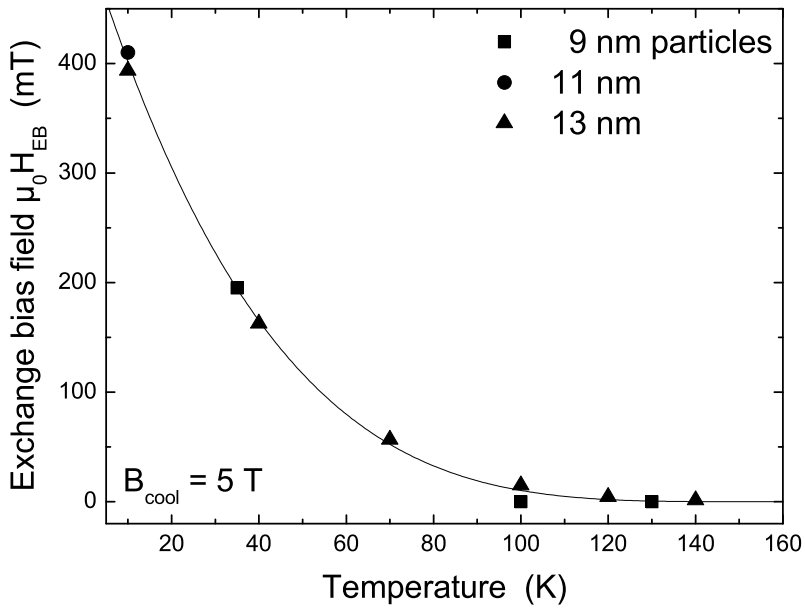

Figure 5.11.: Temperature dependence of the exchange bias field $\mu_0 H_{EB}$ for the nominally 9 nm, 11 nm, and 13 nm Co/CoO particles deposited on native Si(001) substrates. All samples were cooled in an in-plane applied field of B = 5 T from a temperature above $T_N = 293K$ of the antiferromagnetic CoO shell to 10 K. FC hysteresis loops were taken with increasing temperature. The solid line is a fit according $H_{EB}(T) = H_{EB}(0\mathrm{K})\left(1 - T/T_B^{AFM}\right)^{\mathrm{n}}$ with n = 3.2 and $H_{EB}(0\mathrm{K}) = 0.49$ T.

More detailed investigations for the 13 nm particles have been published elsewhere [42,60, 134]. For example, the ratio of remanent-to-saturation magnetization M_{rem}/M_S is influenced by the exchange anisotropy. At low temperatures ZFC hysteresis loops show small values of the remanent magnetization. The ratio M_{rem}/M_S at 4 T is 0.17 at 5 K; it increases with increasing temperature, reaches the maximum value of 0.45 at 80 K and decreases with further increasing temperature. A similar behaviour of the ZFC magnetization was recently observed in an assembly of gas-phase prepared oxidized Co particles [133]. For an assembly of non-interacting randomly oriented particles $M_{rem}/M_S \approx 0.5$ is expected for uniaxial anisotropy and 0.7 for cubic four-fold anisotropy of the individual particle. For an array of interacting particles one can expect an increased M_{rem} in comparison to the case of non-interacting particles. The 13 nm Co/CoO particles have an approximately 9 nm ferromagnetic Co core. The particles are surrounded by a $\approx$ 2 nm thick organic molecules (surfactant) shell. Thus, the particle cores are separated by a $\approx$ 10 nm thick layer of non-ferromagnetic materials. Dipolar interaction plays no significant role when the sample is cooled in zero field. The 8 nm Co core is ferromagnetic and provides a local magnetic field to its CoO shell during ZFC process. Unidirectional exchange

anisotropy is induced in every particle. Due to the random orientation of the easy axes of the particle magnetizations, the exchange bias averages out. No hysteresis loop shift is observed, but the effective remanence of the nanoparticle assembly resulting from a summation over shifted hysteresis loops of individual particles is expected to be smaller than half of the saturation magnetization. In other words, in a ZFC sample unidirectional anisotropy is induced due to local magnetic fields produced by ferromagnetic Co cores. A decrease of the symmetry of the particle anisotropy results in a decrease of the ratio of the remanent to the saturation magnetization in an assembly of particles. With increasing temperature the unidirectional anisotropy decreases and the remanence approaches half of the saturation magnetization value typical of an assembly of nanoparticles with uniaxial magnetic anisotropy.

5.1.4. Magnetic Anisotropy

The magnetic anisotropy of the individual particles is the key parameter to understand the phenomenon of superparamagnetism of magnetic nanoparticles. From FMR information on the magnetic anisotropy energy density can be achieved with μeV resolution. However, the extraction of the energy barrier E_A which prevents the flipping of the magnetization is very complicated for interacting particles with randomly distributed anisotropy axes. Especially for core-shell particles like Co/CoO showing ferromagnetic order in the core and antiferromagnetic order in the shell below their ordering temperatures the determination of the temperature-dependent anisotropy energy density is not directly possible. On the other hand in certain temperature intervals some conclusions can be drawn assuming a very simplified picture.

In order to quantify the anisotropy of 9 nm Co/CoO particles, temperature-dependent FMR at 9.24 GHz was measured. In the upper panel of Figure 5.12 the temperature dependence of the resonance fields B_{res} in parallel configuration is shown. A monotonous increase of B_{res} from about 50 mT to 270 mT is observed. At T = 120 K $B_{res}(T)$ shows a kink above which the resonance field increases stronger with temperature. At around 300 K the resonance field saturates around 270 mT. The correspondent measurements in normal configuration (not shown here) exhibit a similar temperature dependence. The resonance fields at temperatures below 150 K coincide within the error bar of 10 mT. At higher temperatures a slight difference between parallel and normal configurations has been observed on the order of 70 mT which can be understood in terms of an effective magnetization M_{eff} of quasi 2D superparamagnetic particle ensembles (section 5.1.2).

To determine the average anisotropy field B_A of single nanoparticles the FMR relation for arbitrary angles of the external field with respect to the anisotropy axes (equation 2.9) must be

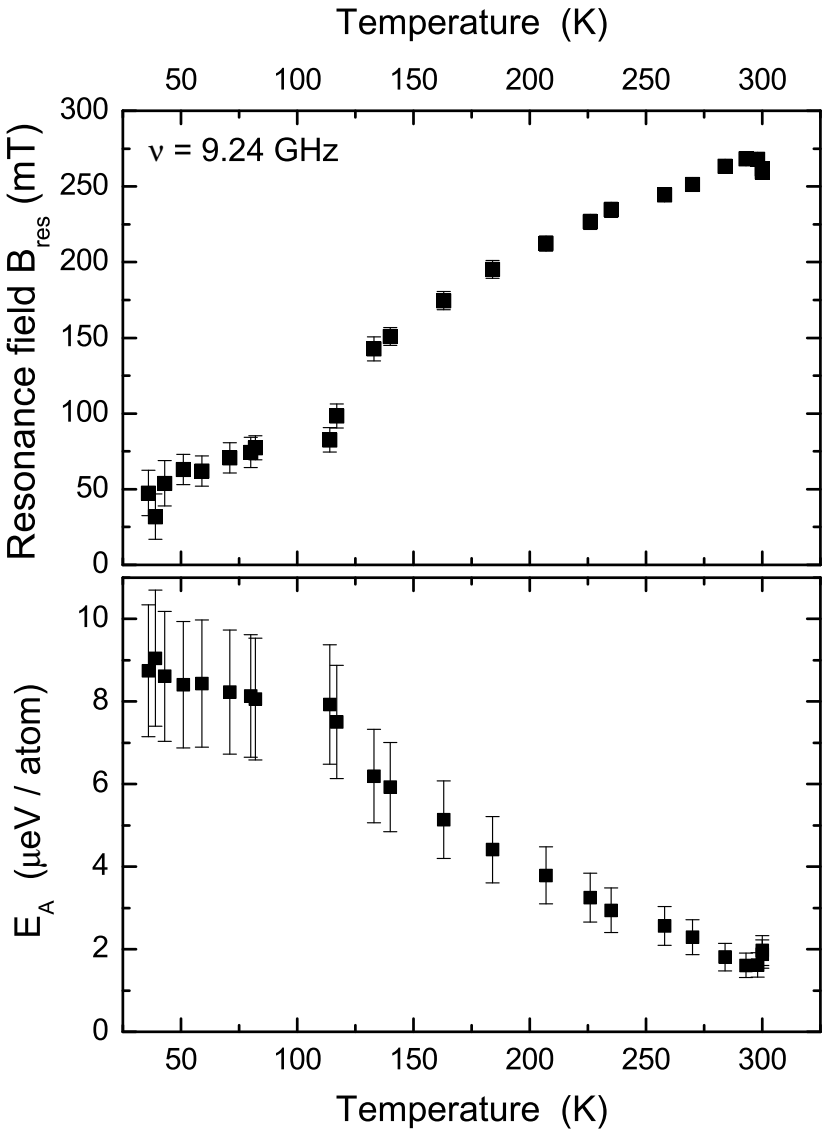

Figure 5.12.: Temperature dependence of the resonance fields B_{res} for the 9 nm Co/CoO particles in parallel geometry measured at a microwave frequency of 9.24 GHz (upper panel). In the lower panel the anisotropy energy density on a per atom basis is given as deduced from the model described in chapter 2. The figure has been adapted from [60].

used. In equation 2.10 the experimental B_{res} and the gyromagnetic ratio ω/γ (section 5.1.2) enter the resonance condition. The anisotropy energy E_A of a nanoparticle is given by $B_A = 2\mu_0 E_A/\mu_P$ with μ_P being the total particle magnetic moment. The result of this scaling is given in the lower panel of Figure 5.12 normalized to the number of atoms per particle contributing to the FMR signal. Starting from $E_A = 9$ μeV/atom at T = 40 K a monotonic decrease is revealed towards higher temperatures. At T = 300 K E_A has reached a value of 2 μeV/atom.

Strictly speaking this evaluation is only valid as long as (i) interactions between particles are small, (ii) the CoO shell does not change its magnetic properties with temperature, and (iii) $T_C \gg T_B$. The first point is nearly fulfilled since the particle's dipolar interactions has been estimated being on the order of $E_{dip}/k_B \approx 23$ K [135]. To account for the CoO shell the first layer of CoO surrounding the metallic Co core has been included in the calculation. However, ZFC/FC hysteresis loops have shown that below a field cooling temperature of T_{FC} = 120 - 150 K exchange bias appears, definitely changing the magnetic response of the metallic core (section 5.1.3). This effect is not taken into account here. The magnetic anisotropy of ligand-free Co particles without a CoO shell is $E_A = 1.5$ μeV/atom at 15 K found by micromagnetic simulations (chapter 6.2). The 6 times larger anisotropy of Co/CoO core-shell particles is attributed to the exchange coupling between ferromagnetic Co core and the antiferromagnetic CoO shell.

Furthermore, the comparison to the anisotropy energy density of hcp Co which is 65 μeV/atom in the bulk at T = 0 K shows once more that the inner part of the particles exhibits an fcc-like ordering of the Co atoms leading to a much smaller value of E_A.

5.1.5. Magnetization Dynamics

Magnetic relaxation and the magnetization dynamics have become an intensively studied subject in the last years. Both, the development of ultrafast (fs-ps) probing techniques and the demand of the detailed understanding of reversal mechanisms of the magnetization for designing fast-switching devices drives the ongoing research. As described in chapter 2 FMR is a technique that probes the precession of the magnetization around the effective field axis in a time window of nanoseconds (GHz frequency). The relaxation of the sample magnetization is described by the relaxation term in the Landau-Lifshitz-Gilbert equation (eq. 2.3). From the frequency dependence of the peak-to-peak linewidth ΔB_{pp} one can distinguish between different relaxation mechanisms [28,79]: (i) intrinsic relaxation due to magnon-magnon or magnon-phonon interaction and (ii) relaxation due to magnetic inhomogeneities in the nanomagnet. Accordingly, the FMR linewidth ΔB_{pp} can be split up in a frequency-dependent contribution ΔB_{hom} which is described by equation 2.3 and an inhomogeneous broadening ΔB_{inhom}

$$\Delta B_{pp} = \Delta B_{hom} + \Delta B_{inhom} = \frac{2}{\sqrt{3}}\frac{\alpha}{\gamma}\omega + \Delta B_{inhom}. \tag{5.3}$$

The first term on the right hand side is linear in frequency while the second is frequency-independent. Thus, both contributions can be extracted from a multifrequency FMR experiment.

Figure 5.13 shows the frequency dependence of the linewidth ΔB_{pp} of the nominally 11 nm Co/CoO particles deposited on manganin substrate. The FMR absorption spectra were fitted by

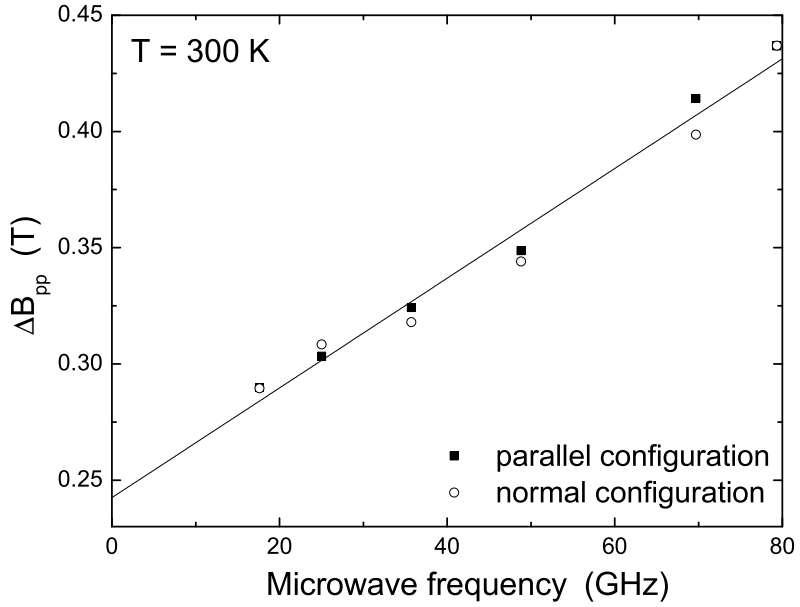

Figure 5.13.: Frequency dependence of the FMR linewidth of the 11 nm Co/CoO particles in parallel and normal configuration at 300 K. The particle ensemble is superparamagnetic but magnetostatically coupled. The solid line is a linear fit to all data points. The inhomogeneous linewidth is $\Delta B_{inhom} = 242$ mT. From the slope of the fit one finds the Gilbert damping parameter $G = 1.6$ GHz.

a Lorentzian line shape which does not perfectly fit the experimental data. A Gaussian line shape fitting, however, produces much larger deviations to the experiments. Experiments in parallel and normal configuration at T = 300 K (superparamagnetic) show clearly a linear dependence. Within the error bar the evolution with frequency does not depend on the measuring geometry. This finding predicts an isotropic g-factor [28] of the array of particles supporting the results discussed in section 5.1.2. A single linear fit of the linewidth ΔB_{pp} as a function of frequency of both, parallel and normal configuration, yield an inhomogeneous part of the linewidth 242 ± 10 mT and a slope of 2.36 ± 0.11 mT/GHz. From the slope the damping parameter $\alpha = 0.063 \pm 0.003$ can be calculated. Using the relation $G = \alpha\gamma M$ one finds a Gilbert damping parameter of $G = 1.6$ GHz. Here, M is set to the bulk magnetization of Co of 1.75 T.

The inhomogeneous part of the linewidth ΔB_{inhom} is found strongly enhanced compared to bulk fcc Co $\Delta B_{inhom} = 7.2$ mT [136] and $\Delta B_{inhom} = 0.5$ mT for a 10 monolayer fcc Co film sandwiched in Cu $(20Au/10Cu/10Co/Cu(001))$ [137]. Moreover, recent results on non-interacting 4 nm $CoPt_3$ nanoparticles [138] examined in the isotropic superparamagnetic regime have shown that $\Delta B_{inhom} \approx 15$ mT. Thus, it seems unlikely that the enormous increase of ΔB_{inhom} in Co/CoO particles is due to the finite size of the particles. The experiments

were carried out at room temperature, only a few Kelvin above the irreversibility point of the ZFC/FC magnetization of the particle ensemble ($T_B \approx 290$ K). The FMR linewidth at a phase transition from an ordered to disordered state (e. g. ferromagnetic/paramagnetic or ferromagnetic/superparamagnetic) show an maximum around the temperature of the phase transition. Moreover, the superparamagnetism might be anisotropic and the particles are magnetostatically coupled. Variations of the easy axes of magnetization increase ΔB_{inhom} at this temperature. At higher temperatures the isotropic superparamagnetic regime is reached and particle interactions play a minor role. In summary, from the inhomogeneous part of the FMR linewidth one cannot conclude that the particles are magnetically inhomogeneous. Frequency-dependent measurements at higher and lower temperatures and larger interparticle distance are needed to exclude the effect of an anisotropic superparamagnetism of magnetostatic interactions.

The homogeneous part of ΔB_{pp} follows the linear law described by the Landau-Lifshitz-Gilbert equation. The observed damping parameter $G = 1.6$ GHz is much larger than for bulk fcc Co ($G = 0.1$ GHz) [136] or a 10 monolayer sandwiched Co film ($G = 0.3$ GHz) [137]. Moreover, detailed investigations of the switching behavior of single 20 nm hcp Co particles show damping parameters of up to 1.3 GHz [139]. Besides the possible increase of the FMR linewidth by the inspection close to the irreversibility point of ZFC/FC magnetization of the particle ensemble, one may conclude from the experiments that the magnitude of damping depends on the dimensionality of the studied system. Nanoparticles show the largest relaxation rate while in ultrathin films a gradual decrease of G towards the bulk is observed. The variation of ΔB_{hom} by more than one order of magnitude is probably caused by the differences in the spin structure. In ultrathin films surface moments play an important role while in nanoparticles additionally the shape influences the spin orientations. Nanoparticles may easily relax their motion of magnetization at imperfectly aligned moments at the surface or interface with respect to the nanoparticle core. One may note that for Co/CoO particles the magnetization most probably relaxes at the interface superparamagnetic core/paramagnetic shell. However, a detailed understanding of relaxation mechanisms can only be achieved by temperature-dependent measurements at least two microwave frequencies in the ferromagnetic and isotropic superparamagnetic regime which has not been conducted, yet.

5.1.6. Nanoparticle Aging

Most structural and magnetic characterization techniques such as TEM, SEM, FMR, or XMCD demand the deposition of the nanoparticles on flat substrates. For this purpose the particle solution was put on the appropriate substrate and the organic solvent was let to evaporate. After the

evaporation the samples were exposed (at least for a short time) to air. Thus, some additional oxidation might took place with time which is called "aging" in the following.

The nanoparticle aging has been investigated by FMR over a period of 18 months. Two independent samples have been examined by FMR at three different microwave frequencies. The samples were kept in air between the measurements. Figure 5.14 shows the effective magnetization fM_{eff} determined from FMR spectra in parallel and perpendicular geometry as a function of time after the sample preparation from concentrated, toluene-based 11 nm Co/CoO particle solution. The spectra taken within 1-3 h after the sample preparation reveal an effective magnetization fM_{eff} of about 110 mT found by measurements at three different frequencies. The error bar of fM_{eff} lies around 20% indicated by the bars in Figure 5.14. Within the first three weeks after sample preparation a strong decrease of fM_{eff} to 60-70 mT is observed. Thus, the oxidation initially proceeds quite fast, and slows down at longer times of air exposure (Figure 5.14). The g-factor determination presented in section 5.1.2 has been conducted in this later

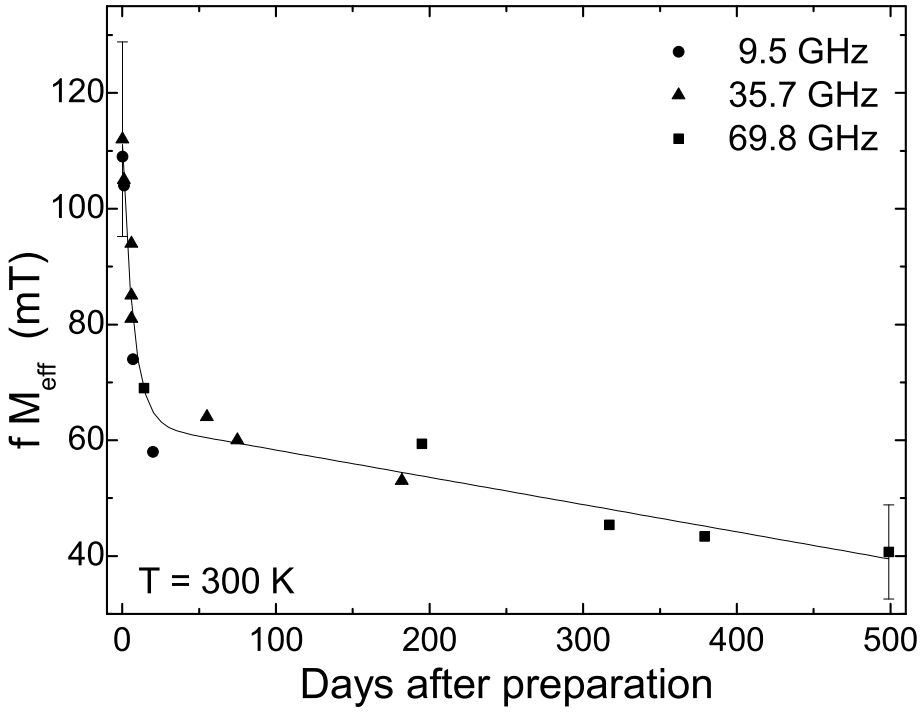

Figure 5.14.: Effective Magnetization fM_{eff} of the 11 nm Co/CoO particles as a function of time after the preparation of the samples. The samples were kept in ambient conditions. fM_{eff} has been determined from FMR spectra at parallel and perpendicular configurations at three different frequencies. The line is a guide to the eye. The figure has been adapted from [60].

period of time to exclude influences of fM_{eff} on the g-factor analysis. The line in Figure 5.14 is a guide to the eye.

The experimentally determined effective magnetization fM_{eff} can be translated to a metallic Co core diameter using several assumptions. It should be emphasized that in principle an FMR setup can detect a resonance signal of CoO which is paramagnetic at room temperature, but, however, the signal is expected much smaller than the resonance signal of ferromagnetically coupled Co moments in the core of each superparamagnetic particle as discussed in section 5.1.2. Here, however, no hints of a paramagnetic CoO signal were found. Thus, fM_{eff} can be attributed to the metallic Co core alone. Using the crude assumption of a bulk-like Co magnetization[1] $M_{eff} = 1.75$ T of the Co core a simple scaling of fM_{eff} to the bulk values becomes possible. The volumetric filling factor f can be calculated from TEM images. Directly after the sample preparation the filling factor of metallic Co was found to decrease from $f = 6.4\%$ to $f = 2.3\%$ after 18 months. The relative scaling factor f can now be transformed into an equivalent Co core diameter of Co/CoO particles by scaling to the standard volume of a nanoparticle including the organic ligands.

Assuming a densely-packed (fcc) 3D superlattice of particles with the superlattice filling factor $F_{SL} = 0.74$ and the average center-to-center distance d_{cc} of 15.9 nm determined by TEM of the nominally 11 nm Co/CoO particles one calculates the standard volume of a single particle to

$$V_S = \frac{\pi}{6F_{SL}} d_{cc}^3 = 2844 \text{ nm}^3. \tag{5.4}$$

One should note that this calculation reflects the minimum standard volume of a single particle. The superlattice filling factor F_{SL} might be reduced by imperfect ordering or an excess of ligands in the sample and thus the standard volume of a single particle increases. By simple multiplication $V_S \cdot f$ one obtains the volume from which the FMR signal is generated. The result of this calculation is shown in Figure 5.15. Spherical particles of identical diameter are assumed here. Directly after the sample preparation a Co core diameter of 7 nm is found which decreases rapidly to 6 nm after three weeks. Afterwards, the Co core diameter decreases very slowly with time. The formation of a well-passivating CoO shell is evident. One should note that the slow decrease after the fast creation of a passivating CoO shell within the first weeks can be explained by assuming a further oxidation of only a few atoms/day, as one has to recall that the whole number of atoms within a 5 nm Co particle core is only on the order of 6000. 18 months after sample preparation the model suggests a remaining Co core diameter of 5 nm that corresponds to a CoO layer thickness of 3.2 nm. Besides the possible systematic error of

[1] $M_{eff} = 1.75$ T is equivalent to the bulk magnetization of 1400 kA/m. The conversion is due to the crossover from one SI system $B = \mu_0(H + M)$ to another $B = \mu_0 H + M$ [140].

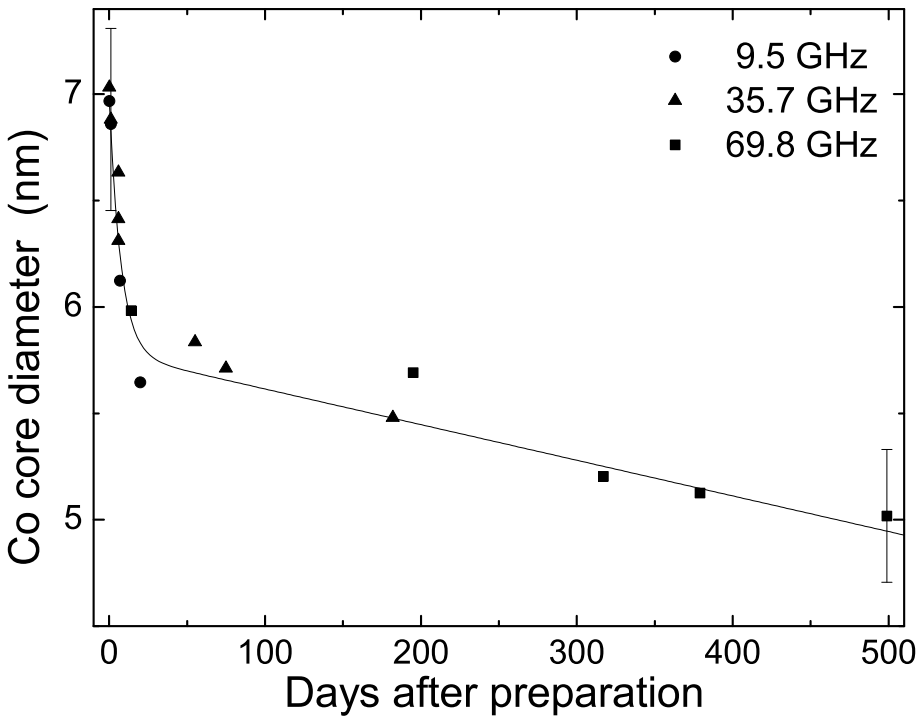

Figure 5.15.: Effective Co core diameter of the 11 nm Co/CoO particles as a function of time after preparation of the sample from concentrated solution. The diameter is scaled from the effective magnetization fM_{eff} using the fcc bulk magnetization of 1.75 T. The line is a guide to the eye. The figure has been adapted from [60].

the superlattice filling factor F_{SL} the error bar is on the order of 0.5 nm indicated by the bars in Figure 5.15. The error is mainly due to the fM_{eff} determination by FMR experiments.

The HR-TEM EELS measurements in Figure 4.4 show a CoO layer thickness of 2-2.5 nm and a core diameter of 6.5-7.5 nm. These particles have been investigated two weeks after the deposition on the TEM grid. The further oxidation after the deposition on a substrate is found less dramatic than the fM_{eff} scaling suggests. Probably the disagreement is due an overestimation of the superlattice filling factor F_{SL}. Experimental data of F_{SL} is not available for 3D self-assembled structures investigated by FMR. Nevertheless the scaling of the effective magnetization provides the possibility of an indirect measurement of the FMR "active" Co core diameter by simple FMR experiments. The reliability of the method used here is supported by the fact that the model fits to the data obtained at different microwave frequencies.

5.2. Collective Phenomena

The magnetic response of regular array of stripes consisting of 11 nm Co/CoO particles is discussed in this section. As shown in section 4.2 the magnetophoretic deposition technique can be employed to form a regular array of stripes on a carbon-coated Cu grid (Figure 4.8). This array of stripes has been investigated by FMR at 9.51 GHz and T = 300 K directly after the particle deposition. Full azimuthal and polar angular dependencies were taken. The results of these experiments are shown in Figure 5.16. For in-plane measurements the azimuthal angle ϕ_B is measured from the direction parallel to the stripes. The polar angle θ_B is measured from the normal to the sample plane. The lowest resonance field found at $B_{res} = 0.233$ T is observed in the film plane parallel to the stripes. It is smaller than the paramagnetic resonance field $\omega/\gamma = 0.3085$ T, which shows that an intrinsic magnetic field due to an effective magnetization M_{eff} is present in the sample. The easy axis of magnetization is found in the film plane parallel to the stripes. In the analysis of the obtained angular dependencies one has to consider three origins of the anisotropy field: (i) the shape anisotropy due to the stripe structure, (ii) configurational magnetic anisotropy originating from magnetostatic interactions between particles within the fcc superlattice inside the stripes, and (iii) the effective magnetic anisotropy of the individual particles. The latter includes shape, volume, and surface contributions as discussed in the last section.

In a first step, it is assumed that all anisotropies produced by spin-orbit coupling vanish due to the random orientation of individual anisotropy axes. Consequently only shape anisotropy is present. Moreover, the shape of an individual particle is assumed to be spherical. In this case equation 2.9 reads for $\theta = \psi = 0$ (normal configuration and sufficiently strong external magnetic field to rotate the magnetization into the direction of the external field):

$$\left(\frac{\omega}{\gamma}\right)^2 = [B_{res} - f(N_z - N_x)M_{eff}(B_{res})] \times [B_{res} - f(N_z - N_y)M_{eff}(B_{res})]\,. \qquad (5.5)$$

The anisotropy field B_A from equation 2.9 is here replaced by the effective magnetization M_{eff}, the volumetric filling factor f and the demagnetization factors N_x, N_y, and N_z along the axes of an ellipsoid. The filling factor within the stripes is $f = 0.31$ [127]. The demagnetization factors ($N_x = 0.005$, $N_y = 0.095$, and $N_z = 0.9$) are calculated assuming an ellipsoidal shape of the stripes in a first approximation [34]. The semi axes of the ellipsoid are $l_x = 1000$ nm, $l_y = 125$ nm, and $l_z = 20$ nm. These dimensions correspond to the average ones of the stripes as determined by TEM. It turns out that the observed angular dependence of $B_{res}(\phi_B, \theta_B)$ cannot be described by the shape anisotropy of the stripes alone [127]. Other contributions to the total magnetic anisotropy must exist in the investigated sample.

Consequently, an alternative approach is used to fit the angular dependencies of the FMR resonance field which includes spin-orbit driven anisotropies. The resonance condition of a homogeneous thin film with cubic symmetry and an additional in-plane uniaxial anisotropy that includes the small in-plane shape anisotropy ($N_x, N_y << N_z \approx 1$) is employed in the case of the azimuthal angular dependence of the FMR resonance field [141]:

$$\left(\frac{\omega}{\gamma}\right)^2 = \left[B_{res} + 2B_{an}^{4\|}\cos 4\phi - B_{an}^{2\|}\cos\left(2(\phi-\phi_u)\right)\right] \times$$
$$\times \left[B_{res} + B_{eff} + B_{an}^{4\|}(2-\sin^2(2\phi)) - B_{an}^{2\|}\cos^2(\phi-\phi_u)\right]. \quad (5.6)$$

Resonance is observed at the magnetic field B_{res} which depends on the equilibrium angle of the magnetization $M(B)$ and the angle of the external magnetic field B with respect to the axis of uniaxial in-plane anisotropy. $B_{an}^{2\|}$ is an effective in-plane uniaxial anisotropy field and $B_{an}^{4\|}$ is a fourfold in-plane anisotropy field. The effective anisotropy field is defined as $B_{eff} = (-2K_{2\perp}/M_S) + f \cdot M_S$ with the perpendicular anisotropy energy $K_{2\perp}$, the volumetric filling factor f of the stripes and the bulk-like saturation magnetization M_S of individual Co/CoO nanoparticles. In Figure 5.16 (a) the best fit (solid line) to the experimental data is shown. The fit according to equation 5.6 yields $B_{an}^{4\|} = 0$ T, $B_{eff} = 0.127$ T, and $B_{an}^{2\|} = 0.037$ T. These results yield that any cubic contribution is absent and only an in-plane uniaxial anisotropy is present.

Figure 5.16 (b) shows the polar angular dependence of B_{res} when the external dc field is rotated in a plane normal to the film plane starting parallel to the in-plane easy axis ($\phi_B = 0°$). Note that $B_{res}(\phi_B = 0°)$ of Figure 5.16 (a) is identical to $B_{res}(\theta_B = 90°)$ in Figure 5.16 (b). The resonance condition

$$\left(\frac{\omega}{\gamma}\right)^2 = [B_{res}\cos(\theta-\theta_B) - B_{eff}\cos(2\theta)] \times \left[B_{res}\cos(\theta-\theta_B) - B_{eff}\cos^2\theta + B_{an}^{2\|}\right] \quad (5.7)$$

yields $B_{eff} = 0.13$ T and $B_{an}^{2\|} = 0.037$ T. Once more, an excellent fit is obtained with the identical $B_{an}^{2\|}$ without the need to include fourth-order contributions. This uniaxial anisotropy is the result of shape anisotropy of the stripes and a possible alignment of crystalline anisotropy axes of the individual crystals. B_{eff} cannot be explained by assuming a bulk-like magnetization per particle ($M_S = 1400$ kA/m = 1.75 T) alone. The Co volume fraction f inside the stripes is about 0.31 (12 nm diameter Co particles ordered in fcc structure with the nearest-neighbor distance of about 16 nm) and the stripes cover about 40% of the substrate. This yields the smallest possible average magnetization $f \cdot M_S = 0.222$ T which is still larger than B_{eff} obtained from the FMR analysis. To explain the difference one has to include a perpendicular anisotropy field $2K_{2\perp}/M_S$ and/or the existence of antiferromagnetic CoO layers at the particle

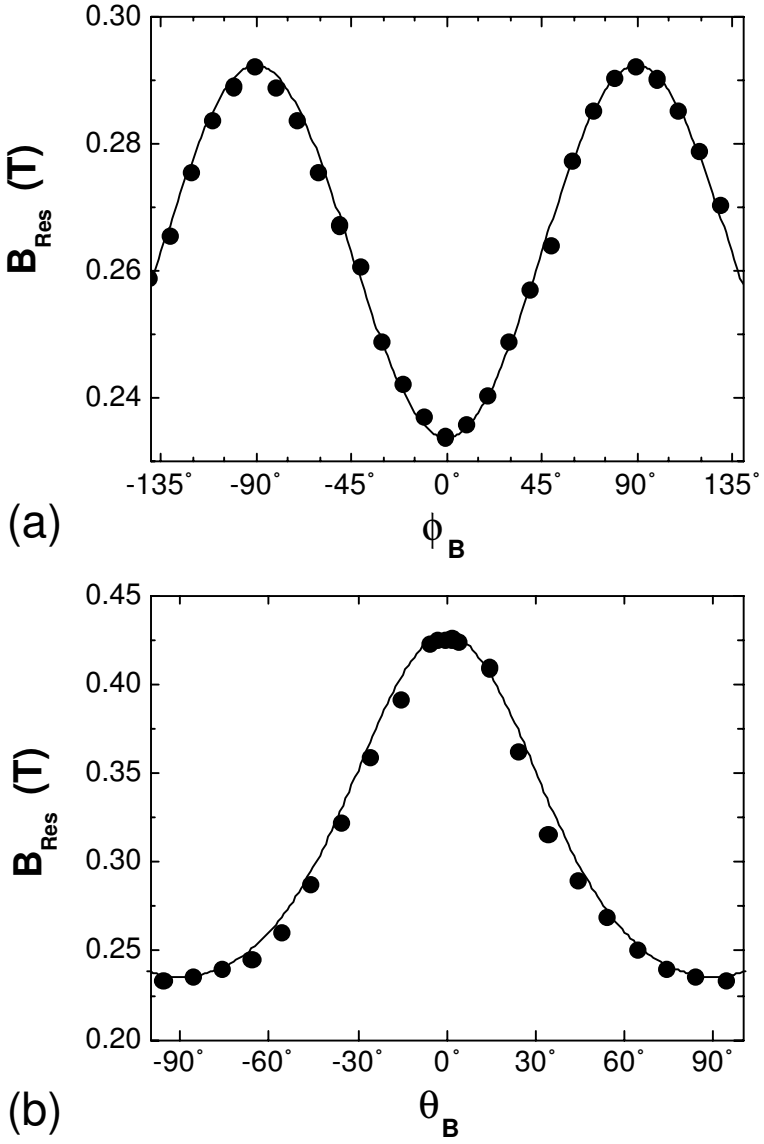

Figure 5.16.: Dependence of the resonance field B_{res} on the direction of the external magnetic field: (a) in-plane angular dependence ϕ_B (measured from the stripe's longest axis) and (b) out-of-plane angular dependence θ_B (measured from the normal to the sample). The error bar is on the order of the symbol size. The full lines are fits as described in the text. The figure has been adapted from [127].

surface which reduces M_S. As discussed throughout this thesis the CoO shell is present in all particles.

To gain further insights into the origin of B_{eff} remanent magnetization measurements have been performed using a home-built HTS-SQUID magnetometer in ambient conditions (not shown). The details of the apparatus have been presented in [142]. Before the SQUID measurement the sample was magnetized at 1.3 T parallel to the stripes. The magnetic stray field

of the stripes can be precisely simulated by employing the model of an homogeneously magnetized film using the parameters sample area and thickness d, and the unknown magnetization M parallel to the stripes [127]. From the experiment one can conclude that firstly, an excellent agreement between experimental data and theoretical model is observed. This finding shows that the approximation of a quasi-continuous layer with an average magnetization is a very reasonable assumption in the FMR analysis. Secondly, the fit yields the remanent magnetization $M_{rem} = 0.059$ T. This is only 25% of the value one would expect for $f = 0.124$ when the nominally 11 nm diameter particle carries a bulk magnetic moment. If one assumes that a spherical outer shell of 2 nm thickness carries no net magnetic moment due to CoO formation, the reduced magnetization is quantitatively explained, since the volume of the inner metallic core ($\approx$ 7 nm diameter) is 29% of the volume of the shell. This estimate is obviously very crude, since it does not take temperature-dependent magnetic excitations and domain formation into account. Moreover, it is assumed that remanent and saturation magnetization are equal. With the experimental SQUID value M and $B_{eff} = 0.13$ T one can calculate M_S = 0.038 T and $K_{2\perp} \approx 1$ μeV/atom. This value is very small compared to bulk hcp Co, which can be explained by the cubic structure of the particles and the thermal excitations inherent to the dipolar coupled system close to its blocking temperature. Compared to the total magnetic anisotropy energy density (≈ 2 μeV/atom) of 9 nm particles arranged by droplet evaporation (section 5.1.4) both approaches yield reasonable agreement taking into account the crude assumptions.

In summary, the angular-dependent FMR analysis of an 2D self-assembled array of stripes consisting of 11 nm Co/CoO particles has been presented above. The magnetic response of the ordered stripes can be well approximated by assuming a homogeneously in-plane magnetized film with a volumetric filling factor f obtained by TEM analysis. Evidence for the loss of magnetization due to the about 2 nm thick shell around each particle is found by SQUID measurements. The magnetic anisotropy energy density has been found on the same order of magnitude as randomly oriented 9 nm particle array employing a different analysis approach.

6. Metallic Co Nanoparticles: Magnetic Dichroism and Micromagnetic Simulations

This chapter presents the results of the magnetic characterization of metallic Co particles after H and O plasma exposure. In section 4.3 the efficiency of the plasma treatment for particle reduction and removal of ligands has been described in detail. Here, the focus is set to the magnetic properties of the metallic particles. In section 6.1 the magnetic moment per atom of metallic particles surrounded by ligands and naked particles on native $Si(001)$ is conducted by means of magneto-optical sum-rules. The effective exchange interaction in a double layer of metallic Co particles is studied in section 6.2. Element-specific hysteresis loops and detailed structural and morphological investigations (section 4.3) are used as input parameters for quantitative simulations using a Landau-Lifshitz-Gilbert equation based approach. The simulations allow to determine (i) the effective magnetic anisotropy energy density and (ii) the effective exchange interaction between bottom and top layer particles touching each other.

6.1. Magnetic Moment of Metallic Co Particles

In this section the magnetic magnetic moment of metallic Co nanoparticles is evaluated from XMCD investigations. The Co particles were examined (i) after the hydrogen reduction process and the full $H/O/H$ plasma cycle, and (ii) the effect of annealing on free metallic particles is presented.

The upper panel of Figure 6.1 presents the XAS white lines and the XMCD response of both, 8 nm metallic Co particles surrounded by modified ligands (H plasma exposure) and free metallic particles after the $H/O/H$ plasma cycle of the identical sample. The morphology of the sample has been discussed in section 4.3. The spectra were taken at normal incidence, in external fields of 1.5 and 1.25 T, respectively, and T = 15 K. XAS in the H plasma treated

state reveals a pure metallic character. A multiplet fine structure of CoO has not been detected. After further stepwise O and H plasma exposure the XAS response is found very similar to the H plasma treated state. However, small differences in the L_3 peak intensity are visible and a shoulder at the onset of the L_3 edge is evident (arrow in Figure 6.1). From these findings it is obvious that a small amount of Co in an oxidic environment remains in the particles after the $H/O/H$ plasma cycle. Simulations by XAS reference spectra (not shown) suggest a maximum amount of oxidic Co of 5%. The origin of CoO after the $H/O/H$ plasma cycle cannot be explicitly assigned to a distinct location in the particles. Since particles were arranged on a flat surface and the isotropic plasma acts in a top-bottom and outside-inside manner to the particles, most probably the small oxidic contribution originates at the lower side of the particles in contact to the substrate. At this position the H plasma cannot reduce the particles as efficiently as on the upper side. Moreover, the SEM imaging has shown that the particles are fixed to the substrate after ligand removal. The nature of this bond is unknown and cannot be detected by XAS in the TEY detection mode since (i) the number of bonds per particle is small and (ii) the contribution to the measured spectra is tiny due to the surface sensitivity of TEY detection mode. These considerations are supported by the XMCD signals as discussed below. The comparison of the measured XAS spectra to the one of a bulk-like Co film [91] shows an additional small shoulder about 0.6 eV after the L_3 peak position. This small feature is assigned to hydrogen loading of the particles during the plasma reduction.

The XMCD signals of metallic Co particles with and without ligands coincide within the experimental error bar in the whole spectral range (Figure 6.1). In both cases the external field is sufficient to fully saturate the sample as shown by the hysteresis loops in the lower panel of Figure 6.1. The white line intensity after step function substraction enters the determination of the orbital and spin moments as a measure of unoccupied states above the Fermi level (section 2.2). However, the difference of the L_3 peak intensities only leads to a tiny difference of the magnetic moments as shown in Table 6.1. The orbital moment per 3d hole n_h is determined to $\mu_L/n_h = 0.05\ (0.06)\ \mu_B$ for the ligand surrounded (free) Co particles. The spin moment shows a magnitude of $\mu_S/n_h = 0.58 - 0.59\ \mu_B$. The total magnetic moment is $\mu_{tot}/n_h = 0.64\ \mu_B$ for both states of particle manipulation. The experimental error bar is estimated to be about 0.03 μ_B. The magnetic dipole moment is set to zero as suggested for cubic symmetries [89]. Using the reported number of d-holes of bulk Co $n_h = 2.49$ [104] one finds a total magnetic moment $\mu_{tot} = \mu_L + \mu_S = 1.56\ \mu_B$ per atom that is remarkably reduced compared to the fcc bulk Co magnetic moment of 1.72 μ_B per atom. Self-absorption effects have not been taken into account so far. To explain the low total magnetic moment found in the experiments one has to consider two possible origins: (i) changes of the band structure by the plasma exposure which can not be due to oxygen, since pure metallic spectra have been observed. The only pos-

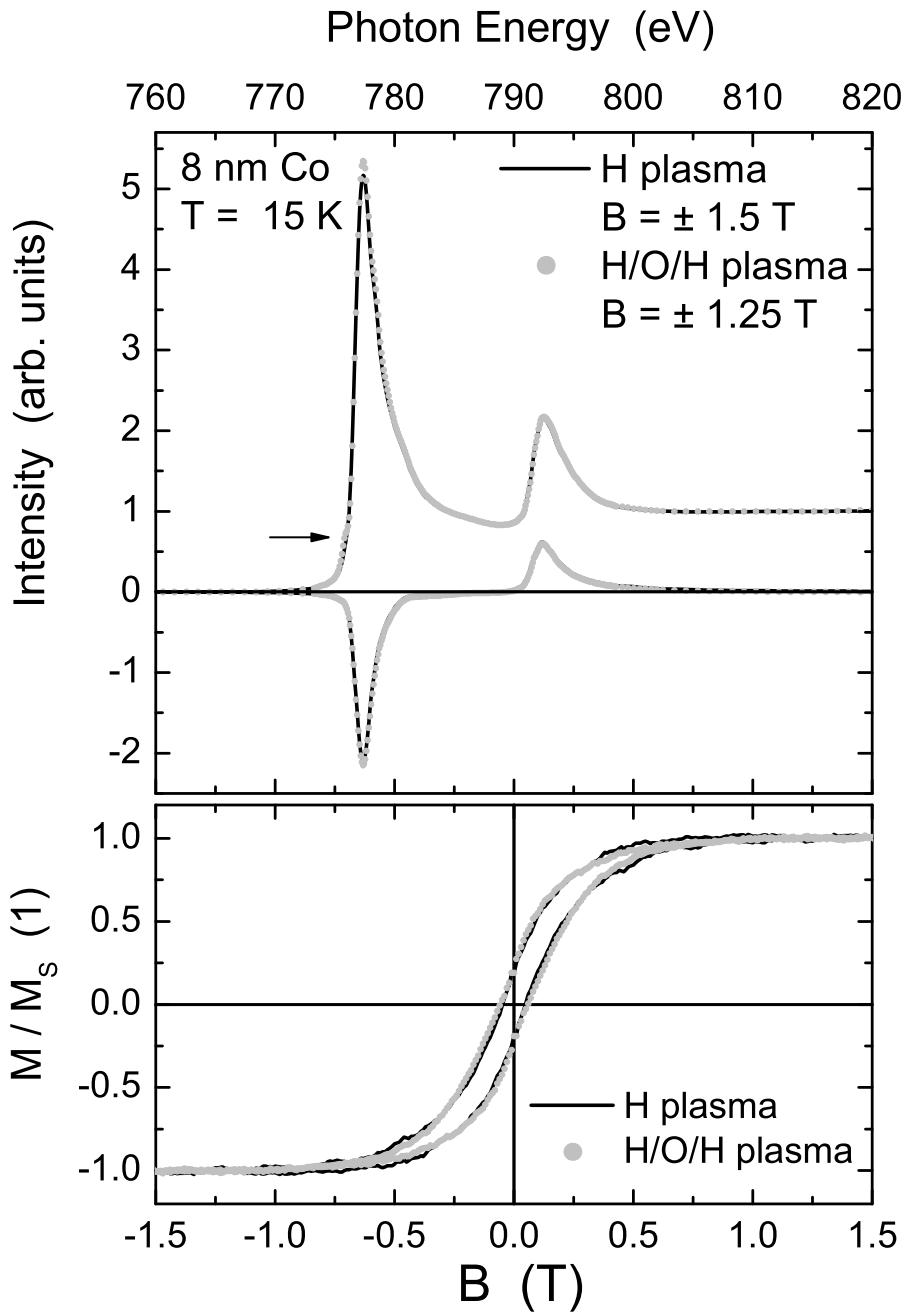

Figure 6.1.: The upper panel shows the XAS white lines and XMCD spectra of the initially 9.5 nm particles after 46 min H plasma reduction and after the complete H/O/H plasma cycle. The spectra were taken at normal incidence and T = 15 K. External fields of 1.5 T and 1.25 T were used, respectively. After the reduction process the particle diameter shrinks to about 8 nm (section 4.3). Details are given in the text. The lower panel shows the hysteresis loops of the particles in both states at normal incidence and T = 15 K. Saturation is reached at about 1 T.

sible origin is the deposition of hydrogen inside the particles as discussed below in terms of annealing experiments. (ii) the self-absorption in the nanoparticles (section 2.2). The latter is discussed first.

Model calculations for 10 nm metallic particles employing enhanced surface moments have shown that self-absorption reduces the apparent orbital μ_L and spin μ_S magnetic moments by 14% (μ_L) and 4% (μ_S), respectively [94,143]. The calculations are based on a bulk-like volume magnetic moment and a one monolayer thick surface layer exhibiting an 10% increase of the spin moment and a 100% increase of the orbital moment as found by theory and experiment for ultrathin films [93,144]. The apparent total magnetic moment detected by XMCD in the TEY mode is expected to be μ_{tot} = 1.68 μ_B. The results are also listed in Table 6.1. For smaller particles the simulations reveal a decreasing influence of self-absorption. The apparent reduction by self-absorption of the total magnetic moment for 8 nm particles is expected to be 0.03$\pm$0.01 μ_B. Thus, the experimental result of a lower magnetic moment than bulk fcc Co of plasma treated particles can partially be explained by the self-absorption in the special geometry of spherical particles. The large discrepancy of experimental and the expected bulk-like total magnetic moment of more than 0.1 μ_B, however, must be provoked by changes of the Co band structure.

In order to clarify the origin of the low magnetic moment an annealing experiment has

Table 6.1.: Magnetic moments of ligand stabilized and free metallic Co particles on Si(001). The separated magnetic moments per d-hole n_h are given. Using $n_h = 2.49$ [91] leads to a total magnetic moment $\mu_{tot} = 1.56\mu_B$. The ratios of orbital-to-spin magnetic moment are bulk-like. Here, no saturation effects are taken into account. Additionally, the results of model calculations including the self-absorption of 10 nm particles are given for direct comparison [143]. The details are discussed in the text. The coercive field and the remanent magnetization are also listed.

Quantity	8 nm ligand-stabilized Co particles on $Si(001)$	8 nm ligand-free Co particles on $Si(001)$	10 nm supported Co particles [143]
μ_L/n_h	0.04 μ_B	0.05 μ_B	0.05 μ_B
μ_S/n_h	0.59 μ_B	0.58 μ_B	0.62 μ_B
μ_L	0.10 μ_B	0.11 μ_B	0.13 μ_B
μ_S	1.46 μ_B	1.45 μ_B	1.55 μ_B
μ_{tot}	1.56 μ_B	1.56 μ_B	1.68 μ_B
μ_L/μ_S	0.07	0.08	0.08
$\mu_0 H_C$	49 mT	58 mT	-
M_{rem}/M_S	18%	23%	-

been performed to a spin-coated nanoparticle array. Nominally 9 nm Co/CoO particles were deposited at 4500 rotations per minute on native $Si(001)$. The sample was directly freed from the surrounding ligands by O plasma (0.1 mbar, 100 W, 5 min) and afterwards reduced by stepwise H plasma (0.1 mbar, 100 W, 35 min). In this state the specimen has been annealed (i) at T = 700 K for 8 min and (ii) the temperature was ramped to T = 950 K in 5 min and kept at constant temperature for another 5 min.

The XAS white lines of both states of sample manipulation after O/H plasma transformation and further annealing are shown in Figure 6.3. After O/H plasma exposure the $L_{3,2}$ peak amplitudes are found slightly reduced compared to the annealed state while the edge jump remains nearly constant. At both resonances of the non-annealed sample one finds shoulders at energies slightly higher than the peak position. These shoulders directly reveal a smear-out in the band structure of unoccupied 3d/4s states or their hybridizations above the Fermi level to higher energies compared to a pure bulk-like Co spectrum [89,91,145]. After annealing at T = 950 K these shoulders vanish and the shape of the spectrum reveals strong similarities compared to thin film reference data [91]. Although the spectral shape of O/H plasma exposed and the additionally annealed specimen is different, the integrals after removal of the continuum states only show an increase of the white line intensity of 2% which lies within the experimental error bar. Hence, the total number of holes above the Fermi level is nearly constant. Figure 6.3 also presents the XMCD difference spectrum of the annealed Co particle array taken at an angle of incidence of 30° with respect to the substrate plane, T = 15 K and B = $\pm$ 1 T. The latter is sufficient for reaching the saturation magnetization. The total magnetic moment and its orbital and spin part are independent of the incident angle of x-rays (normal and 60° off-normal) and temperature (15 K, 100 K). A total magnetic moment of $\mu_{tot} = 1.83 \pm 0.02\ \mu_B$ is found consisting of an orbital moment $\mu_L = 0.15 \pm 0.01\ \mu_B$ and a spin moment $\mu_S = 1.68 \pm 0.04\ \mu_B$ and $\mu_L/\mu_S = 0.09$. The number of d-holes is set to $n_h = 2.49$. Note that so far the nonlinear TEY response has not been taken into account. For 13 nm particles with a wide size distribution TEY simulations are not available. However, interpolation of the reported results [143] of 10 nm and 30 nm particles suggests a total magnetic moment of about $1.95 \pm 0.05\ \mu_B$. These calculations seem to overestimate the influence of the nonlinear TEY response due to self-absorption or the contribution of the surface layer carrying an enhanced magnetic moment since 2.0 nm particles show only a total magnetic moment of 1.9 μ_B [19]. A 13 nm ferromagnetic sphere consists of more than 100000 atoms and the ratio of surface-to-total number of atoms per particle decreases from 70% (2 nm) to about 10% (13 nm). Thus, a bulk-like magnetic moment is expected that is possibly slightly enhanced by the surface magnetism. Measurements of self-absorption in different systems are needed to verify the validity of the assumptions of the simulations described in section 2.2. On the other hand, it has been shown that the sampling depth in particles is lim-

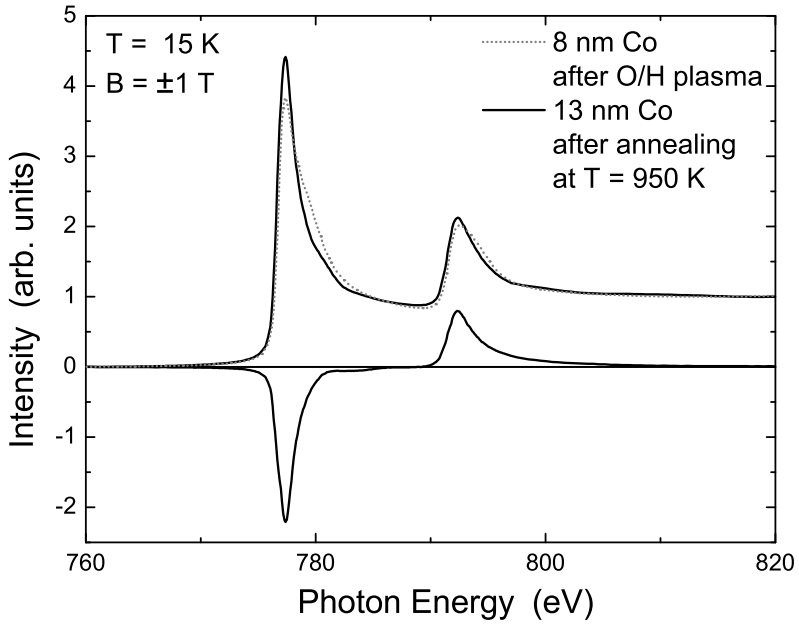

Figure 6.2.: XAS spectra of 8 nm Co particles after O/H plasma exposure (dots) and after annealing at T = 950 K for 5 min (line) of a similarly prepared sample. The spectra were taken at an angle of incidence of x-rays of 30° with respect to the sample plane. At the $L_{3,2}$ edges of the plasma exposed particles one finds shoulders at energies slightly higher than the resonance positions. The shoulder is assigned to hydrogen loading of the particles during the plasma exposure. After annealing the shoulders vanish. Additionally the XMCD spectrum after annealing is plotted.

ited to about 3-5 nm depending on the absorption coefficient. As a result, 10 nm and 13 nm particles should produce nearly identical partially-saturated TEY signals.

After XAS/XMCD characterization the sample was examined by SEM imaging which is discussed in the following. Figure 6.3 shows a large scale SEM image of the sample after plasma exposure and annealing. A homogeneous coverage is observed. The sample area that was examined by XAS with a spot size of about 1 mm^2 is as uniformly covered as shown in the SEM micrograph. Detailed investigations of the size distribution using high-resolution SEM images show a most probable diameter of 14.6 nm and a FWHM of 10.7 nm. The size distribution is best described by a Gaussian fit function. Obviously the particles grew during the plasma exposure and/or the annealing at T = 950 K. Moreover, the medium distance of particles is found irregularly enhanced compared to the $H/O/H$ plasma exposed sample. Since here only O/H plasmas were used to prepare free metallic particles it cannot by directly concluded that the annealing let the particles sinter. However, annealing at T = 950 K might admit sufficient thermal energy to activate a slight particle movement. Once they overcome the typical distance

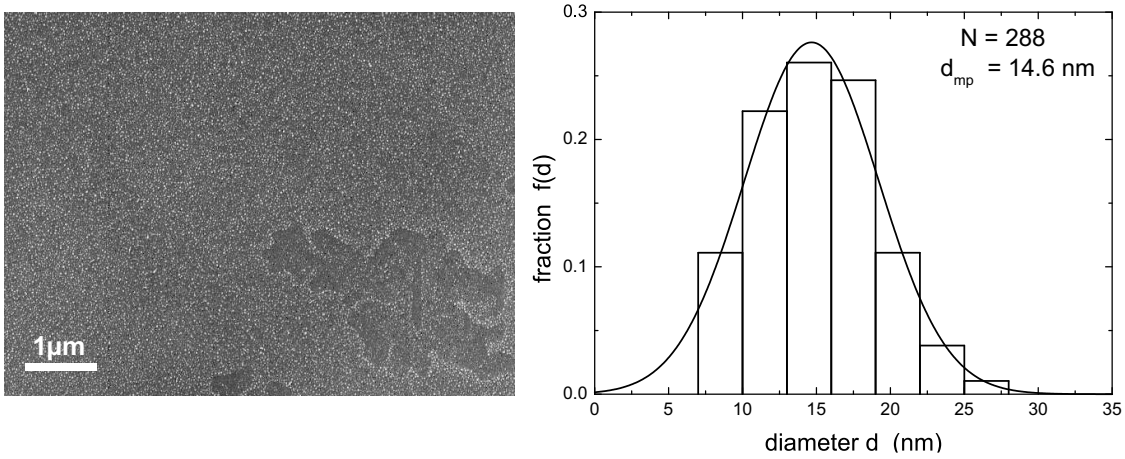

Figure 6.3.: The SEM image on the left shows a large area of Co particles after O/H plasma treatment and annealing at T = 950 K. Each light spot represents a single or a group of particles. For details see text. The right panel shows the corresponding size distribution. For sufficient statistics the diameters of 288 particles were measured. The particles show a most probable diameter of 14.6 nm and a broad size distribution (FWHM = 10.7 nm). High-resolution SEM images were employed for the size evaluation.

of about 3-4 nm the particles are free to sinter. One may note that the particle diameter in the metallic state is smaller than SEM suggests. Assuming the formation of a 3 nm CoO layer after storage for one week in ambient conditions one finds a medium diameter of about 13 nm pure Co particles on $Si(001)$ after O/H plasma treatment and annealing.

Element-specific hysteresis loops of the annealed particle array is presented in Figure 6.4 for normal and 60° off-normal angles of incidence of x-rays and directions of the external field at T = 15 K and 100 K. All hysteresis loops reached their saturation values below B = 1 T where the XMCD spectra have been taken. As expected, the easy direction of magnetization lies in the film plane. The experimental results for the coercive field and the remanent magnetization are listed in Table 6.2. From 15 K to 100 K the coercivity decreases from 53 mT (63 mT) to 30 mT (35 mT) when the external field is applied normal (60° off-normal) to the surface plane. The error bar of the external field determination is about 5 mT. Similar coercive fields and remanent magnetizations are found for the 13 nm O/H plasma exposed and annealed particles and the 8 nm $H/O/H$ plasma treated particles. The estimate of the anisotropy energy from the blocking temperature or the temperature dependence of the coercive fields is not possible since the temperature variation is restricted by the use of different cooling media (lHe or lN_2). Future micromagnetic simulations taking into account the sample morphology will extract the anisotropy energy of individual particles. This type of simulation is used in the next section for interpreting the hysteresis loops of a metallic particle array consisting of a double layer of particles.

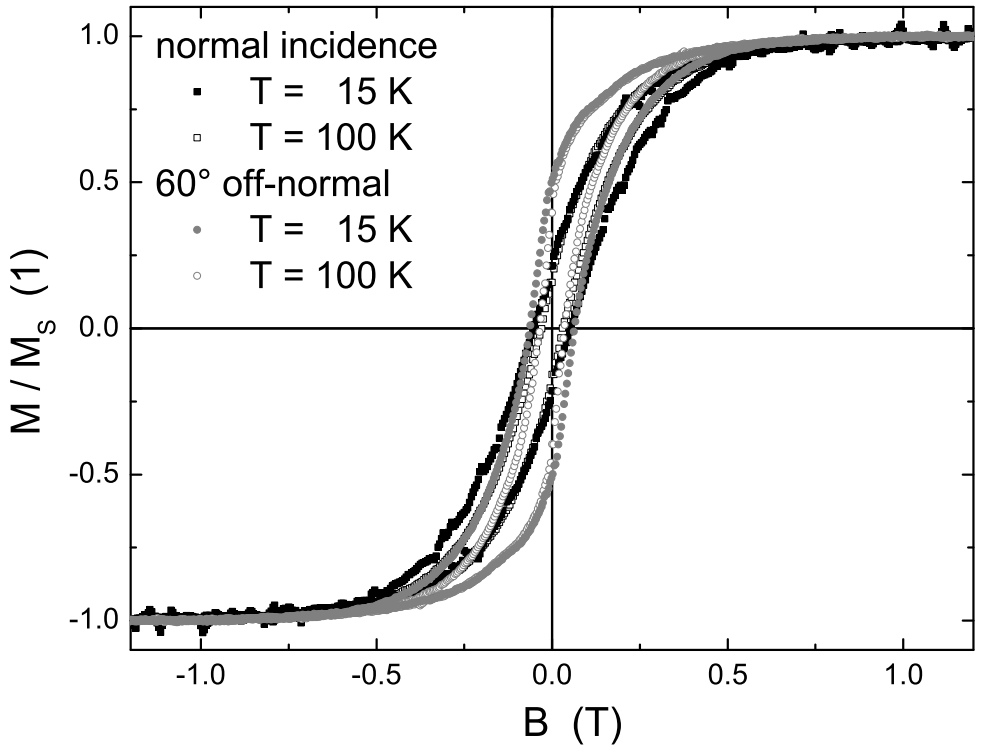

Figure 6.4.: Element-specific hysteresis loops taken at the Co L_3 energy position of maximum dichroic response of free metallic particles after annealing at T = 950 K for 5 min. The angles of incidence are 0° and 60° with respect to the sample normal. The observed coercive fields and remanent magnetizations are listed in Table 6.2.

Table 6.2.: Results of the element-specific hysteresis loops of 13 nm Co particles after O/H plasma exposure and annealing at T = 950 K. Coercive fields and the ratio of remanent-to-saturation magnetization are given for external fields applied normal (0°) and 60° off-normal with respect to the sample plane at T = 15 K and 100 K. For comparison, the results of the 8 nm particles are also listed.

Quantity	13 nm particles O/H plasma exposed and annealed				8 nm particles $H/O/H$ plasma exposed
Temperature	T = 15 K		T = 100 K		T = 15 K
Angle	0°	60°	0°	60°	0°
$\mu_0 H_C$	53 mT	63 mT	30 mT	35 mT	58 mT
M_{rem}/M_S	22%	51%	16 %	41%	23%

In summary, the element-specific examination of metallic particles reveals a slightly decreased magnetic moment while annealing experiments show an enhanced total magnetic moment compared to bulk fcc Co. This increase can be explained qualitatively by an enhanced total magnetic moment at the surface of the particles and the self-absorption in the TEY detection mode modifying the measured signal. The low magnetic moment of $H/O/H$ plasma exposed particles can only be assigned to hydrogen inclusion inside the particles. This phenomenon is discussed in the following.

Hydrogen solubility in bulk Co crystals at a ambient pressure is very low [146]. Under high H_2 gas pressure of up to 9 GPa a hcp Co crystal can be loaded with hydrogen forming CoH_x with $0 \leq x \leq 1$ [147]. It has been reported that hydrogen occupies interstitial sites and the hcp Co lattice remains nearly unaffected in the range $0 \leq x \leq 0.65$. For higher hydrogen content the fcc lattices structure is favored. In ambient conditions CoH is metastable. The hydrogen content reduces with time. The activation energy of H migration has been estimated to 200-250 K [147, 148]. In this thesis the presented experiments suggest the load of Co nanoparticles by hydrogen during the H plasma exposure. The sample is positioned far away from the intense plasma cloud. Only free radicals are let to reach the sample with maximum energies of 100-150 eV. The loading process has not been investigated in detail, yet. However, when all Co_3O_4 is reduced the excess supply of H radicals may form CoH_x with H contents dependent on the plasma conditions and exposure time. Since free radicals were used the H loading process is expected to be more efficient than experiments under high H_2 pressures. Addicted to the sample temperature and time period between plasma-assisted H load and the XAS experiments one expects CoH_x with different H contents. This can be seen at the XAS spectra of the two samples presented in Figure 6.1 and Figure 6.3. The high-energy shoulders of the $L_{3,2}$ resonances appear with different intensity. Here, a quantitative relation can not be drawn since the sample temperature during the transfer and the exact period of time before the sample is cooled to T = 15 K are unknown.

The influence of hydrogen on the magnetism of transition metals and alloys has been investigated with different elaborateness, e. g. in case of Fe and its alloys many experiments have been performed [149]. Generally, it is accepted that H transfers its electron - at least partly - to the host crystal. This charge transfer modifies the band structure by hybridization and increases the number of electrons in the 3d band. As a result, the Fermi-level is raised and the number of 3d holes decreases. Consequently, the total magnetic moment of hydrides are smaller than the one of the pure ferromagnetic material. For cobalt hydrides, however, only a few results have been published. Belash $et\ al.$ [147] reported for single and polycrystalline Co a reduction of the atomic magnetic moment of -0.36 μ_B per hydrogen atom. The reduction of the magnetic mo-

ment has been found to be linear with increasing H content in the range $0 \leq x \leq 0.9$. Adapting this result to the observed reduction of the total magnetic moment of 0.12 μ_B (Table 6.1) compared to the model calculations these studies suggest that $CoH_{0.33}$ has been investigated in the experiments presented in Figure 6.1.

In principle, the charge transfer from H to Co can be detected by changes of the white line intensity that measures the number of holes above the Fermi level. Additional 0.18 electrons per Co atom would cause a decrease of about 7% of the XAS white line intensity. The comparison of the white lines of O/H plasma exposed and annealed particles yields a reduction of only 2% for the CoH_x sample before annealing. Note that the particle diameter had changed by annealing. In case of $H/O/H$ plasma exposed particles annealing experiments have not been performed. The fully quantitative understanding of hydrogen load in Co nanoparticles would need a complete set of investigations as functions of time of the plasma exposure, annealing time, and annealing temperature. Band structure calculations may answer the questions of charge transfer and slight modifications of the band structure as proven by XAS experiments. These data are not available, yet. Qualitatively, similar behavior has been observed in H plasma treated micellar Co [20] and $FePt$ nanoparticles [150]. The detailed investigation of a decreasing magnetic moment as a function of hydrogen load in magnetic nanoparticles and thin films can be performed in our home laboratory, soon. SQUID magnetometry in UHV conditions is an adequate method to answer the open questions.

6.2. Effective Exchange Interaction

Magnetic interactions between particles in a ligand-stabilized array of nanoparticles are due to dipolar coupling only, since distances between nanoparticles (> 2 nm) are larger than the range of exchange interaction. When more than one monolayer of Co/CoO particles has been deposited on a substrate and the ligand shell is removed, e. g. by reactive plasma etching, laterally separated and normally touching particle arrays are prepared. Thus, an exchange coupling between the particles exists in a preferential orientation being directed normal to the substrate. The magnetic response, e. g. the hysteresis loops, should differ from one to the other. A two-dimensional particle array which only interacts via dipolar interaction has its easy axis of magnetization in the film plane. When an exchange interaction exists normal to the sample plane, one expects depending on the strength of exchange, i. e. the number of touching atoms, that (i) the effective magnetic anisotropy between parallel and normal orientation decreases and (ii) the easy axis of magnetization flips out-of-plane if the exchange anisotropy is stronger than the shape anisotropy favoring a in-plane alignment of magnetization of the array of nanoparticles.

In order to study this effect a Co particle array with 1.7 particle layers has been prepared (Figure 4.13) and successively exposed to a reactive plasma as discussed in section 4.3.2. Element-specific hysteresis loops using the XMCD signal were taken at angles of 0° and 60° with respect to the sample normal. In Figure 6.5 the experimental hysteresis loops are shown. The loops have been measured up to 1.5 T (≈ 1200 kA/m). The remanent magnetization at 60° is 47% and at 0° 5% of the saturation magnetization which is reached at about 0.6 T (≈ 480 kA/m). The coercitive fields H_C are $H_{C,60°} = 14$ mT (≈ 11 kA/m) and $H_{C,0°} = 20$ mT (≈ 16 kA/m), respectively. These fields are more than one order of magnitude smaller than the coercive field measured before the plasma treatment for Co/CoO core-shell nanoparticles, which reflects the strong influence of exchange anisotropy at the CoO/Co interface that magnetically hardens the particles.

The investigated quasi two-dimensional array of 1.7 layers of particles after the plasma exposure is shown in Figure 4.13. The magnetic hysteresis loop of a quasi two-dimensional array of interacting metallic particles cannot be described within easy models. Thus, micromagnetic

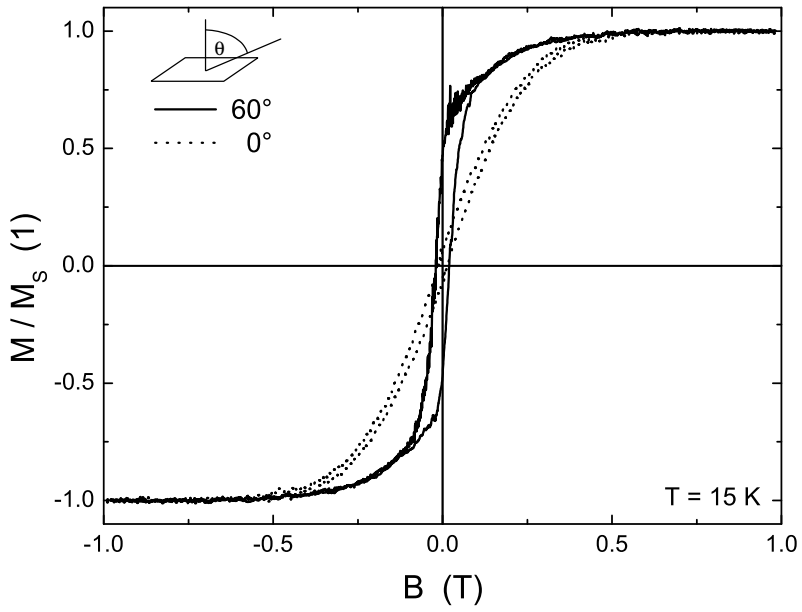

Figure 6.5.: Experimental hysteresis loops of the metallic Co particle array with a coverage of 1.7 layers of particles. A SEM image of the particle array is shown in Figure 4.13. The hysteresis loops were taken at external fields applied at angles of 0° (normal) and 60° with respect to the sample normal. The incident x-rays beam was parallel/antiparallel to the external field. The loops were taken at the maximum of the L_3 dichroic signal at 778 eV. It is obvious that an in-plane magnetization is favored by the nanoparticle array.

simulations have been performed taking into account the exact size, size distribution, separation, and morphology of the particles as determined from SEM (Figure 4.13) and AFM (Figure 4.14).

The system used in the simulations is shown in Figure 6.6. It consists of an array of 1600 particles positioned on a rectangular substrate plane. 1200 particles log-normally distributed in size with a mean diameter of 8 nm were randomly dropped on the substrate forming the bottom layer. The position of the particles was generated to simulate the packing density of the experimentally deposited array of the nominally 9 nm particles, followed by the reduction of the mean particle diameter to 8 nm corresponding to the plasma exposure experiments. In the second layer 400 particles with a coverage of just 70% were dropped one by one and left to fall until they get into contact with the particles in the bottom layer, finally reaching the 1.7 monolayer array (Figure 6.6) as suggested from the morphology of the experimentally examined sample. Hard spheres were assumed during the positioning. Particles in the top layer exhibit also a lognormal size distribution but, however, the mean volume is five times larger than the mean volume in the bottom layer, as observed experimentally.

For the micromagnetic simulations each particle has been attributed by its volume magnetization using the bulk value of the magnetic moment of 1.72 μ_B and the number of Co atoms

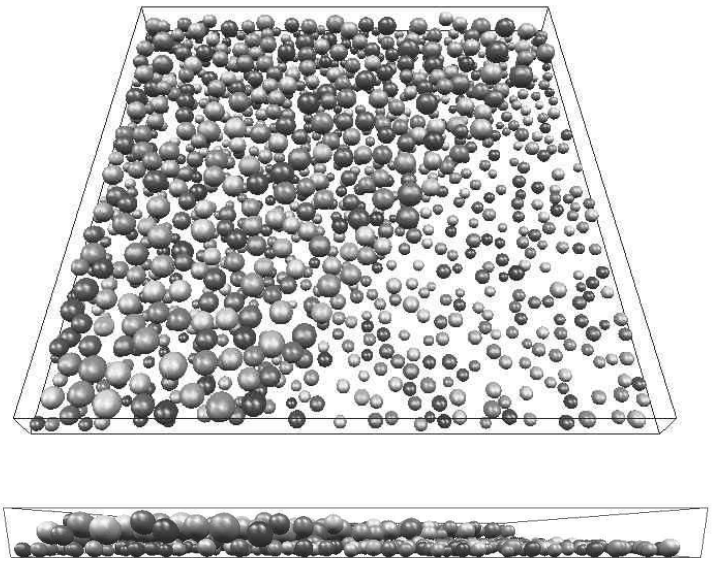

Figure 6.6.: Arrangement of particles used in the simulations. The array has been constructed according to the experimental observations by TEM, SEM, and AFM. The bottom layer has a filling factor of 41% and a mean diameter of 8 nm. The top layer has been built on 70% of the bottom layer by dropping particles having on average a five times larger volume than the ones of the bottom layer. The level of shading is proportional to the projection of the magnetic moment of each of the particles on the applied field direction. The figure has been adapted from [151].

per individual particle. The Landau-Lifshitz-Gilbert equation which describes the dynamics of the magnetization of a single entity when a magnetic field is applied has already been introduced in equation 2.3. The effective field $\vec{B}_{eff}$ is the sum of external, anisotropy and interaction fields [152]. To reduce the computation time to a reasonable value, the realistic assumptions are made that coherent rotation is the mechanism of reversal in each magnetic particle which is also considered to exhibit an uniaxial effective magnetic anisotropy. The equation has been solved for equilibrium considering that the field $\vec{B}_{eff}$ effectively applied to each particle is given by the interaction field and the external applied field $\vec{H}_{ext}$

$$\vec{B}_{eff} = \vec{B}_{ext} + \mu_0 \sum_{\substack{j=1-N \\ j>i}} \vec{H}_{ij} \tag{6.1}$$

with N the total number of particles in the simulated cell and

$$\vec{H}_{ij} = \frac{1}{4\pi} \left[\frac{3\left(\vec{\mu}_j \cdot \vec{r}_{ij}\right)\vec{r}_{ij}}{r_{ij}^5} - \frac{\vec{\mu}_j}{r_{ij}^3} \right] + C^* H_K \frac{\vec{\mu}_j}{|\vec{\mu}_j|} \tag{6.2}$$

the magnetic field in units of (A/m) produced by the particle j on the site of particle i [153], $\vec{\mu}_j$ is the vector magnetization of the particle in units of (Am^2). The position of the particle i with respect to particle j is given by the vector $\vec{r}_{ij}$. The second term on the right hand side in equation 6.2 is the so called exchange field where C^* is a phenomenological parameter which can be interpreted as being the result of the average interparticle exchange coupling due to the moments at the surface of the particles in contact with each other. H_K denotes the anisotropy field from which the uniaxial anisotropy constant K_2 can be calculated by the relation $H_K = 2K_2/\mu_0 M_S$ with the saturation magnetization M_S. Each particle interacts with its neighbors via magnetostatic fields that are situated within a range of four times the diameter of the particle. Exchange interaction is taken into account for particles in very close distance which can be considered as touching particles. Boundary free conditions have been used in the plane of the sample but not in the direction perpendicular to the sample plane, so that the geometry effect plays an important role in the simulations as well as in experiments.

In order to obtain information about the type of interaction in this system, several simulations have been performed considering a large range of magnetic anisotropies and only magnetostatic (dipole) interactions between the particles which is the case for well-separated particles. In Figure 6.7 simulations for the hysteresis loops at polar angles θ = 0° and 60° with respect to the sample normal are compared with the experimental ones for second order anisotropy constants of $K_2 = 2.0 \cdot 10^5$ J / m^3 and $K_2 = 0.2 \cdot 10^5$ J / m^3. The simulations are always performed for the two directions of the experimental hysteresis loops such that one set of parameters would have to fit both hysteresis loops measured at 0° and 60°. Considering only magnetostatic interactions ($C^* = 0$) the best possible fits were found for $K_2 = 0.2 \cdot 10^5$ J / m^3. However, it is

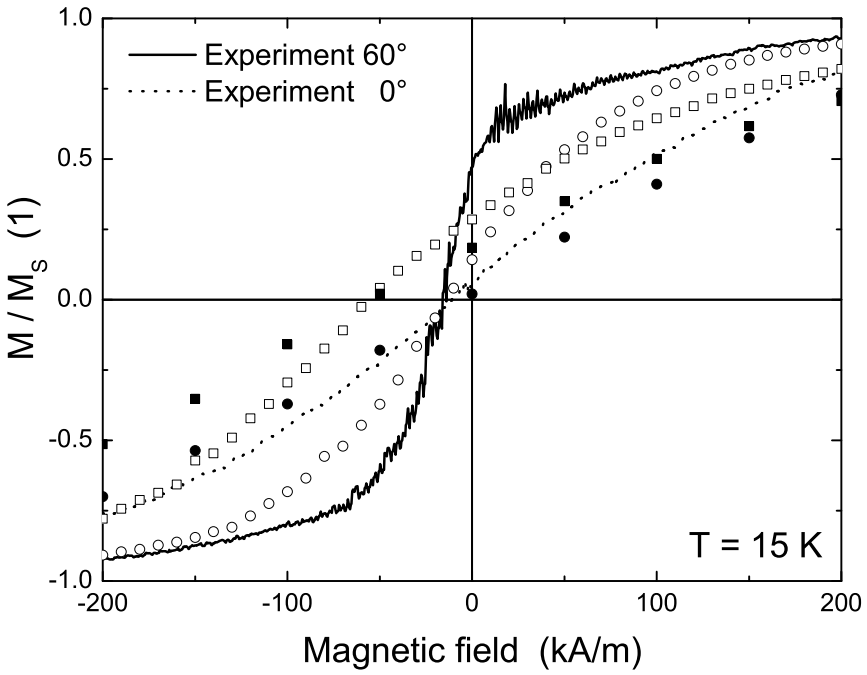

Figure 6.7.: Results of the simulations of the metallic Co particles array with a coverage of 1.7 monolayers taking into account dipolar coupling only ($C^* = 0$). The simulations were performed at polar angles of 0° (normal) and 60° according to the experiments shown as solid line (60°) and dotted line (0°) of the applied field with respect to the sample normal. For clarity, only the left part of the hysteresis is shown. The anisotropy constants are $K_2 = 0.2 \cdot 10^5$ J/m^3 (○ at 60° and • at 0°) and $K_2 = 2.0 \cdot 10^5$ J/m^3 (□ at 60° and ■ at 0°). The figure has been adapted from [151].

obvious from Figure 6.7 that magnetostatic interactions alone cannot describe the experiment satisfactory. The large discrepancy between experiment and simulations especially at an angle of 60° (open circles in Figure 6.7) shows that the consideration of dipolar interaction alone which energetically favors the in-plane direction overestimates the effective anisotropy present in the sample.

Consequently, one interactions is missing so far in the simulations, which is given by the exchange interaction between particles of the top and bottom layer in metallic contact to each other. The inclusion of this inter-particle exchange is well justified, since the organic ligands have been removed and the oxide shell has been reduced to metallic Co. Thus, the bigger top particles touch the smaller bottom ones. The averaged inter-particle exchange interaction is phenomenologically included in equation 6.2 by considering a non-vanishing exchange term ($C^* \neq 0$). The result is an increase of the remanence and an apparent enhancement of the out-

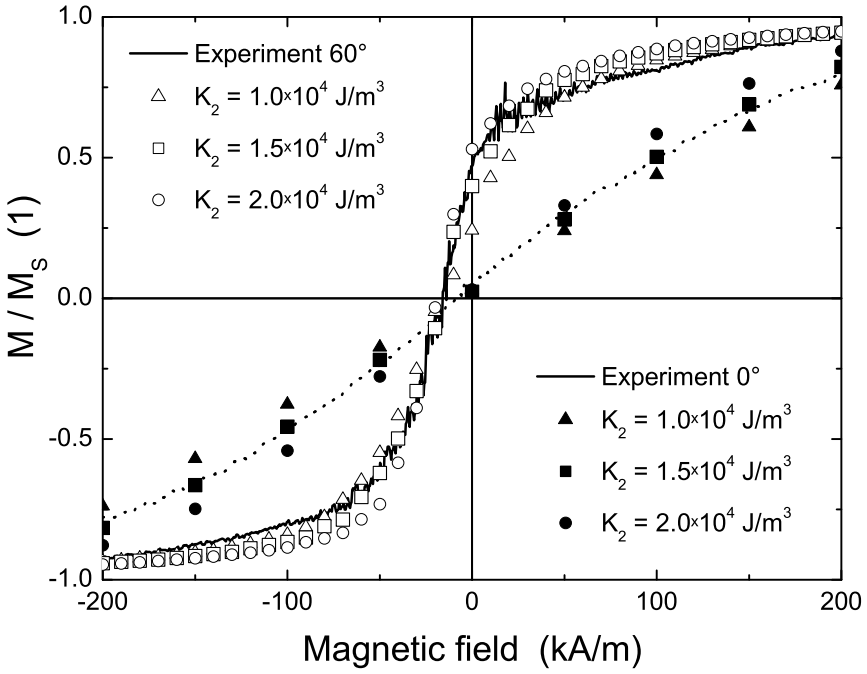

Figure 6.8.: Simulations of the Co nanoparticle array taking into account exchange interaction perpendicular to the surface ($C^* \neq 0$). The experimental hysteresis loops are shown as a solid line (60°) and a dotted line (0°). For clarity, only the left part of the symmetric hysteresis is shown. The second order anisotropy constants are given in the figure legend. The best result is obtained for $K_2 = 0.15 \cdot 10^5$ J/m^3. For details see text. The figure has been adapted from [151].

of-plane anisotropy which becomes understandable in terms of an additional shape anisotropy of the particles. The exchange interaction acts predominantly in a vertical direction between the particles in the top and bottom layer. The exchange interaction ties particles together from the bottom and the top layer forming a "new" particle with an elongated shape and shape anisotropy favoring a vertical magnetization direction.

The systematic variation of complete sets of simulations were performed for various values of $0 < C^* \leq 1$. The best result has been obtained for $C^* = 0.8$. The variation of the anisotropy constant K_2 yields the best agreement with $K_2 = 0.15 \cdot 10^5$ J/m^3 for both experimental hysteresis loops. The accuracy of the effective anisotropy constant is visible in Figure 6.8 for larger and smaller values of K_2. The anisotropy constant K_2 is about 25% of the bulk fcc Co value [2]. This low value can be explained by the polycrystalline fcc structure of the particles. Each nanoparticle consists of several tens to one hundred individual grains separated by twinning boundaries and imperfections of the crystallinity (see section 4 for details). The result of such a polycrystal

is a remarkably reduced magnetocrystalline anisotropy forming an effective uniaxial anisotropy as a sum of all grains.

To obtain a physical understanding of the parameter C^*, one may consider two ferromagnetic Co particles with parallel magnetization and diameters of 8 nm and 14 nm (bottom and top layer) which are in metallic contact to each other. Using the uniaxial anisotropy of $K_2 = 0.15 \cdot 10^5$ J/m^3, the bulk Co saturation magnetization $M_S = 1.4 \cdot 10^6$ A/m one can calculate that $C^* = 0.8$ is equivalent to an average exchange energy between the particles of about 170 meV. Assuming a bulk-like exchange energy ($\approx$ 20 meV per bond) one may conclude that eight to nine atoms of the top and bottom particle are in metallic contact to each other, which appears reasonable based on our SEM and AFM observations.

A. Self-assembly: Growth of Nanoparticle Dendritic Structures

The self-assembly of colloidal Co/CoO nanoparticles has been described in section 4.2. Another self-assembly mechanism - the ordering of hydrocarbons - is briefly discussed in this appendix. Wet-chemical prepared nanoparticles are usually coated by hydrocarbonic shells to prevent agglomeration of nanoparticles and make them soluble in organic solvents [115,119,154]. The bond of the polar head of the hydrocarbon stabilizer to the nanoparticles surface is not strong enough to form a fixed nanoparticle-hydrocarbon complex at ambient conditions. Hence, an excess supply of hydrocarbonic ligands (here oleic acid and oleyl amine) is used in the solution to substitute dissociated hydrocarbons from the nanoparticle surface. A dynamic equilibrium is adjusted to conserve isolated nanoparticles which results in a long term stability of the nanoparticle solution. If the excess surfactants is extremely increased the self-assembly process on flat substrates is not longer determined by the self-assembly properties of the nanoparticles but by the organization of free hydrocarbons.

In the experiments described in section 6.2 the solvent toluene has been exchanged by hexane to achieve enhanced wetting properties on naturally oxidized Si substrates. During this process 80% to 90% of the nanoparticles lost parts of their protective shell and agglomeration took place. By centrifugation of the nanoparticle solution at 14000 rounds per minute for 30 min the agglomerated nanoparticles sedimented to the bottom of the spinning vessel while the hydrocarbons remained in the solution enhancing the excess supply of ligands extremely. A 5 μl drop of a hexane-based Co/CoO nanoparticle solution was spin coated at 4000 rotations per minute on a native Si(001) substrate at room temperature. An array of Co particles with a coverage of 1.7 particle layers was formed over macroscopic areas (mm^2). After transfer into an ultrahigh vacuum chamber the ligand shell was removed and the CoO shell was transformed to metallic Co by a oxygen/hydrogen plasma treatment yielding an array of metallic particles partially in contact to each other. After the XAS/XMCD examination (section 6.2) the particle array has been examined by means of SEM and AFM.

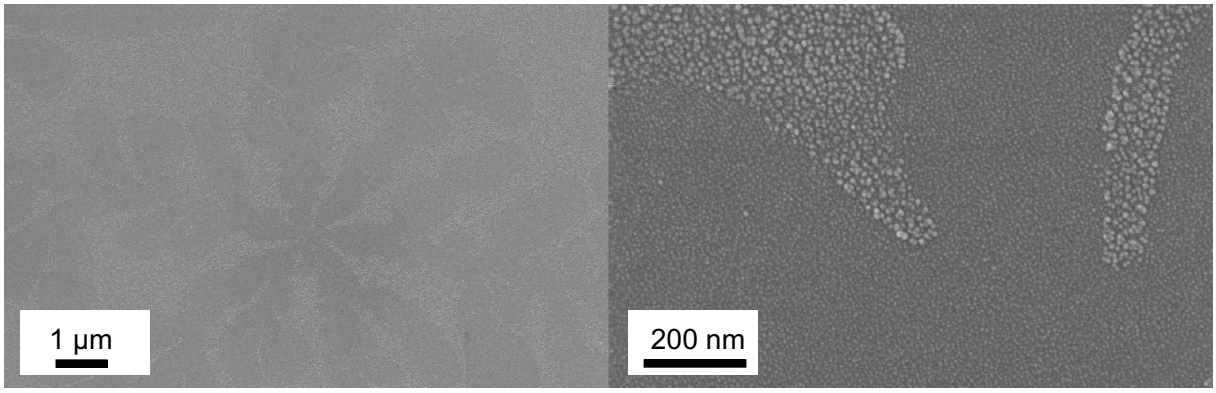

Figure A.1.: SEM images of Co particles on a $Si(001)$ substrate. The left image shows a low magnification. An dendritic structure is visible. The darker area consists of a single layer of nanoparticles while in the brighter area a double layer of particles has been formed. Single particles become visible on the high magnification image on the right hand side. The particles in the single layer region have a diameter of 8 nm while the top layer particles in the double layer region show a larger diameter of 14 nm (section 6.2).

Figure A.1 shows SEM images of the sample with different magnifications. On the left image areas of different brightness are visible. The right image with a higher magnification shows that the darker region consists of a single layer of 8 nm Co particles after the plasma exposure (compare to Figure 4.13). In the brighter region a double layer of particles has been formed. The bottom layer particles have a mean diameter of 8 nm while the top layer particles show a larger mean diameter of 14 nm after the plasma treatment.

The AFM imaging confirms the SEM results. Figure A.2 shows on the left a large scale AFM image. Obviously, a dentritic structure has been formed. The single leaves have a length of about 20 μm. The brighter region (double layer of particles) covers around 70% of the total sample area ($8 \cdot 4$ mm^2) and surrounds the dendrites. The right image in Figure A.2 presents a higher magnification of the single layer region. The AFM detects the dendrites as nearly flat. A maximum roughness about 1 nm has been observed. One may note that the standard Si tip used in the experiments with a tip radius of 30 nm cannot properly detect the height variation between the particles.

Dip-coating experiments of $FePt$ nanoparticles stabilized by oleic acid and oleyl amine and dispersed in hexane have shown that the excess surfactants dramatically change the self-assembly properties of particles on $Si(001)$ substrates [125]. Experiments by droplet evaporation of $FePt$ particles on native $Si(001)$ substrates can lead to the formation of self-organized dentritic structures [155]. An large-scale arrangement (mm^2), however, has not been observed. The importance of the free surfactants in the solution for the growth of dendrites can be un-

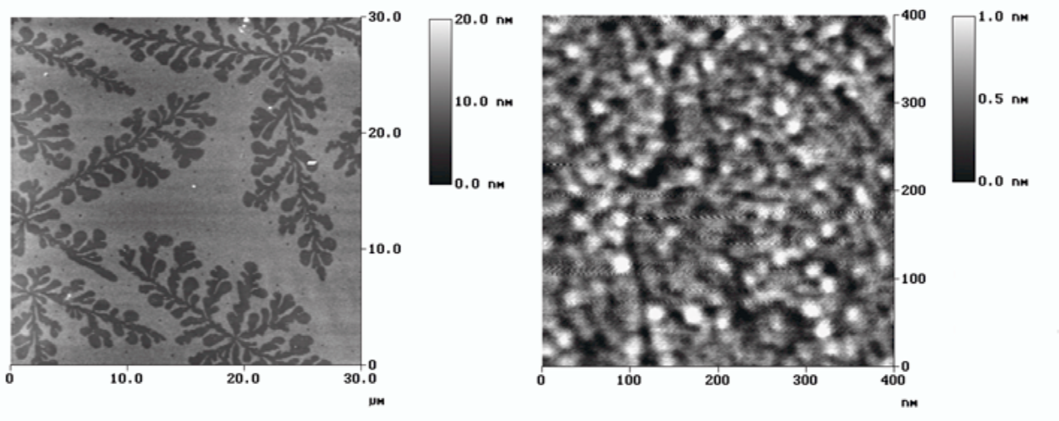

Figure A.2.: AFM images of Co particles on a $Si(001)$ substrate. The left image shows a large sample area. The darker region consists of a single layer of nanoparticles while in the brighter area a double layer of particles has been formed. The dendrites consists of leaves with a length of about 20 μm. The right image shows a higher magnification of the single layer region. For the AFM tip with a radius of 30 nm the single layer region appears nearly flat.

derstood in terms of self-assembly of alkanes on SiO_x/air interfaces. Triacontane [156], for example, forms similar dendritic structures as the ones observed in Figure A.2. The role of the removal of hydrocarbons by the plasma treatment remains unclear, so far. Interestingly, the inverse ordering of nanoparticles has been observed compared to the structure of alkanes. In sample regions, where the hydrocarbons have ordered, the nanoparticles have been found as single layers. In the region, which is not covered by the free hydrocarbons, more particles were deposited. During the plasma-assisted removal of the hydrocarbons the particles are free to sinter. To clarify the mechanisms of the dendritic growth of nanoparticles both, the self-assembly process and the morphological changes by the plasma treatment have to be studied in more detail.

B. Selected Area Electron Diffraction

Besides HR-TEM on single particles selected area electron diffraction (SAED) reflects another TEM-based method to determine the lattice structure of the nanoparticles. The SAED results of 11 nm Co/CoO particles are presented in this appendix. The diffraction pattern shown in Figure B.1 has been taken from about 100 particles deposited on a carbon-coated Cu grid. Several diffraction rings are visible. Most of the rings appear diffuse which is due to (i) the overlapping of fcc Co and fcc CoO rings and (ii) the poor crystallinity of the particles. The image has been calibrated by a Au specimen diffraction pattern by $Rd_{hkl} = \lambda L$ with R the radius of the diffraction ring, d_{hkl} the interplane spacing, and λL the camera constant. The diffraction rings could be ascribed to the fcc Co and fcc CoO as indicated in Figure B.1. The interplane spacings d_{hkl} and their relative intensities are listed in Table B.1 for fcc Co, fcc CoO, and the ϵ-*Co* lattices. The recently discovered ϵ-*Co* phase [157] has not been found in these nanoparticles. The diffraction rings of CoO appear (i) more pronounced and (ii) sharper in the diffraction pattern, since (i) the total CoO volume per particle is more than three times larger than the volume of metallic Co and (ii) Co shows a poor crystallinity within in the core as proven by HR-TEM images (Figure 4.2).

Table B.1.: Interplane spacings d_{hkl} for fcc Co (a = 0.3544 nm), fcc CoO (a = 0.4261 nm), and ϵ-*Co* (a = 0.6097 nm) lattice structures and their relative intensities. The data has been taken from [24,157,158].

fcc Co (a = 0.3544 nm)			fcc CoO (a = 0.4261 nm)			ϵ-*Co* (a = 0.6097 nm)		
hkl	d_{hkl}	rel. Intensity	hkl	d_{hkl}	rel. Intensity	hkl	d_{hkl}	rel. Intensity
111	0.2046	100	111	0.2455	100	221	0.2032	100
200	0.1772	40	200	0.2126	40	310	0.1928	58
220	0.1253	38	220	0.1503	38	311	0.1838	25
311	0.1069	50	311	0.1282	50	510	0.1196	21
222	0.1023	15	222	0.1227	15	520	0.1132	19

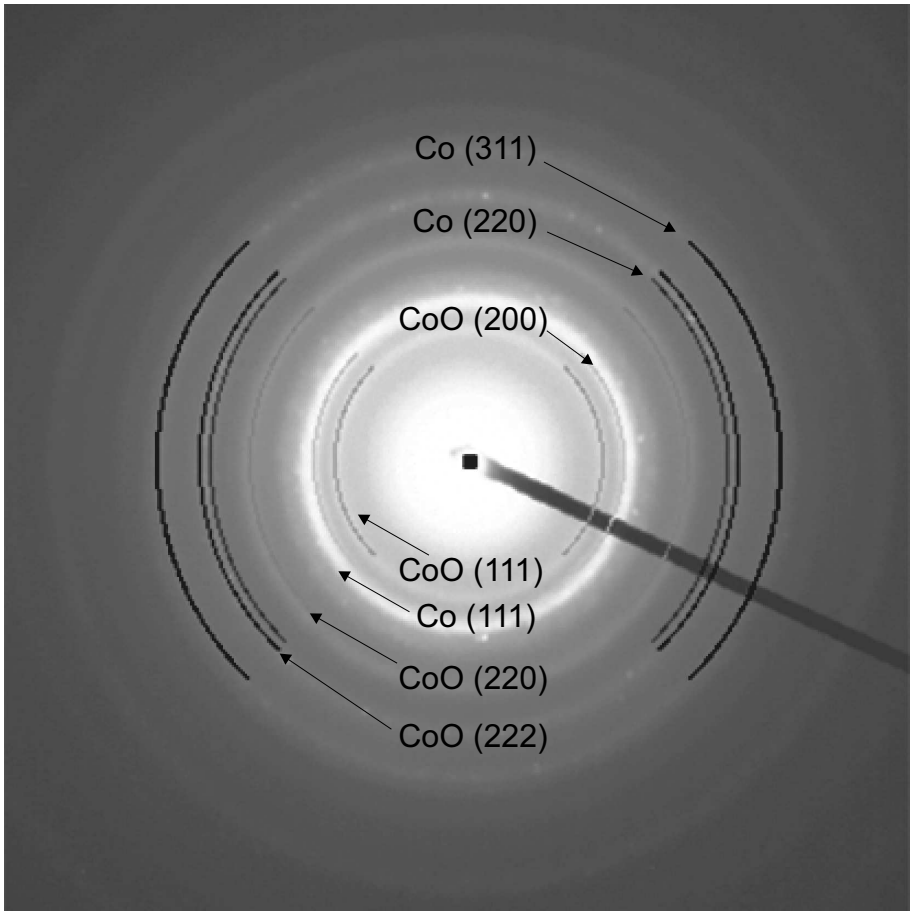

Figure B.1.: SAED pattern of 11 nm Co/CoO particles deposited on a carbon-coated Cu grid. The diffraction pattern has been calibrated by a Au reference. The diffraction rings could be ascribed to the fcc Co and fcc CoO lattice structures as indicated in the image.

References

[1] M. B. Stearns. *Magnetocrystalline anisotropy constant*, vol. Landold-Börnstein New Series III/19a. Springer-Verlag, Berlin (1986).

[2] C. A. F. Vaz, L. Lopez-Diaz, M. Kläui, J. A. C. Bland, T. L. Monchesky, J. Unguris, and Z. Cui. Direct observation of remanent magnetic states in epitaxial fcc Co small disks, Phys. Rev. B **67**, 140405 (2003).

[3] C. Kittel. *Einführung in die Festkörperphysik*. Oldenbourg Verlag, München, Wien (1999).

[4] Haken and Wolf. *Atom- und Quantenphysik*. Springer (1995).

[5] Sóshin Chikazumi. *Physics of Ferromagnetism*. Oxford University Press, 2nd ed. (1997).

[6] W. Jauch and M Reehuis. Electron density distribution in paramagnetic and antiferromagnetic CoO: A γ-ray diffraction study, Phys. Rev. B **65**, 125111 (2002).

[7] D. Jiles. *Introduction to Magnetism and Magnetic Materials*. Chapman and Hall (1991).

[8] Charles Kittel. On the Gyromagnetic Ratio and Spectroscopic Splitting Factor of Ferromagnetic Substances, Phys. Rev. **76**, 743 (1949).

[9] S. E. Apsel, J. W. Emmert, J. Deng, and L. A. Bloomfield. Surface-Enhanced Magnetism in Nickel Clusters, Phys. Rev. Lett. **76**, 1441 (1996).

[10] I. M. L. Billas, J. A. Becker, A. Chatelain, and W. A. de Heer. Magnetic moments of Iron Clusters with 25 to 700 Atoms and Their Dependence on Temperature, Phys. Rev. Lett. **71**, 4067 (1993).

[11] J. P. Bucher, D. C. Douglass, and L. A. Bloomfield. Magnetic Properties of Free Cobalt Clusters, Phys. Rev. Lett. **66**, 3052 (1991).

[12] D. C. Douglass, A. J. Cox, J. P. Bucher, and L. A. Bloomfield. Magnetic properties of free cobalt and gadolinium clusters, Phys. Rev. B **47**, 12874 (1993).

[13] J. T. Lau, A Föhlisch, R. Nietubye, M. Reif, and W. Wurth. Size-Dependent Magnetism of Deposited Small Iron Clusters Studied by X-ray Magnetic Circular Dichroism, Phys. Rev. Lett. **89**, 057201 (2002).

[14] P. Gambardella, S. Rusponi, M. Veronese, S. S. Dhesi, C. Grazioli, A. Dallmeyer, I. Cabria, R. Zeller, P. H. Dederichs, K. Kern, C. Carbone, and H. Brune. Giant Magnetic Anisotropy of Single Cobalt Atoms and Nanoparticles, Science **300**, 1130 (2003).

[15] P. Gambardella. Magnetism in monatomic metal wires, J. Phys.: Condens. Matter **15**, S2533 (2003).

[16] T. Koide, M. Miyauchi, J. Okamoto, T. Shidara, A. Fujimori, H. Fukutani, K. Amemiya, H. Takeshita, S. Yuasa, T. Katayama, and Y. Suzuki. Direct Determination of Interfacial Magnetic Moments with a Magnetic Phase Transition in Co Nanoclusters on Au(111), Phys. Rev. Lett. **87**, 257201 (2001).

[17] H. A. Dürr, S. S. Dhesi, E. Dudzik, D. Knabben, G. van der Laan, J. B. Goedkoop, and F. U. Hillebrecht. Spin and orbital magnetization in self-assembled Co clusters on Au(111), Phys. Rev. B **59**, R701 (1999).

[18] P. Gambardella, S. S. Dhesi, S. Gardonio, C. Grazioli, P. Ohresser, and C. Carbone. Localized Magnetic States of Fe, Co, and Ni Impurities on Alkali Metal Films, Phys. Rev. Lett. **88**, 047202 (2002).

[19] M. Respaud, J. M. Broto, H. Rakoto, A. R. Fert, L. Thomas, B. Barbara, M Verelst, E. Snoeck, P. Lecante, A. Mosset, J. Osuna, T. Ould Ely, C. Amiens, and B. Chaudret. Surface effects on the magnetic properties of ultrafine cobalt particles, Phys. Rev. B **57**, 2925 (1998).

[20] K. Zürn. Private communication. to appear in his PhD thesis (2004).

[21] M. Respaud, M Goiran, J. M. Broto, F. H. Yang, T. Ould Ely, C. Amiens, and B. Chaudret. High-frequency ferromagnetic resonance on ultrafine cobalt particles, Phys. Rev. B **59**, R3934 (1999).

[22] R. H. Kadoma. Magnetic nanoparticles, J. Magn. Magn. Mater. **200**, 359 (1999).

[23] H.-G. Boyen, G. Kästle, F. Weigl, P. Ziemann, K. Fauth, M. Heßler, G. Schütz, B. Stahl, J. Ellrich, H. Hahn, F. Banhart, M. Büttner, M. G. Garnier, and P. Oelhafen. Electronic and Magnetic Properties of Ligand-Free FePt Nanoparticles, submitted to Adv. Mater. (2003).

[24] W. Jauch, M. Reehuis, H. J. Bleif, and F. Kubanek. Crystallographic symmetry and magnetic structure of CoO, Phys. Rev. B **64**, 052102 (2001).

[25] M. R. Norman. Crystal-field polarization and the insulating gap in FeO, CoO, NiO, and La_2CuO_4, Phys. Rev. B **44**, 1364 (1991).

[26] C. F. J. Flipse, C. B. Rouwelaar, and F. M. F. de Groot. Magnetic properties of CoO nanoparticles, Eur. Phys. J. D **9**, 479 (1999).

[27] M. Verelst, T. Ould Ely, C. Amiens, E. Snoeck, P. Lecante, A. Mosset, M. Respaud, J. M. Broto, and B. Chaudret. Synthesis and Characterization of CoO, Co_3O_4 and Mixed Co/CoO Nanoparticles, Chem. Matter. **11**, 2702 (1999).

[28] M. Farle. Ferromagnetic resonance of ultrathin metallic layers, Rep. Prog. Phys. **61**, 755 (1998).

[29] W. Kleemann, O. Petracic, Ch. Binek, G. N. Kakazei, Yu. G. Pogorelov, J. B. Sousa, S. Cardoso, and P. P. Freitas. Interacting ferromagnetic nanoparticles in discontinuous Co80Fe20 'Al2O3 multilayers:, Phys. Rev. B **63**, 134423 (2001).

[30] S. Sahoo, O. Petracic, W. Kleemann, S. Stappert, G. Dumpich, P. Nordblad, S. Cardoso, and P. P. Freitas. Cooperative versus superparamagnetic behavior of dense magnetic nanoparticles in $Co_{80}Fe_{20}/Al_2O_3$ multilayers, Appl. Phys. Lett. **82**, 4116 (2003).

[31] J. H. van Vleck. On the Anisotropy of Cubic Ferromagnetic Crystals, Phys. Rev. **52**, 1178 (1937).

[32] J. Lindner. *Ferromagnetische Resonanz an ultradünnen magnetischen Einfach- und Mehrfachlagen der 3d-Übergangsmetalle - Statik und Dynamik*. Ph.D. thesis, Freie Universität Berlin (2002).

[33] S. V. Vonsovskii. *Ferromagnetic Resonance*. Pergamon Press Ltd. (1966).

[34] J. A. Osborn. Demagnetization Factors of the General Ellipsoid, Phys. Rev. **67**, 351 (1945).

[35] P. Bruno. Tight-binding approach to the orbital magnetic moment and magnetocrystalline anisotropy of transition-metal monolayers, Phys. Rev. B **39**, 865 (1989).

[36] C. Uiberacker, J. Zabloudil, P. Weinberger, L. Szunyogh, and C. Sommers. Lattice Relaxation Driven Reorientation Transition in $\mathrm{Ni_nCu(100)}$, Phys. Rev. Lett. **82**, 1289 (1999).

[37] O. Hjortstam, J. Trygg, J. M. Wills, B. Johansson, and O. Eriksson. Calculated spin and orbital moments in the surfaces of the 3d metals Fe, Co, and Ni and their overlayers on Cu(001), Phys. Rev. B **53**, 9204 (1996).

[38] A. Scherz, H. Wende, K. Baberschke, J. Minar, D. Benea, and H. Ebert. Relation between $L_{2,3}$ XMCD and the magnetic ground-state properties for the early 3d element V, Phys. Rev. B **66**, 184401 (2002).

[39] B. Nonas, I. Cabria, R. Zeller, P. H. Dederichs, T. Huhne, and H. Ebert. Strongly Enhanced Orbital Moments and Anisotropies of Adatoms on the Ag(001) Surface, Phys. Rev. Lett. **86**, 2146 (2001).

[40] O. Hjortstam, K. Baberschke, J.M. Wills, B. Johansson, and O. Eriksson. Magnetic anisotropy and magnetostriction in tetragonal and cubic Ni, Phys. Rev. B **55**, 15026 (1997).

[41] P. Bruno and J.-P. Renard. Magnetic surface anisotropy of transition metal ultrathin films, Appl. Phys. A **49**, 499 (1989).

[42] M. Spasova and M. Farle. Magnetism of monodisperse core/shell particles. In L. M. Liz-Marzán and M. Giersig, eds., *Low-Dimensional systems: Theory, Preparation, and Some Applications*, 173. Kluwer Academic Publishers (2003).

[43] R. C. O'Handley. *Modern Magnetic Materials: Principal and Applications*. Wiley-Interscience, New York (2000).

[44] E. C. Stoner and P. Wohlfarth. A mechanism of magnetic hysteresis in heterogeneous alloys, Philos. Trans. R. Soc. London **A240**, 599 (1948).

[45] L. Néel. Theorie du trainage magnetique des ferromagntiques en grains fins avec applications aux terres cuites, Ann. Geophys. **5**, 99 (1949).

[46] W. F. Brown Jr. Thermal Fluctuations of a Single-Domain Particle, Phys. Rev. **130**, 1677 (1963).

[47] J. Kliava and R. Berger. Size and shape distribution of magnetic nanoparticles in disordered systems: computer simulations of superparamagnetic resonance spectra, J. Magn. Magn. Mater. **205**, 328 (1999).

[48] C. Antoniak, J. Lindner, and M. Farle. Magnetic Anisotropy and its Temperature Dependence in Fe-rich Fe_xPt_{1-x} Nanoparticles, Euro Phys. Lett. in press (2005).

[49] K. Kopitzki. *Einführung in die Festkörpephysik*. Teubner, Suttgart (1993).

[50] J. M. Luttinger and L. Tisza. Theory of Dipole Interaction in Crystals, Phys. Rev. **70**, 954 (1946).

[51] S. Morup, P. H. Christensen, and B. S. Clausen. Magnetic hyperfine splitting in superparamagnetic particles in external magnetic fields, J. Magn. Magn. Mater. **68**, 160 (1987).

[52] W. Luo, S. R. Nagel, T. F. Rosenbaum, and R. E. Rosenzweig. Dipole interactions with random anisotropy in a frozen ferrofluid, Phys. Rev. Lett. **67**, 2721 (1991).

[53] M. Cerchez, L. Stoleriu, and A. Stancu. Magnetic characterization of strongly correlated magnetic particulate systems, J. Optoelectron. Adv. M. **5**, 933 (2003).

[54] A. E. Berkowitz and K. Takano. Exchange anisotropy - a review, J. Magn. Magn. Mater. **200**, 552 (1999).

[55] J. Nogués and I. K. Schuller. Exchange bias, J. Magn. Magn. Mater. **192**, 203 (1999).

[56] W. H. Meiklejohn and C. P. Bean. New Magnetic Anisotropy, Phys. Rev. **105**, 904 (1957).

[57] H. Ohldag, A. Scholl, F. Nolting, E. Arenholz, S. Maat, A. T. Young, M. Carey, and J. Stöhr. Correlation between Exchange Bias and Pinned Interfacial Spins, Phys. Rev. Lett. **91**, 017203 (2003).

[58] D. L. Peng, K. Sumiyama, T. Hihara, S. Yamamuro, and T. J. Konno. Magnetic properties of monodispersed Co/CoO clusters, Phys. Rev. B **61**, 3103 (2000).

[59] S. Gangopadhyay, G. C. Hadjipanayis, C. M. Sorensen, and K. J. Klabunde. Exchange anisotropy in oxide passivated Co fine particles, J. Appl. Phys. **73**, 6964 (1993).

[60] U. Wiedwald, J. Lindner, M. Spasova, Z. Frait, and M. Farle. Effect of an oxidic overlayer on the magnetism of Co nanoparticles, Phase Transit. **78**, 85 (2005).

[61] M. Spasova, T. Radetic, N. S. Sobal, M. Hilgendorff, U. Wiedwald, M. Farle, M. Giersig, and U. Dahmen. Structure and Magnetism of Co and AgCo Nanocrystals, Mat. Res. Soc. Symp. Proc. **721**, 195 (2002).

[62] A. P. Malozemoff. Mechanism of exchange anisotropy, J. Appl. Phys. **63**, 3874 (1988).

[63] M. D. Stiles and R. D. McMichael. Temperature dependence of exchange bias in polycrystalline ferromagnet-antiferromagnet bilayers, Phys. Rev. B **60**, 12950 (1999).

[64] F. Radu, M. Etzkorn, R. Siebrecht, T. Schmitte, K. Westerholt, and H. Zabel. Interfacial domain formation during magnetization reversal in exchange-biased CoO/Co bilayers, Phys. Rev. B **67**, 134409 (2003).

[65] V. Skumryev, S. Stoyanov, Y. Zhang, G. Hadjipanayis, D. Givord, and J. Nogués. Beating the superparamagnetic limit with exchange bias, Nature **423**, 850 (2003).

[66] I. N. Krivorotov, H. Yan, E. D. Dahlberg, and A. Stein. Exchange bias in macroporous Co/CoO, J. Magn. Magn. Mater. **226-230**, 1800 (2001).

[67] C. P. Poole. *Electron Spin Resonance*. Intercience Pulishers, New York (1967).

[68] G.E. Pake. *Paramagnetic Resonance*. W. A. Benjamin, New York (1962).

[69] J. W. Orton. *Electron Paramagnetic Resonance*. Gordon and Breach Science Publishers, New York (1968).

[70] J. Lindner and K. Baberschke. In situ ferromagnetic resonance: an ultimate tool to investigate the coupling in ultrathin films, J. Phys.: Condens. Matter **15**, R193 (2003).

[71] R. Meckenstock. *Untersuchung der magnetischen Eigenschaften von Fe/Ag-Schichtsystemen mit der konventionellen und der ortsaufgelösten ferromagnetischen Resonanz*. Ph.D. thesis, Ruhr-Universität Bochum (1997).

[72] B. Heinrich and J. A. C. Bland. *Ultrathin Magnetic Structures I and II*. Springer Verlag, Berlin (1994).

[73] J. Smith and H.-G. Beljers. Philips Res. Rep. **10**, 113 (1955).

[74] T. L. Gilbert. A Lagrangian Formulation of the Gyromagnetic Equation, Phys. Rev. **100**, 1243 (1955).

[75] F. Wiekhorst, E. Shevchenko, H. Weller, and J. Kötzler. Temperature-dependent anisotropy effects on FMR and magnetization of $FePt_2$- and $CoPt_3$-nanocrystals, J. Magn. Magn. Mater. **272-274**, 1559 (2004).

[76] U. Wiedwald, J. Lindner, M. Spasova, Z. Frait, M. Hilgendorff, M. Giersig, and M. Farle. Frequency- and temperature-dependent Ferromagnetic Resonance of Co/CoO core-shell nanoparticles, Mat. Res. Soc. Symp. Proc. **818**, M1.5 (2004).

[77] F. Wiekhorst, E. Shevchenko, H. Weller, and J. Kötzler. Anisotropic Superparamagnetism of Monodispersive Cobalt-Platinum Nanocrystals, Phys. Rev. B **67**, 224416 (2003).

[78] J. Pelzl, R. Meckenstock, D. Spoddig, F. Schreiber, J. Pflaum, and Z. Frait. Spin-orbit-coupling effects on g-value and damping factor of the ferromagnetic resonance in Co and Fe films, J. Phys.: Condens. Matter **15**, S451 (2003).

[79] J. Lindner. *Ferromagnetische Resonanz an ultradünnen magnetischen Einfach- und Mehrfachlagen der 3d-Übergangsmetalle - Statik und Dynamik*. Ph.D. thesis, Freie Universität Berlin (2002).

[80] M. Faraday. Experimental research in electricity: On the magnetization of light and the illumination of magnetic lines of force, Phil. Trans. Roy. Soc. London **136**, 1 (1846).

[81] J. Kerr. On rotation of the plane of polarization by reflection from the pole of a magnet, London, Edinburgh, and Dublin Phil. Mag. **3**, 321 (1877).

[82] B. Fromme. *d-d Exitations in Transition-Metal Oxides*. Springer, Berlin (2001).

[83] G. Schütz, W. Wagner, W. Wilhelm, P. Kienle, R. Zeller, R. Frahm, and G. Materlik. Absorption of circularly polarized x-rays in iron, Phys. Rev. Lett. **58**, 737 (1987).

[84] J. H. Hubbel. J. Phys. C **32**, 4 (1971).

[85] Reiko Nakajima, J. Stöhr, and Y. U. Idzerda. Electron-yield saturation effects in L-edge x-ray magnetic circular dichroism spectra of Fe, Co, and Ni, Phys. Rev. B **59**, 6421 (1999).

[86] J. Stöhr. *Elements of Modern X-ray Physics*. John Wiley & Sons, Ltd., Chichester, 1st ed. (2001).

[87] J. J. Rehr and R. C. Albers. Theoretical approaches to x-ray absorption fine structure, Rev. Mod. Phys. **72**, 621 (2000).

[88] V. L. Aksenov, A. Yu. Kuzmin, J. Purans, and S. I. Tyutunnikov. EXAFS Spectroscopy at Synchrotron-Radiation Beams, Physics of Particles and Nuclei **32**, 1 (2001).

[89] A. Scherz. *Spin-dependent X-ray Absorption Spectroscopy of 3d Transition Metals*. Ph.D. thesis, Freie Universität Berlin (2003).

[90] J. Stöhr and Y. Wu. *New Directions in Research with Third-Generation Soft X-ray Synchrotron Radiation Sources*. Kluwer Academic Publishers, Netherland (1994).

[91] T. J. Reagan, H. Ohldag, C. Stamm, F. Nolting, J. Lüning, J. Stöhr, and R. L. White. Chemical effects at metal/oxide interfaces by x-ray-absorption spectroscopy, Phys. Rev. B **64**, 214422 (2001).

[92] Fabrice Wilhelm. *Magnetic Properties of Ultrathin Films, Coupled Trilayers and 3d/5d Multilayers studied by X-ray Magnetic Circular Dichroism*. Ph.D. thesis, Freie Universität Berlin (2000).

[93] M. Tischer, O. Hjortstam, D. Arvanitis, J. Hunter Dunn, F. May, K. Baberschke, J. Trygg, J. M. Wills, B. Johansson, and O. Eriksson. Enhancement of Orbital Magnetism at Surfaces: Co on Cu(100), Phys. Rev Lett. **75**, 1602 (1995).

[94] K. Fauth et al. Total electron yield as a measure of x-ray absorption in nanoparticles, Preprint (2004).

[95] U. Wiedwald, M. Spasova, E. L. Salabas, M. Ulmeanu, M. Farle, Z. Frait, A. Fraile Rodriguez, D. Arvanitis, N. S. Sobal, M. Hilgendorff, and M. Giersig. Ratio of orbital-to-spin magnetic moment in Co core-shell nanoparticles, Phys. Rev. B **68**, 064424 (2003).

[96] H. Sakurai, F. Itoh, H. Oike, T. Tsurui, S. Yamamuro, K Sumiyama, and T. Hihara. X-ray magnetic circular dichroism on Co monodispersive cluster assemblies, J. Phys.: Condes. Matter **12**, 3451 (2000).

[97] A. J. Starace. Potential-Barrier Effects in Photoabsorption. I. General Theory, Phys. Rev. B **5**, 1773 (1972).

[98] B. T. Thole and G. van der Laan. Linear relation between x-ray absorption branching ratio and valence-band spin-orbit expectation value, Phys. Rev. A **38**, 1943 (1988).

[99] B. T. Thole, P. Carra, F. Sette, and G. van der Laan. X-ray circular dichroism as a probe of orbital magnetization, Phys. Rev. Lett. **68**, 1943 (1992).

[100] P. Carra, B. T. Thole, M. Altarelli, and X. D. Wang. X-ray circular dichroism and local magnetic fields, Phys. Rev. Lett. **70**, 694 (1993).

[101] M. Altarelli and P. Sainctavit. Sum Rules for XMCD. In *Magnetism and Synchrotron Radiation* (1996).

[102] B. K. Teo. *EXAFS: Basic Principles and Data Analysis*. Springer, Berlin (1986).

[103] R. Q. Wu and A. J. Freeman. Limitation of the MCD Spin Sum Rule and Importance of the Magnetic Dipole Term for Transition Metal Systems, Phys. Rev. Lett. **73**, 1994 (1994).

[104] C. T. Chen, Y. U. Idzerda, H.-J. Lin, N. V. Smith, G. Meigs, E. Chaban, G. H. Ho, E. Pellegrin, and F. Settle. Experimental Confirmation of the X-ray Magnetic Circular Dichroism Sum Rules for Iron and Cobalt, Phys. Rev. Lett. **75**, 152 (1995).

[105] D. S. Wang, R. Q. Wu, L. P. Zhong, and A. J. Freeman. First Principle Determination of Spin-orbit Induced Phenomena at Surfaces, Interfaces and Superlattices, J. Magn. Magn. Mater. **140-144**, 643 (1995).

[106] J. Stöhr. Exploring the microscopic origin of magnetic anisotropies with x-ray magnetic circular dichroism (XMCD) spectroscopy, J. Magn. Magn. Mater. **200**, 470 (1999).

[107] J. Stöhr, H. A. Padmore, S. Anders, T. Stammler, and M. R. Scheinfein. Principles of x-ray magnetic dichroism spectroscopy, Surf. Rev. Lett. **5**, 1297 (1998).

[108] D. Arvanitis, M. Tischer, J. Hunter Dunn, F. May, N. Martensson, and K. Baberschke. Experimental determination of the orbital and spin magnetic moments from MCXD on 3d metal overlayers. In H. Ebert and G. Schütz, eds., *Spin Influenced Spectroscopies of Magnetic Solids*. Spriger Verlag (1996).

[109] A. Hahlin. *Magnetism and Structure of Thin 3d Transition Metal Films*. Ph.D. thesis, Uppsala University, Sweden (2003).

[110] URL:. http://maxsun5.maxlab.lu.se/beamlines/bld1011 (2004).

[111] URL:. http://www.bessy.de/users_info/02.beamlines/linespdf/D_11_1A.pdf (2004).

[112] E. Goering, A. Fuss, W. Weber, J. Will, and G. Schütz. Element specific x-ray magnetic circular dichroism magnetization curves using total electron yield, J. Appl. Phys. **88**, 5920 (2000).

[113] D. L. Peng, K. Sumiyama, T. J. Konno, T. Hihara, and S. Yamamuro. Characteristic transport properties of CoO-coated monodispersive Co cluster assemblies, Phys. Rev. B **60**, 2093 (1999).

[114] J. S. Yin and Z. L. Wang. Synthesis of cobalt oxide nanocrystal self-assembled materials, J. Mater. Res. **14**, 503 (1999).

[115] M. Hilgendorff, B. Tesche, and M. Giersig. Creation of 3-D Crystals from Single Cobalt Nanoparticles in External Magnetic Fields, Aust. J. Chem. **54**, 497 (2001).

[116] H.-G. Boyen, G. Kästle, K. Zürn, T. Herzof, F. Weigl, P. Ziemann, O. Mayer, C. Jerome, M. Möller, J. P. Spatz, M. G. Garnier, and P. Oelhafen. A Micellar Route to Ordered Arrays of Magnetic Nanoparticles: From Size-Selected Pure Cobalt Dots to Cobalt-Cobalt Oxide Core-Shell Systems, Adv. Funct. Mater. **13**, 359 (2003).

[117] Shouheng Sun, C. B. Murray, Dieter Weller, and and Andreas Moser Liesl Folks. Monodisperse FePt Nanoparticles and Ferromagnetic FePt Nanocrystal Superlattices, Science **287**, 1989 (2000).

[118] D. Zitoun, M. Respaud, M.-C. Fromen, M. J. Casanove, P. Lecante, C. Amiens, and B. Chaudret. Magnetic Enhancement in Nanoscale CoRh Particles, Phys. Rev. Lett. **89**, 037203 (2002).

[119] N. S. Sobal, M. Hilgendorff, H. Möhwald, and M. Giersig. Synthesis and Structure of Colloidal Bimetallic Nanocrystals: The Non-Alloying System Ag/Co, Nano Lett. **2**, 621 (2002).

[120] V. F. Puntes and K. M. Krishnan. Synthesis, self-assembly, and magnetic behavior of a two-dimensional superlattice of single-crystal ϵ-Co nanoparticles, Appl. Phys. Lett **78**, 2187 (2001).

[121] J. S. Yin and Z. L. Wang. Ordered self-assembling of tetrahedral oxide nanocrystals, Phys. Rev. Lett. **79**, 2570 (1997).

[122] C. B. Murray, Shouheng Sun, W. Gaschler, H. Doyle, and C. R. Kagan. Colloidal synthesis of nanocrystals and nanocrystal superlattices, IBM J. Res. Dev. **45**, 47 (2001).

[123] C. B. Murray, Shouheng Sun, Hugh Doyle, and T. Betley. Monodisperse 3d Transition-Metal (Co, Ni, Fe) Nanoparticles and Their Assembly into Nanoparticle Superlattices, MRS Bulletin 985 (2001).

[124] K. Fauth. private communations.

[125] N. Shukla, J. Ahner, and D. Weller. Dip-coating of FePt nanoparticle films: surfactant effects, J. Magn. Magn. Mater. **272-276**, E1349 (2004).

[126] U. Wiedwald, M. Spasova, M. Farle, M. Hilgendorff, and M. Giersig. Ferromagnetic resonance of monodisperse Co particles, J. Vac. Sci. Technol. A **19**, 1773 (2001).

[127] M. Spasova, U. Wiedwald, R. Ramchal, M. Farle, M. Hilgendorff, and M. Giersig. Magnetic properties of arrays of interacting Co nanocrystals, J. Magn. Magn. Mater. **240**, 40 (2002).

[128] M. Sugawara. *Plama Etching. Fundamentals and Applicatios*. Oxford Science Publications (1998).

[129] Gerd Kaestle. *Electron Transport in nanomodulated, epitaxial Gold films*. Ph.D. thesis, Universität Ulm (2003).

[130] J. L. Dormann, L. Bessais, and D. Fiorani. A dynamic study of small interacting particles: superparamagnetic model and spin-glass laws, J. Phys. C: Solid State Phys. **21**, 2015 (1988).

[131] G. Ghiringhelli, L. H. Tjeng, A Tanaka, O. Tjernberg, T. Mizokawa, J. L. de Boer, and N. B. Brookes. 3d spin-orbit photoemission spectrum of nonferromagnetic materials: The test cases of CoO and Cu, Phys. Rev. B **66**, 075101 (2002).

[132] G. van der Laan and B. T. Thole. Strong magnetic x-ray dichroism in 2p absorption spectra of 3d transition-metal ions, Phys. Rev. B **43**, 13401 (1991).

[133] G. H. Wen, R. K. Zheng, K. K. Fung, and X. X. Zhang. Microstructural and magnetic properties of passivated Co nanoparticle films, J. Magn. Magn. Mater. **270**, 407 (2004).

[134] M. Spasova, U. Wiedwald, M. Farle, T. Radetic, U. Dahmen, M. Hilgendorff, and M. Giersig. Temperature dependence of exchange anisotropy in monodisperse cobalt nanoparticles with a cobalt oxide shell, J. Magn. Magn. Mater. **272-276**, 1508 (2004).

[135] U. Wiedwald, J. Lindner, M. Spasova, Z. Frait, M. Hilgendorff, M. Giersig, and M. Farle. Frequency- and temperature-dependent Ferromagnetic Resonance of Co/CoO core-shell nanoparticles, Mat. Res. Soc. Symp. Proc. **818**, M1.5 (2004).

[136] M. B. Stearns. *g factors and ferromagnetic resonance properties*, vol. Landold-Börnstein New Series III/19a. Springer-Verlag, Berlin (1986).

[137] B. Heinrich, J. F. Cochran, M. Kowalewski, J. Kirschner, Z. Celinski, A. S. Arrott, and K. Myrtle. Magnetic anisotropies and exchange coupling in ultrathin fcc Co(001) structures, Phys. Rev. B **44**, 9348 (1991).

[138] C. Raeder. Private communication (2004).

[139] C. Thirion, W. Wernsdorfer, and D. Mailly. Switching of magnetization by nonlinear resonance studied in single nanoparticles, Nature Materials **2**, 524 (2003).

[140] P. C. Scholten. Which SI?, J. Magn. Magn. Mater. **149**, 57 (1995).

[141] B. Heinrich, A. S. Arrot, J. F. Cochran, K. B. Urquhart, K. Myrtle, Z. Celinski, and Q. M. Zhong. In-SITU Techniques for Studying Epitaxially Grown Layers and Determining their Magnetic Properties, Mat. Res. Soc. Symp. Proc. **151**, 177 (1989).

[142] R. Ramchal. Aufbau und Inbetriebnahme eines Hochtemperatur-SQUID-Magnetometers und -Gradiometers, TU Braunschweig (2001).

[143] K. Fauth et al. Surface and volume contribution to the x-ray magnetic circular dichroism of supported nanoparticles, Preprint (2004).

[144] O. Eriksson, A. M. Boring, R. C. Albers, G. W. Fernando, and B. R. Cooper. Spin and orbital contributions to surface magnetism in 3d elements, Phys. Rev. B **45**, 2868 (1992).

[145] Jonathan Hunter Dunn. *Very Thin Magnets: X-rays, Lasers and Spectroscopy*. Ph.D. thesis, Uppsala University (1998).

[146] M. Hansen and K. Anderko. *Constitution of Binary Alloys*. Genium Publishing Corporation, 2nd edition ed. (1988).

[147] I. T. Belash, V. Yu. Malyshev, B. K. Ponomarev, E. G. Ponyatovskii, and A. Yu. Sokolov. Magnetization of coblat hydrides, Sov. Phys. Solid State **28**, 741 (1986).

[148] G. Alefeld and J. Völkl. *Hydrogen in metals*. Springer, Berlin (1978).

[149] W. Pepperhoff and M. Acet. *Constitution and Magnetism of Iron and its Alloys*. Springer, Berlin (2001). And references therin.

[150] U. Wiedwald et al. to be published.

[151] U. Wiedwald, M. Cerchez, M. Farle, K. Fauth, G. Schütz, K. Zürn, and H.-G. Boyen. Effective exchange interaction in a quasi-two dimensional self-assembled nanoparticle array, Phys. Rev. B **70**, 214412 (2004).

[152] P. R. Gilette and K. Oshima. Thin Film Magnetization Reversal by Coherent Rotation, J. Appl. Phys. **29**, 1465 (1958).

[153] M. El-Hilo, R. W. Chantrell, and K. O'Grady. A model of interaction effects in granular magnetic solids, J. Appl. Phys. **84**, 5114 (1998).

[154] M. Giersig and M. Hilgendorff. The preparation of ordered colloidal magnetic particles by magnetophoretic deposition, J. Phys. D: Appl. Phys **32**, L1 (1999).

[155] M. Ulmeanu and N. Friedenberger. private communications .

[156] A. Holzwarth, S. Leporatti, and H. Riegler. Molecular ordering and domain morphology of molecularly thin triacontane films at SiO_2/air interfaces, Europhys. Lett. **52**, 653 (2000).

[157] D. P. Dinega and M. G. Bawendi. Eine aus der Lösung zugängliche neue Kristallstruktur von Cobalt, Angew. Chem. **111**, 1906 (1999).

[158] NIST. PDF-2 powder diffraction database (Release 2003).

List of Publications / Contributions to Conferences

Publications in Refereed Journals

1. **Ferromagnetic Resonance of Monodisperse Co Particles**
   U. Wiedwald, M. Spasova, M. Farle, M. Hilgendorff, and M. Giersig
   J. Vac. Sci. Technol. A **19**, 1773 (2001)

2. **Magnetization and Magnetic Anisotropy of Co/W Multilayers**
   M. Spasova, U. Wiedwald, R. Ramchal, M. Farle, M. Jergel, E. Majkova, S. Luby, and R. Senderak
   Phys. Stat. Sol. (b) **225**, 449 (2001)

3. **Magnetic Properties of Arrays of Interacting Co Nanocrystals**
   M. Spasova, U. Wiedwald, R. Ramchal, M. Farle, M. Hilgendorff, and M. Giersig
   J. Mag. Mag. Mater. **240**, 40 (2002)

4. **Structure and Magnetism of Co and AgCo Nanocrystals**
   M. Spasova, T. Radetic, N. S. Sobal, M. Hilgendorff, U. Wiedwald, M. Farle, M. Giersig, and U. Dahmen
   Mat. Res. Soc. Symp. Proc. **721**, 195 (2002)

5. **Ratio of orbital-to-spin magnetic moment in Co core-shell nanoparticles**
   U. Wiedwald, M. Spasova, E. L. Salabas, M. Ulmeanu, M. Farle, Z. Frait, A. Fraile Rodriguez, D. Arvanitis, N. S. Sobal, M. Hilgendorff, and M. Giersig
   Phys. Rev. B **68**, 064424 (2003)

6. **Composition-dependent ratio of orbital-to-spin magnetic moment in structurally disordered $\mathrm{Fe_xPt_{1-x}}$ nanoparticles**
   M. Ulmeanu, C. Antoniak, U. Wiedwald, M. Farle, Z. Frait, and S. Sun
   Phys. Rev. B **69**, 054417 (2004)

7. **Temperature dependence of exchange anisotropy in monodisperse cobalt nanoparticles with a cobalt oxide shell**
   M. Spasova, U. Wiedwald, M. Farle, T. Radetic, U. Dahmen, M. Hilgendorff, and M. Giersig
   J. Magn. Magn. Mater. **272-276**, 1508 (2004)

8. **Local structure of monodisperse Co nanoparticles**
   A. Fraile Rodriguez, N. S. Sobal, U. Wiedwald, M. Spasova, M. Hilgendorff, M. Giersig, M. Farle, and D. Arvanitis
   J. Magn. Magn. Mater. **272-276**, E1207 (2004)

9. **Frequency- and temperature-dependent Ferromagnetic Resonance of Co/CoO core-shell nanoparticles**
   U. Wiedwald, J. Lindner, M. Spasova, Z. Frait, M. Hilgendorff, M.Giersig, and M. Farle
   Mat. Res. Soc. Symp. Proc. **818**, M1.5 (2004)

10. **Effective exchange interaction in a quasi-two-dimensional self-assembled nanoparticle array**
    U. Wiedwald, M. Cerchez, M. Farle, K. Fauth, G. Schütz, K. Zürn, H.-G. Boyen, and P. Ziemann
    Phys. Rev. B **70**, 214412 (2004)

11. **Effect of an oxidic overlayer on the magnetism of Co nanoparticles**
    U. Wiedwald, J. Lindner, M. Spasova, Z. Frait and M. Farle
    Phase Transit. **78**, 85 (2005)

12. **Magnetic properties of quasi-monolayers of Co metallic nanoparticles by in-situ experiments and simulations**
    M. Cerchez, U. Wiedwald, and M. Farle
    J. Magn. Magn. Mater. in press

13. **Ferromagnetic Resonance: An Ultimate Tool to Study the Dynamical Resoponse of Nanostructured Magnetic Systems**
    J. Lindner, U. Wiedwald, K. Baberschke, and M. Farle
    J. Vac. Sci. Technol. in press

14. **From Colloidal Co/CoO Nanoparticles to Arrays of Metallic Nanomagnets: Surface Modification by Plasma Processing and its Impact on Magnetic Properties**
    U. Wiedwald, K. Fauth, M. Hessler, H.-G. Boyen, F. Weigl, M. Hilgendorff M. Giersig, G. Schütz P. Ziemann, and M. Farle
    submitted to Chem Phys Chem

Reports and Contributions to Books

1. **Ordered Arrays of Magnetic Nanoscale Particles: Core level spectroscopic investigations**
   U. Wiedwald, E. L. Bizdoaca, M. Spasova, and M. Farle
   Max-Lab Activity Report 2000

2. **Ordered Arrays of Magnetic Nanoscale Particles: Composition dependence of the orbital magnetic moment**
   U. Wiedwald, M. Ulmeanu, M. Farle, N. S. Sobal, M. Giersig, A. Fraile Rodriguez, and D. Arvanitis
   Max-Lab Activity Report 2001

3. **Characterization of Nanoparticles for magnetic data storage media**
   U. Wiedwald and M. Albrecht
   Magnetische Dünnschichtmedien, DVD, Halbleiterspeicher, ... - was kommt danach? ed. by M. Albrecht, PTB Bericht E-78, ISBN 3-89701-911-6

4. **X-ray Absorption Spectroscopy and X-ray Magnetic Circular Dichroism of $\mathbf{Ag}_x\mathbf{Co}_{100-x}$ Nanoparticles**
   U. Wiedwald, M. Spasova, M. Farle, N. S. Sobal, M. Giersig, A. Fraile Rodriguez, and D. Arvanitis
   Max-Lab Activity Report 2002

Invited Talks

1. U. Wiedwald and M. Albrecht, *Characterization of Nano-particles for magnetic data storage media*, Seminar of the Physikalisch-Technische Bundesanstalt, Germany, 2002, February 27

2. U. Wiedwald, *Bestimmung der magnetischen Anisotropieenergie von Co Nanopartikeln*, Zweites Physikalisches Institut, Universität Göttingen, 2002, July 1

3. U. Wiedwald, *g-factor and ratio of orbital-to-spin magnetic moment in Co/CoO nanoparticles*, Struktur und Magnetismus ultradünner Metallfilme VII, Chandolin, Switzerland, 2003, January 28

4. U. Wiedwald, M. Spasova, and M. Farle, *Self-organization and Intrinsic Magnetism of Co nanoparticles*, Structure and Dynamics of Heterogeneous Systems - SDHS'03, Duisburg, Germany, 2003, November 20-21

5. U. Wiedwald, *Grenzschichtmagnetismus in Co/CoO Kern-Hülle Partikeln*, Kolloquium des Sonderforschunsbereichs 569, Universität Ulm, Germany, 2004, October 8

Contributions to Conferences

1. M. Spasova, U. Wiedwald, R. Ramchal, M. Farle, S. Luby, R. Senderak, and E. Majkova, Magnetization and Magnetic Anisotropy of Co/W Multilayers, Frühjahrstagung der DPG, Regensburg, Germany, 2000 - poster

2. U. Wiedwald, M. Spasova, M. Farle, M. Giersig, and M. Hilgendorff, Ferromagnetische Resonanz an monodispersen Co-Partikeln, DFG Rundgespräch Anwendung der magnetischen Resonanz in der Bio- und Materialwissenschaft, Hirschegg, Austria, 2000 - poster

3. M. Spasova, M. Farle, U. Wiedwald, J. Kliava, M. Hilgendorff, and M. Giersig, Structure and Magnetic Properties of Arrays of Interacting Single-domain Co Particles, 1st Workshop on Correlation of Structure and Magnetism in Novel Nanoscale Magnetic Particles, Smolenice Castle, Slovakia, 2000 - poster

4. U. Wiedwald, M. Spasova, M. Hilgendorff, M. Giersig, and M. Farle, Ferromagnetische Resonanz an hexagonalen Netzwerken aus monodispersen Co-Partikeln, Frühjahrstagung der DPG, Hamburg, Germany, 2001 - talk

5. M. Spasova, U. Wiedwald, R. Ramchal, M. Farle, M. Hilgendorff, and M. Giersig, Magnetic Properties of Magnetophoretically Deposited Co Nanocrystals, Joint Summer Workshop on Mesomagnetism, Spin Dynamics and Spin Electronics, Santorini, Greece, 2001 - poster

6. U. Wiedwald, M. Spasova, E. L. Bizdoaca, M. Farle, T. Radetic, and U. Dahmen, Struktur und Magnetismus von zweidimensional angeordneten monodispersen Co Nanokristallen, Frühjahrstagung der Deutschen Physikalischen Gesellschaft, Regensburg, Germany, 2002, March - talk

7. U. Wiedwald, M. Spasova, E. L. Bizdoaca, M. Farle, T. Radetic, U. Dahmen, A. Popa, U. Ebels, A. Hahlin, D. Arvanitis, M. Hilgendorff, and M. Giersig, Magnetic Properties of Co/CoO nanoparticles, 4th Workshop on Correlation of Structure and Magnetism in Novel Nanoscale Magnetic Particles, Autrans, France, 2002, March 15 - talk

8. U. Wiedwald, M. Bleckmann, C. Antoniak, M. Ulmeanu, M. Farle, S. Martinez-Mendez, F. Gonzales-Gimenez, C. Amiens, and B. Chaudret, Ferromagnetic resonance of FeNi nanoparticles from 5 to 375 K, 4th Workshop on Correlation of Structure and Magnetism in Novel Nanoscale Magnetic Particles, Autrans, France, 2002, March 16 - talk

9. U. Wiedwald, M. Spasova, M. Ulmeanu, E. L. Bizdoaca, N. S. Sobal, A. Fraile Rodriguez, M. Bleckmann, M. Hilgendorff, M. Giersig, and M. Farle, Magnetic Resonance and X-ray Magnetic Circular Dichroism of Monodisperse Co Nanoparticles, 281. WE Heraeus Seminar, Spin-Orbit Interaction and Local Structure in Magnetic Systems with Reduced Dimensions, Wandlitz, Germany, 2002, June 13 - poster

10. U. Wiedwald, M. Spasova, M. Ulmeanu, E. L. Bizdoaca, M. Farle, A. Fraile Rodriguez, D. Arvanitis, N. S. Sobal, M. Hilgendorff, M. Giersig, Z. Frait, T. Radetic, and U. Dahmen, Magnetic Resonance and X-ray Magnetic Circular Dichroism of Monodisperse Co Nanoparticles, 5th Workshop on Correlation of Structure and Magnetism in Novel Nanoscale Magnetic Particles, Thessaloniki, Greece, 2002, October 4 - talk

11. U. Wiedwald, M. Spasova, M. Ulmeanu, E. L. Bizdoaca, M. Farle, Z. Frait, A. Fraile Rodriguez, D. Arvanitis, N. S. Sobal, M. Hilgendorff, M. Giersig, T. Radetic, and U. Dahmen, Magnetic Resonance and X-ray Magnetic Circular Dichroism of Monodisperse Co Nanoparticles, AVS 49th International Symposium, Denver, Co, USA, 2002, November 4 - talk

12. U. Wiedwald, M. Spasova, C. Raeder, M. Farle, T. Radetic, U. Dahmen, N. S. Sobal, M. Hilgendorff, and M. Giersig, Structure and Magnetism of Colloidal Composite AgCo Nanoparticles", AVS 49th International Symposium, Denver, Co, USA, 2002, November 4 - talk

13. U. Wiedwald, M. Spasova, Z. Frait, M. Hilgendorff, M. Giersig, and M. Farle, Orbital Magnetism in 12 nm monodisperse Co/CoO nanoparticles studied by XMCD and Magnetic Resonance, 6th Workshop on Correlation of Structure and Magnetism in Novel Nanoscale Magnetic Particles, Duisburg, Germany, 2003, March 21 - poster

14. U. Wiedwald, M. Spasova, N. Sobal, Z. Frait, M. Hilgendorff, M. Giersig, and M. Farle, Erhöhtes Bahnmoment und Exchange Bias in kolloidalen Co/CoO Nanopartikeln, Frühjahrstagung der Deutschen Physikalischen Gesellschaft, Dresden, Germany, 2003, March 24 - talk

15. M. Spasova, U. Wiedwald, M. Farle, T. Radetic, U. Dahmen, M. Hilgendorff, and M. Giersig, Temperature dependence of exchange anisotropy in monodisperse 12 nm Co nanoparticles with a CoO shell, Structure and Dynamics of Heterogeneous Systems - SDHS'03, Duisburg, Germany, 2003, November 20-21 - poster

16. U. Wiedwald, M. Spasova, and M. Farle, Orbital magnetism of metallic, non-oxidized Co nanoparticles, Combined Winter Workshop and School on Correlation of Structure and Magnetism in Novel Nanoscale Magnetic Particles, Bonn, Germany, 2004, February 25-29 - talk

17. U. Wiedwald, M. Spasova, K. Fauth, M. Hessler, H.-G. Boyen, and M. Farle, Orbital Magnetism in Monodisperse Co/CoO Nanoparticles, Spring Meeting of the Material Research Society IUMRS-ICEM, San Francisco, CA, 2004, April 12-16 - talk

18. U. Wiedwald, K. Fauth, H.-G. Boyen, J. Lindner, M. Spasova, and M. Farle, Magnetic hardening of Co nanoparticles by an oxidic overlayer, Satellite Workshop "Nanoparticles: Synthesis, Characterization and Properties" of the 7^{th} International Conference on Nanostructured Materials, Duisburg, Germany, 2004 June 25-26 - poster

19. U. Wiedwald, K. Fauth, H.-G. Boyen, P. Ziemann, Z. Frait, J. Lindner, M. Spasova, and M. Farle, Interface Magnetism in Co/CoO core-shell nanoparticles, 338. WE Heraeus Seminar, Nanomagnetism: New Insights with Synchrotron Radiation, Bad Honnef, Germany, 2005, January 5-7 - poster

Acknowledgments

The collected results achieved in a Ph. D. thesis are never the work of one person alone. I would like to thank all the persons who contributed in various ways in the realization of this thesis.

First of all, it is a honor for me to express all my gratitude to Prof. Dr. Michael Farle, who supervised this work with great enthusiasm throughout the years. His patience in teaching and the support of young scientists are really outstanding. Especially his faith in me managing beamtimes at the synchrotron facilities generated both, self assurance and a tired Ph. D. student.

I appreciate Dr. Marina Spasova who co-supervised this work from the very beginning. Her interest in science is exceptional and does not stop after office hours. Marina, thanks a lot for the successful collaborations in the last years. I wish you all the best and great success for your future in physics as well as in your private life.

Dr. Michael Hilgendorff and Prof. Dr. Michael Giersig who provided me several batches of Co/CoO nanoparticles are gratefully acknowledged. M. H. is thanked for the patience in explaining chemical problems in the sample preparation in a for a physicist understandable way.

For stimulating discussions and the use of the end station at BESSY II with high magnetic field I would like to thank Dr. Kai Fauth. He brought me some more insight into x-ray absorption spectroscopy. His curiosity and perseverance in physics are exemplary. I owe him the insight that some pencils are paramagnetic and some diamagnetic.

Priv. Doz. Dr. Hans-Gerd Boyen gave very useful hints and advices for sample preparation of two-dimensional arrays of nanoparticles. The use of his home-built plasma etching chamber brought new aspects of pure metallic nanoparticles into this thesis.

Dr. Zdenek Frait contributed high-frequency FMR measurements putting the g-factor determination on a solid base. His 50 years of experience in science brought a couple of old ideas into the student's mind.

Dr. Mihai Cerchez has performed the micromagnetic simulations of hysteresis loops of metallic particles. The interaction between experiment and theory worked ideally in our collaboration. Thank you, Mihai!

Dr. Jürgen Lindner is acknowledged for many discussions, especially about the interpretation of FMR spectra in nanoparticle systems. I wish you great success with all the projects you started in Duisburg.

The former "Braunschweig-Crew" Dr. Lorena Salabas, Dr. Magdalena Ulmeanu, Carolin Antoniak, Robert Ramchal and Christian Raeder made things often easier in Braunschweig as well as in the start-up period in Duisburg. Christian and Robert, nearly ten years we went together through the world of physics. Thanks a lot and all the best for the future! Thomas Kebe and Khalil Zakeri Lori are acknowledged for beeing cooperative colleagues sharing the office with me. Thomas Kebe is acknowledged for the AFM images.

Without the nanoparticle imaging techniques the correlation of structure and magnetism would not be possible. Burkhard Stahlmecke, Dr. Sonja Stappert and Dr. Britta Hausmanns are acknowledged for image acquisition.

Beamtimes at synchrotron facilities require the help of many hands. Prof. Dr. M. Acet, Prof. Dr. Dimitri Arvanitis, Matthias Bleckmann, Dr. Johannes Eisenmenger, Dr. Arantxa Fraile Rodríguez, Dr. Anders Hahlin, Markus Heßler, Dr. Gerd Kästle, Dr. Nelli Sobal, Frank Weigl, and Klaus Zürn are gratefully acknowledged. I would like to thank the MAX-Lab and BESSY II staff for their encouragement.

As representants of the technical staff Lutz Nagatz and Lutz Nowacki from the University of Braunschweig and Dieter Schädel and Horst Zähres from Duisburg I appreciate for solving technical problems, e. g. in sample holder design.

All other member of the "Experimentalphysik - AG Farle" I would like to thank for the stimulating discussions and their cooperative attitude. Especially the team assistance is acknowledged for their help in administration.

Finally, I appreciate my parents Erhard and Gudrun Wiedwald who brought me with their education, patience, and financial support where I stand now. Dr. Astrid Westendorf I thank for her love and support.